STUDY OF THE EFFECTS OF UNSTEADY HEAT RELEASE IN COMBUSTION INSTABILITY

A Dissertation

Submitted to the Faculty

of

Purdue University

by

Arnau Pons

In Partial Fulfillment of the

Requirements for the Degree

of

Doctor of Philosophy

August 2020

Purdue University

West Lafayette, Indiana

THE PURDUE UNIVERSITY GRADUATE SCHOOL
STATEMENT OF DISSERTATION APPROVAL

Prof. William E. Anderson, Chair

School of Aeronautics and Astronautics

Prof. Charles L. Merkle

School of Mechanical Engineering, and School of Aeronautics and Astronautics

Prof. Carson Slabaugh

School of Aeronautics and Astronautics

Prof. Carlo Scalo

School of Mechanical Engineering

Dr. Swanand Sardeshmukh

School of Aeronautics and Astronautics

Approved by:

Prof. Gregory A. Blaisdell

Head of the Graduate Program

To my family and friends. Per aspera ad astra.

ACKNOWLEDGMENTS

First of all, I would like to thank my advisor Prof. William Anderson for giving me this wonderful opportunity and for his continuous guidance and insightful advice. I would also like to acknowledge the thoughtful comments of my committee members, Dr. Merkle, Dr. Slabaugh, Dr. Scalo and Dr. Sardeshmukh. Their inputs inspired me to seek a deeper understanding in this research.

I would also like to acknowledge the support of the Obra Social "la Caixa" Fellowship Program for the financial support provided for my Ph.D. studies at Purdue University. In addition, I would also like to thank the financial support received from the Air Force Office of Scientific Research, and the Air Force Center of Excellence Multy-Fidelity Modeling of Rocket Combustion Dynamics with Dr. Mitat Birkan as program manager.

I would like to thank Dr. Swanand V. Sardeshmukh for his help and mentorship on high-fidelity simulations as well as my fellow colleagues, Dr. Gowtham Manikanta Reddy Tamanampudi, Dr. Tristan Fuller, Mr. Michael Orth and Dr. Michael Bedard. All in all, I would like to show my gratefulness to all the Zucrow team for their kindness and friendship over this time. A special mention goes to my fellow magnificent seven Rufat, Timo, Kota, Vlad, Dasheng, and Wes.

I would like to acknowledge the encouragement of my parents, sister, grandma, and entire family to complete this studies. I would also like to acknowledge the support received from the Space Generation Advisory Council family during all this time. Foremost, I would like to thank my wife Orzuri for her unwavering support, help, love, and patience.

TABLE OF CONTENTS

LIST OF TABLES

LIST OF FIGURES

Figure Page

Figure Page

Figure Page

Figure Page

Figure Page

Figure Page

Figure Page

Figure Page

Figure Page

SYMBOLS

A_{p1}, A_{p2}, A_{p3},	Pressure amplitude constant
A_{p4}, A_{p5}, A_{p6}	of profiles 1, 2, 3, 4, 5, and 6
c	Speed of Sound [m/s]
c_p	Constant pressure specific heat capacity [J/kg/K]
c_v	Constant volume specific heat capacity [J/kg/K]
Da	Damköhler number
e	Specific internal energy [J/kg]
E_{ha}	Total energy of heat addition [J]
f	Frequency [Hz]
$\vec{f_b}$	Body force per unit mass [m/s^2]
h	Specific enthalpy [J/kg]
He	Helmholtz number
H_{ha}	Height of heat addition source [m]
K_{ha1}, K_{ha2}, K_{ha3},	Heat source magnitude
K_{ha4}, K_{ha5}, K_{ha6}	of profiles 1, 2, 3, 4, 5, and 6
L_{ha}	Length of heat addition source [m]
p	Pressure [Pa]
q	Volumetric heat release rate [W/m^3]
q_{ha}	Flat profile volumetric heat addition [W/m^3]
R_u	Universal gas constant [J/mol/K]
s	Specific entropy [J/kg/K]
T	Temperature [K]
t_{hab}	Time heat addition begins [s]
t_{hae}	Time heat addition ends [s]
$\vec{u}$	Velocity vector [m/s]

u	Velocity in the x-direction [m/s]
v	Velocity in the y-direction [m/s]
V	Volume [m^3]
V_{ha}	Volume of heat addition source [m^3]
w	Velocity in the z-direction [m/s]
W	Molecular weight [kg/mol]
W_{ha}	Depth of heat addition source [m]
x_{hac}	x-coordinate of the center of heat addition application [m]
γ	Ratio of specific heats
Δt_{ha}	Duration of heat addition [s]
ζ_{xt}	Ratio of characteristic times
λ	Thermal conductivity [W/m/K]
μ	Dynamic viscosity [Pa·s]
ρ	Density [kg/m^3]
σ_x	Standard deviation of the Gaussian spatial distribution [m]
σ_t	Standard deviation of the Gaussian temporal distribution [s]
$\vec{\vec{\tau}}$	Viscous stress tensor [Pa]
τ_{ac}	Characteristic acoustic time [s]
ϕ_{pq}	Phase shift between the longitudinal fluctuating pressure and the heat source
ω	Angular frequency [rad/s]

Subscripts

0	Mean flow value
1	Small-amplitude linear fluctuation value
cr	Critical value
ff	Far field

ABBREVIATIONS

CFD	Computational fluid dynamics
CVC	Constant volume combustion
CVRC	Continuously variable resonance combustors
DES	Detached eddy simulation
DNS	Direct numerical simulation
GEMS	Purdue's in-house Navier-Stokes solver "General Equation and Mesh Solver"
LEE	Linearized Euler equations
LES	Large eddy simulation
PDE	Partial differential equation
PR	Peng-Robinson equation of state
RANS	Reynolds-averaged Navier-Stokes
TIC	Transverse instability combustor
TPG	Thermally perfect gas

ABSTRACT

Pons, Arnau Ph.D., Purdue University, August 2020. Study of the effects of unsteady heat release in combustion instability. Major Professor: William E. Anderson.

Rocket combustors and other high-performance chemical propulsion systems are prone to combustion instability. Recent simulations of rocket combustors using detailed chemical kinetics show that the constant pressure assumption used in classical treatments may be suspect due to high rates of heat release. This study is a exploration on the effects of these extraordinary rates of heat addition on the local pressure field, and interactions between the heat release and an acoustic field.

The full problem is decomposed into simpler unit problems focused on the particular interactions of physical phenomena involved in combustion instability. The overall strategy consists of analyzing fundamental problems with simplified scenarios and then build up the complexity by adding more phenomena to the analysis. Seven unit problems are proposed in this study.

The first unit problem consists of the pressure response to an unsteady heat release source in an unconfined one-dimensional domain. An analytical model based on the acoustic wave equation with planar symmetry and an unsteady heat source is derived and then compared against results from highly-resolved numerical simulations. Two different heat release profiles, one a Gaussian spatial distribution with a step temporal profile, and the other a Gaussian spatial distribution with a Gaussian temporal distribution, are used to model the heat source. The analytical solutions predict two different regimes in the pressure response depending on the Helmholtz number, which is defined as the ratio of the acoustic time over the duration of the heat release pulse. A critical Helmholtz number is found to dictate the pressure response regime. For compact cases, in the subcritical regime, the amplitude of the pressure pulse remains

constant in space. For noncompact cases, above the critical Helmholtz number, the pressure pulse reaches a maximum at the center of the heat source, and then decays in space converging to a lower far field amplitude. At the limits of very small and very large Helmholtz numbers, the heat release response tends to be a constant pressure process and a constant volume process, respectively. The parameters of the study are chosen to be representative of the extreme conditions in a rocket combustor. The analytical models for both heat source profiles closely match the simulations with a slight overprediction. The differences observed in the analytical solutions are due to neglecting mean flow property variations and the absence of loss mechanisms. The numerical simulations also reveal the presence of nonlinear effects such as weak shocks that cannot be captured by the linear acoustic wave equation.

The second unit problem extends the analysis of the pressure response of an unsteady heat release source to an unconfined three-dimensional domain. An analytical model based on the spherical acoustic wave equation with an unsteady heat source is derived and then compared against results from highly-resolved three-dimensional numerical simulations. Two different heat release profiles, a three-dimensional Gaussian spherical distribution with either a step or a Gaussian temporal distribution, are used to model the heat source. Two different regimes in the pressure response depending on the Helmholtz number are found. This analysis also reveals that whereas for the one-dimensional case the pressure amplitude is constant over the distance, for the three-dimensional case it decays with the radial distance from the heat source. In addition, although for moderate heat release values the analytical solution is able to capture the dynamics of the fluid response, for large heat release values the nonlinear effects deviate the highly-resolved numerical solution from the analytical model.

The third unit problem studies the pressure response of a fluctuating unsteady heat release source to an unconfined one-dimensional domain. An analytical model based on the acoustic wave equation with planar symmetry and an unsteady heat source is derived and then compared against results from highly-resolved numerical simulations. Two different heat release profiles, a flat spatial distribution with sinu-

soidal temporal profile and a Gaussian spatial distribution and sinusoidal temporal profile, are used to model the heat source. For both cases, the acoustically compact and noncompact regimes depending on the Helmholtz number are analyzed. While in the compact regime the amplitude of the pressure is constant over the distance, in the noncompact regime the amplitude of the pressure fluctuation is larger within the heat source area of application, and once outside the heat source decays to a far field pressure value. In addition, the analytical model does not capture the nonlinear effects present in the highly-resolved numerical simulations for large rates of heat release such as the ones present in rocket combustors.

Finally, the last four unit problems focus on the interaction between unsteady heat release and the longitudinal acoustic modes of a combustor. The goal is to assess and quantify how pressure fluctuations due to unsteady heat release amplify a longitudinal acoustic mode. To investigate the nonlinear effects and the limitations based on the acoustic wave equation, the analytical models are compared against highly-resolved numerical simulations. The fourth unit problem consists of the pressure response to a moving rigid surface that generates a forced sinusoidal velocity fluctuation in a one-dimensional open-ended cavity. The fifth unit problem combines an analytical solution from the velocity harmonic fluctuation with an unsteady heat pulse with Gaussian spatial and temporal distribution developed in the first unit problem. The choice of an open-ended cavity simplifies the analysis and serves as a stepping stone to the sixth unit problem, which also includes the pressure reflections provoked by the acoustic boundaries of the duct. This sixth unit problem describes the establishment of a 1L acoustic longitudinal mode inside a closed duct using the harmonic velocity fluctuations from the fourth unit problem. A wall on the left end of the duct is only moved for one cycle at the 1L mode frequency to establish a 1L mode in the initially quiescent fluid. The last unit problem combines the analytical solution of the 1L mode acoustic field developed in the sixth unit problem with an unsteady heat pulse with Gaussian spatial and temporal distribution, and also accounts for pressure reflections. The derivation of the present analytical models includes the identification

of relevant length and time scales that are condensed into the Helmholtz number, the phase shift between the longitudinal fluctuating pressure field and the heat source, and ratio of the fluctuating periods. The analytical solution is able to capture with an acceptable degree of accuracy the pressure trace of the numerical solution during the fist few cycles of the 1L mode, but it quickly deviates very significantly from the numerical solution due to wave steepening and the formation of weak shocks. Therefore, models based on the acoustic wave equation can provide a good understanding of the combustion instability behavior, but not accurately predict the evolution of the pressure fluctuations as the nonlinear effects play a major role in the combustion dynamics of liquid rocket engines.

1. INTRODUCTION

1.1 Motivation and Background

The presence of combustion instabilities in gas turbines and liquid rocket engines can lead to high-amplitude pressure oscillations with the potential to damage or destroy combustors [1–3]. Liquid rocket engines may experience more severe pressure fluctuations than gas turbines due to the high rates of volumetric heat release driven by the high operating pressure in near-stoichiometric conditions. The accurate prediction of combustion instability represents a formidable challenge in the development of propulsion and power systems. The nonlinear coupling of physical phenomena such as acoustics, hydrodynamics and chemical kinetics, which occurs at different spatial and temporal scales, further complicates the task of modeling combustion instabilities. The coupling between the unsteady pressure field and heat release represents a primary mechanism that drives combustion instability [4]. Thus, correctly capturing the unsteady heat release and its coupling with pressure fluctuations has a paramount importance in the construction of relevant combustion instability models.

The fluctuation of chemical heat release generates acoustic waves that propagate across the combustor and interact with the present acoustic field. These interactions are not necessarily a linear superposition of acoustic signals due to the nonlinearity of the governing equations and physics involved. Furthermore, the combustion regime for rockets is characterized by high rates of heat release, which can surpass $\mathrm{TW/m^3}$ and generate very high amplitude pressure oscillations, which are orders of magnitude larger than gas turbines. In addition, the non-premixed turbulent combustion of rockets differs from the smoother more continuous flames encountered in gas turbines.

Many researchers have analytically modeled unsteady heat release as harmonic oscillations with smooth temporal variations [5,6]. This idealized view of combustion

instability is quite different than the physics that occur in a rocket combustor, where the level of unsteadiness, large gradients of mixture, high pressure, and high energy of the propellants provokes extremely large heat release fluctuations. These characteristics of rockets along with the non-premixed turbulent combustion regime introduce stochastic behavior to the system that differs from purely harmonic fluctuations. As Dowling showed [7], in turbulent combustion the acoustic pressure is a stochastic variable. Ignition and extinction events result in a discontinuous flame that can be thought of as a combination of pockets of propellants that burn to produce unsteady heat release fluctuations. Bragg [8] proposed a theory envisioning turbulent flame as a collection of statistically uncorrelated eddies, undergoing various stages of chemical reaction. Each eddy, which acts as a monopole source of sound, has its own heat release rate that is statistically independent of the neighboring eddies. Altogether, in his theory the rate at which the combustion volume is contracting or expanding is the sum of the contraction or expansion of the individual eddies [8, 9]. However, in turbulent flames, turbulence and chemistry affect each other in a mutual nonlinear interaction [10]. In a real combustor, the unsteady heat release in an eddy generates a pressure fluctuation that propagates in all directions perturbing the local flow field of neighboring eddies, and hence, their turbulence-chemistry interactions. All these factors contribute to a highly stochastic behavior that is not included in the classical harmonic treatments. In addition, there are no prior analytical models to predict the pressure response to unsteady heat release sources typical of rocket engines. Thus, the complexity of the problem calls for the use of high-fidelity numerical simulations. Modern LES/DES methods have shown the ability to model and reproduce combustion instability in real combustors [11, 12]. However, the high degree of complexity of the system makes it very difficult to isolate the different mechanisms and assess the relative contribution of each physical phenomena to combustion instability.

An analytical solution of the pressure response to an unsteady heat release source with a Gaussian profile can be used to extract physical insight of turbulent flame noise, and study its effects on combustion instability. Moreover, the detailed study of

the pressure response to unsteady heat release facilitates the comprehension of how the combination of a large number of unsteady heat release events interact with the acoustic modes of a combustor. The analysis can be improved by adding vortex shedding to the interactions between acoustics and heat release. Indeed, vortex shedding is a common flow phenomenon seen in rocket combustors that has important effects on combustion instability. Altogether the research goal is to contribute to the understanding of the effects of high rates of unsteady heat release on combustion instability in liquid rockets.

1.2 Combustion Instability

Combustion instability occurs when unsteady heat release couples with the acoustic modes of a combustor, which in turn may generate high-amplitude pressure oscillations. This coupling is governed by the nonlinear interactions of multiple physical mechanisms that can be encompassed in three phenomena: unsteady heat release, acoustics, and hydrodynamics. Fig. 1.1 shows the traditional direction of the feedback mechanisms that may lead to combustion instability. Although this diagram sets a given direction for the combustion instability feedback mechanisms, the interactions happen in both directions. For instance, acoustic pressure fluctuations may vary the chemical equilibrium of combustion reactions thereby affecting heat release, vortex shedding can generate pressure oscillations, and unsteady heat release generates turbulence-chemistry interactions that can perturb the vortex dynamics in the combustor, to name a few.

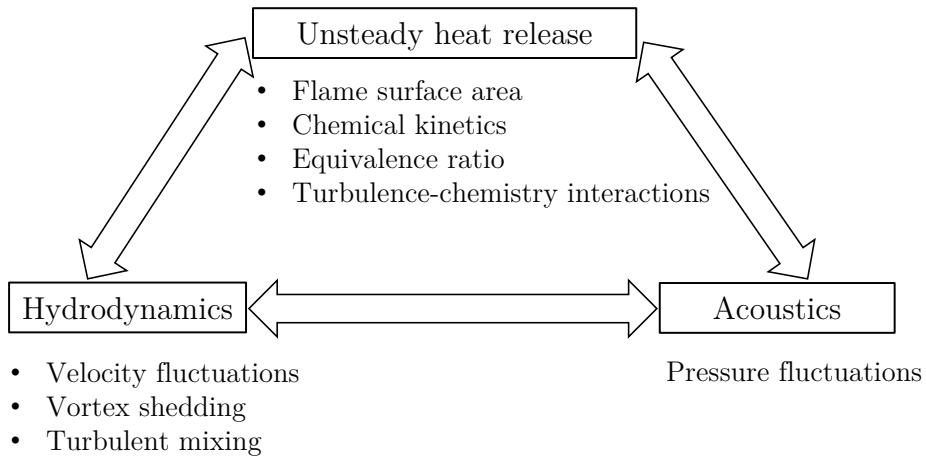

Figure 1.1. Feedback mechanisms involved in combustion instability.

Acoustic modes are in general longitudinal, transverse, or Helmholtz-type with the type of mode determined by the geometry of the combustion chamber [13, 14]. Longitudinal and transverse modes have been extensively studied in the literature. However, Helmholtz-type combustion instabilities, which are also known as bulk mode instabilities, are barely addressed in case of non-premixed flames. Unlike longitudinal modes which resonate at higher frequencies and vary with the span of the combustor depending on the boundary conditions, Helmholtz-type combustion instabilities are characterized by low frequencies and no spatial dependence for the pressure. Combustors may exhibit low frequency instabilities identified as bulk modes, which in turn interact with the heat release dynamics of the chamber [14].

Fig. 1.2 depicts a diagram of the main physical phenomena involved in combustion instability in liquid rocket engines with a gas centered swirl coaxial injector. This research work focuses on the regime of high-performance methane-LOX liquid rocket engines.

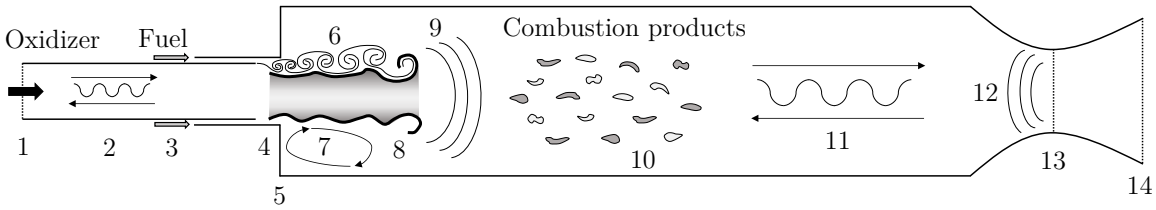

1. Oxidizer feed system fluctuations
2. Acoustic modes in the oxidizer post
3. Fuel feed system fluctuations
4. Injector recess
5. Dump plane
6. Shear layer mixing and vortex shedding
7. Hot gas recirculation
8. Flame, unsteady heat release
9. Direct combustion noise
10. Entropy waves (hot and cold spots)
11. Acoustic modes in the combustion chamber
12. Indirect combustion noise
13. Nozzle throat acoustic boundary
14. Nozzle exit

Figure 1.2. Diagram of the main processes that can cause combustion instabilities in a liquid rocket combustor with a gas centered swirl coaxial injector.

Combustion Instability Mechanisms

- **Unsteady heat release:**

a) Flame area fluctuations and turbulence-chemistry interactions: the rate of chemical heat release is directly linked to the flame surface area [15]. In a combustor, the flame surface area fluctuates due to effects such as acoustic velocity oscillations (stretching-contraction) as well as hydrodynamic phenomena that perturb the flame e.g vortex shedding, flow separation, large scale mixing [1]. The variation of the flame surface area provokes fluctuations in heat release. In turbulent flames, the mutual interactions between turbulence and flame are nonlinear and depend on the relative strengths of chemical and turbulent processes [10]. For instance, turbulence effects such as straining and wrinkling of the flame provoke variations of the flame surface area with the consequent unsteady heat release fluctuations [16]. In turn, chemical heat release provokes changes to fluid properties such as the density and viscosity that affect the structure and dynamics of the turbulence. As turbulence transports the reactants and products, it affects the structure of the flame thereby closing the feedback mechanism [10].

b) Equivalence ratio fluctuations: the fluctuations in the mixing processes of fuel and oxidizer downstream the injectors along with the oscillations in the propellant feed systems provoke variations in the reactive mixture equivalence ratio [1]. As the mixture is convected downstream and reacts at the flame, the variations of the equivalence ratio generate fluctuations in heat release.

- **Direct combustion noise:** the fluctuation of chemical heat release provokes acoustic pressure perturbations that propagate in all directions. Effectively, the fluctuation of heat release generates a volumetric expansion or contraction in the local flow field that propagates in the form of acoustic perturbations. In contrast, steady combustion leads to a constant rate of expansion, and hence, does not generate combustion noise [7]. The coupling of unsteady combustion heat release with the acoustic modes of the combustor may provoke high amplitude pressure fluctuations that lead to combustion instability [2].

- **Indirect combustion noise:** the interaction of the vortical and entropic perturbations with the mean flow velocity gradient at the nozzle results in energy transfer to an acoustic mode [17].

  a) Entropy waves: the spatial and temporal fluctuations of heat release generate entropy fluctuations in the form of hot and cold spots, which are convected downstream the flame with the mean flow. The imperfect mixing of propellants also provokes entropy inhomogeneities. These entropy fluctuations, known as entropy waves, propagate across the combustor at the flow bulk velocity. At the nozzle, the acceleration of entropy waves with the mean flow generates acoustic pressure fluctuations because regions of fluid with different densities undergo a volume contraction [18]. In turn, the acoustic pressure waves caused by the acceleration of entropy waves propagate upstream where they can perturb the flame, thereby closing the feedback mechanism [7].

  b) Vorticity inhomogeneities: similarly to entropy waves, the advection of vorticity inhomogeneities with the mean flow and its acceleration through the

nozzle generates pressure perturbations, which are then propagated back into the combustor.

- **Fluctuations in the propellant feed systems:** the pressure drop across nonchocked injectors varies for constant upstream pressure of the combustion chamber. As the pressure in the combustor varies, the pressure drop across the injectors is perturbed provoking fluctuations of the propellants mass flow rate [1]. The oscillation of the oxidizer and fuel mass flow rate perturbs the mixture equivalence ratio as well as the mixing processes thereby generating fluctuations in the chemical heat release. The feedback mechanism is closed as the variations in heat release provoke pressure fluctuations that perturb the combustor pressure, with the consequent change in pressure drop across the injectors.

- **Vortex shedding:** in a combustor, the areas of flow separation or rapid expansion can cause the formation of large-scale vortical structures [1]. In Fig. 1.2, the dump plane represents a sudden expansion where vortex shedding may occur. As vortices from the mixing shear layer convect downstream the dump plane, there is mixing of cold reactants with hot gases from the recirculation zone. As these eddies with fresh reactants heat up with the surrounding hot gas, they ignite and generate unsteady heat release with the consequent pressure fluctuations. In strong combustion instabilities, large pressure oscillations create vortices by inducing large velocity variations of the inlet flow rate [13]. These vortices are then convected downstream affecting the mixing processes and distorting the flame structure with the consequent fluctuations in heat release.

1.3 Literature Review

1.3.1 Thermoacoustic Modeling

Combustion instabilities can be modeled through different levels of fidelity, ranging from low-order models to Large Eddy Simulations (LES). Their major differences consist of the degree of mathematical modeling, their capability to predict linear or nonlinear instability, geometrical simplifications, and associated computational cost [19]. Additionally, frequency-domain and time-domain methods can be used to capture combustion instabilities. The former describes the system by means of periodical domains; the latter, follows a more physical approach modeling the processes that take place in initial, transient and long-term stages. The main advantage of the frequency-domain is that it allows the identification of patterns such as the most unstable mode that could not be visualized in the time-domain. Nonetheless, the frequency-domain does not allow the prediction of the amplitude of the actual perturbations in a straightforward way.

On the low-order side, the linear acoustic wave equation has been extensively used to model the coupling between unsteady heat release and acoustic modes in a combustor [5,6,20]. As the acoustic wave equation assumes zero Mach number, these models cannot capture mean flow effects such as entropy waves, which puts some limitations on their use and accuracy [6]. The mean flow effects can be considered instead by modeling the thermoacoustic problem with Linearized Euler Equations (LEE) [7]. Both methods can also be extended for the study of more complex configurations by using network models that connect the different cavities of a combustor [5, 21]. In this latter approach, the geometry of the combustor is modeled by a network of one- or two dimensional axisymmetric acoustic elements of constant density where the acoustic problem can be solved analytically [13]. Infinitely thin flame is only added at the interface between the large and low temperature segments and jump relations are used to enforce flow rate conservation and pressure continuity between the elements. The main benefit of this approach is that few lumped elements are

only used to describe the complex system providing an extremely low order model adequate for design purposes [22]. However, the geometrical details of the combustor cannot be accounted for and only the first equivalent longitudinal modes are sought for.

As an intermediate approach between low-order models and LES, Helmholtz solvers have been widely employed in the prediction of thermoacoustic instabilities [22]. The Helmholtz equation is derived by transforming the acoustic wave equation into the frequency domain, which can then be treated as an eigenvalue problem that solves for the thermoacoustic modes of the combustor. However, the zero Mach number assumption in Helmholtz solvers leads to errors that can be quantified by means of LEE solvers [23, 24]. Helmholtz solvers require flame transfer functions. These transfer functions are often in the form of Crocco's $n - \tau$ model [25, 26], but other forms such as flame describing functions [27,28] can also be combined with Helmholtz solvers. The flame transfer functions are calibrated either by using data sets from LES simulations [22] or from experiments [29]. A comparison of different levels of modeling fidelity is presented by Selle et al. [30] in a study of a liquid rocket engine combustor using a Helmholtz solver, LEE solver and LES.

1.4 Pressure Response to Unsteady Heat Release

In liquid rocket engines, due to non-premixed injection, the ignition and extinction of heterogeneous mixtures may result in intermittent and discontinuous flames that produce exceptional degrees of unsteadiness and localized pressure pulsations. Bragg [8] proposed a theory envisioning turbulent flames as a collection of statistically uncorrelated eddies undergoing various stages of chemical reaction. Each eddy, acting as a monopole source of sound, has a statistically independent heat release rate. The rate of expansion or contraction of the total combustion volume is then postulated as the sum of the contraction or expansion of the individual eddies [8, 9]. However, in

turbulent flames, turbulence and chemistry affect each other in a mutual nonlinear manner [10].

To model the energy deposition process, Kassoy [31] performed asymptotic-based analyses of the governing equations that study the response of an inert gas volume to localized, spatially distributed, transient energy deposition. A later work broadened the analysis to a systematic formulation for the thermomechanical response of a finite volume of inert gas to a very general, spatially distributed, transient heat deposition with arbitrary profile [32]. This work was later extended to gain a deeper understanding of the cause-effect relationship between combustion-generated energy deposition and pressure oscillations in liquid rocket engines [33–35]. The pressure response of a fluid kernel subject to an external heat source can also be expressed as an integral equation that can be numerically integrated using a given heat pulse profile as an input [36]. For reacting cases, the dynamic response of a chemically homogeneous reacting center has been modeled by integrating numerically the simplified conservation equations and kinetic rate equations [37, 38].

Damköhler numbers, representing ratios of characteristic physical time scales, provide substantive information to classify and understand a combustion process. One such Damköhler number can be defined as the ratio of the characteristic conduction time over the chemical reaction time. For gaseous reacting mixtures subject to localized and instantaneous energy sources, there is a critical value of this Damköhler number that leads to an ignition [39, 40]. The third Damköhler number, which is equivalent to the Helmholtz number,He and defined as the ratio of acoustic time over chemical time, was proposed by Zhang et al. [41] as a metric to distinguish whether a combustion process operates in constant volume or constant pressure regime. The Helmholtz number can also be defined for other cases such as a fluctuating pressure field in a nozzle [42, 43]. For large He, the expansion induced by the combustion process has not enough time to be completed leading to a constant volume combustion process, whereas for low He the pressure expansion results in a constant pressure combustion process [41]. A parameter "m" equivalent to He was also used

by Crighton [44] to study the pressure response to defined heat source profiles and distinguish between different regimes with compact cases for $m \ll 1$ and noncompact cases for $m \gg 1$. For compact cases, the pressure fluctuations follow the temporal variation of the heat release profile, whereas for noncompact cases the sound follows the spatial variations of the heat release profile [44].

The unsteady heat release that occurs when a pocket of propellants, carried along within an eddy, ignites and burns can be modeled as a heat source with a Gaussian spatial and temporal distribution. A Gaussian distribution in time and space deposited at the beam focus location was proposed to numerically study the ignition sequence measured in a laboratory-scale single-injector rocket chamber ignited by a laser that used gaseous oxygen and hydrogen as propellants [45]. The Gaussian profile represented fairly well the experimentally measured fluctuating heat release rate [46] and it was proved that the temporal rate of the fluctuating heat release rate relates well with the spatial correlation of the Gaussian profile [46]. The direct numerical simulation (DNS) study also revealed that the planar laminar flame thermal thickness can be used as the characteristic length scale of the unsteady heat release profile [46]. Gaussian distribution is also a typical representation of the laminar flame structure for methane-air flame as shown in Fig. 1.3 [47]. Therefore, a Gaussian spatial distribution has been chosen in this work to consider the effects of the flame thickness in the pressure response to unsteady heat release. Although there exist simpler heat source spatial distributions such as the Dirac delta [48, 49], these do not consider the effects of the flame thickness which is key for the study of acoustically noncompact flames. The temporal profile used in the heat source is either a step or a Gaussian temporal distribution. Whereas the step temporal profile is an idealized simplification with less physical significance, it exhibits more marked trends which serve as a stepping stone to better understand the dynamics of the more realistic Gaussian temporal distribution. The step temporal profile has been chosen for its simplicity in spite of its limited applications, one of which could be the study of a heat deposition process using a planar laser sheet. In contrast, the Gaussian temporal profile can be used

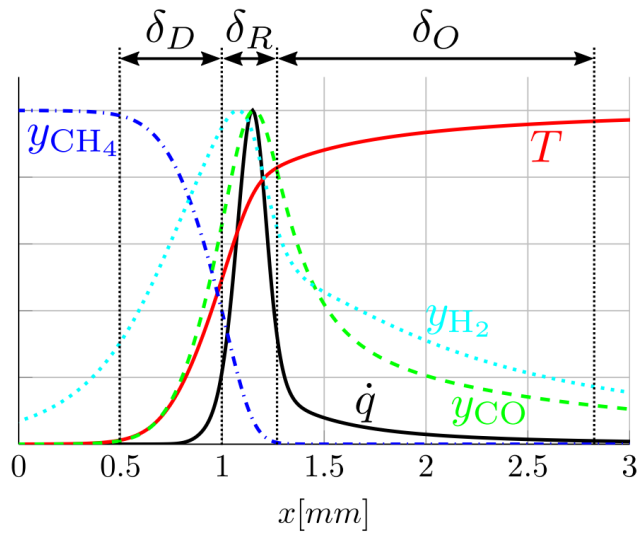

Figure 1.3. Laminar flame structure for methane-air flame (Source [47]).

to model the fluctuating combustion heat release rate in turbulent flames [46]. Low order models that established the proportionality between the pressure oscillation at a previous time step and heat release through a Gaussian distribution multiplied by a constant have also been used to reproduce some of the main characteristics of combustion instability such as the growth rates or the amplitude of the limit cycle [50].

1.4.1 Lighthill's Analogy

There exist more complex acoustic pressure wave equations which take into account more physical phenomena and reduce the number of assumptions. Departing from the work of Lighthill [51], Dowling [52] derived an inhomogeneous wave equa-

tion that includes unsteady heat release, non-isomolar combustion, species and heat diffusion, viscous dissipation, inter-alia, as follows

$$\frac{1}{c_0^2}\frac{\partial^2 p_1}{\partial t^2} - \frac{\partial^2 p_1}{\partial x_i \partial x_i} = -\frac{\partial}{\partial t}\left[\frac{\alpha\rho_0}{c_p\rho}\left(\frac{\partial q_i}{\partial x_i} - \tau_{ij}\frac{\partial u_i}{\partial x_j} - \sum_{n=1}^{N}\frac{\partial h}{\partial Y_n}\bigg|_{\rho,p,Y_m}\nabla\cdot J_n \right.\right.$$
$$\left.\left. + \sum_{n=1}^{N}\frac{\partial h}{\partial Y_n}\bigg|_{T,p,Y_m}\omega_n - \frac{\partial h}{\partial \rho}\bigg|_{p,Y_n}\left(\sum_{n=1}^{N}\frac{\partial \rho}{\partial Y_n}\bigg|_{T,p,Y_m}\omega_n\right)\right)\right] \tag{1.1}$$
$$+\frac{1}{c_0^2}\frac{\partial}{\partial t}\left[\left(1-\frac{\rho_0 c_0^2}{\rho c^2}\right)\frac{Dp}{Dt} - \frac{p-p_0}{\rho}\frac{D\rho}{Dt}\right] + \frac{\partial^2}{\partial x_i \partial x_j}\left(\rho u_i u_j - \tau_{ij}\right) + \frac{\partial^2}{\partial x_i \partial t}\left(\rho_e u_i\right)$$

where the terms responsible for acoustic propagation are presented in the left-hand-side and the sources in the right-hand-side. It is noted that in Eq. (1.1) D/Dt represents the substantial derivative and ρ_e is the excess mass density defined as

$$p_e = \rho - \rho_\infty - \frac{p - p_\infty}{c_0^2} \tag{1.2}$$

which for small perturbations, it corresponds to the difference of the mass density fluctuation generated by an isentropic compression (i.e. acoustics) with respect to the overall mass density fluctuation. In the right-hand-side of Eq. (1.1), the fourth term corresponds to the quadrupole source and drives to the aerodynamic noise found in the original work of Lighthil [51]. The fifth term of the right-hand-side appear when the propagation medium is not uniform. Based on Dowling's work [6,7], the first two terms are responsible for the combustion noise as it accounts for the variation of the heat release rate, and are classified as monopole type. Finally, the last term of the right-hand-side that contains ρ_e is related with the indirect combustion noise, also known as entropy noise and is a dipole type. Indeed, this latter term captures the noise when ρ_e is accelerated.

An alternative expression was provided by Bailly et al. [53] based on the Phillip's equation for low Mach numbers.

Based on the framework of Lighthill's analogy [51], Crighton et al. [52] and Dowling et al. [7] also demonstrated that the far-field sound pressure fluctuation resulting from the direct noise is given by

$$p_1(\vec{x},t) = \frac{\gamma - 1}{4\pi c_0^2 |\vec{x}|} \int_V \frac{\partial}{\partial t} \left[q\left(t - \frac{|\vec{x}|}{c_0} \right) \right] d^3\vec{y} \tag{1.3}$$

where V represents the volume containing the combustion region. For the derivation of Eq. (1.3), it was assumed that the ratio of specific heats, γ is independent of the temperature, that the combustion is isobaric taking place in ambient pressure and consequently, $\rho c^2 = \gamma p_0 = \rho_0 c_0^2$ applies. In addition, it was considered that the unsteady heat release term is the dominant term and that flame is compact as $\vec{x}$ was located in the far-field.

1.4.2 Energy Balance

Energy balance methods are very useful for enhancing the understanding of combustion processes by means of computing the energy budget and integrating the fluctuating energy mechanisms in a combustor. Chu and Kovsznay work [17, 54] laid a solid theoretical foundation for the development of an energy balance framework for the analysis of fluctuations in a fluid flow. Departing from their work, successive authors such as Myers [55] and Flandro [56] built their theories including more phenomena and reducing the level of assumptions.

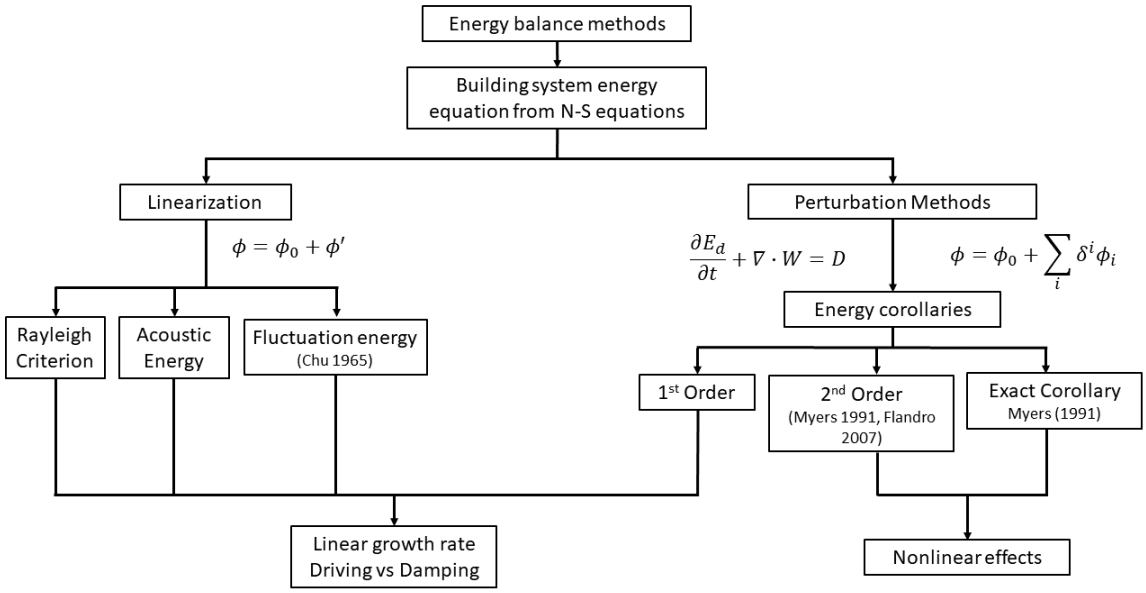

Figure 1.4. Historical evolution of energy balance analysis methods.

To study the nonlinear interactions in a compressible flow, Chu [17,54] and Kovsznay [17] proposed a framework based on three basic fluctuation modes, i.e. vorticity, entropy and sound (acoustic) modes. Their view was that "the non-linearity of the Full Navier-Stokes equations can be interpreted as an interaction between the three basic modes". In this way, they showed that the linearized theory does not indicate any interaction between the modes. Thus, the flow field fluctuations can be interpreted as a superposition and interaction of the three basic modes of fluctuation. Departing from this principle, they decomposed systematically the nonlinear phenomena as interactions between the three basic fluctuation modes. In turn, these fluctuation modes were expressed as a large or infinite number of Fourier components, which for limitations of their time, could only be expressed theoretically and not quantitatively assessed. Their analysis included a detailed study of the second-order nonlinear interactions of the three modes assessing the relative order of magnitude of each cross-interaction.

Rayleigh Criterion

The Rayleigh criterion, which computes the coupling between heat release and pressure fluctuations, is the most common measure for assessing the stability of a combustor. This criterion states that if pressure and heat release fluctuations are in phase, then instability can be amplified by the flame/acoustics coupling. In 1878, Lord Rayleigh [4] described the phenomenon of vibrating tones in a Rijke tube as follows:

> "If heat be periodically communicated to, and abstracted from, a mass of air vibrating (for example) in a cylinder bounded by a piston, the effect produced will depend upon the phase of the vibration at which the transfer of heat takes place. If heat be given to the air at the moment of greatest condensation, or be taken from it at the moment of greatest rarefaction, the vibration is encouraged. On the other hand, if heat be given at the moment of greatest rarefaction, or abstracted at the moment of greatest condensation, the vibration is discouraged."

This explanation of the physical phenomena of pressure fluctuations in a Rijke tube came to be known as the "Rayleigh criterion". Mathematically, the classical Rayleigh criterion states that combustion instability will occur if the fluctuating heat release and the acoustic field are in phase as:

$$\int_V p'q'dV > 0 \tag{1.4}$$

where V is the volume of the flow field domain and p' and q' represent the pressure and heat release fluctuations, respectively. This equation is integrated across the combustor volume over a time period to determine the stability of the system for a given frequency and its sign may change with the phase alignment between p' and q'.

Fluctuation energy budgets are often used to discuss the validity of the Rayleigh criterion. These methods consist of the assessment of the balance of all energy disturbances in a flow accounting for mechanisms such as acoustics, hydrodynamics,

turbulence, species diffusion, viscous effects, chemical reactions, heat transfer, inter-alia. In this way, fluctuation energy balances contribute to the understanding of the driving mechanisms and transfer of energy between different modes and mechanisms. To study thermoacoustic instabilities, Chu [54] proposed a fluctuation energy that integrates the fluctuations of three variables (i.e. pressure, velocity, and entropy) and provides a more complete picture with respect to the Rayleigh criterion, which only accounts for pressure and velocity perturbations.

However, the linearization of the problem neglects the influence of the nonlinear effects present in actual combustors. This non-linearity is all the more important in high-pressure rockets due to the high-density heat release rates within a non-premixed unsteady combustion. The large magnitude of the heat release provokes non-linear responses that may not be adequately captured by linearized methods. The intermittency of the unsteady heat release also deviates from the assumption of a flame with smooth fluctuations in a constant pressure combustion regime. Taking advantage of modern high-fidelity computational fluid dynamics (CFD) simulations, we can now compute the nonlinear terms such as the continuous generation of vorticity due to turbulence, the generation of aerodynamic sound, acoustic streaming, or scattering of sound waves by turbulence, inter-alia.

Energy Corollaries

Building from the previous work, researchers such as Myers [55] and Flandro [56] developed Energy Corollary Methods as a framework to analyze the perturbations in a flow field from an energy perspective. The basic energy equation is derived from a combination of the Navier-Stokes equations and written as a conservation equation

$$\frac{\partial E_d}{\partial t} + \nabla \cdot W = D \tag{1.5}$$

where E_d is the system energy, W is the energy flux vector accounting for all the driving and damping mechanisms through the boundaries of the system, and D is the source term adding or subtracting energy to the system as a result of effects such as

heat release, viscous losses, vorticity, body forces, etc. Over time, researchers have varied the level of assumptions such as zero Mach number mean flow, small-amplitude perturbations, isentropic flow, homentropic flow, etc. depending on their particular applications. Furthermore, the formulations of energy balance corollaries have been developed for first order, second order, and exact (under certain conditions).

The energy balance analysis of combustion is essential for assessing the effects and coupling that drive the stability of combustors. Computing the energy balance of the system allows the quantification of the efficiency and the relative contribution of each physical phenomena involved in combustion instability. High-fidelity CFD simulations provide a complete picture of the combustion processes with access to areas that cannot be studied experimentally due to physical limitations. In this work, the energy balance analysis is used to post-process high-fidelity simulations to quantify the relative contribution of each mechanism to combustion instability.

1.4.3 High-Fidelity Simulations

In liquid rocket engines, the non-premixed turbulent combustion regime is characterized by high levels of unsteadiness, large gradients of mixture, high pressure, and extreme rates of heat release, all of which contribute to making the problem highly nonlinear. Several studies have assessed this nonlinear nature of combustion instability [57–60], including the presence of shock waves in rocket combustors [61]. The linear methods in such cases are therefore inherently limited [62–64]. The complexity of combustion instability thus requires the use of high-fidelity numerical simulations to account for all the nonlinear interactions. Modern LES and Detached Eddy Simulations (DES) have demonstrated the ability to reproduce combustion instability in gas turbines and model rocket combustors [65–74]. Nevertheless, even when LES simulations determine the stability of a combustor, these do not necessarily explain the causes of instability and how to control them [22].

LES explicitly compute the three-dimensional unsteady Navier-Stokes equations, and thus, include both a solution for the mean flow field and for the fluctuations [19]. The LES method resolves eddies larger than the computational mesh whereas the effects of the smallest eddies are modeled [13]. Altogether, LES allows the consideration of the effects of chemical reactions, compressibility and viscosity as well as turbulence, allowing to capture the interactions between the flame dynamics, acoustics and mixing. The method does not present any constraint in terms of geometrical complexity or flow configurations.

LES can capture the onset of the instability and its quasi-linear growth as well as the non-linear mechanisms such as the limit cycle [19]. However, in rocket engine calculations, LES simulations are in general still limited to scaled domains such as single-element injector cases due to the prohibitive requirements for full scale designs in terms of computational time and memory [22]. In addition, even when LES can predict the appearance of combustion instability in a combustor, it is an open research task to determine its cause and mechanisms to control it [19, 22]. Additional tools for the analysis of LES results and for application to practical problems are required for that purpose.

Chemical kinetics, high-pressure and local effects due to unsteady heat release are critical parameters that need to be addressed for high-fidelity modeling of unsteady combustion [12]. The accuracy of chemical kinetics models can be improved by increasing the number of species but this in turn increases the computational demand for modeling reacting flows. The high-pressures present in rocket engines challenge unsteady combustion modeling due to trans- and supercritical effects that affect the injection of propellants under normal [75] or acoustically excited cases [76]. Finally, local unsteady heat release not only interacts with the acoustics but also acts as triggering mechanism of large scale phenomena under the conditions of coherence [11]. The understanding of these local-global relationships is of paramount importance to properly capture unsteady heat release dynamics in LES and its effects over the rocket engine.

The complex interactions between acoustics, hydrodynamics, and chemical reactions add great difficulty to the task of assessing the relative contribution of each physical phenomena in the prediction of combustion instability. The overall system may be better understood by breaking down the problem into simpler models and then building up the complexity by adding one physical process at a time. An examination of the high-fidelity simulations of the Continuously Variable Resonance Chamber (CVRC) and other rocket combustors developed at Purdue University reveals the presence of highly unsteady intermittent flames and localized high-amplitude pressure pulses as a result of the extreme rates of heat release [69, 70, 73]. The fluctuations of heat release generate a flow expansion proportional to the time rate of change of the heat release rate [15, 77]. The analysis of this phenomenon motivated the present study on the flow field response to heat release rates typical of high-pressure rocket combustors, which can surpass TW/m^3.

1.5 Objectives and Methodology

The goal of this research work is to gain insight into the fundamental effects of high rates of unsteady heat release in combustion instability in liquid rocket engines. In addition, the aim is to establish the limitations of classical treatments based on linear analysis when studying combustion instability in liquid rockets. To do so, the full problem is decomposed into fundamental unit problems focused on the particular interactions of physical phenomena involved in combustion instability. The overall strategy consists of analyzing these fundamental problems with simplified scenarios and then building up the complexity by adding more phenomena to the study. In particular, the focus is the fluid response to unsteady heat release.

The unit problems start with a heat release pulse in an unconfined one-dimensional domain, which is then extended to three dimensions to study the dimensionality of the problem. Then, a continuously fluctuating heat source is studied in order to further resemble the combustion heat release from actual flames responding to

acoustic modes in a combustor. Finally, the heat source is introduced in a closed duct to study the interactions of unsteady heat release with a longitudinal acoustic mode in a combustor.

There are five main objectives to this study as follows:

- Analytically model the local pressure response to an unsteady heat release source.
- Analytically model the interaction between an unsteady heat release source and the longitudinal acoustic modes in a combustor.
- Compare the analytical models to high-fidelity numerical simulations to assess its range of application, and the relative importance of nonlinear effects.
- Identify relevant physical parameters from the analytical models such as characteristic length and time scales, as well as characterize different regimes of operation.
- Compute the energy efficiency of the pressure expansion due to unsteady heat release.

Research Approach

Departing from the linearized Navier-Stokes equations, analytical models of the pressure response to unsteady heat release are derived based on the inhomogeneous acoustic wave equation. In addition, the acoustic wave equation can model the interaction between unsteady heat release and longitudinal acoustic modes in a combustor. Two different heat release source profiles are used: Gaussian spatial distribution with a step temporal profile, and Gaussian spatial distribution with a Gaussian temporal distribution. From each analytical solution, relevant physical parameters like characteristic length and time scales are identified, which are later used to characterize different regimes of operation. High-fidelity simulations using Purdue's in-house Navier-Stokes solver "General Equation and Mesh Solver" (GEMS) are performed

with the aim of assessing the validity of the analytical models and their limitations. Furthermore, parametric studies are also carried out to study the different regimes of operation of unsteady heat release response, and quantify relevant metrics such as $p\nu$ work efficiency and energy budget of the mechanisms.

As shown in Fig. 1.1, the physical mechanisms that can lead to combustion instability can be encompassed in three main physical phenomena: unsteady heat release, acoustics, and hydrodynamics. This research seeks to gain insight into the effects of unsteady heat release on acoustics in the context of combustion instability in liquid rockets. To do so, four fundamental unit problems are proposed as simplified representations of important mechanisms by which unsteady heat release impacts combustion instability. The analysis of these unit problems allows to isolate the particular interactions between physical phenomena and assess how their behavior changes as more mechanisms are included in the study. These four unit problems are presented in Chapters 3-6 of this work.

This dissertation is organized in eight chapters as follows:

Chapter 1 introduces the research carried out as part of this PhD thesis. It provides a literature review of the current state of the art in the study of unsteady heat release effects in combustion instability, outlines the objectives and the research approach.

Chapter 2 provides the baseline formulation of the analytical models used to compute the results presented in Chapters 3-6. It derives the acoustic wave equation with an unsteady heat source departing from the Navier-Stokes equations. It also presents in detail the assumptions and simplifications carried out in the linearization process. Finally, the derivation of the Rayleigh criterion from the linearization process is also provided.

Chapter 3 studies the pressure response to an unsteady unsteady heat release source in an open one-dimensional domain. This unit problem is a simplified representation of an unsteady heat release event provoked by the sudden ignition of a small pocket of propellants. The sudden ignition of these small pockets of propellant

generates unsteady heat release that in turn provoke pressure fluctuations. For this unit problem, quiescent perfect gas with properties like that of CO_2 in an enclosed open domain is heated in a small band, allowing careful control of the spatio-temporal variations of the heat source parameters. A Gaussian profile is specified spanning the bandsize chosen for heat addition and the time duration is specified such that the total energy added to the flow is constant for all the conditions investigated. The variations studied represent flames of varied thickness and intensity. The derivation of the present analytical model includes the identification of relevant length and time scales that are condensed into the Helmholtz number. Unsteady heat release, and linear and nonlinear acoustics are the key physics that manifest in this unit problem.

Chapter 4 extends the analysis of the pressure response to an unsteady heat release source from a one-dimensional domain to a three-dimensional open domain. The aim of the chapter is to examine the differences between the one-dimensional results and a three-dimensional case, which more realistically models the sudden ignition of a small pocket of propellants. A quiescent perfect gas with properties like that of CO_2 in an open spherical domain is heated in the center, allowing careful control of the spatio-temporal variations of the heat source parameter. A Gaussian spherical profile is specified spanning the radius chosen for heat addition and the time duration is specified such that the total energy added to the flow is constant for all the conditions investigated. The analytical solutions are assessed against highly-resolved numerical simulations so that the analytical modeling limitations are highlighted.

Chapter 5 also presents an unit problem to analyze the pressure response to an unsteady heat release source in a one-dimensional open domain. However, instead of focusing on a single pressure pulse generated by the heat release source as in the previous two chapters, this chapter aims to model heat release sources that fluctuate over a time at the frequency of acoustic modes of a combustor. In this unit problem, a quiescent perfect gas with properties like that of CO_2 in an open domain is also heated in a small band, allowing careful control of the spatio-temporal variations of the heat source parameter. The fluctuating heat release source is modeled by means

of a sinusoidal temporal profile for both a flat and a Gaussian spatial distribution. The pressure response is therefore a continuous pressure signal and the variations studied represent flames of varied thickness and intensity relevant to rocket combustors. Highly-resolved numerical solutions are used to evaluate the limitations of the analytical solutions derived.

Chapter 6 analyzes the effects of high rates of unsteady heat release on longitudinal acoustic modes in a combustor. The mechanism by which unsteady heat release pressure fluctuations interact with the acoustic modes of a combustor to amplify or damp them is of paramount importance in the study of combustion instability. Indeed, the Rayleigh criterion, which is a fundamental concept for combustion instability, is centered around the assessment of the relative phase between unsteady heat release and pressure fluctuations. In turn, this criterion is used as a measure of how unsteady heat release amplifies acoustic pressure modes, thereby determining the stability of a combustor. However, the nonlinearities of the governing equations deviate the problem of adding pressure fluctuations due to unsteady heat release and acoustic pressure oscillations from a purely linear superposition. This unit problem represents a simplification of a flame generating pressure fluctuations that interact with the longitudinal acoustic modes of a combustor. The flame is modeled as an external heat source in a non-reacting fluid. An analytical solution is derived based on the acoustic wave equation following the same strategy as the first unit problem and then compared against highly-resolved numerical simulations. A parametric study varying the Gaussian heat source temporal and spatial parameters as well as the flame location and its phase with the 1L mode pressure field. The results assess the evolution of the amplitude of the pressure fluctuations, and the overall effects after multiple compression-expansion cycles.

Chapter 7 summarizes the research work presented, and outlines future work that could be performed as a result of the current research work.

Chapter 8 presents the main references of this work.

Finally, Appendix A and B provide additional formulation complementary for the derivation of the analytical solutions.

2. MODELING OF THERMOACOUSTIC INSTABILITIES

This chapter presents the derivation of the acoustic wave equation with an unsteady heat source departing from the Navier-Stokes equations. The assumptions and simplifications carried out in the linearization process are described in detail. This derivation forms the basis of the analytical models and results presented in Chapters 3-6. Finally, this chapter also presents the derivation of the Rayleigh criterion using the linearized conservation equations.

2.1 Conservation Equations

The Navier-Stokes equations describe the conservation of mass, momentum and energy for a compressible viscous fluid

$$\frac{D\rho}{Dt} + \rho\nabla\cdot\vec{u} = 0 \tag{2.1}$$

$$\rho\frac{D\vec{u}}{Dt} = -\nabla p + \nabla\cdot\vec{\vec{\tau}} + \rho\vec{f_b} \tag{2.2}$$

$$\rho\frac{D}{Dt}\left(e + \frac{u^2}{2}\right) = -\nabla\cdot(p\vec{u}) + \nabla\cdot(\lambda\nabla T) + \nabla\cdot\left(\vec{u}\cdot\vec{\vec{\tau}}\right) + q + \rho\vec{u}\cdot\vec{f_b} \tag{2.3}$$

where ρ, $\vec{u}$, p, T, $\vec{\vec{\tau}}$, $\vec{f_b}$, e, q, λ are the density, velocity, pressure, temperature, tensor of viscous stress, body force per unit mass, internal energy, heat release rate per unit volume, and thermal conductivity, respectively. The equations Eqs. (2.1, 2.2, 2.3) are written in the non-conservation form. In the formulation, the substantial derivative in the equations is expressed as $\frac{D}{Dt} = \frac{\partial}{\partial t} + \vec{u}\cdot\nabla$. Taking the dot product of the

momentum equation Eq. (2.2) with $\vec{u}$ yields to the equation of conservation of the kinetic energy

$$\rho \frac{D}{Dt}\left(\frac{u^2}{2}\right) = -\nabla \cdot (p\vec{u}\ ) + p\,(\nabla \cdot \vec{u}\ ) + \vec{u} \cdot \left(\nabla \cdot \vec{\vec{\tau}}\right) + \rho \vec{u} \cdot \vec{f_b} \tag{2.4}$$

where the identity $\nabla \cdot (p\vec{u}\ ) = p\,(\nabla \cdot \vec{u}\ ) + \vec{u} \cdot \nabla p$ has been used. The subtraction of Eq. (2.4) from Eq. (2.3) yields to the internal energy conservation equation

$$\rho \frac{De}{Dt} = -p\,(\nabla \cdot \vec{u}\ ) + \nabla \cdot (\lambda \nabla T) + \vec{\vec{\tau}}\ : \nabla \vec{u} + q \tag{2.5}$$

where the identity $\nabla \cdot \left(\vec{u} \cdot \vec{\vec{\tau}}\right) = \vec{u} \cdot \left(\nabla \cdot \vec{\vec{\tau}}\right) + \vec{\vec{\tau}}\ : \nabla \vec{u}$ has been used, in which the second term is the viscous dissipation $\Phi = \vec{\vec{\tau}}\ : \nabla \vec{u}$.

The combination of the 1st and 2nd Laws of Thermodynamics yields to the known thermodynamic expression of the Gibbs equation ($Tds = de + pd\nu$), which can be applied on a fluid element as

$$T\frac{Ds}{Dt} = \frac{De}{Dt} + p\frac{D\nu}{Dt} \tag{2.6}$$

Multiplying Eq. 2.6 by the density and writing the specific volume ν in terms of ρ yields to

$$\rho T\frac{Ds}{Dt} = \rho\frac{De}{Dt} - \frac{p}{\rho}\frac{D\rho}{Dt} \tag{2.7}$$

where s is the entropy. The second term on the right hand side can be computed from the mass conservation equation, Eq. (2.1) using $\frac{D\rho}{Dt} = -\rho \nabla \cdot \vec{u}$. Combining Eq. (2.5) with Eq. (2.7) yields to the entropy conservation equation

$$\rho T\frac{Ds}{Dt} = \nabla \cdot (\lambda \nabla T) + \vec{\vec{\tau}}\ : \nabla \vec{u} + q \tag{2.8}$$

2.2 Acoustic Wave Equation with an Unsteady Heat Source

An acoustic wave equation with an unsteady heat source can be derived by simplifying and linearizing the equations of conservation of mass, momentum and entropy. We assume inviscid flow and neglect thermal conduction and body forces. The single species gas mixture is assumed to behave as a perfect gas with the equation of state given by $p = \rho RT$, where the gas constant R is given by $R = c_p - c_v$ in which c_p and c_v are the specific heat capacities at constant pressure and volume, respectively. In turn, $R = \frac{R_u}{W}$, where R_u is the universal gas constant and W is the molecular weight of the fluid. Under these assumptions the conservation equations become

$$\frac{D\rho}{Dt} + \rho \nabla \cdot \vec{u} = 0 \tag{2.9}$$

$$\rho \frac{D\vec{u}}{Dt} = -\nabla p \tag{2.10}$$

$$\rho T \frac{Ds}{Dt} = q \tag{2.11}$$

The linearization of the equations begins with the decomposition of the variables into mean flow (subscript 0) and fluctuation parts (subscript 1) as $\phi(\vec{x}) = \phi_0(\vec{x}) + \phi_1(\vec{x}, t)$, where ϕ_0 is the mean flow value and ϕ_1 is the small-amplitude fluctuation ($\frac{\phi_1}{\phi_0} = \epsilon \ll 1$). It is assumed that the mean flow variables are function of the space alone.

$$\frac{\partial (\rho_0 + \rho_1)}{\partial t} + (\vec{u}_0 + \vec{u}_1) \cdot \nabla (\rho_0 + \rho_1) + (\rho_0 + \rho_1) \nabla \cdot (\vec{u}_0 + \vec{u}_1) = 0 \tag{2.12}$$

$$(\rho_0 + \rho_1) \left[\frac{\partial (\vec{u}_0 + \vec{u}_1)}{\partial t} + (\vec{u}_0 + \vec{u}_1) \cdot \nabla (\vec{u}_0 + \vec{u}_1) \right] = -\nabla (p_0 + p_1) \tag{2.13}$$

$$(\rho_0 + \rho_1)(T_0 + T_1) \left[\frac{\partial (s_0 + s_1)}{\partial t} + (\vec{u}_0 + \vec{u}_1) \cdot \nabla (s_0 + s_1) \right] = q_0 + q_1 \tag{2.14}$$

Furthermore, the mean flow has also to satisfy the equations of conservation of mass, momentum and entropy as follows

$$\frac{D\rho_0}{Dt} + \rho_0 \nabla \cdot \vec{u}_0 = 0 \tag{2.15}$$

$$\rho_0 \frac{D\vec{u}_0}{Dt} = -\nabla p_0 \tag{2.16}$$

$$\rho_0 T_0 \frac{Ds_0}{Dt} = q_0 \tag{2.17}$$

The equations Eqs. (2.12, 2.13, 2.14) are further simplified by keeping only the linear terms (order ϵ) and neglecting higher order terms. In addition, the mean flow is assumed to have zero Mach number ($u_0 \simeq 0$). The zero Mach number assumption, which greatly simplifies the equations, is valid as long as the characteristic Mach number of the mean flow is small compared to the ratio of the reaction zone length over the acoustic wavelength [22]. In a combustor, the reaction zone length is typically related to the flame thickness whereas the acoustic length is the characteristic length of the main acoustic modes of a combustor. For instance, the characteristic acoustic length in longitudinal modes and transverse modes is the length of the combustor and the diameter, respectively. Under these assumptions, the simplified and linearized conservation equations read as follows

$$\frac{\partial \rho_1}{\partial t} + \vec{u}_1 \cdot \nabla \rho_0 + \rho_0 \nabla \cdot \vec{u}_1 = 0 \tag{2.18}$$

$$\rho_0 \frac{\partial \vec{u}_1}{\partial t} = -\nabla p_1 \tag{2.19}$$

$$\frac{\partial s_1}{\partial t} + \vec{u}_1 \cdot \nabla s_0 = \frac{q_1}{\rho_0 T_0} \tag{2.20}$$

In the mean flow, the time independence and zero Mach number condition imply that $\nabla p_0 = 0$ and $q_0 = 0$. These two results are derived from the fact that the mean flow satisfies the momentum and entropy conservation equations, Eqs. (2.16, 2.17),

respectively. Using the Gibbs equation, the entropy is rewritten in terms of the state variables as

$$Tds = de - \frac{p}{\rho^2} d\rho \tag{2.21}$$

Under the perfect gas assumption, the Gibbs equation can be rewritten as

$$ds = c_v \frac{dT}{T} - \frac{p}{\rho^2 T} d\rho \tag{2.22}$$

Using the differential form of the ideal gas equation of state

$$\frac{dp}{p} = \frac{d\rho}{\rho} + \frac{dT}{T} \tag{2.23}$$

Substituting Eq. (2.23) into Eq. (2.22) yields to

$$ds = c_v \frac{dp}{p} - c_v \frac{d\rho}{\rho} - \frac{p}{\rho^2 T} d\rho = c_v \frac{dp}{p} - \left(c_v + \frac{p}{\rho T} \right) \frac{d\rho}{\rho} \tag{2.24}$$

Using $p = \rho RT$ and the relation $R = c_p - c_v$, the Eq. (2.24) becomes

$$ds = c_v \frac{dp}{p} - c_p \frac{d\rho}{\rho} \tag{2.25}$$

The term ∇s_0 on the l.h.s. of the entropy equation, Eq. (2.20) can be calculated by taking the gradient of the Gibbs equation on the mean flow

$$\nabla s_0 = \frac{c_v}{p_0} \nabla p_0 - \frac{c_p}{\rho_0} \nabla \rho_0 = \frac{c_p}{T_0} \nabla T_0 + \frac{R}{p_0} \nabla p_0 \tag{2.26}$$

Since $\nabla p_0 = 0$ due to the zero Mach number condition, it follows that $\nabla s_0 = -\frac{c_p}{\rho_0} \nabla \rho_0 = \frac{c_p}{T_0} \nabla T_0$. Then, applying the Gibbs equation in the form of Eq. (2.25), reads as

$$\frac{Ds}{Dt} = \frac{c_v}{p} \frac{Dp}{Dt} - \frac{c_p}{\rho} \frac{D\rho}{Dt} \tag{2.27}$$

Linearizing Eq. (2.27) following the above mentioned process and imposing the zero Mach number mean flow condition results in

$$\frac{\partial s_1}{\partial t} + \vec{u}_1 \cdot \nabla s_0 = \frac{c_v}{p_0}\frac{\partial p_1}{\partial t} - \frac{c_p}{\rho_0}\frac{\partial \rho_1}{\partial t} - \frac{c_p}{\rho_0}\vec{u}_1 \cdot \nabla \rho_0 \tag{2.28}$$

Substituting Eq. (2.28) and $\frac{\partial \rho_1}{\partial t}$ from Eq. (2.18) into Eq. (2.20) yields to

$$\frac{c_v}{p_0}\frac{\partial p_1}{\partial t} + \frac{c_p}{\rho_0}\left(\vec{u}_1 \cdot \nabla \rho_0 + \rho_0 \nabla \cdot \vec{u}_1\right) - \frac{c_p}{\rho_0}\vec{u}_1 \cdot \nabla \rho_0 = \frac{q_1}{\rho_0 T_0} \tag{2.29}$$

Using the ideal gas equation, the relation $R = c_p - c_v$ and the ratio of specific heats, $\gamma = c_p/c_v$, Eq. (2.29) can be rewritten as

$$\frac{\partial p_1}{\partial t} + \gamma p_0 \nabla \cdot \vec{u}_1 = (\gamma - 1)\, q_1 \tag{2.30}$$

Taking the time derivative of Eq. (2.30) and substituting $\frac{\partial \vec{u}_1}{\partial t}$ from Eq. (2.19) yields to the acoustic wave equation with an unsteady heat source, as obtained in [22], reading as

$$\frac{1}{\rho_0 c_0^2}\frac{\partial^2 p_1}{\partial t^2} - \nabla \cdot \left(\frac{1}{\rho_0}\nabla p_1\right) = \frac{\gamma - 1}{\rho_0 c_0^2}\frac{\partial q_1}{\partial t} \tag{2.31}$$

where $c_0^2 = \gamma R T_0$ is the square of the speed of sound of the mean flow. In Eq. (2.31), ρ_0 and c_0 may vary spatially, whereas γ can have a small dependence on the temperature. Assuming that the mean flow properties are spatially uniform, the acoustic wave equation with an unsteady heat source simplifies, resulting in the most common form of the acoustic wave equation with an unsteady heat source as derived in [6],

$$\frac{1}{c_0^2}\frac{\partial^2 p_1}{\partial t^2} - \nabla^2 p_1 = \frac{\gamma - 1}{c_0^2}\frac{\partial q_1}{\partial t} \tag{2.32}$$

2.3 Initial Value Problem of the Acoustic Wave Equation

The problem considered in this work consists of the response of a quiescent fluid with uniform properties subjected to an unsteady heat release source in an unconfined

one-dimensional domain. This can be posed as an initial value problem governed by the one-dimensional inhomogeneous acoustic wave equation. The initial conditions correspond to a quiescent flow with constant $p = p_0$ across the domain. The mean flow properties c_0 and γ are uniform and assumed to remain constant. The initial conditions $\phi(x)$ and $\psi(x)$, and the source term $f(x,t)$ can be expressed as together with the inhomogeneous acoustic wave equation as

$$\text{Initial value problem} \begin{cases} \frac{\partial^2 p_1}{\partial t^2} - c_0^2 \frac{\partial^2 p_1}{\partial x^2} = f(x,t) \\ p_1(x,0) = \phi(x) = 0 \\ \frac{\partial p_1}{\partial t}(x,0) = \psi(x) = 0 \\ f(x,t) = (\gamma - 1)\frac{\partial q_1}{\partial t} \end{cases} \tag{2.33}$$

for $-\infty < x < \infty,\ t > 0$. The solution of the above problem gives the pressure response of the fluid, consisting of a mean flow pressure and a fluctuation part, i.e. $p(x,t) = p_0 + p_1(x,t)$. In turn, the fluctuation part is composed of a homogeneous and a particular solution as $p_1(x,t) = p_{1,h}(x,t) + p_{1,p}(x,t)$. Applying the initial conditions $\phi(x)$ and $\psi(x)$ on d'Alembert's solution, the homogeneous solution vanishes

$$p_{1,h}\ (x,t) = \frac{1}{2}\left[\phi(x + c_0 t) + \phi(x - c_0 t)\right] + \frac{1}{2c_0}\int_{x-c_0 t}^{x+c_0 t} \psi(s)ds = 0 \tag{2.34}$$

The particular solution $p_{1,p}(x,t)$ can be calculated by applying Duhamel's principle to d'Alembert's solution, which results in the following integral

$$p_{1,p}(x,t) = \frac{1}{2c_0}\int_0^t \int_{x-c_0(t-s)}^{x+c_0(t-s)} f(z,s)dzds \tag{2.35}$$

As the initial conditions imply that $p_{1,h}(x,t) = 0$, it follows that the pressure fluctuation $p_1(x,t)$ is determined by the particular solution $p_{1,p}(x,t)$ alone, which is driven by the unsteady heat source term $(\gamma - 1)\frac{\partial q_1}{\partial t}$.

2.4 Rayleigh Criterion

The Rayleigh criterion can be derived from the combination of Eq. (2.30) divided by c_0^2 and Eq. (2.19), as presented in [13]. For reference, both equations are recalled below

$$\frac{1}{c_0^2}\frac{\partial p_1}{\partial t} + \rho_0 \nabla \cdot \vec{u}_1 = \frac{\gamma - 1}{c_0^2} q_1 \tag{2.36}$$

$$\rho_0 \frac{\partial \vec{u}_1}{\partial t} + \nabla p_1 = 0 \tag{2.37}$$

Multiplying Eq. (2.36) by p_1/ρ_0 and performing the dot product of Eq. (2.37) by $\vec{u}_1$

$$\frac{\partial}{\partial t}\left(\frac{1}{2\rho_0 c_0^2} p_1^2 + \frac{1}{2}\rho_0 u_1^2\right) + \nabla \cdot (p_1 \vec{u}_1) = \frac{\gamma - 1}{\rho_0 c_0^2} p_1 q_1 \tag{2.38}$$

where the p_1^2 term represents the acoustic pressure energy and u_1^2 is the kinetic energy, respectively. The $\nabla \cdot (p_1 \vec{u}_1)$ term represents the boundary work or $p\nu$ work conducted by the fluid in the control surfaces. The $p_1 q_1$ term on the right hand side is precisely the Rayleigh index, which is the source term that relates the interaction between the unsteady heat release and the fluctuating pressure field. Eq. (2.38) can be integrated over the combustor control volume and during an acoustic cycle period (e.g. 1L acoustic mode period) to determine whether the interaction between the pressure field and the unsteady heat release results in combustion instability.

$$\frac{\partial}{\partial t}\int_V \left(\frac{1}{2\rho_0 c_0^2} p_1^2 + \frac{1}{2}\rho_0 u_1^2\right) dV = \int_V \frac{\gamma - 1}{\rho_0 c_0^2} p_1 q_1 dV - \oint_S p_1 \vec{u}_1 \cdot \vec{n}\, dS \tag{2.39}$$

$$\frac{dE}{dt} = R - B \tag{2.40}$$

where E is the energy of the combustor system, R the Rayleigh index and B the boundary work, respectively. If the pressure and heat release fluctuations are in phase, the $p_1 q_1$ term will be positive thereby increasing the energy of the system. The boundary work term acts as a sink that draws energy from the system. If the $p_1 q_1$ term is larger than the boundary work term, the energy of the system will build

up cycle after cycle as the boundaries (combustor's inlets and outlets) will not be able to evacuate sufficient energy, hence leading to combustion instability.

Eq. (2.39) assumes linear fluctuations and omits several terms such as viscosity, heat conduction and other energy loss mechanisms, which are present in a real combustor. However, even in this simplified version, the Rayleigh criterion offers a clear picture of the most important terms in thermoacoustic instabilities. In essence, the Rayleigh criterion is an energy balance that compares the sources and sinks of energy present in the fluid to assess the stability behavior of a combustor.

The Rayleigh criterion has traditionally been used to determine the stability of a combustor by assessing the relative phase of unsteady heat release with respect to acoustic pressure fluctuations. A positive Rayleigh index is a necessary but not sufficient condition for a combustor to be unstable. As presented in Eq. (2.39) the combustor boundaries may act as energy sinks that evacuate energy from the system stabilizing the combustor. Moreover, as described in Section 1.4.2, there are a number of terms that act as energy sources and sinks in a real combustor, such as vortex shedding, Kelvin-Helmholtz instabilities, or viscous dissipation and heat losses, all of which contribute to the stability behavior of a liquid rocket engine.

3. FLOW RESPONSE TO A HEAT RELEASE PULSE IN 1D

This chapter is a slightly modified version of *"Analytical and numerical solution of the pressure response to an unsteady heat release pulse in 1D"* submitted to *Combustion and Flame* and has been reproduced here with the permission of the copyright holder.

This chapter presents an analytical model based on the linear acoustic wave equation of the fluid response to an unsteady heat release pulse for two different Gaussian heat source profiles. The choice of a non-reacting fluid in an unconfined one-dimensional domain simplifies the analysis while maintaining the physical significance of the effects of unsteady heat release. The derivation of the present analytical model includes the identification of relevant length and time scales that are condensed into the Helmholtz number, He. The Helmholtz number represents the ratio of the acoustic time over the duration of the heat release pulse. The study parameters are selected to be representative of the extreme conditions in a rocket combustor. The analytical solutions distinguish between two regimes of the pressure response depending on He. The accuracy and limitations of the model are assessed by comparing the analytical solution to highly-resolved computational fluid dynamics simulations. Finally, the concepts developed in the analytical model are applied to a real combustor: CVRC [78]. Such an application is useful for assessing the extent to which the combustion process approximates to a constant pressure or a constant volume process. These observations also reflect on the feasibility of employing simplified models in the areas of a combustor with significant local flow variations.

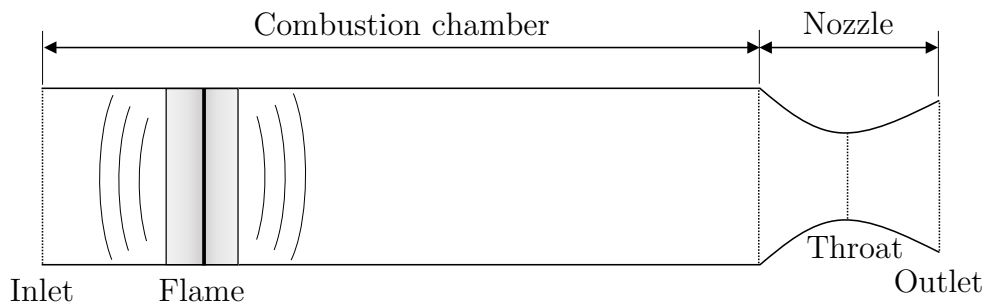

Figure 3.1. Schematic of a general one-dimensional combustor model. The fluctuations of heat release in the flame provoke pressure fluctuations that propagate across the combustor.

3.1 Overview of the Cases

The pressure response to unsteady combustion heat release is one of the most important mechanisms of combustion instability. The fluctuation of combustion heat release generates pressure oscillations that propagate in all directions and interact with the acoustic field present in the combustor. Combustion instability will occur if the oscillations of heat release couple and align with those of the acoustic modes in the combustor.

Figs. 3.3 and 3.4 show the temporal and spatial profiles of chemical heat release during the ignition of a stoichiometric mixture of gaseous methane and oxygen. In this case, the initial temperature and pressure of the mixture are 300 K and 0.5 MPa, respectively. The heat release is computed with a single-step reaction model. This case represents a general combustor example of an ignition event of a pocket mixture of cold reactants. In spite of unsteady heat release events in liquid rockets deviate from ideal Gaussian spatial and temporal profiles, the Gaussian distribution, from which an analytical solution can be derived, offers a simplified representation of complex real heat release events. In addition, the choice of a non-reacting fluid in an unconfined one-dimensional domain simplifies the analysis while maintaining the physical significance of the effects of unsteady heat release. As Cohen et al. noted [38], the artifice of a perfect gas with constant specific heats, when subjected to a heat source,

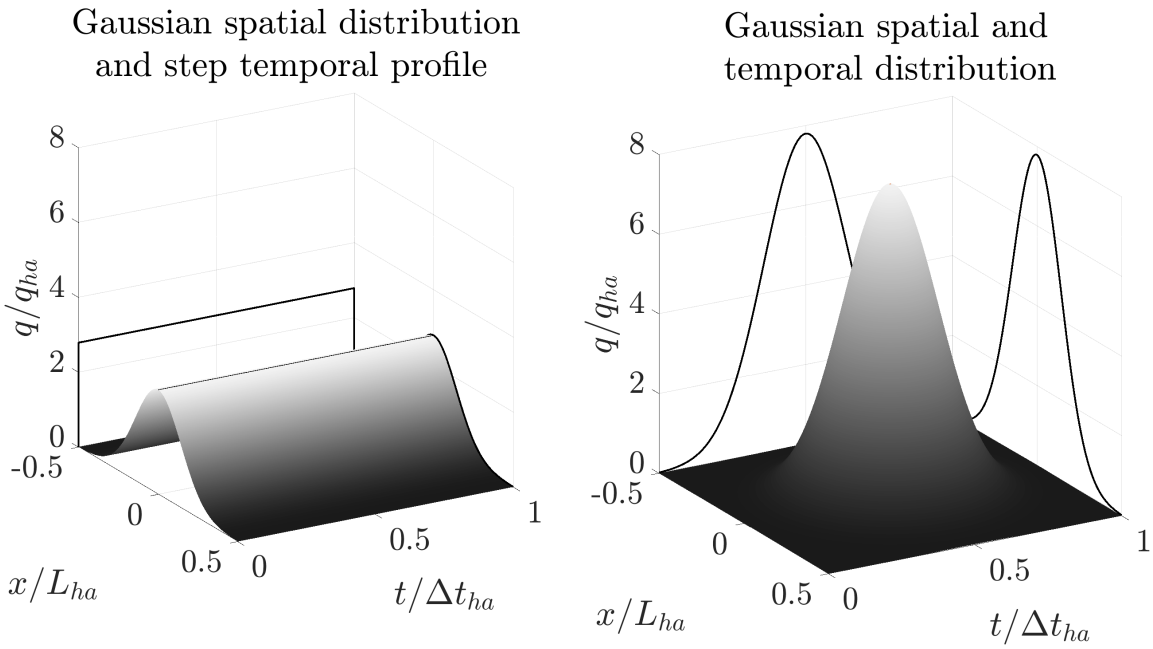

Figure 3.2. Normalized Gaussian heat release profiles with respect to the flat profile heat release intensity, q_{ha}, heat release length, L_{ha}, and heat release duration, Δt_{ha}. Both heat source profiles input the same total energy, E_{ha}.

would experience essentially the same dynamic behavior as that of a reacting mixture. All in all, the objective of this study is to gain insight into the key physics that govern the behavior of the pressure response to unsteady heat release. Although the analytical solutions derived in this study have limitations as consequence of the modeling assumptions, they capture the main physics and provide useful knowledge and quantification on the how unsteady heat release events generate acoustic waves.

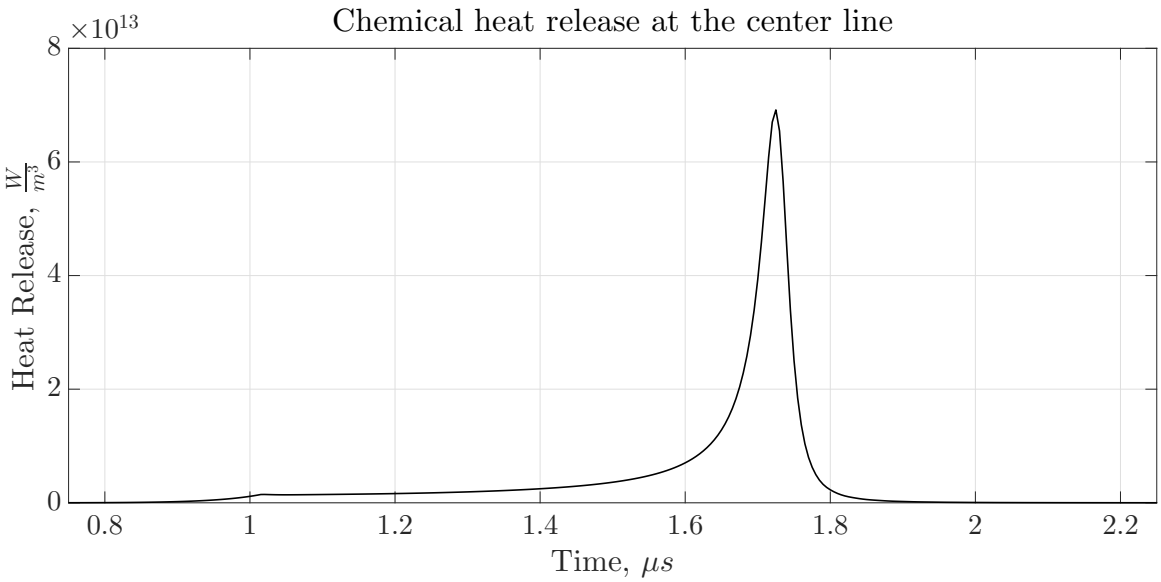

Figure 3.3. Time evolution of the chemical heat release during the ignition process of a stoichiometric mixture of gaseous methane and oxygen (T_0 = 300 K and p_0 = 0.5 MPa).

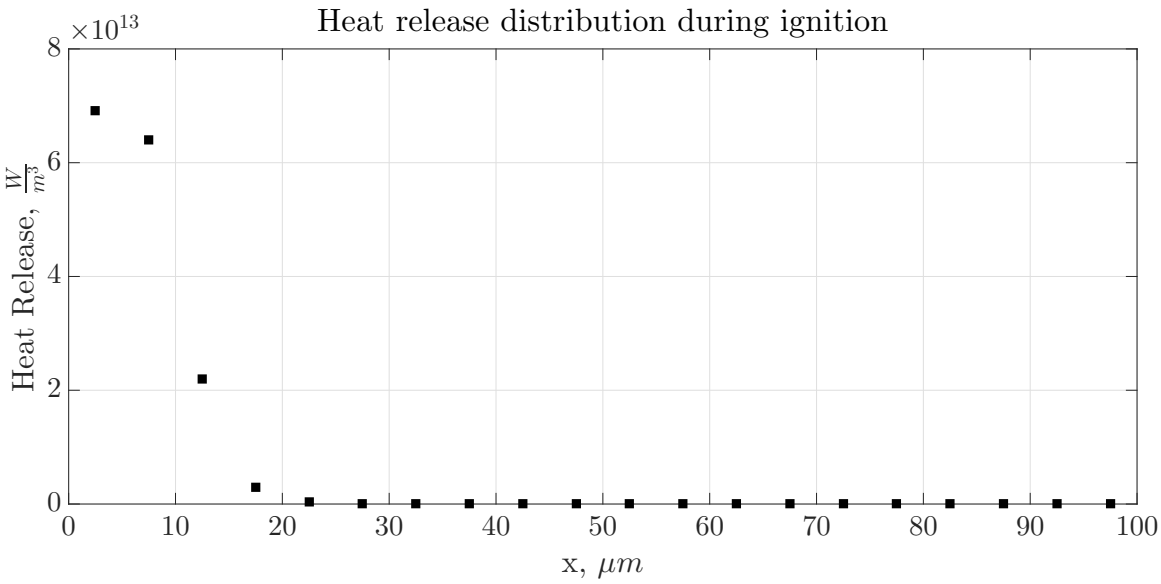

Figure 3.4. Chemical heat release spatial distribution during the maximum intensity of the ignition process of a stoichiometric mixture of gaseous methane and oxygen ($T_0 = 300$ K and $p_0 = 0.5$ MPa).

3.2 Heat Source with Gaussian Spatial Distribution and Step Temporal Profile

The present case consists of a heat source per unit volume $q_1(x,t)$ with a Gaussian spatial distribution and a step temporal profile defined as

$$q_1(x,t) = K_{ha_1} exp\left[-\frac{1}{2}\left(\frac{x}{\sigma_x}\right)^2\right](H(t-t_{hab}) - H(t-t_{hae})) \tag{3.1}$$

where $H(t-\tau)$ is the unit Heaviside function, t_{hab} is the time in which the heat pulse begins, t_{hae} is the time in which the heat pulse ends, and K_{ha_1} is the heat source magnitude parameter of the first heat source profile, defined as

$$K_{ha_1} = \frac{E_{ha}}{\sqrt{2\pi}\sigma_x H_{ha} W_{ha}(t_{hae} - t_{hab})} = \frac{q_{ha} L_{ha}}{\sqrt{2\pi}\sigma_x} \tag{3.2}$$

where E_{ha} is the total energy input, and V_{ha}, L_{ha}, H_{ha}, and W_{ha} stand for the volume, length, height, and depth of the heat source, respectively. The standard deviation

of the Gaussian spatial profile is set to $\sigma_x = L_{ha}/7$ for all the cases described subsequently in this chapter. The flat profile heat release rate q_{ha} corresponds to an equivalent constant heat release value, which gives the same total energy input as that obtained by integrating the heat source profile over space and time

$$E_{ha} = \int_{-\infty}^{\infty}\int_{-\infty}^{\infty} q_1(x,t)\ dVdt = \int_{-\infty}^{\infty}\int_{-\infty}^{\infty} q_{ha}\ dVdt = q_{ha}V_{ha}\Delta t_{ha} \tag{3.3}$$

where Δt_{ha} stands for the duration of the heat pulse as $\Delta t_{ha} = t_{hae} - t_{hab}$. The flat profile heat release value, q_{ha} is given by

$$q_{ha} = \frac{E_{ha}}{V_{ha}\Delta t_{ha}} = \frac{E_{ha}}{L_{ha}H_{ha}W_{ha}(t_{hae} - t_{hab})} \tag{3.4}$$

Hereinafter, the values of heat source intensity for the study cases are reported using the equivalent flat profile value, q_{ha}, which inputs the same heat as the Gaussian profile. Applying the temporal derivative of the heat source of Eq. (3.1) as stated in Eq. (2.33) yields to

$$\begin{aligned} f(x,t) =& (\gamma - 1)\frac{\partial q_1}{\partial t} \\ =& (\gamma - 1)K_{ha_1} exp\left[-\frac{1}{2}\left(\frac{x}{\sigma_x}\right)^2\right](\delta(t - t_{hab}) - \delta(t - t_{hae})) \end{aligned} \tag{3.5}$$

where $\delta(t - \tau)$ is the Dirac delta function. The substitution of Eq. (3.5) into Eq. (2.35) provides the expression to be integrated for obtaining the pressure response

$$p_{1,p}(x,t) = \frac{1}{2c_0}\int_0^t \int_{x-c_0(t-s)}^{x+c_0(t-s)} (\gamma - 1)K_{ha_1} e^{-\frac{1}{2}(\frac{z}{\sigma_x})^2}[\delta(s - t_{hab}) - \delta(s - t_{hae})]dzds \tag{3.6}$$

The Gaussian heat addition profile in Eq. (3.6) can be integrated using the error function

$$erf(x) = \frac{2}{\sqrt{\pi}}\int_0^x e^{-z^2}dz \tag{3.7}$$

Changing the integration variable in Eq. (3.7) to $z = \frac{x}{\sqrt{2}\sigma_x}$ allows to relate the error function with the Gaussian distribution, and write the Gaussian cumulative distribution function $\Phi_g(x)$ as follows

$$\Phi_g(x) = \frac{1}{\sqrt{2\pi}\sigma_x}\int_{-\infty}^{x} e^{-\frac{1}{2}\left(\frac{z}{\sigma_x}\right)^2} dz = \frac{1}{2}\left[1 + erf\left(\frac{x}{\sqrt{2}\sigma_x}\right)\right] \tag{3.8}$$

Changing the limits of integration to generic values x_1 and x_2 (with $x_2 > x_1$) provides the expression needed to integrate the pressure response of Eq. (3.6)

$$\Phi_g(x_2) - \Phi_g(x_1) = \frac{1}{\sqrt{2\pi}\sigma_x}\int_{x_1}^{x_2} e^{-\frac{1}{2}\left(\frac{z}{\sigma_x}\right)^2} dz = \frac{1}{2}\left[erf\left(\frac{x_2}{\sqrt{2}\sigma_x}\right) - erf\left(\frac{x_1}{\sqrt{2}\sigma_x}\right)\right] \tag{3.9}$$

Integrating Eq. (3.6) and writing $x \pm c_0 t$ as $c_0\left(x/c_0 \pm t\right)$ lead to the solution of the pressure response of a quiescent fluid to an unsteady heat source with Gaussian spatial distribution and step temporal profile

$$\begin{aligned} p_1(x,t) = \frac{A_{p_1}}{2}\Bigg[\Bigg\{ & erf\left(\frac{c_0}{\sqrt{2}\sigma_x}\left(\frac{x}{c_0} + (t - t_{hab})\right)\right) \\ & -erf\left(\frac{c_0}{\sqrt{2}\sigma_x}\left(\frac{x}{c_0} - (t - t_{hab})\right)\right)\Bigg\} H(t - t_{hab}) \\ & -\Bigg\{ erf\left(\frac{c_0}{\sqrt{2}\sigma_x}\left(\frac{x}{c_0} + (t - t_{hae})\right)\right) \\ & -erf\left(\frac{c_0}{\sqrt{2}\sigma_x}\left(\frac{x}{c_0} - (t - t_{hae})\right)\right)\Bigg\} H(t - t_{hae})\Bigg] \end{aligned} \tag{3.10}$$

where the pressure fluctuation solution is the particular solution ($p_1(x,t) = p_{1,p}(x,t)$) due to $p_{1,h}(x,t) = 0$ as presented in Section 2.3. The constant multiplying all terms in Eq. (3.10) is given by

$$A_{p_1} = 2\frac{(\gamma - 1)K_{ha_1}\sigma_x\sqrt{2\pi}}{4c_0} = \frac{E_{ha}(\gamma - 1)}{2c_0 H_{ha} W_{ha}\Delta t_{ha}} = \frac{(\gamma - 1)q_{ha}L_{ha}}{2c_0} \tag{3.11}$$

The result of the amplitude of the pressure fluctuations (see Eq. (3.11)) is consistent with the result obtained by Chu [48] for an infinitely thin heat source (modeled as $q_1(x,t) = \omega_0 \delta(x) H(t)$)) and step temporal profile

$$A_{p_{1,Chu}} = \frac{(\gamma - 1) q_{ha}}{2 c_0} \tag{3.12}$$

where ω_0 is the constant heat release rate with units of energy per unit area per unit time (W/m^2). Chu [48] indicated that this result would be valid for $\frac{\omega_0}{c_0 p_0} \ll 1$. Instead of using the Duhamel's principle applied to d'Alembert's solution as presented in Eq. (2.35), Chu [48] used the mathematical analogy of two pistons moving away from each other thereby generating acoustic pressure fluctuations. Indeed, the heat addition process generates a localized gas expansion known as "piston effect" that provokes mechanical disturbances in the surrounding gas adjacent to the heated volume [35]. Small values of energy deposition can be modeled with linear acoustic waves, whereas larger values lead to shocks [35]. Chu [48] predicted that for large rates of heat release two shock waves would form and propagate in opposite directions. As later presented in Section 3.6, the numerical results reveal that large magnitudes of heat release provoke the formation of weak shocks that propagate as steepened front waves.

The solution described by Eq. (3.10) contains two characteristic time scales that determine the type of pressure response a fluid will exhibit when subjected to the heat source of Eq. (3.1). The first time scale is the duration of heat release Δt_{ha}. The second time scale is the characteristic acoustic time, τ_{ac}, which appears as a constant inside the error function terms of Eq. (3.10), given by

$$\tau_{ac} = \frac{\sqrt{2}\sigma_x}{c_0} \tag{3.13}$$

The Helmholtz number can therefore be defined as the ratio of the characteristic acoustic time over the heat release duration as

$$He = \frac{\tau_{ac}}{\Delta t_{ha}} \ . \tag{3.14}$$

Rewriting the solution of Eq. (3.10) in terms of the characteristic acoustic time scale τ_{ac} yields to

$$\begin{aligned} p_1(x,t) = \frac{A_{p_1}}{2}\Bigg[&\left\{erf\left(\frac{\frac{x}{c_0}+(t-t_{hab})}{\tau_{ac}}\right) - erf\left(\frac{\frac{x}{c_0}-(t-t_{hab})}{\tau_{ac}}\right)\right\}H(t-t_{hab}) \\ &-\left\{erf\left(\frac{\frac{x}{c_0}+(t-t_{hae})}{\tau_{ac}}\right) - erf\left(\frac{\frac{x}{c_0}-(t-t_{hae})}{\tau_{ac}}\right)\right\}H(t-t_{hae})\Bigg] \end{aligned} \tag{3.15}$$

The pressure solution is then used to derive the solutions for velocity, density and temperature. Using the linearized momentum conservation equation (Eq. (2.19)), the velocity field can be derived from the pressure solution as

$$\begin{aligned} u_1(x,t) = -\frac{A_{p_1}}{2\rho_0 c_0}\Bigg[&\left\{erf\left(\frac{\frac{x}{c_0}+(t-t_{hab})}{\tau_{ac}}\right) + erf\left(\frac{\frac{x}{c_0}-(t-t_{hab})}{\tau_{ac}}\right)\right. \\ &\left.-2\ erf\left(\frac{x}{c_0\tau_{ac}}\right)\right\}H(t-t_{hab}) - \left\{erf\left(\frac{\frac{x}{c_0}+(t-t_{hae})}{\tau_{ac}}\right)\right. \\ &\left.+erf\left(\frac{\frac{x}{c_0}-(t-t_{hae})}{\tau_{ac}}\right) - 2\ erf\left(\frac{x}{c_0\tau_{ac}}\right)\right\}H(t-t_{hae})\Bigg] \end{aligned} \tag{3.16}$$

The density field can be computed using the linearized mass conservation equation (Eq. (2.18)). As the mean flow properties are assumed to be uniform across the domain, it follows that $\nabla\rho_0 = 0$ so that Eq. (2.18) is simplified into

$$\frac{\partial \rho_1}{\partial t} = -\rho_0 \frac{\partial u_1}{\partial x} \tag{3.17}$$

Following the same methodology as for the derivation of the velocity field and using Eq.(3.17), the density field can be computed as

$$\rho_1(x,t) = \frac{A_{p_1}}{2c_0^2}\left[\left\{erf\left(\frac{\frac{x}{c_0}+(t-t_{hab})}{\tau_{ac}}\right) - erf\left(\frac{\frac{x}{c_0}-(t-t_{hab})}{\tau_{ac}}\right)\right.\right.$$
$$\left. - \frac{4}{\sqrt{\pi}\tau_{ac}}\, exp\left(-\left(\frac{x}{c_0\tau_{ac}}\right)^2\right)(t-t_{hab})\right\}H(t-t_{hab}) - \left\{erf\left(\frac{\frac{x}{c_0}+(t-t_{hae})}{\tau_{ac}}\right)\right.$$
$$\left.\left. - erf\left(\frac{\frac{x}{c_0}-(t-t_{hae})}{\tau_{ac}}\right) - \frac{4}{\sqrt{\pi}\tau_{ac}}\, exp\left(-\left(\frac{x}{c_0\tau_{ac}}\right)^2\right)(t-t_{hae})\right\}H(t-t_{hae})\right] \tag{3.18}$$

Finally, the temperature field can be calculated from the pressure and density solutions using the linearized equation of state

$$\frac{p_1}{p_0} = \frac{\rho_1}{\rho_0} + \frac{T_1}{T_0}\ . \tag{3.19}$$

The temperature field then reads as

$$\begin{aligned} T_1(x,t) = \frac{(\gamma-1)T_0A_{p_1}}{2\rho_0c_0^2}\Bigg[&\left\{erf\left(\frac{\frac{x}{c_0}+(t-t_{hab})}{\tau_{ac}}\right) - erf\left(\frac{\frac{x}{c_0}-(t-t_{hab})}{\tau_{ac}}\right)\right. \\ &\left. + \frac{4}{(\gamma-1)\sqrt{\pi}\tau_{ac}}\, exp\left(-\left(\frac{x}{c_0\tau_{ac}}\right)^2\right)(t-t_{hab})\right\}H(t-t_{hab}) \\ &- \left\{erf\left(\frac{\frac{x}{c_0}+(t-t_{hae})}{\tau_{ac}}\right) - erf\left(\frac{\frac{x}{c_0}-(t-t_{hae})}{\tau_{ac}}\right)\right. \\ &\left. + \frac{4}{(\gamma-1)\sqrt{\pi}\tau_{ac}}\, exp\left(-\left(\frac{x}{c_0\tau_{ac}}\right)^2\right)(t-t_{hae})\right\}H(t-t_{hae})\Bigg] \end{aligned} \tag{3.20}$$

A careful examination of the solutions of pressure, velocity, density, and temperature from Eqs. (3.15, 3.16, 3.18, 3.20) allows the extraction of the limits for the primitive variables as presented in Table 3.1. The analysis of the pressure limits reveals that the ratio between the acoustic time and heat release duration, i.e. $He = \tau_{ac}/\Delta t_{ha}$, determines the behavior of the pressure response to the heat release pulse. As shown in Fig. 3.7 (L), there appears to be a critical Helmholtz number, He_{cr}, that separates

Table 3.1. Limiting expressions for the flow field response to a heat source with Gaussian spatial distribution and step temporal profile. The subscript "ff" refers to far field values.

Variable	Location	Formula
p_{max}	$x = 0$	$p_0 + \frac{(\gamma-1)E_{ha}}{2c_0 H_{ha} W_{ha} \Delta t_{ha}} erf\left(\frac{\Delta t_{ha}}{\tau_{ac}}\right)$
p_{ff}	$\lvert x\rvert > L_{ff}$	$p_0 + \frac{(\gamma-1)E_{ha}}{2c_0 H_{ha} W_{ha} \Delta t_{ha}} erf\left(\frac{\Delta t_{ha}}{2\tau_{ac}}\right)$
u_{ff}	$\lvert x\rvert > L_{ff}$	$\frac{(\gamma-1)E_{ha}}{2\rho_0 c_0^2 H_{ha} W_{ha} \Delta t_{ha}} erf\left(\frac{\Delta t_{ha}}{2\tau_{ac}}\right)$
ρ_{min}	$x = 0$	$\rho_0 - \frac{(\gamma-1)E_{ha}}{\sqrt{2\pi} c_0^2 \sigma_x H_{ha} W_{ha}}$
T_{max}	$x = 0$	$T_0 + \frac{(\gamma-1)E_{ha} T_0}{\sqrt{2\pi}\rho_0 c_0^2 \sigma_x H_{ha} W_{ha}} \left\{1 + \frac{(\gamma-1)\sqrt{\pi}\tau_{ac}}{2\Delta t_{ha}} erf\left(\frac{\Delta t_{ha}}{\tau_{ac}}\right)\right\}$

the pressure response into two distinct regimes. To determine He_{cr}, we analyze the amplitude of the pressure pulse in the far field for a constant value of q_{ha}, which is equivalent to setting the product $L_{ha}\Delta t_{ha}$ equal to a constant, while also maintaining E_{ha}, H_{ha}, and W_{ha} constant. With these considerations, removing the constants and writing the remaining variables in terms of He, the second expression of Table 3.1 becomes $\sqrt{He}\ erf(1/(2He))$. This expression peaks at $He_{cr} = 1/2$, which divides the pressure response into compact and noncompact regimes.

In the compact regime ($He < He_{cr} = 1/2$), the amplitude of the pressure response is determined by the heat release duration and is independent of the length scale L_{ha} or the standard deviation σ_x of the Gaussian profile of the heat source. Applied to a flame, this implies that the amplitude of the pressure pulse will depend on the time rate of change of the heat release and not on the flame thickness. The dependence is an inverse proportionality, i.e. $p_{max},\ p_{ff} \propto 1/\Delta t_{ha}$, indicating that sharp temporal variations in heat release provoke stronger pressure fluctuations. In this regime, the pressure pulse reaches its full amplitude at $x = 0$ and propagates in both directions maintaining the amplitude of the pulse constant. The constant amplitude is due to the fact that the model is one-dimensional and neglects viscous losses and heat conduction. In this regime, the pulse time width is of the order of Δt_{ha}. The temporal variation of the heat source also determines the shape of the pressure pulse, which is consistent with the compact cases described by Crighton [44]. The maximum pressure reads as

$$p_{max,comp} = p_0 + \frac{E_{ha}(\gamma - 1)}{2c_0 H_{ha} W_{ha} \Delta t_{ha}} \tag{3.21}$$

In the noncompact regime ($He > He_{cr} = 1/2$), the amplitude of the pressure response is determined by both the duration and the length scale of the heat source. In compact cases, the error function term disappears from Eq. (3.21) as $erf(1/He) \approx 1$. In contrast, in the noncompact regime the erf term is important as $0 \leq erf(1/He) \leq 1$, revealing that the amplitude of the pressure pulse depends on He. In this regime, the maximum pressure amplitude occurs at $x = 0$ (center of the heat release profile) and then decays over the distance converging to a far field value, as defined in Eq.

(3.24). After reaching the far field amplitude value at a distance L_{ff}, the pressure pulse amplitude remains constant due to the absence of loss mechanisms and the restriction of the problem to one dimension. In the noncompact regime, the pulse time width is of the order of L_{ha}/c_0. The spatial distribution of the heat source profile determines the shape of the pressure pulse, which is in agreement with the observations by Crighton [44] for the so-called noncompact cases. At $x = 0$ the pressure reaches a maximum value of

$$p_{max,noncomp}(x = 0) = p_0 + \frac{E_{ha}(\gamma - 1)}{2c_0 H_{ha} W_{ha} \Delta t_{ha}} erf\left(\frac{\Delta t_{ha}}{\tau_{ac}}\right) \tag{3.22}$$

The far field response occurs at a distance L_{ff} away from the center of the heat release profile corresponding to

$$L_{ff} = 2\tau_{ac} c_0 = 2\sqrt{2}\sigma_x \tag{3.23}$$

The pressure amplitude in the far field is given by

$$p_{max,noncomp}(x > L_{ff}) = p_0 + \frac{E_{ha}(\gamma - 1)}{2c_0 H_{ha} W_{ha} \Delta t_{ha}} erf\left(\frac{\Delta t_{ha}}{2\tau_{ac}}\right) \tag{3.24}$$

Both Eq. (3.22) and Eq. (3.24) are listed in Table 3.1. However, it should be noted that the expressions of Table 3.1 apply to both regimes, irrespective of the value of the He.

Fig. 3.5 depicts a compact and noncompact case of the analytical pressure response of perfect gas with properties like that of CO_2 to a heat release source with Gaussian spatial distribution and step temporal profile. Both cases have the same total energy input E_{ha} (see Table 3.3) as well as the same heat release magnitude q_{ha}. The two cases are set apart by their He which is determined by their different length scale and duration of the heat source. Fig. 3.5 (L) shows that in the compact case the amplitude of the pressure pulse remains constant over the distance. In contrast, the noncompact case depicted in Fig. 3.5 (R) shows a maximum pressure amplitude at

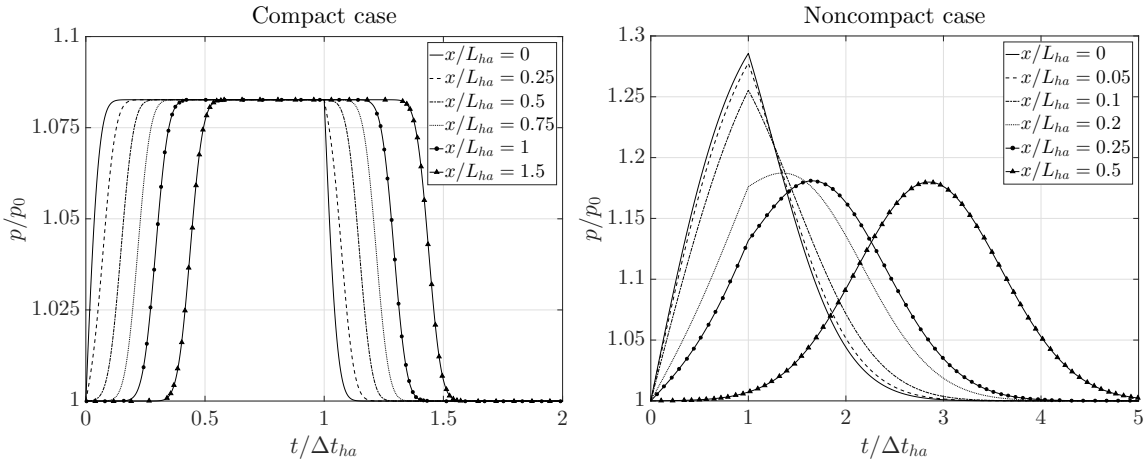

Figure 3.5. Pressure response of a perfect gas with properties like that of CO_2 to a heat release source with Gaussian spatial distribution and step temporal profile. Compact case (L): $He = 0.0593 < 1/2$, $q_{ha} = 2.5 \cdot 10^{12}$ W/m^3, $L_{ha} = 100$ μm and $\Delta t_{ha} = 1$ μs. Noncompact case (R): $He = 0.9487 > 1/2$, $q_{ha} = 2.5 \cdot 10^{12}$ W/m^3, $L_{ha} = 400$ μm, $L_{ff} = 166.62$ μm ($L_{ff} = 0.42 L_{ha}$) and $\Delta t_{ha} = 0.25$ μs.

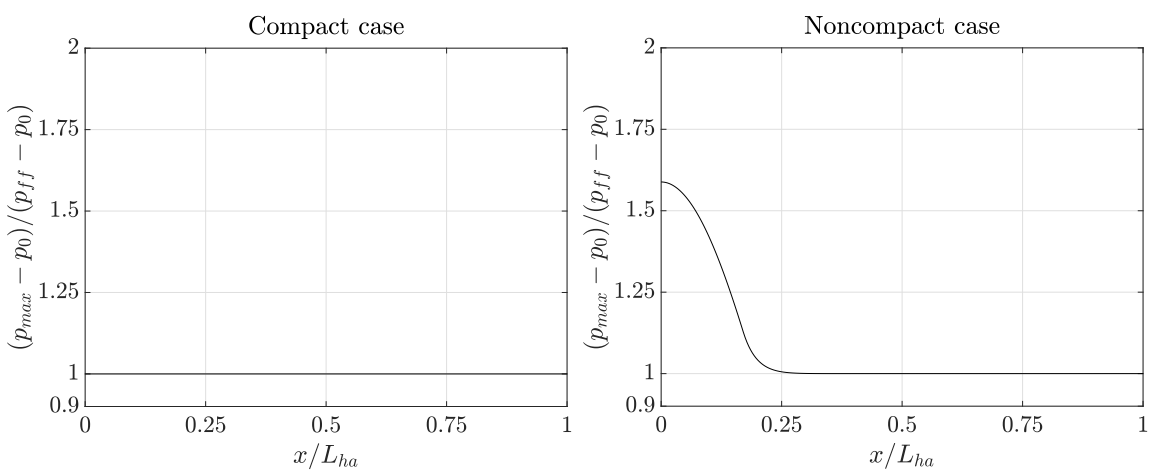

Figure 3.6. Evolution of pressure amplitude of a perfect gas with properties like that of CO_2 over the distance for the response to a heat release source with Gaussian spatial distribution and step temporal profile. Compact case (L): $He = 0.0593$, $q_{ha} = 2.5 \cdot 10^{12}$ W/m^3, $L_{ha} = 100$ μm and $\Delta t_{ha} = 1$ μs; Noncompact case (R): $He = 0.9487$, $q_{ha} = 2.5 \cdot 10^{12}$ W/m^3, $L_{ha} = 400$ μm and $\Delta t_{ha} = 0.25$ μs. $E_{ha}/(H_{ha} W_{ha}) = 250$ J/m^2 for both cases.

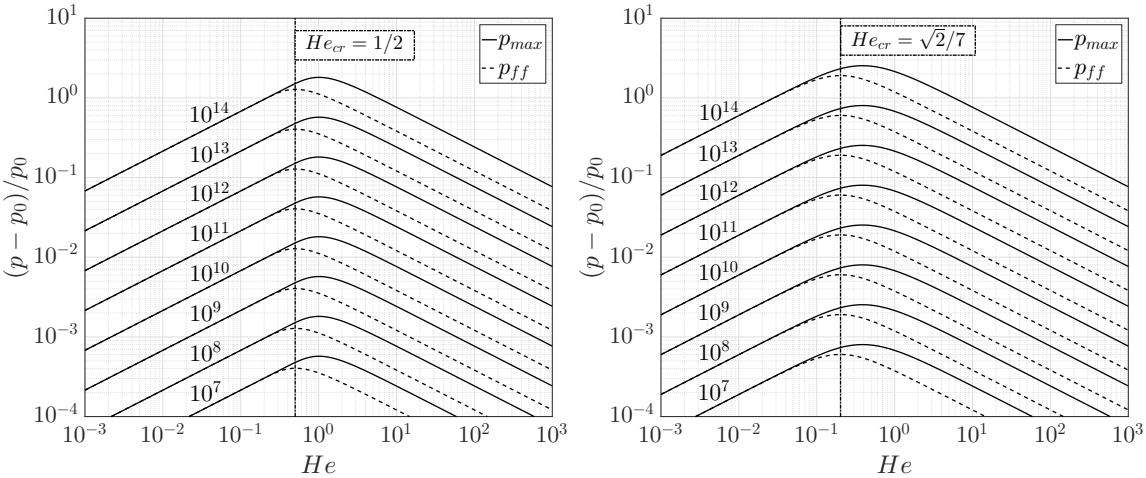

Figure 3.7. Map of the pressure amplitude for constant values of heat release intensity q_{ha} in W/m^3 for a heat source with Gaussian spatial distribution and step temporal profile (L), and a Gaussian spatio-temporal distribution (R), respectively.

$x = 0$, which then decays over the distance until converging to the far field pressure p_{ff} after the pulse travels a distance L_{ff}. It is noteworthy that the far field pressure in this case remains higher than the compact case.

3.3 Heat Source with Gaussian Spatial and Temporal Distribution

The pressure response of a fluid to an unsteady heat source with Gaussian spatial and temporal distribution is analyzed, where the heat source is given by

$$q_1(x,t) = K_{ha_2}\ exp\left[-\frac{1}{2}\left(\frac{x}{\sigma_x}\right)^2\right] exp\left[-\frac{1}{2}\left(\frac{t-t_c}{\sigma_t}\right)^2\right] \tag{3.25}$$

where t_c is the center time of the Gaussian temporal profile, and K_{ha_2} is the heat source magnitude parameter of the second heat source profile, defined as

$$K_{ha_2} = \frac{E_{ha}}{2\pi\sigma_x\sigma_t H_{ha} W_{ha}} = \frac{q_{ha} L_{ha} \Delta t_{ha}}{2\pi\sigma_x\sigma_t} \tag{3.26}$$

where q_{ha} is the flat profile heat release value defined in Eq. (3.4). The shape of the heat source is depicted in Fig. 3.2 (R). The standard deviations that define the Gaussian spatial and temporal profiles are set to $\sigma_x = L_{ha}/7$ and $\sigma_t = \Delta t_{ha}/7$. The source term $f(x,t)$ in Eq. (2.33) is obtained by taking the temporal derivative of the heat source of Eq. (3.25) as follows

$$\begin{aligned} f(x,t) &= (\gamma-1)\frac{\partial q_1}{\partial t} \\ &= -\frac{(\gamma-1)K_{ha_2}}{\sigma_t^2} exp\left[-\frac{1}{2}\left(\frac{x}{\sigma_x}\right)^2\right](t-t_c)\ exp\left[-\frac{1}{2}\left(\frac{t-t_c}{\sigma_t}\right)^2\right] \end{aligned} \tag{3.27}$$

Substitution of Eq. (3.27) into Eq. (2.35) provides the integral expression required to compute the pressure response as

$$p_{1,p}(x,t) = \frac{1}{2c_0}\int_0^t \int_{x-c_0(t-s)}^{x+c_0(t-s)} \frac{(1-\gamma)K_{ha_2}}{\sigma_t^2} e^{-\frac{1}{2}\left(\frac{z}{\sigma_x}\right)^2}(s-t_c)\ e^{-\frac{1}{2}\left(\frac{s-t_c}{\sigma_t}\right)^2} dzds \tag{3.28}$$

After integrating with respect to the spatial variable z, and recalling that $p_1(x,t) = p_{1,p}(x,t)$ as presented in Section 2.3, the resulting expression is

$$p_1(x,t) = \frac{(1-\gamma)K_{ha_2}}{2c_0\sigma_t^2}\int_0^t \left[\frac{\sqrt{2\pi}\sigma_x}{2} erf\left(\frac{z}{\sqrt{2}\sigma_x}\right)\right]_{x-c_0(t-s)}^{x+c_0(t-s)} (s-t_c)\; e^{-\frac{1}{2}\left(\frac{s-t_c}{\sigma_t}\right)^2} ds\ . \tag{3.29}$$

Subsequently integrating Eq. (3.29) with respect to the temporal variable s leads to the pressure response solution as

$$\begin{aligned} p_1(x,t) = \\ A_{p,2}\Bigg[& erf\left(\frac{c_0}{\sqrt{2}\sigma_x}\left(\frac{x}{c_0}-t\right)\right) e^{-\frac{1}{2}\left(\frac{t_c}{\sigma_t}\right)^2} - erf\left(\frac{c_0}{\sqrt{2}\sigma_x}\left(\frac{x}{c_0}+t\right)\right) e^{-\frac{1}{2}\left(\frac{t_c}{\sigma_t}\right)^2} \\ & + \frac{1}{\sqrt{1+\frac{\sigma_x^2}{c_0^2\sigma_t^2}}}\; exp\left(-\frac{\left(\frac{x}{c_0}-t+t_c\right)^2}{2\sigma_t^2\left(1+\frac{\sigma_x^2}{c_0^2\sigma_t^2}\right)}\right)\cdot \\ & \left\{erf\left(\frac{c_0}{\sqrt{2}\sigma_x}\sqrt{1+\frac{\sigma_x^2}{c_0^2\sigma_t^2}}\; t + \frac{c_0}{\sqrt{2}\sigma_x}\frac{\frac{x}{c_0}-t-\frac{\sigma_x^2}{c_0^2\sigma_t^2}t_c}{\sqrt{1+\frac{\sigma_x^2}{c_0^2\sigma_t^2}}}\right)\right. \\ & \left. -erf\left(\frac{c_0}{\sqrt{2}\sigma_x}\frac{\frac{x}{c_0}-t-\frac{\sigma_x^2}{c_0^2\sigma_t^2}t_c}{\sqrt{1+\frac{\sigma_x^2}{c_0^2\sigma_t^2}}}\right)\right\} + \frac{1}{\sqrt{1+\frac{\sigma_x^2}{c_0^2\sigma_t^2}}} exp\left(-\frac{\left(\frac{x}{c_0}+t-t_c\right)^2}{2\sigma_t^2\left(1+\frac{\sigma_x^2}{c_0^2\sigma_t^2}\right)}\right)\cdot \\ & \left\{erf\left(\frac{c_0}{\sqrt{2}\sigma_x}\sqrt{1+\frac{\sigma_x^2}{c_0^2\sigma_t^2}}\; t - \frac{c_0}{\sqrt{2}\sigma_x}\frac{\frac{x}{c_0}+t+\frac{\sigma_x^2}{c_0^2\sigma_t^2}t_c}{\sqrt{1+\frac{\sigma_x^2}{c_0^2\sigma_t^2}}}\right)\right. \\ & \left. +erf\left(\frac{c_0}{\sqrt{2}\sigma_x}\frac{\frac{x}{c_0}+t+\frac{\sigma_x^2}{c_0^2\sigma_t^2}t_c}{\sqrt{1+\frac{\sigma_x^2}{c_0^2\sigma_t^2}}}\right)\right\}\Bigg]\ , \end{aligned} \tag{3.30}$$

where the constant $A_{p,2}$ is defined in Eq. (3.34). The center time of the Gaussian temporal profile should be set to $t_c \geq 3.5\sigma_t$ to ensure that the Gaussian temporal profile is effectively represented and is not truncated to a fraction of the total energy input. Under this condition, the two terms multiplied by $e^{-\frac{1}{2}\left(\frac{t_c}{\sigma_t}\right)^2}$ can be dropped as the exponential term at this point becomes negligible. Hereinafter, for all the analytical and numerical cases t_c is set to be equal to $(t_{hab}+t_{hae})/2$.

The characteristic acoustic time τ_{ac} also appears in the solution of the pressure response to an unsteady heat source with Gaussian spatial and temporal distribution given by Eq. (3.30) as

$$\tau_{ac} = \frac{\sqrt{2}\sigma_x}{c_0} \ . \tag{3.31}$$

The Helmholtz number can be defined in the same manner as in the previous case as the ratio of the characteristic acoustic time over the duration of heat release as

$$He = \frac{\tau_{ac}}{\Delta t_{ha}} = \frac{\tau_{ac}}{7\sigma_t}, \tag{3.32}$$

with the temporal standard deviation of the Gaussian profile set to $\sigma_t = \Delta t_{ha}/7$ for all cases. The definition of He for the current case could also be based on the standard deviation σ_t, as an alternative to the heat release duration Δt_{ha}, which in turn will imply no having the factor of 7 in the denominator. However, in the interest of maintaining consistency and for the purpose of comparison, Δt_{ha} is kept as the parameter of choice. In addition to τ_{ac} and Δt_{ha}, the solution for this case contains another time scale, ζ_{xt}, which is the ratio of characteristic times defined as

$$\zeta_{xt} = \sqrt{1 + \frac{\sigma_x^2}{c_0^2\sigma_t^2}} = \sqrt{1 + \frac{1}{2}\left(\frac{\tau_{ac}}{\sigma_t}\right)^2} = \sqrt{1 + \frac{7^2}{2}He^2} \ . \tag{3.33}$$

ζ_{xt} is a measure of how fast the fluid responds with respect to the duration of the unsteady heat release pulse. The constant $A_{p,2}$ multiplying all the terms in Eq. (3.30) reads as

$$A_{p,2} = \frac{(\gamma - 1)E_{ha}}{4c_0\sqrt{2\pi}\sigma_t\zeta_{xt}H_{ha}W_{ha}} \ . \tag{3.34}$$

Rewriting the solution of Eq. (3.30) in terms of the characteristic time scales τ_{ac}, ζ_{xt} and the constant $A_{p,2}$ yields to

$$
\begin{aligned}
&p_1(x,t) = \\
&A_{p,2}\Bigg[\, exp\left(-\left(\frac{\frac{x}{c_0}-(t-t_c)}{\sqrt{2}\sigma_t\zeta_{xt}}\right)^2\right)\Bigg\{erf\left(\frac{\frac{x}{c_0}+(\zeta_{xt}^2-1)(t-t_c)}{\tau_{ac}\zeta_{xt}}\right) \\
&-erf\left(\frac{\frac{x}{c_0}-t-(\zeta_{xt}^2-1)t_c}{\tau_{ac}\zeta_{xt}}\right)\Bigg\}+exp\left(-\left(\frac{\frac{x}{c_0}+(t-t_c)}{\sqrt{2}\sigma_t\zeta_{xt}}\right)^2\right)\cdot \\
&\Bigg\{erf\left(\frac{-\frac{x}{c_0}+(\zeta_{xt}^2-1)(t-t_c)}{\tau_{ac}\zeta_{xt}}\right)+erf\left(\frac{\frac{x}{c_0}+t+(\zeta_{xt}^2-1)t_c}{\tau_{ac}\zeta_{xt}}\right)\Bigg\}\Bigg]\,.
\end{aligned}
\tag{3.35}
$$

The velocity field can be computed from the pressure solution Eq. (3.35) using the linearized momentum conservation equation (Eq. (2.19)), reading as

$$
\begin{aligned}
&u_1(x,t) = \\
&\frac{A_{p,2}}{\rho_0 c_0}\Bigg[\, exp\left(-\left(\frac{\frac{x}{c_0}-(t-t_c)}{\sqrt{2}\sigma_t\zeta_{xt}}\right)^2\right)\Bigg\{erf\left(\frac{\frac{x}{c_0}+(\zeta_{xt}^2-1)(t-t_c)}{\tau_{ac}\zeta_{xt}}\right) \\
&-erf\left(\frac{\frac{x}{c_0}-t-(\zeta_{xt}^2-1)t_c}{\tau_{ac}\zeta_{xt}}\right)\Bigg\}-exp\left(-\left(\frac{\frac{x}{c_0}+(t-t_c)}{\sqrt{2}\sigma_t\zeta_{xt}}\right)^2\right)\cdot \\
&\Bigg\{erf\left(\frac{-\frac{x}{c_0}+(\zeta_{xt}^2-1)(t-t_c)}{\tau_{ac}\zeta_{xt}}\right)+erf\left(\frac{\frac{x}{c_0}+t+(\zeta_{xt}^2-1)t_c}{\tau_{ac}\zeta_{xt}}\right)\Bigg\}\Bigg]\,.
\end{aligned}
\tag{3.36}
$$

The density field can also be calculated using the linearized mass conservation equation assuming uniform mean flow properties (see Eq. (3.17)), resulting in

$$\begin{aligned}
\rho_1(x,t) = \frac{A_{p,2}}{c_0^2}\Bigg[& -\frac{2\sqrt{2}\sigma_t\zeta_{xt}}{\tau_{ac}} exp\left(-\left(\frac{x}{c_0\tau_{ac}}\right)^2\right)\left\{erf\left(\frac{t-t_c}{\sqrt{2}\sigma_t}\right)+erf\left(\frac{t_c}{\sqrt{2}\sigma_t}\right)\right\} \\
& + \ exp\left(-\left(\frac{\frac{x}{c_0}-(t-t_c)}{\sqrt{2}\sigma_t\zeta_{xt}}\right)^2\right)\left\{erf\left(\frac{\frac{x}{c_0}+(\zeta_{xt}^2-1)(t-t_c)}{\tau_{ac}\zeta_{xt}}\right)\right. \\
& \left. - erf\left(\frac{\frac{x}{c_0}-t-(\zeta_{xt}^2-1)t_c}{\tau_{ac}\zeta_{xt}}\right)\right\} + exp\left(-\left(\frac{\frac{x}{c_0}+(t-t_c)}{\sqrt{2}\sigma_t\zeta_{xt}}\right)^2\right)\cdot \\
& \left\{erf\left(\frac{-\frac{x}{c_0}+(\zeta_{xt}^2-1)(t-t_c)}{\tau_{ac}\zeta_{xt}}\right)+erf\left(\frac{\frac{x}{c_0}+t+(\zeta_{xt}^2-1)t_c}{\tau_{ac}\zeta_{xt}}\right)\right\}\Bigg] .
\end{aligned} \tag{3.37}$$

Finally, the temperature field can be calculated using the linearized equation of state, Eq. (3.19) as

$$\begin{aligned}
T_1(x,t) = & \frac{(\gamma-1)T_0A_{p,2}}{\rho_0c_0^2}\cdot \\
& \Bigg[\frac{2\sqrt{2}\sigma_t\zeta_{xt}}{(\gamma-1)\tau_{ac}} exp\left(-\left(\frac{x}{c_0\tau_{ac}}\right)^2\right)\left\{erf\left(\frac{t-t_c}{\sqrt{2}\sigma_t}\right)+erf\left(\frac{t_c}{\sqrt{2}\sigma_t}\right)\right\} \\
& + \ exp\left(-\left(\frac{\frac{x}{c_0}-(t-t_c)}{\sqrt{2}\sigma_t\zeta_{xt}}\right)^2\right)\left\{erf\left(\frac{\frac{x}{c_0}+(\zeta_{xt}^2-1)(t-t_c)}{\tau_{ac}\zeta_{xt}}\right)\right. \\
& \left. - erf\left(\frac{\frac{x}{c_0}-t-(\zeta_{xt}^2-1)t_c}{\tau_{ac}\zeta_{xt}}\right)\right\} + exp\left(-\left(\frac{\frac{x}{c_0}+(t-t_c)}{\sqrt{2}\sigma_t\zeta_{xt}}\right)^2\right)\cdot \\
& \left\{erf\left(\frac{-\frac{x}{c_0}+(\zeta_{xt}^2-1)(t-t_c)}{\tau_{ac}\zeta_{xt}}\right)+erf\left(\frac{\frac{x}{c_0}+t+(\zeta_{xt}^2-1)t_c}{\tau_{ac}\zeta_{xt}}\right)\right\}\Bigg] .
\end{aligned} \tag{3.38}$$

Table 3.2 presents the summary of the limiting cases of pressure, velocity, density and temperature derived from the solutions of Eqs. (3.35, 3.36, 3.37, 3.38).

Following the same behavior as the previous case, the pressure response to a Gaussian spatio-temporal heat source exhibits two distinct regimes separated by He_{cr}. Both the compact and noncompact regimes feature the same trends and characteristics described in Section 3.2. Figs. 3.19 and 3.20 depict an example of compact and

Table 3.2. Limiting expressions for the flow field response to a heat source with Gaussian spatial and temporal distribution.

Variable	Location	Formula
$p_{max}\Big\vert_{He \ll He_{cr}}$	$x = 0$	$p_0 + \frac{(\gamma-1)E_{ha}}{2\sqrt{2\pi}c_0\sigma_t\zeta_{xt}H_{ha}W_{ha}} erf\left(\frac{\zeta_{xt}t_c}{\tau_{ac}}\right)$
$p_{max}\Big\vert_{He \gg He_{cr}}$	$x = 0$	$p_0 + \frac{(\gamma-1)E_{ha}}{\sqrt{2\pi}c_0\sigma_t\zeta_{xt}H_{ha}W_{ha}} exp\left[-\left(\frac{\Delta t_{ha}}{2\sqrt{2}\sigma_t\zeta_{xt}}\right)^2\right]$
p_{ff}	$\vert x\vert > L_{ff}$	$p_0 + \frac{(\gamma-1)E_{ha}}{4\sqrt{2\pi}c_0\sigma_t\zeta_{xt}H_{ha}W_{ha}}\left\{1 + erf\left(\frac{\zeta_{xt}t_c}{\tau_{ac}}\right)\right\}$
u_{ff}	$\vert x\vert > L_{ff}$	$\frac{(\gamma-1)E_{ha}}{4\sqrt{2\pi}\rho_0 c_0^2\sigma_t\zeta_{xt}H_{ha}W_{ha}}\left\{1 + erf\left(\frac{\zeta_{xt}t_c}{\tau_{ac}}\right)\right\}$
ρ_{min}	$x = 0$	$\rho_0 - \frac{(\gamma-1)E_{ha}}{2\sqrt{2\pi}c_0^2\sigma_x H_{ha}W_{ha}}\left\{1 + erf\left(\frac{t_c}{\sqrt{2}\sigma_t}\right)\right\}$
$T_{max}\Big\vert_{He \ll He_{cr}}$	$x = 0$	$T_0 + \frac{(\gamma-1)E_{ha}T_0}{2\sqrt{2\pi}\rho_0 c_0^2\sigma_x H_{ha}W_{ha}}\left\{1 + erf\left(\frac{t_c}{\sqrt{2}\sigma_t}\right)\right\}$
$T_{max}\Big\vert_{He \gg He_{cr}}$	$x = 0$	$T_0 + \frac{(\gamma-1)E_{ha}T_0}{2\sqrt{2\pi}\rho_0 c_0^2\sigma_x H_{ha}W_{ha}}\left\{1 + erf\left(\frac{t_c}{\sqrt{2}\sigma_t}\right) + \frac{2(\gamma-1)\tau_{ac}}{\sqrt{2}\sigma_t\zeta_{xt}}\right\}$

noncompact case, respectively. In compact cases, once the pressure pulse reaches its maximum amplitude, it maintains that amplitude during its propagation. In contrast, for noncompact cases, the maximum pressure amplitude occurs at $x = 0$ and then decays over the distance converging to a far field value p_{ff}. The far field response can be observed beyond the distance L_{ff} away from the center of the Gaussian heat release profile corresponding to $L_{ff} = 2\tau_{ac}c_0 = 2\sqrt{2}\sigma_x$, which is the same as that obtained for the first heat source profile in Eq. (3.23).

The analysis of the pressure limits in Table 3.2 allows us to deduct the He_{cr} for this type of heat source. We focus on the constant A_{p2} (see Eq. (3.34)) and explore the amplitude of the pressure pulse for a constant heat release intensity q_{ha}, which is equivalent to setting the product $L_{ha}\Delta t_{ha}$ equal to a constant (noting that E_{ha}, H_{ha} and W_{ha} are also constant). Under these conditions, the variation of the pressure pulse amplitude exhibits a turning point at the He that minimizes the product $\sigma_t\zeta_{xt}$. Recalling that $He = \tau_{ac}/\Delta t_{ha} = \tau_{ac}/(7\sigma_t)$, this corresponds, for a fixed heat release intensity q_{ha}, to minimizing the term $\sqrt{\frac{1}{He} + \frac{7^2}{2}He}$. In this way, the latter expression

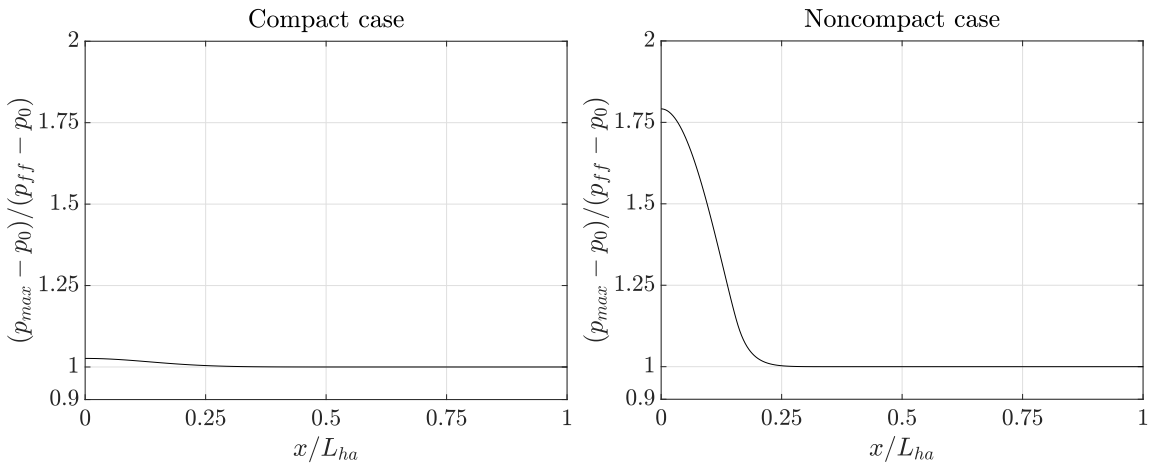

Figure 3.8. Evolution of pressure amplitude of a perfect gas with properties like that of CO_2 over the distance for the response to a heat release source with Gaussian spatio-temporal distribution. Compact case (L): $He = 0.0593$, $q_{ha} = 2.5 \cdot 10^{12}$ W/m^3, $L_{ha} = 100$ μm and $\Delta t_{ha} = 1$ μs; Noncompact case (R): $He = 0.9487$, $q_{ha} = 2.5 \cdot 10^{12}$ W/m^3, $L_{ha} = 400$ μm and $\Delta t_{ha} = 0.25$ μs. $E_{ha}/(H_{ha}W_{ha}) = 250$ J/m^2 for both cases.

reaches its minimum for $He = \sqrt{2}/7$. Thus, in this case the critical value of He is $He_{cr} = \sqrt{2}/7$.

3.4 Parametric Study

A parametric study with quiescent perfect gas with properties like that of CO_2 has been conducted to assess the trends of the fluid response to the two heat release profiles used in this study. Table 3.3 summarizes the mean flow conditions and heat release total energy input used for all the cases in this work. The heat release band size L_{ha} varies from 10 to 10^5 μm, and the heat release duration Δt_{ha} ranges from 0.1 to 10^3 μs. The energy level, mean flow conditions, and range of length and time scales of the heat source have been sized to be representative of unsteady heat release events in a high pressure rocket engine.

Fig. 3.9 (L) depicts the map of far field pressure p_{ff} for the range of length and time scales explored. The critical line $He = He_{cr}$ separates the two regimes of the pressure response. Above the critical line, in the compact regime, the far field

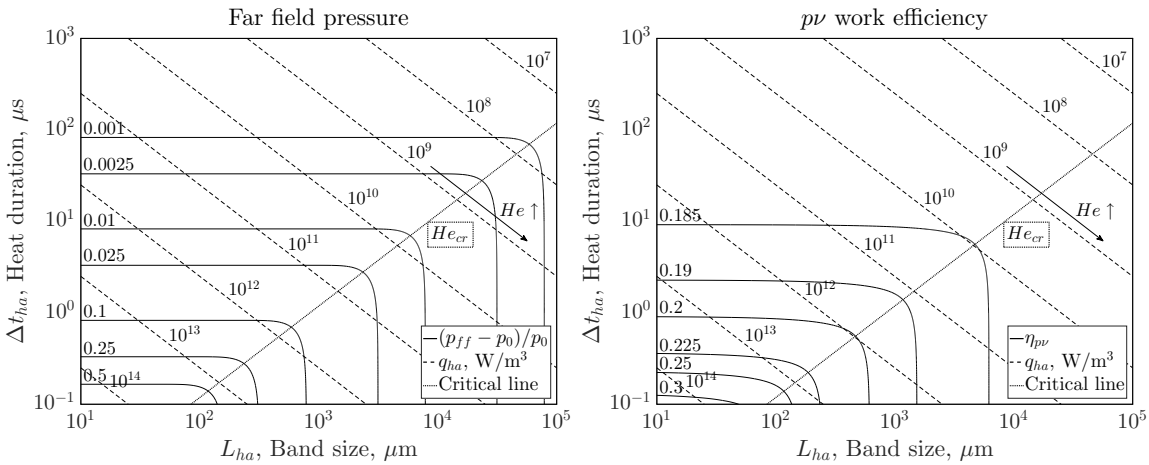

Figure 3.9. Map of the far field pressure amplitude (L) and $p\nu$ work efficiency (R) of the response of a perfect gas with properties like that of CO_2 to a heat release source with Gaussian spatial distribution and step temporal profile ($He_{cr} = 1/2$).

amplitude of the pressure pulse is inversely proportional to the heat release duration but independent of the length scale L_{ha}. Below the critical line, in the noncompact regime, for a given length L_{ha} the far field amplitude of the pressure pulse converges to a constant volume limiting value irrespective of the heat release duration Δt_{ha}. Effectively, the pressure response in the compact regime is controlled by the temporal profile of the heat source (Δt_{ha}) whereas in the noncompact regime it is controlled by the spatial distribution (L_{ha}).

The $p\nu$ work efficiency, $\eta_{p\nu}$, is a metric of interest that represents the efficiency of converting heat release into acoustic pressure energy. This quantity is very similar to the thermoacoustic efficiency term $\eta_{ac} = P_{ac}/(\dot{m}_f H)$ used in combustion noise studies such as Swaminathan [46], in which P_{ac} is the acoustic power, $\dot{m}_f$ is the fuel mass flow rate, and H is the lower heating value of the fuel. The $p\nu$ work efficiency can be defined as the $p\nu$ work generated by the pressure at the control volume boundaries divided by the total heat energy released, E_{ha}. The control volume is located away from the center of the heat release source in order to capture the far field pressure response. The $p\nu$ work efficiency reads as

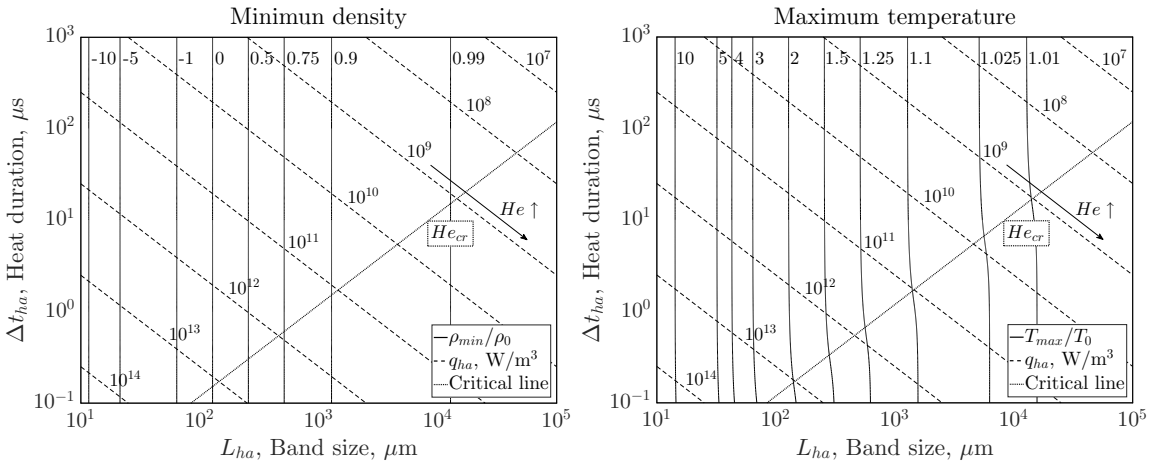

Figure 3.10. Map of the minimum density (L) and maximum temperature (R) of the response of a perfect gas with properties like that of CO_2 to a heat release source with Gaussian spatial distribution and step temporal profile ($He_{cr} = 1/2$).

$$\eta_{p\nu} = \frac{W_b}{E_{ha}} = \frac{\int_0^T \oint_{\partial\Omega} p\,(\vec{u}\cdot\vec{n})\,dsdt}{\int_0^T \int_\Omega q dV dt} = \frac{1}{E_{ha}} \int_0^T \oint_{\partial\Omega} (p_0 + p_1)\,(\vec{u_1}\cdot\vec{n})\,dsdt \tag{3.39}$$

noting that $\vec{u} = \vec{u}_1$ due to the zero Mach number assumption ($\vec{u}_0 = 0$).

Fig. 3.9 (R) shows a map of the $p\nu$ work efficiency, $\eta_{p\nu}$, as defined in Eq. (3.39). The $p\nu$ work efficiency map reveals that for large length and time scales of the heat source profile (L_{ha} and Δt_{ha}), the efficiency of converting heat release into acoustic pressure energy decreases until it plateaus to a lower limit approaching to a constant pressure process. In contrast, for very small length and time scales, when the heat release values per unit length and time are extremely large, the $p\nu$ work efficiency increases as the process tends to become a constant volume process. However, this increasing $p\nu$ work efficiency for large values of q_{ha} can materialize only to a certain extent as nonlinear effects start to become important due to the significant deviations from the model assumptions including constant mean flow properties, linear fluctuations, inviscid flow and negligible heat conduction.

Fig. 3.10 depicts the minimum density and maximum temperature predicted by the analytical solution. The minimum density plot is particularly useful as the zero level clearly marks the threshold at which the above mentioned assumptions of the acoustic wave equation break down. For short heat release lengths L_{ha} the density transitions from positive to negative, and starts to asymptotically tend to $-\infty$ for $L_{ha} \to 0$. The temperature tends to ∞ for $L_{ha} \to 0$.

The map of far field pressure amplitude (L) and the $p\nu$ work efficiency (R) for the heat source with Gaussian spatio-temporal distribution is shown in Fig. 3.11. Both of these quantities exhibit the same trends and characteristics as the previous case. However, a comparison reveals that the Gaussian spatial and temporal distribution features higher far field pressure amplitude and $p\nu$ work efficiency for the same value of heat release length and time scale. This is a result of the differences in the peak values of the heat source profiles (i.e. higher q_{max}), as shown in Fig. 3.2.

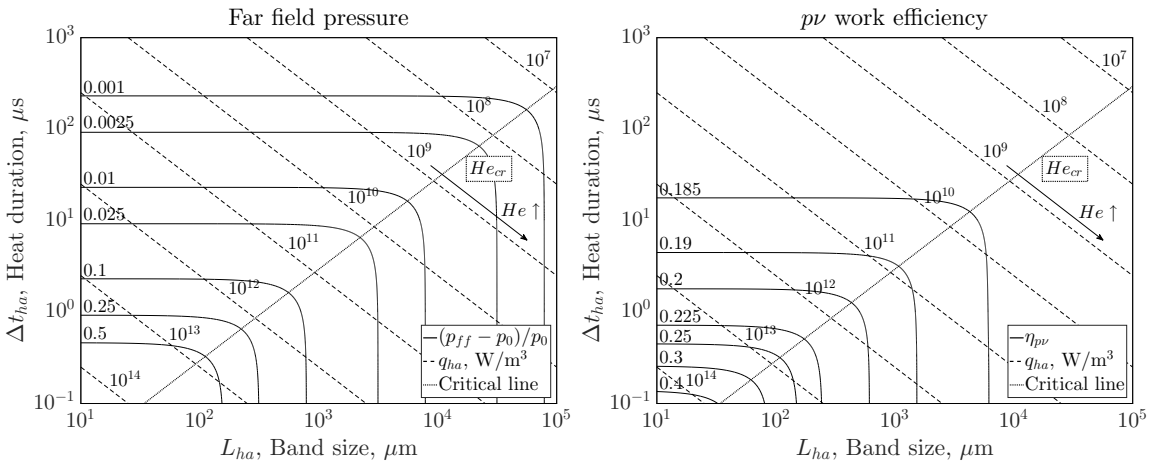

Figure 3.11. Map of the far field pressure amplitude (L) and $p\nu$ work efficiency (R) of the response of a perfect gas with properties like that of CO_2 to a heat release source with Gaussian spatial and temporal distribution ($He_{cr} = \sqrt{2}/7$).

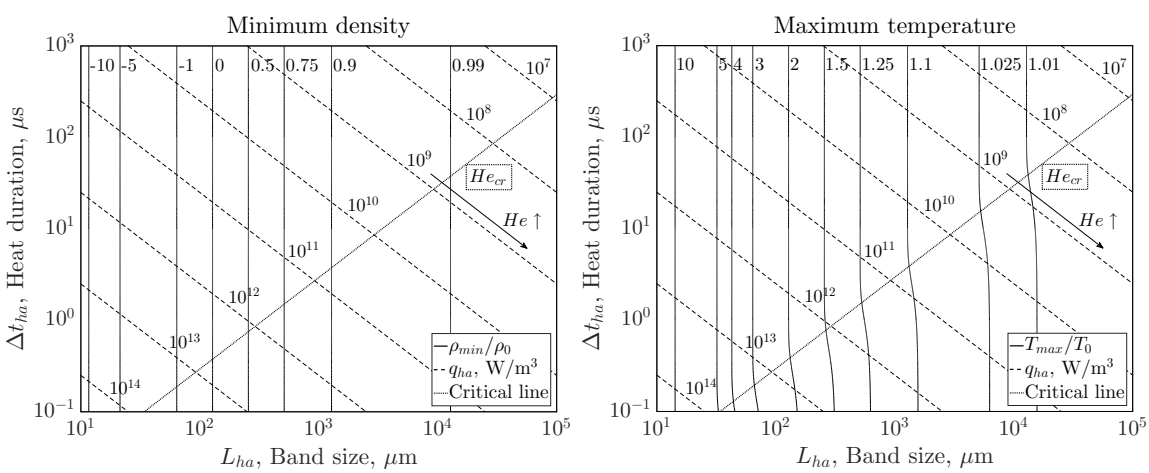

Figure 3.12. Map of the minimum density (L) and maximum temperature (R) of the response of a perfect gas with properties like that of CO_2 to a heat release source with Gaussian spatial and temporal distribution ($He_{cr} = \sqrt{2}/7$).

Fig. 3.12 shows the map of minimum density (L) and maximum temperature (R) for the heat source with Gaussian spatial and temporal distribution. The observed trends are consistent with those observed with the Gaussian spatial distribution and step temporal profile.

For large rates of heat release ($q_{ha} > 10^{11}$ W/m^3), the analytical model starts to deviate from the numerical solution due to the presence of nonlinear effects such as temperature dependence of the local speed of sound, wave front steepening, formation of weak shocks, and neglecting loss mechanisms such as viscosity and heat conduction. Although the parametric study covers a wide range of length and time scales, the applicability of the analytical model is limited to low and moderate heat release rates. For large heat release values the assumptions of the analytical model deviate from the actual conditions provoking a loss of accuracy as the conditions become more extreme.

3.5 Constant Pressure and Constant Volume Limits

The Helmholtz number condenses the effects of relevant length and time scales that characterize the different regimes of pressure response of a fluid to an unsteady heat release event. In addition to distinguishing between regimes of operation, He also determines whether the pressure response to unsteady heat release tends towards a constant pressure or a constant volume process. Fig. 3.13 depicts a diagram of the thermodynamic process paths of pressure and specific volume for both heat release profiles. For $He \ll He_{cr}$ the pressure response tends to a constant pressure process, whereas for $He \gg He_{cr}$ the response tends to a constant volume process. As noted by Meyer and Oppenheim [36], at the $He = 0$ limit the heat addition process occurs at constant pressure, whereas for $He = \infty$ this results in a constant volume process.

All the curves in Fig. 3.13 start at $(\nu/\nu_0,\ p/p_0) = (1, 1)$, which corresponds to the initial conditions of ρ_0 and p_0, then follow with an increase in pressure and specific volume during the heat addition phase, and finally proceed to an expansion as the

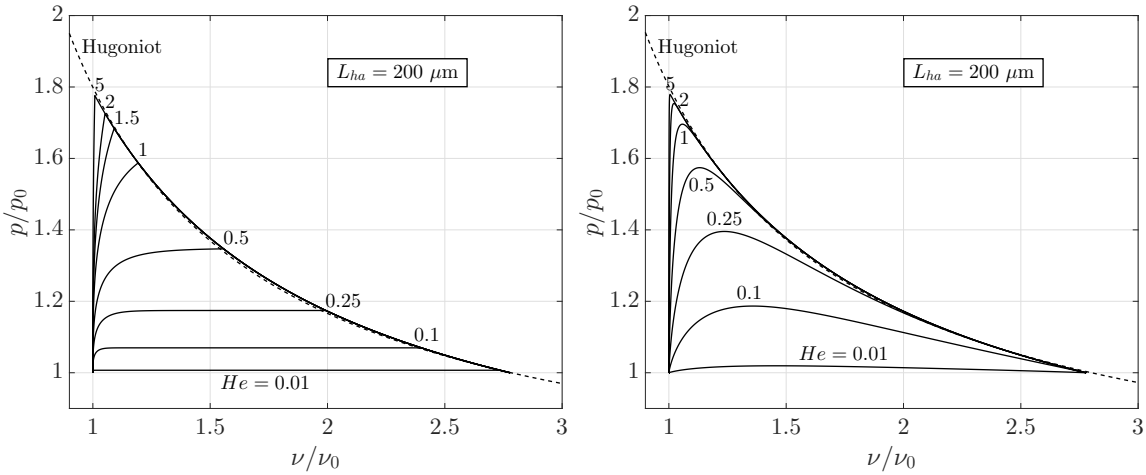

Figure 3.13. Diagram of pressure and specific volume at $x = 0$ for a fixed heat release length $L_{ha} = 200\ \mu$m and for different He. The heat release sources are a Gaussian spatial distribution and step temporal profile (L), and Gaussian spatial and temporal distribution (R), respectively.

heat release abates. In this final phase, the paths collapse towards the Hugoniot curve [36, 38, 79], which is given by

$$\frac{p}{p_0} = \frac{\frac{2Q_H}{p_0\nu_0} + \frac{\gamma+1}{\gamma-1} - \frac{\nu}{\nu_0}}{\left(\frac{\gamma+1}{\gamma-1}\right)\frac{\nu}{\nu_0} - 1}\ , \tag{3.40}$$

where Q_H represents the energy per unit mass added during the heat addition process.

For both heat source profiles of Fig. 3.13, $He = 0.01$ represents a compact case with a low He that approaches to a constant pressure process. In contrast, $He = 5$ represents a noncompact case with a high He that tends towards a constant volume heat addition process. In Fig. 3.13 (L), the heat source with Gaussian spatial distribution and step temporal profile shows a clear distinction between compact and noncompact cases, below and above $He_{cr} = 1/2$, respectively. Below He_{cr}, once the pressure reaches its maximum amplitude it remains constant until the expansion begins once the heat addition finalizes. Above He_{cr}, the pressure reaches its maximum at the time at which the heat addition ends, and then it decays as there is no longer heat release to continue supporting the pressure increase. The evolution of the pressure amplitude for the compact and noncompact cases of Fig. 3.13 (L) follows the same trends exhibited by the two cases from Fig. 3.5. For both compact and noncompact cases, the time at which heat addition ends marks a sharp change in the pressure response leading to a sudden pressure expansion that coincides with the Hugoniot curve. This sharp change is caused by the abrupt removal of the heat source in just a time instant ($t = t_{hae}$). In constraint, in Fig. 3.13 (R), for the heat source with Gaussian spatial and temporal distribution, the difference between compact and noncompact cases is not as clear since the temporal profile varies smoothly. The Gaussian temporal profile therefore experiences a smooth-varying expansion that collapses to the Hugoniot curve as the heat release decreases. The distinction of both pressure response regimes for the second heat source profile is shown in Fig. 3.19 and Fig. 3.20 by comparing the pressure pulse amplitude at different locations.

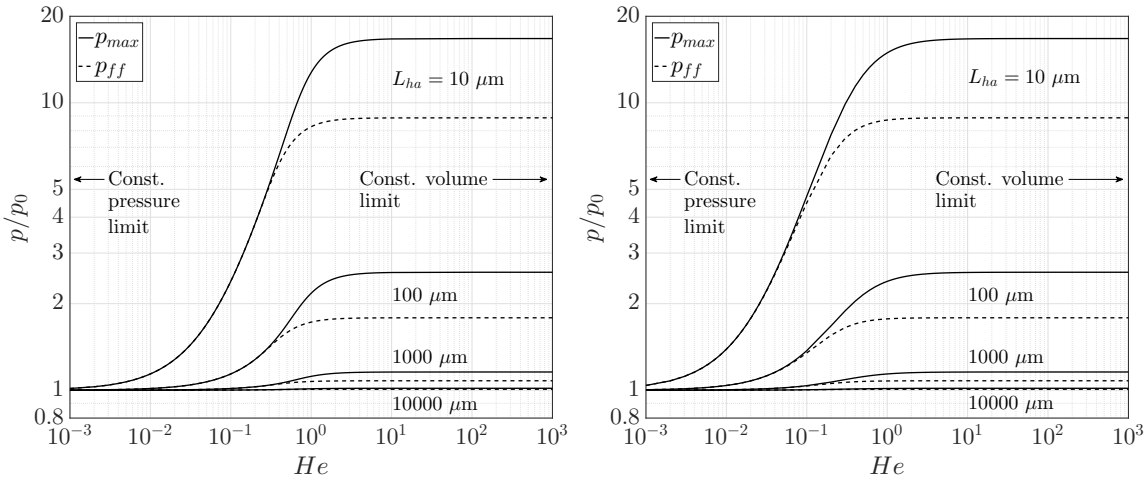

Figure 3.14. Evolution of the maximum pressure and far field pressure amplitude for fixed heat release lengths L_{ha} with respect to He. The heat release sources are a Gaussian spatial distribution and step temporal profile (L), and Gaussian spatial and temporal distribution (R), respectively.

Fig. 3.14 shows the maximum and the far field pressure amplitude as a function of He. At a given heat release length scale L_{ha}, the amplitude of the pressure pulse grows as He increases until reaching the maximum value corresponding to the constant volume limit. For a given length scale L_{ha}, regardless of how short the duration of the heat addition becomes, the pressure amplitude will reach an upper constant volume process limit. Thus, the constant volume limit of the pressure response to a heat source with Gaussian spatial distribution and step temporal profile can be calculated by fixing σ_x (equivalent to fixing L_{ha}), and computing the limit of p_{max} in Table 3.1 for $He \to \infty$ as

$$\begin{aligned} p_{max1,CVC} = \lim_{He\to\infty} p_0 + \frac{(\gamma-1)E_{ha}}{2c_0 H_{ha} W_{ha} \Delta t_{ha}} erf\left(\frac{\Delta t_{ha}}{\tau_{ac}}\right) = \\ \lim_{He\to\infty} p_0 + \frac{(\gamma-1)E_{ha} He}{2\sqrt{2}\sigma_x H_{ha} W_{ha}} erf\left(\frac{1}{He}\right) = p_0 + \frac{(\gamma-1)E_{ha}}{\sqrt{2\pi}\sigma_x H_{ha} W_{ha}} \ , \end{aligned} \tag{3.41}$$

where Δt_{ha} is expressed in terms of He by substituting $\Delta t_{ha} = \frac{\tau_{ac}}{He} = \frac{\sqrt{2}\sigma_x}{c_0 He}$. It should be noted that $He \cdot erf(1/He) = 2/\sqrt{\pi}$ in the limit $He \to \infty$. For the far field pressure amplitude constant volume limit, the term $He \cdot erf(\frac{1}{2Da})$ becomes $1/\sqrt{\pi}$ when $He \to \infty$. On the other side, the constant volume limit of the pressure response to a heat source with Gaussian spatial and temporal distribution can be computed in the same fashion departing from the second equation from Table 3.2 as

$$\begin{aligned} p_{max2,CVC} = \lim_{He\to\infty} p_0 + \frac{(\gamma-1)E_{ha}}{\sqrt{2\pi} c_0 \sigma_t \zeta_{xt} H_{ha} W_{ha}} exp\left[-\left(\frac{\Delta t_{ha}}{2\sqrt{2}\sigma_t \zeta_{xt}}\right)^2\right] = \\ \lim_{He\to\infty} p_0 + \frac{7(\gamma-1)E_{ha}}{\sqrt{2\pi}\sqrt{2}\sigma_x \frac{1}{He}\sqrt{1+\frac{7^2}{2}He^2} H_{ha} W_{ha}} exp\left[-\left(\frac{7}{2\sqrt{2}\sqrt{1+\frac{7^2}{2}He^2}}\right)^2\right] \\ = p_0 + \frac{7(\gamma-1)E_{ha}}{\sqrt{2\pi}\sqrt{2}\sigma_x \sqrt{\frac{7^2}{2}} H_{ha} W_{ha}} = p_0 + \frac{(\gamma-1)E_{ha}}{\sqrt{2\pi}\sigma_x H_{ha} W_{ha}} \ . \end{aligned} \tag{3.42}$$

The results of Eqs. (3.41-3.42) are remarkable as they reveal that for noncompact cases with $He \gg He_{cr}$, the maximum amplitude of the pressure response to an unsteady heat release event is limited to the same constant volume limit regardless

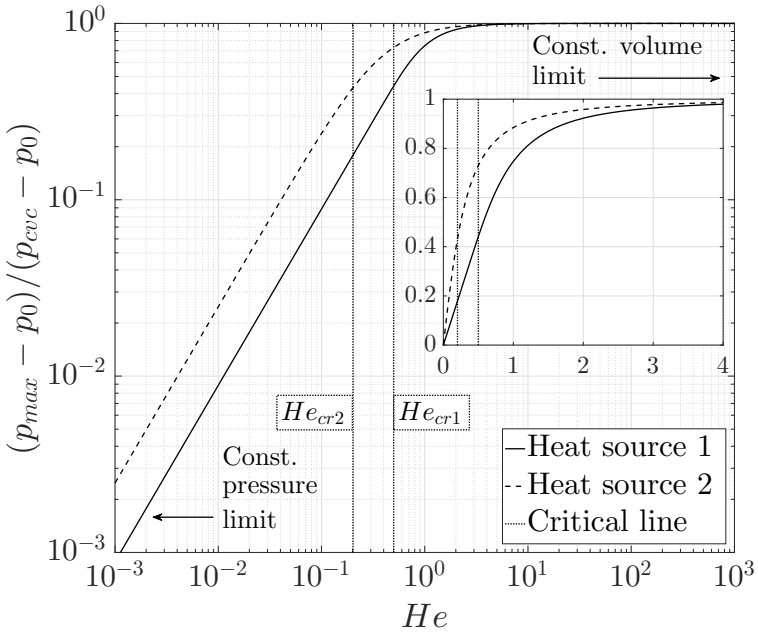

Figure 3.15. Evolution of the maximum pressure with respect to the constant volume pressure limit as a function of He. Heat source 1 and 2 are the Gaussian spatial distribution and step temporal profile, and Gaussian spatial and temporal distribution, respectively.

of the temporal profile of the heat source. Furthermore, for a fixed γ and energy level $E_{ha}/(H_{ha}W_{ha})$, the constant volume limit pressure amplitude is controlled by the heat release length scale σ_x (equivalently L_{ha}).

In Fig. 3.14 (R) the Gaussian spatial and temporal distribution follows the same trends and same limits as the Gaussian spatial distribution and step temporal profile (Fig. 3.14 (L)) but with the curves slightly shifted towards lower He values. Fig. 3.15 shows that the ratio $(p_{max} - p_0)/(p_{cvc} - p_0)$ only depends on He since γ, E_{ha}, H_{ha}, W_{ha}, and σ_x cancel out. For the first heat source, which has a simple solution, this ratio is equal to $(\sqrt{\pi}/2)He \cdot erf(1/He)$. Therefore, within the range of application of the analytical model, each heat release source has a single curve that uniquely relates He with said ratio.

3.6 Comparison of Analytical and Numerical Results

3.6.1 Solver Details

High-fidelity DES simulations have been conducted with the aim of assessing the accuracy and limitations of the analytical solutions derived in this study. The numerical simulations are performed using an in-house Navier-Stokes solver called General Equation and Mesh Solver (GEMS) [80–82]. GEMS is an implicit dual time stepping coupled solver. The numerical integration of the conservation equations is second-order accurate in both space and time. The solution of the linear system is obtained by line Gauss-Seidel method. This solver is capable of handling multi-step detailed chemical kinetics. Message passing interface is used for parallelization. The code is capable of handling both unstructured and structured meshes. GEMS has been extensively developed and used to analyze high-pressure turbulent combustion flows in unstable combustors resulting in qualitative good agreement with experimental results [69–74].

3.6.2 Simulation Setup

The case study consists of a uniform quiescent fluid that responds to the two aforementioned heat release source profiles. The dimensions of the domain are set such that the simulation concludes before the induced pressure waves reach the vertical boundaries. This condition eliminates any acoustic reflections at the boundaries and limits the influence of boundary conditions on the solution. The computational domain is depicted in Fig. 3.16 and it consists of a two-dimensional cavity of 15 mm $\times$ 0.015 mm. The top and bottom boundaries are set as periodic boundary conditions so as to maintain a one-dimensional solution. The left and right boundaries are treated as inviscid, adiabatic walls. The heat release is modeled as an external source in the energy equation, located at the center of the domain. The total number of cells is 100,000, and the mesh is divided in 100 partitions. The structured grid is

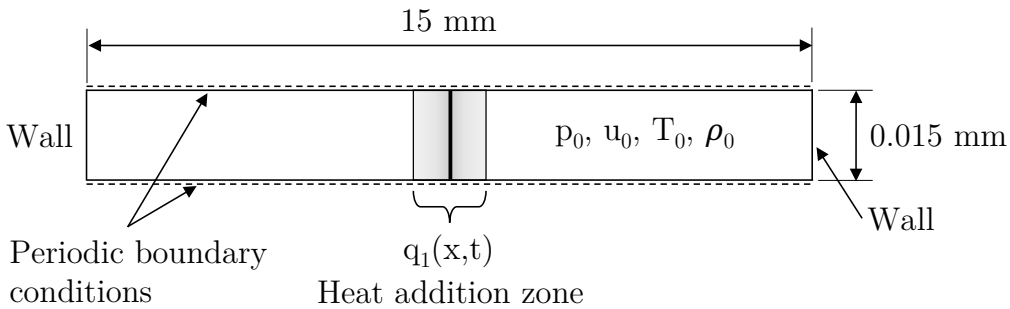

Figure 3.16. Schematic of the computational domain used in the numerical simulations.

Table 3.3. Perfect gas mean flow properties like that of CO_2 and heat release energy used for all the analytical and numerical simulations of Chapter 3.

p_0 (MPa)	T_0 (K)	u_0 (m/s)	ρ_0 (kg/m^3)	c_0 (m/s)	γ_0	$E_{ha}/(H_{ha}W_{ha})$ (J/m^2)
1.0	500.0	0.0	10.59	340.72	1.2253	250.0

uniform with a cell size of 1.5 μm in the x and y directions across all the domain. To accurately capture the transient, the time step is limited to 2 ns and the simulations captures 12.5 μs of physical time.

The study has been conducted using perfect gas with properties like that of CO_2 as the working fluid with the conditions and energy level summarized in Table 3.3. A pressure of 1 MPa and a temperature of 500 K are chosen as the initial conditions, which are representative of the interaction between hot and cold gases in the shear layer region of a non-premixed, shear-coaxial injector used in rocket engines.

3.6.3 Results Discussion

The comparison of the analytical and numerical solutions of the fluid response to a heat source with Gaussian spatial distribution and step temporal profile are depicted in Fig. 3.17 and Fig. 3.18, which represent a compact and a noncompact case, respectively. Although both cases use the same initial conditions, energy level

$E_{ha}/(H_{ha}W_{ha})$ and heat release intensity q_{ha}, the noncompact case features a higher pressure amplitude as it releases the same amount of total energy within a shorter time Δt_{ha}. As it occurred in Fig. 3.5, the compact case maintains the amplitude of the pressure pulse over the distance whereas in the noncompact case the pressure pulse peaks at $x = 0$, and then decays until converging to the far field pressure amplitude.

As shown in Figs. 3.17(L) and 3.18(L), the analytical solution reasonably captures the pressure response with a slight overshoot in the amplitude. The difference between the analytical and numerical solutions is due to the assumption of constant mean flow properties and the absence of loss mechanisms as heat conduction and viscous losses are neglected in the analytical model. At the center of the heat source, as the temperature increases substantially due to the heat release, the speed of sound also increases following its strong temperature dependence. From Eqs. (3.11) and (3.15) it follows that an increase in speed of sound decreases the effectiveness by which unsteady heat release generates acoustic pressure waves. This effect is clearly seen in Fig. 3.17(L) as the pressure from the numerical solution starts to deviate from the analytical solution as the speed of sound increases. After reaching the maximum value (around $t/\Delta t_{ha} = 0.12$), the numerical pressure decays in a quasi-linear fashion following the increasing trend of the speed of sound. As expected, the analytical model does not capture this local effect on account of its constant mean flow properties assumption.

Within the heated zone, the pressure amplitude and drop in density are overestimated by the analytical solution, whereas the temperature rise can be either over- or under-predicted, depending on He. In all the cases, the dominant cause for the deviations is the assumption of constant mean flow properties, as the losses due to heat conduction or viscous effects are estimated to be insignificant. The deviation of the analytical solution from the numerical result becomes notable when the local speed of sound varies over 5% from the mean. Density and temperature analytical solutions exhibit large errors for significant variations of the speed of sound, whereas the pres-

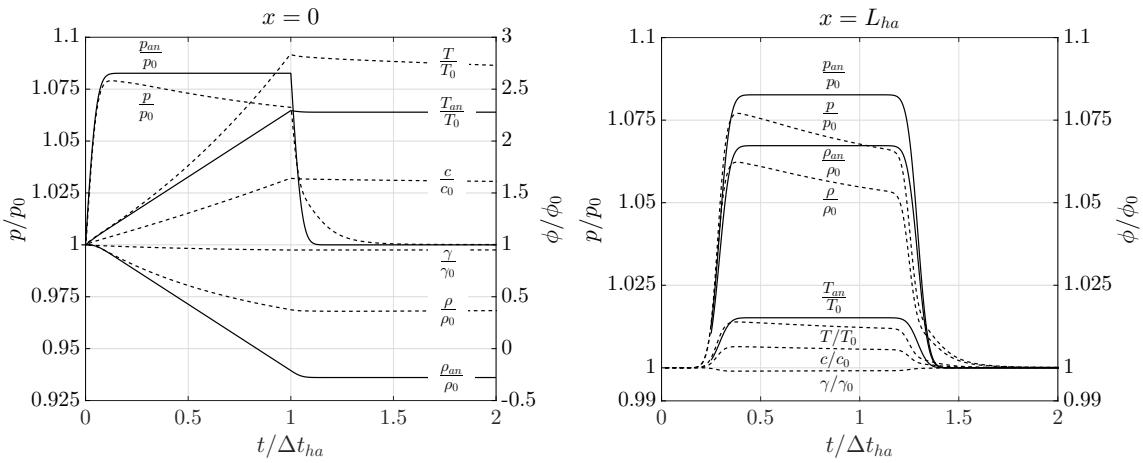

Figure 3.17. Compact case, $He = 0.0593 < 1/2$. Flow field response to a heat source with Gaussian spatial distribution and step temporal profile. Solid lines represent the analytical solution whereas dashed lines are the numerical solution. Heat release parameters: $q_{ha} = 2.5 \cdot 10^{12}$ W/m^3, $L_{ha} = 100$ μm, $\Delta t_{ha} = 1$ μs. In this plot and the subsequent ones, $\phi = \rho$, T, c, γ are scaled with respect to the right hand side axis.

sure solution continues to predict a close amplitude result even for large deviations from the mean value.

The minimum density expression from Table 3.1 shows that an increase in the speed of sound results in a greater density than the value predicted by the analytical solution. For large values of heat release and small length scales, the minimum density predicted by the analytical solution can become negative as seen from Fig. 3.17(L). This result is consistent with Chu's prediction [48] that $\rho(x = 0) \to -\infty$ and $T(x = 0) \to \infty$ for an infinitely thin heat source. A negative density, which is an unphysical result, is therefore an effective threshold to determine the range of applicability of the acoustic wave equation in thermoacoustic problems. It should be noted that away from the heat release zone, the density returns to feasible values. Whereas the relation between pressure, temperature and density are clearly nonisentropic at the centerline due to heat release, outside of the heat release zone ($|x| > L_{ha}/2$) the isentropic gas relations remain valid. The analytical expression for the maximum temperature given in Table 3.1 shows that with increasing speed of sound the temperature can be either over- or under-estimated depending on He. The analytical solution underestimates the temperature for compact cases and slightly overestimates it for noncompact cases, respectively. The deviation of the numerically obtained ratio of specific heats γ from the constant mean flow value appears to be minimal, indicating that a constant γ is a justifiable assumption.

Figs. 3.19-3.20 show the comparison of the numerical and analytical solutions of the fluid response to the second heat release profile, with Gaussian spatial and temporal distribution. The analytical solution captures reasonably well the dynamics of the numerical solution as in the previous case. An overshoot in amplitude is observed due primarily to the constant mean flow assumption. A greater pressure amplitude than the previous case is present due to the heat source is more concentrated at the center (see Fig. 3.2).

The comparison of the analytical and numerical solutions in Figs. 3.17-3.20 also highlights the importance of nonlinear effects that are not captured by the linear

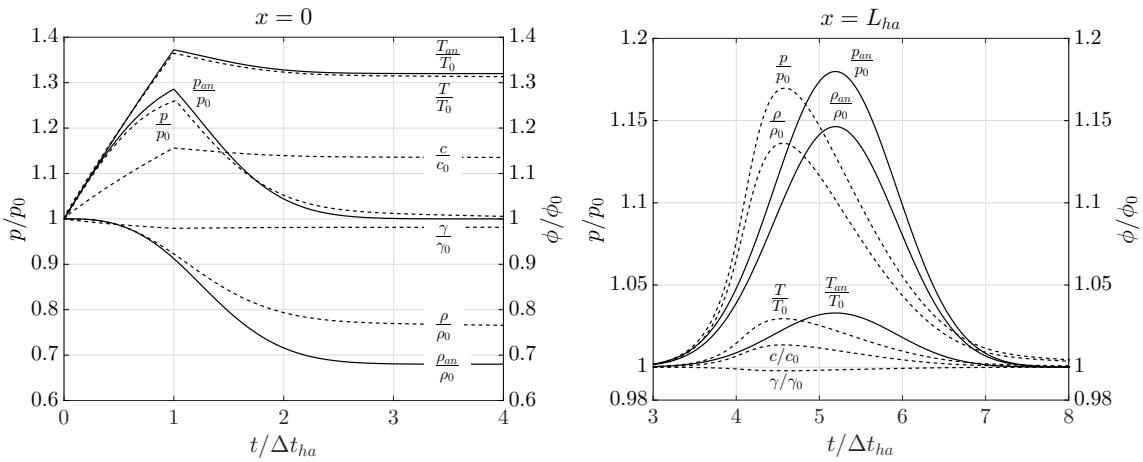

Figure 3.18. Noncompact case, $He = 0.9487 > 1/2$. Flow field response to a heat source with Gaussian spatial distribution and step temporal profile. Solid lines represent the analytical solution whereas dashed lines are the numerical solution. heat release parameters: $q_{ha} = 2.5 \cdot 10^{12}$ W/m^3, $L_{ha} = 400$ μm, $\Delta t_{ha} = 0.25$ μs.

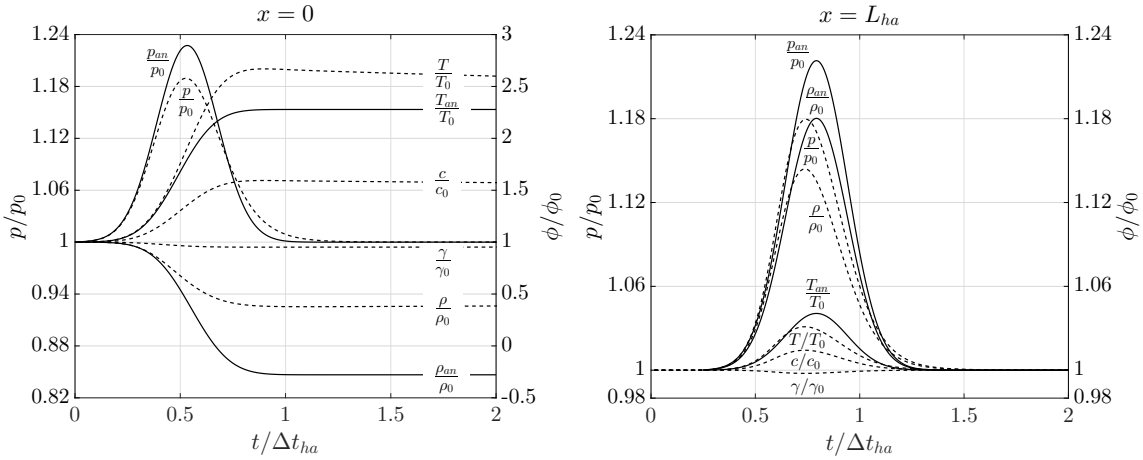

Figure 3.19. Compact case, $He = 0.0593 < \sqrt{2}/7$. Flow field response to a heat source with Gaussian spatial and temporal distribution. Solid lines represent the analytical solution whereas dashed lines are the numerical solution. heat release parameters: $q_{ha} = 2.5 \cdot 10^{12}$ W/m^3, $L_{ha} = 100$ μm, $\Delta t_{ha} = 1$ μs.

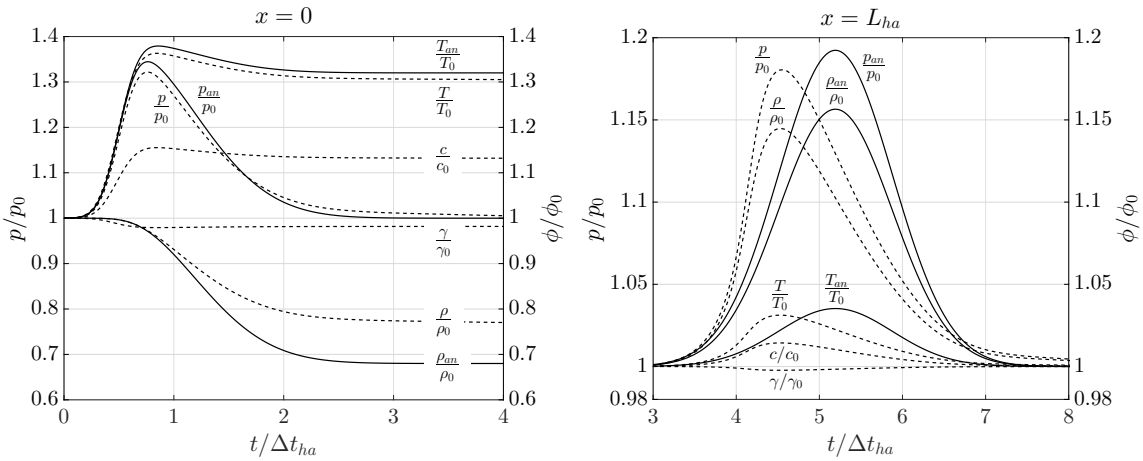

Figure 3.20. Noncompact case, $He = 0.9487 > \sqrt{2}/7$. Flow field response to a heat source with Gaussian spatial and temporal distribution. Solid lines represent the analytical solution whereas dashed lines are the numerical solution. heat release parameters: $q_{ha} = 2.5 \cdot 10^{12}$ W/m^3, $L_{ha} = 400$ μm, $\Delta t_{ha} = 0.25$ μs.

acoustic wave equation. For instance, the extreme rates of heat release induce weak shocks in the pressure pulses. Away from the heat release zone, as shown in Figs. 3.18 (R) and 3.20 (R), the numerical solution shows that the pressure pulse undergoes a wave steepening process. This is a well known nonlinear acoustic phenomenon caused by the local increase in the speed of sound [83]. Over the distance, this effect compounds until the pressure pulse evolves into a weak shock. The numerical solutions for both heat release profiles also show that the pressure pulse slowly decays over the distance. This is due to both physical (viscous losses) and numerical loss mechanisms that are absent in the analytical model.

3.7 Application to a Real Combustor: CVRC

The methodology developed in this paper can be applied to a flow field prediction of a real combustor to assess the degree to which a combustion process tends to constant pressure or constant volume combustion. Furthermore, the application to a real case allows to test the analytical model assumptions, and hence, the applicability of models based on the acoustic wave equation in LRE. The CVRC [78] is selected as example of the real combustor. The numerical simulation of this combustor with detailed chemical kinetics has been previously reported by Sardeshmukh et al. [73] and others [30, 69, 70, 84]. He is computed for a typical instantaneous solution from this simulation and shown in Fig. 3.21. The CVRC is a single element combustor that experimentally demonstrated the dependence of the self-excited instabilities on the length of the oxidizer post. This combustor uses decomposed hydrogen peroxide as oxidizer and gaseous methane injected at room temperature as the fuel. Further details are presented in the prior work reported by Yu [78].

The main feature of the numerical He_{num} calculation is the isolation of the flames and corresponding length scales. This is accomplished by first defining a threshold for the heat release as 50% of the maximum heat release in the domain. The heat release scale is typically exponential and hence the threshold defined herein repre-

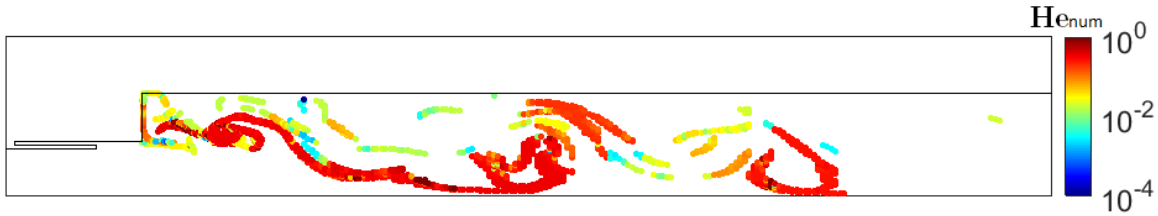

Low part of the cycle

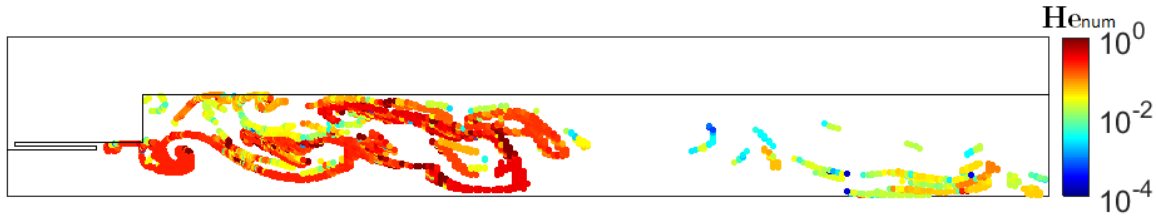

High part of the cycle

Figure 3.21. Contour plot of the numerically computed He_{num} distribution for two time instances of a typical 1L mode acoustic cycle of the CVRC combustor. The nominal chamber pressure is 1.4 MPa [73].

sents the flame zones without pre-heat or post-flame zones. The cells isolated with this criterion are then segregated on the basis of their contiguity. As evident from Fig. 3.21, the length scales of the flame zones are smaller than their span in either $x-$ or $y-$coordinate directions. For the sake of simplicity and conservative approach, the flame length scale is defined as the minimum of the spans of the flame in the Cartesian coordinate directions. This assumption primarily affects the acoustic time scale and estimates this on the higher side. The calculated He_{num} is therefore expected to be greater than the exact value. The chemical time scale is approximated with a numerical derivative of the heat release, computed using a backward difference operator. The estimated numerical Helmholtz number, He_{num} is thus obtained as

$$He_{num} = \frac{\tau_{ac}}{\tau_{ch}} = \frac{L_f/c}{q/\dot{q}} \ , \tag{3.43}$$

where L_f is the length scale of the flame zone (flame thickness), c is the local speed of sound, τ_{ch} is the chemical time (heat release time scale), and $\dot{q}$ is the time rate of change of the volumetric heat release rate q.

The range of He_{num} shown in Fig. 3.21 varies from 10^{-4} to 1, with very few sporadic points overcoming the upper limit of 1. In this case, the reference He has been chosen based on He_{cr} of the Gaussian spatial and temporal distribution ($He_{cr} = \sqrt{2}/7$) as it represents a more realistic heat release profile for a combustion flame than the first profile. As the He_{num} of Eq. (3.43) has a factor of $7/\sqrt{2}$ with respect to the analytical He of Eq. (3.32)(i.e. $\tau_{ac} = (\sqrt{2}L_{ha})/(7c_0)$), the translation of the He_{cr} into the simulation scale results in $He_{cr,num} = 1$. The flame zones around the reacting shear layer feature He numbers close but below the numerical He_{cr} of 1, while other zones outside of this area clearly have compact values below 1. This difference may be attributed to the higher temperatures due to partially burned mixtures. The contrast between the near-critical values at the reacting shear layer with respect to the predominantly compact regions outside this zone, reveal the dominance of moderate He_{num} zones in CVRC. The combustion mostly occurs from compact to

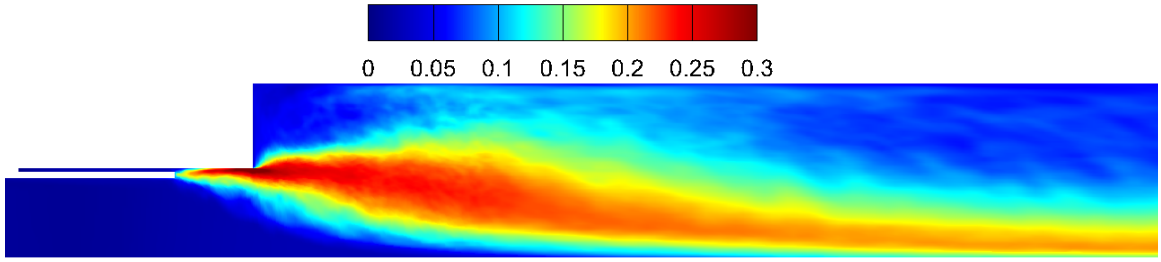

Figure 3.22. Contour plot of the numerically computed standard deviation of the speed of sounds over the local mean speed of sound ($\sigma_c(x)/c_0(x)$) of the CVRC combustor. The nominal chamber pressure is 1.4 MPa [73].

near-critical He_{num} regimes so that the temporal variations of heat release dominate the pressure response with minimal effects from the spatial distribution. The latter only start to appear for noncompact cases as demonstrated previously. The fact that the local He_{num} for the CVRC lies within a range from 0 to 1, reveals that its combustion process is an intermediate state between constant pressure and constant volume combustion. For a clear constant pressure combustion regime, He_{num} would have to be on the order of 0.01 or lower in all flame zones.

Fig. 3.22 shows the magnitude of the standard deviation of the local speed of sound with respect to the mean flow field. The shear layer, which is the primary combustion zone, features a speed of sound variation of the order of 20 to 30% of the local mean value. The shear layer will therefore be susceptible to significant errors in acoustic and Helmholtz solvers as the speed of sound variation is higher than the 5% threshold noted above.

3.8 Summary

Departing from the acoustic wave equation, an analytical model of the pressure response to an unsteady heat release source has been derived for an unconfined one-dimensional domain. A uniform and initially quiescent perfect gas with properties like that of the CO_2 gas is subjected to a heat release source with a Gaussian spatial distribution with either a step or a Gaussian temporal profile. The magnitude of the

heat sources is based on large eddy simulations of a rocket combustor using detailed kinetics. The analytical solutions contain important length and time scales that can be condensed into the Helmholtz number. This non-dimensional number is defined as the ratio between the characteristic acoustic time and the duration of the heat release pulse. For both heat source profiles, a critical Helmholtz number is identified as a threshold to distinguish between two regimes of pressure response. For compact cases, in the subcritical regime, the amplitude of the pressure response is determined by the duration of the heat release and it is independent of the length scale of heat source. Applied to a flame, this implies that the pressure fluctuation amplitude will only depend on the time rate of change of the heat release and not on the flame thickness. For noncompact cases, above the critical Helmholtz number, the amplitude of the pressure response is determined by both the length and time scales of the heat source.

Whereas in compact cases the amplitude of the generated pressure pulse remains constant over the distance, in noncompact cases the pressure pulse peaks at the center of the heat source, and then decays until converging to a constant far field pressure amplitude. As such, He represents an effective metric to determine to which extent the pressure response to an unsteady heat release event approaches to a constant pressure or a constant volume process. For $He \ll He_{cr}$, the pressure response tends to a constant pressure process, whereas for $He \gg He_{cr}$ the response tends to a constant volume process. The analytical model shows that the maximum amplitude of the pressure response to an unsteady heat release event is limited to the same constant volume limit regardless of the temporal profiles of the heat sources considered.

The comparison between the analytical and high-fidelity numerical solutions reveals that, within its range of application, the analytical model effectively captures the dynamics of the pressure response to an unsteady heat release event. The overshoots in the pressure amplitude, however, are observed to be common for both the heat sources. The density drop is shown to be overestimated in general and presence of unphysical values indicate the limitations of the analytical assumptions for

extremes rates of heat release. The maximum temperature error is shown to depend on He. In the heated zone, which determines the shape of the pressure pulse, the assumption of constant mean flow properties is the major cause of discrepancy between the analytical model and the numerical simulation. Away from the heated zone, the numerical solutions reveal the presence of important nonlinear effects that are not captured by methods based on the acoustic wave equation. Indeed, the addition of extreme rates of heat release induces weak shocks in the pressure pulses.

From an application point of view based on the magnitudes of heat release, gas turbines operate in an isentropic compression regime, liquid rocket engines experience weak shocks, and pressure-gain combustion devices feature strong shocks. For low and moderate heat release rates, characteristic of gas turbines, models based on the acoustic wave equation will show a good agreement in the prediction of the amplitude and shape of the pressure response of a fluid to unsteady heat release events. However, this type of methods such as 1D acoustic models, network models, or Helmholtz solvers, will overpredict the pressure response as the local speed of sound deviates more than 5% from the mean flow value. For high-pressure liquid rocket engines, these methods will accumulate significant errors, worsening with increasing operating pressure due to the extreme rates of heat release. In addition, such methods will fail to capture important nonlinear effects such as weak shocks, which are common in longitudinal acoustic modes of liquid rocket engine combustors [61]. Even though some acoustic solvers can incorporate a time-varying mean speed of sound, their inability to capture rapid increases in the local speed of sound due to unsteady combustion of pockets of propellants will remain a source of error.

4. FLOW RESPONSE TO A HEAT RELEASE PULSE IN 3D

This chapter extends the analysis of the fluid response to an unsteady heat release pulse in an unconfined three-dimensional domain. An analytical model based on the acoustic wave equation with spherical symmetry is derived to study the fluid response to two different heat source profiles, corresponding to a Gaussian spherical distribution and step temporal profile, and a Gaussian spherical and temporal profile. The analytical method developed for the one-dimensional cases from Chapter 3 is adapted to model three-dimensional cases with spherical symmetry. The use of a non-reacting fluid simplifies the derivation while maintaining the physical significance of the effects of unsteady heat release. By extending the analysis from one dimension to three dimensions, the model approaches to a more realistic scenario.

In the derivation of the analytical model, the Helmholtz number appears again as an important parameter that condenses the relevant length and time scales of the problem. The Helmholtz number represents the ratio of the acoustic time over the duration of the heat release pulse. The analytical solutions reveal the presence of two distinct regimes of the pressure response, acoustically compact and noncompact, separated by a critical Helmholtz number. In contrast with the one-dimensional case, which maintains a constant pressure amplitude over the distance, the pressure pulse in the spherical case continuously decays with the radial distance from the heat source.

The accuracy and limitations of the model are assessed by comparing the analytical solution to highly-resolved computational fluid dynamics simulations. For moderate values of heat release, the analytical solution is able to capture the dynamics of the fluid response. However, for large values of heat release rate the presence of nonlinear effects deviates the numerical solution from the analytical model.

4.1 Planar Symmetry vs Cylindrical and Spherical Symmetry

The analytical solutions derived in Section 3 correspond to the response of an uniform quiescent fluid to an unsteady heat release pulse in an unconfined domain with one-dimensional planar symmetry. The choice of one-dimensional planar symmetry simplifies the analysis and integration of the analytical solutions, while maintaining the physical significance of the effects of unsteady heat release events in a fluid.

In their study of the ignition process of a gaseous reacting mixture subject to an energy source for different regimes, Vázquez-Espí and Liñán [39] modeled the problem by means of the conservation equations of mass, momentum and energy expressed in terms of a parameter j that defines the level of symmetry, as shown below

$$\frac{\partial \rho}{\partial t} = -\frac{1}{r^j}\frac{\partial}{\partial r}\left(r^j \rho u\right) \tag{4.1}$$

$$\frac{Du}{Dt} = -\frac{1}{\rho}\frac{\partial p}{\partial r} \tag{4.2}$$

$$\rho T \frac{Ds}{Dt} = q \tag{4.3}$$

where r is the radius and the substantial derivative is given by $\frac{D}{Dt} = \frac{\partial}{\partial t} + u\frac{\partial}{\partial r}$. In this case, the energy equation presented in [39] has been substituted for the entropy equation Eq. (4.3) in order to be consistent with the derivation presented in Section 2.2. The parameter j determines the type of symmetry of the flow field as follows:

$$\begin{cases} j = 0 \rightarrow \text{for planar symmetry} \\ j = 1 \rightarrow \text{for cylindrical symmetry} \\ j = 2 \rightarrow \text{for spherical symmetry} \end{cases}$$

Analogously, the acoustic wave equation with uniform mean flow properties and unsteady heat source Eq. (2.32) can also be expressed in terms of the flow field symmetry parameter j as

$$\frac{1}{c_0^2}\frac{\partial^2 p_1}{\partial t^2} - \frac{1}{r^j}\frac{\partial}{\partial r}\left(r^j \frac{\partial p_1}{\partial r}\right) = \frac{\gamma - 1}{c_0^2}\frac{\partial q_1}{\partial t} \tag{4.4}$$

Cohen [38] and Zajac [37] also used the parameter j to specify the type of symmetry for similar problems, although their models were derived from different forms of the conservation equations with respect to Eqs. (4.1-4.3). Both studies analyzed numerically the ignition process of a reacting mixture of hydrogen-oxygen for different types of symmetry. The results from Cohen [38] and Zajac [37] showed that, in the kernel (zone of application of the heat release source), the pressure response to an unsteady heat release event follows the same trends for planar, cylindrical and spherical symmetry cases. However, as shown in Fig. 4.1 the amplitude of the fluctuations is highest for the planar symmetry case, followed in decreasing order by cylindrical symmetry and spherical symmetry, respectively. It should be noted that this behavior occurs at the center location, which is the center of symmetry. Away from the center, as the generated pressure pulse travels outwards, the trends for the cylindrical and spherical cases start to differ from the planar symmetry as the amplitude of the pressure wave decreases with the distance. Therefore, in the vicinity of the center location, the trends obtained from the planar analytical solutions derived in this paper would also occur for cylindrical and spherical cases but featuring lower pressure amplitudes.

The solutions based on the acoustic wave equation will exhibit different trends of pressure decay over the distance based on the type of symmetry as follows

$$\begin{cases} \text{Planar symmetry} \rightarrow \text{Pressure amplitude does not decay} \\ \text{Cylindrical symmetry} \rightarrow \text{Pressure amplitude decays with } \sqrt{r} \\ \text{Spherical symmetry} \rightarrow \text{Pressure amplitude decays with } r \end{cases}$$

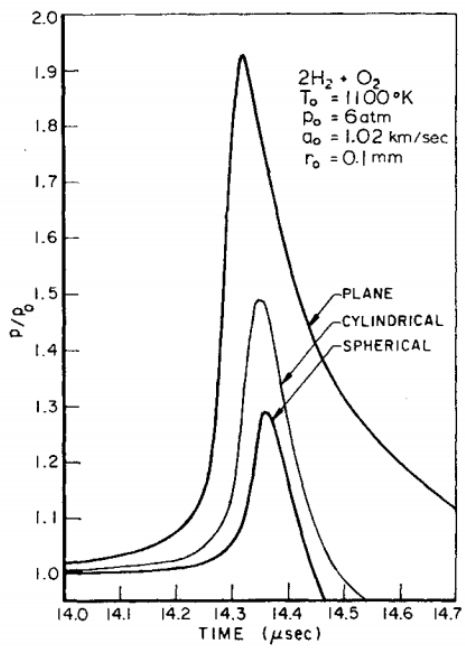

Fig. 5 Time profiles of the pressure in the kernel.

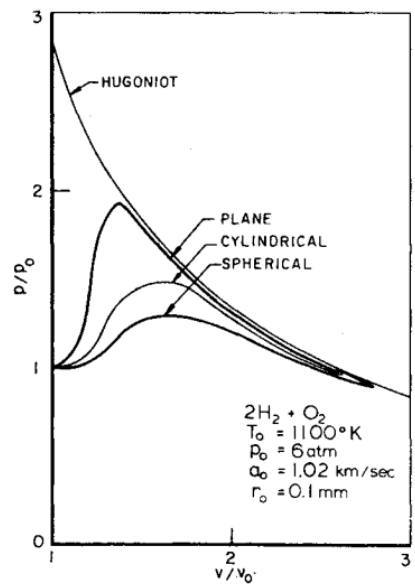

Fig. 7 The pressure-specific volume diagram of the process in the kernel.

Figure 4.1. Comparison of planar vs cylindrical vs spherical symmetry (Source [79]).

4.2 Acoustic Wave Equation with Cylindrical Symmetry

Recalling the three-dimensional acoustic wave equation with an unsteady heat source, Eq. (2.32) reads as

$$\frac{1}{c_0^2}\frac{\partial^2 p_1}{\partial t^2} - \nabla^2 p_1 = \frac{\gamma - 1}{c_0^2}\frac{\partial q_1}{\partial t} \tag{4.5}$$

In cylindrical coordinates, the Laplacian $\nabla^2 p_1$ is given by

$$\nabla^2 p_1 = \frac{1}{r}\frac{\partial}{\partial r}\left(r\frac{\partial p_1}{\partial r}\right) + \frac{1}{r^2}\frac{\partial^2 p_1}{\partial \varphi^2} + \frac{\partial^2 p_1}{\partial z^2} \tag{4.6}$$

Applying z-invariant circular symmetry, the pressure response is only function of the radial distance and time, i.e. $p_1 = f(r, \varphi, z, t) = f(r, t)$. Then, Eq. (4.6) can be simplified as

$$\nabla^2 p_1 = \frac{1}{r}\frac{\partial}{\partial r}\left(r\frac{\partial p_1}{\partial r}\right) \tag{4.7}$$

The substitution of Eq. (4.7) into Eq. (4.5) leads to

$$\frac{1}{c_0^2}\frac{\partial^2 p_1}{\partial t^2} - \frac{1}{r}\frac{\partial}{\partial r}\left(r\frac{\partial p_1}{\partial r}\right) = \frac{\gamma - 1}{c_0^2}\frac{\partial q_1}{\partial t} \tag{4.8}$$

It should be noted that Bessel functions can be used to derive exact solutions to the wave equation with cylindrical symmetry given by of Eq. (4.8) [85]. The use of Bessel functions to develop analytical solutions for pressure, velocity, density, and temperature fields is out of scope of this work due to the difficulty associated with integrating and deriving those exact solutions. However, to understand what happens at large distances from the source (i.e. $r \to \infty$), an approximate solution of Eq. (4.8) can be derived as follows [85]

$$\nabla^2 p_1 = \frac{1}{r}\frac{\partial}{\partial r}\left(r\frac{\partial p_1}{\partial r}\right) = \frac{1}{\sqrt{r}}\frac{\partial^2 (p_1\sqrt{r})}{\partial r^2} + \frac{1}{4r^2}p_1 \tag{4.9}$$

To proof the result of Eq. (4.9), it is noted that the first derivative of $p_1\sqrt{r}$ is given as

$$\frac{\partial(p_1\sqrt{r})}{\partial r} = \frac{\partial p_1}{\partial r}r^{1/2} + \frac{1}{2}p_1 r^{-1/2} \tag{4.10}$$

The second derivative is computed from the differentiation of Eq. (4.10) as

$$\frac{\partial^2(p_1\sqrt{r})}{\partial r^2} = r^{1/2}\left(\frac{\partial^2 p_1}{\partial r^2} + \frac{\partial p_1}{\partial r}r^{-1} - \frac{1}{4}p_1 r^{-2}\right) \tag{4.11}$$

Dividing Eq.(4.11) by $r^{1/2} = \sqrt{r}$ leads to

$$\frac{1}{\sqrt{r}}\frac{\partial^2(p_1\sqrt{r})}{\partial r^2} = \frac{\partial^2 p_1}{\partial r^2} + \frac{\partial p_1}{\partial r}r^{-1} - \frac{1}{4}p_1 r^{-2} = \nabla^2 p_1 - \frac{1}{4}p_1 r^{-2} \tag{4.12}$$

where Eq. (4.9) is computed from the rearrangement of the terms of Eq. (4.12). For values of r far away from the heat source, the term $\frac{1}{4}p_1 r^{-2}$ of Eq. (4.12) becomes negligible and thus, $\nabla^2 p_1\big|_{r\to\infty}$ is given by

$$\nabla^2 p_1\big|_{r\to\infty} \approx \frac{1}{\sqrt{r}}\frac{\partial^2\left(p_1\sqrt{r}\right)}{\partial r^2} \qquad \text{For} \quad r\to\infty \tag{4.13}$$

The substitution of Eq. (4.13) into Eq. (4.5) yields to an approximate solution for the acoustic wave equation in cylindrical coordinates and far away from the heat source as

$$\frac{1}{c_0^2}\frac{\partial^2(p_1\sqrt{r})}{\partial t^2} - \frac{\partial^2\left(p_1\sqrt{r}\right)}{\partial r^2} \approx \frac{\gamma-1}{c_0^2}\frac{\partial\left(q_1\sqrt{r}\right)}{\partial t} \tag{4.14}$$

As the main focus of this work is the analysis of local effects on the flow field, not only far away from the heat source but specifically near it, the use of Eq. (4.14) to develop pressure, velocity, density, and temperature fields has been disregarded.

4.3 Pressure Response to a Heat Release Pulse with Spherical Symmetry

In spherical coordinates, the Laplacian $\nabla^2 p_1$ is given by

$$\nabla^2 p_1 = \frac{1}{r^2}\frac{\partial}{\partial r}\left(r^2\frac{\partial p_1}{\partial r}\right) + \frac{1}{r^2\sin\theta}\frac{\partial}{\partial\theta}\left(\sin\theta\frac{\partial p_1}{\partial\theta}\right) + \frac{1}{r^2\sin^2\theta}\frac{\partial^2 p_1}{\partial\varphi^2} \tag{4.15}$$

where r, θ and φ, are the radial distance, polar angle and azimutal angle, respectively. Considering spherical symmetry, the pressure response is only a function of the radial distance and time, i.e. $p_1 = f(r,\theta,\varphi,t) = f(r,t)$, so that the Laplacian $\nabla^2 p_1$ reads as

$$\nabla^2 p_1 = \frac{1}{r^2}\frac{\partial}{\partial r}\left(r^2\frac{\partial p_1}{\partial r}\right) = \frac{\partial^2 p_1}{\partial r^2} + \frac{2}{r}\frac{\partial p_1}{\partial r} \tag{4.16}$$

Hence, applying spherical symmetry, the acoustic wave equation Eq. (4.5) results in

$$\frac{1}{c_0^2}\frac{\partial^2 p_1}{\partial t^2} - \frac{1}{r^2}\frac{\partial}{\partial r}\left(r^2\frac{\partial p_1}{\partial r}\right) = \frac{\gamma-1}{c_0^2}\frac{\partial q_1}{\partial t} \tag{4.17}$$

The Laplacian from Eq. (4.16) can also be expressed in terms of rp_1 as follows

$$\begin{aligned}\nabla^2 p_1 = \frac{1}{r}\frac{\partial^2}{\partial r^2}(rp_1) = \frac{1}{r}\frac{\partial}{\partial r}\left(\frac{\partial}{\partial r}(rp_1)\right) = \frac{1}{r}\frac{\partial}{\partial r}\left(p_1 + r\frac{\partial p_1}{\partial r}\right)\\ = \frac{1}{r}\left(\frac{\partial p_1}{\partial r} + \frac{\partial p_1}{\partial r} + r\frac{\partial^2 p_1}{\partial r^2}\right) = \frac{\partial^2 p_1}{\partial r^2} + \frac{2}{r}\frac{\partial p_1}{\partial r}\end{aligned} \tag{4.18}$$

Using this expression, Eq. (4.17) can be written as

$$\frac{1}{c_0^2}\frac{\partial^2 p_1}{\partial t^2} - \frac{1}{r}\frac{\partial^2}{\partial r^2}(rp_1) = \frac{\gamma-1}{c_0^2}\frac{\partial q_1}{\partial t} \tag{4.19}$$

Multiplying both sides by r, the acoustic wave equation with an unsteady heat source with spherical symmetry yields to

$$\frac{1}{c_0^2}\frac{\partial^2}{\partial t^2}(rp_1) - \frac{\partial^2}{\partial r^2}(rp_1) = \frac{\gamma-1}{c_0^2}\frac{\partial}{\partial t}(rq_1) \tag{4.20}$$

Eq. (4.20) shares the same form as the one-dimensional acoustic wave equation after replacing p_1 with rp_1, and q_1 with rq_1, respectively. The pressure response to heat release can then be calculated using a modified version of Eq. (2.35), which accounts for the change in variables of p_1 and q_1, to rp_1 and rq_1, respectively. The source team $f(r,t)$ is given by

$$f(r,t) = (\gamma - 1)\frac{\partial}{\partial t}(rq_1) \tag{4.21}$$

The integral of the pressure response then reads as

$$p_1(r,t) = \frac{1}{2c_0 r}\int_0^t \int_{r-c_0(t-s)}^{r+c_0(t-s)} f(z,s)\, dzds \tag{4.22}$$

Applying the heat source results in the final expression to be integrated

$$p_1(r,t) = \frac{\gamma - 1}{2c_0 r}\int_0^t \int_{r-c_0(t-s)}^{r+c_0(t-s)} \frac{\partial}{\partial t}(zq_1)\, dzds \tag{4.23}$$

4.4 Derivation of Velocity, Density, and Temperature Expressions with Spherical Symmetry

The linearized momentum equation (see Eq. (2.19)) allows the derivation of the velocity field from the pressure solution. Eq. (2.19) is recalled here reading as

$$\rho_0 \frac{\partial \vec{u}_1}{\partial t} = -\nabla p_1 \tag{4.24}$$

For spherical coordinates (r, θ, φ), the gradient of p_1 is computed as

$$\nabla p_1 = \frac{\partial p_1}{\partial r}\hat{u}_r + \frac{1}{r}\frac{\partial p_1}{\partial \theta}\hat{u}_\theta + \frac{1}{r\sin\theta}\frac{\partial p_1}{\partial \varphi}\hat{u}_\varphi \tag{4.25}$$

where $\hat{u}_r$, $\hat{u}_\theta$, and $\hat{u}_\varphi$ are the radial, polar, and azimutal direction unit vectors, respectively. Assuming spherical symmetry, the pressure is only a function of the radial distance and time as $p_1(r,\theta,\varphi,t) = p_1(r,t)$, and hence, Eq. (4.25) simplifies to

$$\nabla p_1 = \frac{\partial p_1}{\partial r}\hat{u}_r \tag{4.26}$$

Substituting Eq.(4.26) into Eq. (4.24), the velocity field in spherical coordinates can be calculated from the pressure solution as

$$\frac{\partial u_1}{\partial t} = -\frac{1}{\rho_0}\frac{\partial p_1}{\partial r} \tag{4.27}$$

where u_1 is the velocity field in the radial direction as $\vec{u}_1 = u_1\hat{u}_r$.

In turn, the density field can be obtained from the velocity field using the linearized mass conservation equation given by Eq. (2.18) with the assumption that $\nabla\rho_0 = 0$, reading as

$$\frac{\partial \rho_1}{\partial t} + \rho_0 \nabla \cdot \vec{u}_1 = 0 \tag{4.28}$$

The condition that $\nabla\rho_0 = 0$ comes from the assumption that the mean flow gas mixture has spatially uniform conditions, i.e. $\rho_0(x,y,z) = \rho_0$, $\forall x,\ y,\ z$. The divergence of the velocity field in spherical coordinates is given by

$$\nabla \cdot \vec{u}_1 = \frac{1}{r^2}\frac{\partial}{\partial r}\left(r^2 u_1\right) + \frac{1}{r\sin\theta}\frac{\partial}{\partial\theta}\left(u_1 \sin\theta\right) + \frac{1}{r\sin\theta}\frac{\partial u_1}{\partial\varphi} \tag{4.29}$$

Imposing again the spherical symmetry condition, $\vec{u_1}$ does not dependent on θ and φ and thus, Eq. (4.29) simplifies to

$$\nabla \cdot \vec{u}_1 = \frac{1}{r^2}\frac{\partial}{\partial r}\left(r^2 u_1\right) \tag{4.30}$$

Then, substituting Eq. (4.30) into Eq. (4.28), the density field can be obtained using the velocity field solution as

$$\frac{\partial \rho_1}{\partial t} = -\frac{\rho_0}{r^2}\frac{\partial}{\partial r}\left(r^2 u_1\right) \tag{4.31}$$

Finally, the temperature field can be computed from the results of the pressure and density solutions using the linearized equation of state (Eq. 3.19), which reads as

$$T_1 = T_0\left(\frac{p_1}{p_0} - \frac{\rho_1}{\rho_0}\right) \tag{4.32}$$

4.5 Heat Source with Gaussian Spherical Distribution and Step Temporal Profile

The present case consists of a heat source per unit volume $q_1(x, y, z, t) = q_1(r, t)$ with a Gaussian spherical distribution and step temporal profile defined as

$$q_1(r,t) = K_{ha_3}\ exp\left[-\frac{1}{2}\left(\frac{r}{\sigma_r}\right)^2\right]\left(H(t-t_{hab}) - H(t-t_{hae})\right) \tag{4.33}$$

Fig. 4.7 depicts a schematic of the three-dimensional spherical domain with the heat source at centered at the origin. In Eq. (4.33), $H(t-\tau)$ is the unit Heaviside function, t_{hab} is the time in which heat pulse begins, t_{hae} is the time in which the heat pulse ends, and K_{ha_3} is the heat source magnitude parameter defined as

$$K_{ha_3} = \frac{E_{ha}}{(2\pi)^{3/2}\,\sigma_r^3 \Delta t_{ha}} = \sqrt{\frac{2}{\pi}}\frac{q_{ha,sph}R_{ha}^3}{3\sigma_r^3} \tag{4.34}$$

where σ_r is the standard deviation of the Gaussian spherical profile, and $\Delta t_{ha} = t_{hae} - t_{hab}$. The standard deviation of the Gaussian spherical profile has been set to $\sigma_r = R_{ha}/3.5$ for all the cases in this study, where R_{ha} is the radius of the sphere in

which the heat source is applied. In this case, the flat profile heat release value $q_{ha,sph}$ is given by

$$q_{ha,sph} = \frac{E_{ha}}{V_{ha}\Delta t_{ha}} = \frac{E_{ha}}{\frac{4}{3}\pi R_{ha}^3 \Delta t_{ha}} \tag{4.35}$$

Applying the temporal derivative of the heat source of Eq. (4.33) as stated in Eq. (4.20) yields to

$$\begin{aligned} f(r,t) &= (\gamma-1)\frac{\partial}{\partial t}(rq_1) \\ &= (\gamma-1)K_{ha_3} r\ exp\left[-\frac{1}{2}\left(\frac{r}{\sigma_r}\right)^2\right](\delta(t-t_{hab})-\delta(t-t_{hae})) \end{aligned} \tag{4.36}$$

The substitution of Eq. (4.36) into Eq. (4.22) provides the expression to be integrated to solve the pressure response

$$p_1(r,t) = \frac{1}{2c_0 r}\int_0^t \int_{r-c_0(t-s)}^{r+c_0(t-s)} (\gamma-1)K_{ha_3} z e^{-\frac{1}{2}(\frac{z}{\sigma_r})^2}[\delta(s-t_{hab})-\delta(s-t_{hae})]dzds \tag{4.37}$$

Integrating Eq. (4.37) with respect to the spatial variable z yields to

$$p_1(r,t) = \frac{(1-\gamma)\,K_{ha_3}}{2c_0 r}\int_0^t \left[\sigma_r^2 e^{-\frac{1}{2}(\frac{z}{\sigma_r})^2}\left[\delta(s-t_{hab})-\delta(s-t_{hae})\right]\right]_{r-c_0(t-s)}^{r+c_0(t-s)} ds \tag{4.38}$$

Integrating Eq. (4.38) with respect to the temporal variable s leads to the solution of the pressure response to a heat source with Gaussian spherical distribution and step temporal profile

$$\begin{aligned} \text{For}\ \ r>0 \qquad p_1(r,t) = \frac{A_{p_3}}{r}\Bigg\{\Bigg[exp\left(-\left(\frac{r-c_0(t-t_{hab})}{\sqrt{2}\sigma_r}\right)^2\right) \\ -exp\left(-\left(\frac{r+c_0(t-t_{hab})}{\sqrt{2}\sigma_r}\right)^2\right)\Bigg]H(t-t_{hab}) - \Bigg[exp\left(-\left(\frac{r-c_0(t-t_{hae})}{\sqrt{2}\sigma_r}\right)^2\right) \\ -exp\left(-\left(\frac{r+c_0(t-t_{hae})}{\sqrt{2}\sigma_r}\right)^2\right)\Bigg]H(t-t_{hae})\Bigg\} \end{aligned} \tag{4.39}$$

where the constant multiplying the pressure expression A_{p_3} is given by

$$A_{p_3} = \frac{(\gamma - 1)\, K_{ha_3}\sigma_r^2}{2c_0} = \frac{(\gamma - 1)\, E_{ha}}{\sqrt{32\pi^3}c_0\sigma_r\Delta t_{ha}} \tag{4.40}$$

As it occurred in the one-dimensional cases of Chapter 3, the characteristic acoustic time τ_{ac} appears in the pressure response of Eq. (4.39) as

$$\tau_{ac} = \frac{\sqrt{2}\sigma_r}{c_0} \tag{4.41}$$

Rewriting Eq. (4.39) in terms of the characteristic time scale τ_{ac} yields to

$$\begin{aligned} \text{For} \quad r > 0 \qquad p_1(r,t) = \frac{A_{p_3}}{r}\Bigg\{\Bigg[exp\left(-\left(\frac{\frac{r}{c_0} - (t - t_{hab})}{\tau_{ac}}\right)^2\right) \\ -exp\left(-\left(\frac{\frac{r}{c_0} + (t - t_{hab})}{\tau_{ac}}\right)^2\right)\Bigg]H(t - t_{hab}) - \Bigg[exp\left(-\left(\frac{\frac{r}{c_0} - (t - t_{hae})}{\tau_{ac}}\right)^2\right) \\ -exp\left(-\left(\frac{\frac{r}{c_0} + (t - t_{hae})}{\tau_{ac}}\right)^2\right)\Bigg]H(t - t_{hae})\Bigg\} \end{aligned} \tag{4.42}$$

The Helmholtz number can be defined as the ratio of the characteristic acoustic time over the heat release duration as

$$He = \frac{\tau_{ac}}{\Delta t_{ha}} \tag{4.43}$$

The velocity field can be calculated in the same fashion as in the one-dimensional case by using the linearized momentum equation (Eq. (4.27)), which leads to

$$\text{For} \quad r > 0 \qquad u_1(r,t) = \frac{(\gamma-1)\,E_{ha}}{\sqrt{32\pi^3}\rho_0 c_0^2 \sigma_r \Delta t_{ha}} \cdot \frac{1}{r}$$
$$\left\{ \left[exp\left(-\left(\frac{\frac{r}{c_0} - (t - t_{hab})}{\tau_{ac}} \right)^2 \right) + exp\left(-\left(\frac{\frac{r}{c_0} + (t - t_{hab})}{\tau_{ac}} \right)^2 \right) \right.\right.$$
$$\left. -2exp\left(-\left(\frac{r}{c_0 \tau_{ac}} \right)^2 \right) \right] H(t - t_{hab}) - \left[exp\left(-\left(\frac{\frac{r}{c_0} - (t - t_{hae})}{\tau_{ac}} \right)^2 \right) \right.$$
$$\left.\left. +exp\left(-\left(\frac{\frac{r}{c_0} + (t - t_{hae})}{\tau_{ac}} \right)^2 \right) - 2exp\left(-\left(\frac{r}{c_0 \tau_{ac}} \right)^2 \right) \right] H(t - t_{hae}) \right\}$$
$$-\frac{(\gamma-1)\,E_{ha}}{8\pi\rho_0 c_0^2 \Delta t_{ha}} \cdot \frac{1}{r^2} \left\{ \left[erf\left(\frac{\frac{r}{c_0} - (t - t_{hab})}{\tau_{ac}} \right) \right.\right.$$
$$\left. +erf\left(\frac{\frac{r}{c_0} + (t - t_{hab})}{\tau_{ac}} \right) - 2erf\left(\frac{r}{c_0 \tau_{ac}} \right) \right] H(t - t_{hab})$$
$$\left. -\left[erf\left(\frac{\frac{r}{c_0} - (t - t_{hae})}{\tau_{ac}} \right) + erf\left(\frac{\frac{r}{c_0} + (t - t_{hae})}{\tau_{ac}} \right) - 2erf\left(\frac{r}{c_0 \tau_{ac}} \right) \right] H(t - t_{hae}) \right\} \tag{4.44}$$

The density field can be computed using the linearized mass conservation (Eq. (4.31)), reading as

$$\text{For} \quad r > 0 \qquad \rho_1(r,t) = \frac{(\gamma-1)\,E_{ha}}{\sqrt{32\pi^3} c_0^3 \sigma_r \Delta t_{ha}} \cdot \frac{1}{r}$$
$$\left\{ \left[exp\left(-\left(\frac{\frac{r}{c_0} - (t - t_{hab})}{\tau_{ac}} \right)^2 \right) - exp\left(-\left(\frac{\frac{r}{c_0} + (t - t_{hab})}{\tau_{ac}} \right)^2 \right) \right] H(t - t_{hab}) \right.$$
$$\left. -\left[exp\left(-\left(\frac{\frac{r}{c_0} - (t - t_{hae})}{\tau_{ac}} \right)^2 \right) - exp\left(-\left(\frac{\frac{r}{c_0} + (t - t_{hae})}{\tau_{ac}} \right)^2 \right) \right] H(t - t_{hae}) \right\}$$
$$-\frac{(\gamma-1)\,E_{ha}}{\sqrt{8\pi^3} c_0^2 \sigma_r^3 \Delta t_{ha}} exp\left(-\left(\frac{r}{c_0 \tau_{ac}} \right)^2 \right) \left[(t - t_{hab})\,H(t - t_{hab}) - (t - t_{hae})\,H(t - t_{hae}) \right] \tag{4.45}$$

In turn, the temperature field can be calculated from the results from Eqs. (4.42) and (4.45) using the linearized equation of state (Eq. (4.32)), yielding to

$$\text{For} \quad r > 0 \qquad T_1(r,t) = \frac{(\gamma-1)^2 E_{ha} T_0}{\sqrt{32\pi^3}\rho_0 c_0^3 \sigma_r \Delta t_{ha}} \cdot \frac{1}{r}$$
$$\left\{ \left[exp\left(-\left(\frac{\frac{r}{c_0} - (t - t_{hab})}{\tau_{ac}} \right)^2 \right) - exp\left(-\left(\frac{\frac{r}{c_0} + (t - t_{hab})}{\tau_{ac}} \right)^2 \right) \right] H(t - t_{hab}) \right.$$
$$\left. - \left[exp\left(-\left(\frac{\frac{r}{c_0} - (t - t_{hae})}{\tau_{ac}} \right)^2 \right) - exp\left(-\left(\frac{\frac{r}{c_0} + (t - t_{hae})}{\tau_{ac}} \right)^2 \right) \right] H(t - t_{hae}) \right\}$$
$$+ \frac{(\gamma-1) E_{ha} T_0}{\sqrt{8\pi^3}\rho_0 c_0^2 \sigma_r^3 \Delta t_{ha}} exp\left(-\left(\frac{r}{c_0 \tau_{ac}} \right)^2 \right) \left[(t - t_{hab}) H(t - t_{hab}) - (t - t_{hae}) H(t - t_{hae}) \right] \tag{4.46}$$

4.5.1 Acoustically compact and noncompact cases

The careful analysis of the solutions of pressure, density and temperature from Eqs. (4.42, 4.45, 4.46) allows the extraction of the limits for the main flow field variables as presented in Table 4.1. In the spherical case, the amplitude of the pressure fluctuation decays with r. Therefore, the far field values as described in Chapter 3 are not of interest, and hence the focus is put on the maximum values at the center of the heat source. The Helmholtz number He, which represents the ratio between the acoustic time and heat release duration, distinguishes between the compact and noncompact regimes of the pressure response to the heat release pulse. The maximum and minimum values of the state variables occur at the center of the heat source. Since the direct substitution of $r = 0$ in Eqs. (4.42, 4.45, 4.46) leads to a singularity, a Taylor series expansion around $r = 0$ has been used to find the expressions for p_{mas}, ρ_{min}, and T_{max}, as presented in Table 4.1.

The critical Helmholtz number He_{cr} can be derived from the maximum pressure expression from Table 4.1 for $He > \sqrt{2}$, $p_{max}\Big|_{He>\sqrt{2}}$. Following the same process as in Section 3.2, He is varied for a constant value of heat release $q_{ha,s}$, while maintaining also constant E_{ha}. This is equivalent to maintaining the product of $R_{ha}^3 \Delta t_{ha}$ equal to

Table 4.1. Limiting expressions for the flow field response to a heat source with Gaussian spherical distribution and step temporal profile.

Variable	Location	Formula
$p_{max}\Big\vert_{He\leq\sqrt{2}}$	$r=0$	$p_0+\frac{(\gamma-1)E_{ha}}{\sqrt{8\pi^3}c_0\sigma_r^2\Delta t_{ha}}e^{-\frac{1}{2}}$
$p_{max}\Big\vert_{He>\sqrt{2}}$	$r=0$	$p_0+\frac{(\gamma-1)E_{ha}}{2\sqrt{\pi^3}c_0\sigma_r^2\Delta t_{ha}He}e^{-\frac{1}{He^2}}$
$\rho_{min}\Big\vert_{He\leq\sqrt{2}}$	$r=0$	$\rho_0-\frac{(\gamma-1)E_{ha}}{\sqrt{8\pi}c_0^2\sigma_r^3}\left(1+\frac{He}{\sqrt{2}}e^{-\frac{1}{2}}\right)$
$\rho_{min}\Big\vert_{He\gg\sqrt{2}}$	$r=0$	$\rho_0-\frac{(\gamma-1)E_{ha}}{\sqrt{8\pi}c_0^2\sigma_r^3\Delta t_{ha}}\Bigg((t_m-t_{hab})e^{-\left(\frac{t_m-t_{hab}}{\tau_{ac}}\right)^2}$ $-(t_m-t_{hae})e^{-\left(\frac{t_m-t_{hae}}{\tau_{ac}}\right)^2}+\Delta t_{ha}\Bigg)$ where $t_m=\frac{\tau_{ac}}{He}\left(1+\sqrt{\frac{3He^2}{2}+1}\right)+t_{hab}$
$T_{max}\Big\vert_{He\leq\sqrt{2}}$	$r=0$	$T_0+\frac{(\gamma-1)E_{ha}T_0}{\sqrt{8\pi}c_0^2\sigma_r^3\rho_0}\left(1+\frac{He}{\sqrt{2}}e^{-\frac{1}{2}}\right)$
$T_{max}\Big\vert_{He\gg\sqrt{2}}$	$r=0$	$T_0+\frac{(\gamma-1)E_{ha}T_0}{\sqrt{8\pi}c_0^2\sigma_r^3\Delta t_{ha}\rho_0}\Bigg((t_m-t_{hab})e^{-\left(\frac{t_m-t_{hab}}{\tau_{ac}}\right)^2}$ $-(t_m-t_{hae})e^{-\left(\frac{t_m-t_{hae}}{\tau_{ac}}\right)^2}+\Delta t_{ha}\Bigg)$ where $t_m=\frac{\tau_{ac}}{He}\left(1+\sqrt{\frac{3He^2}{2}+1}\right)+t_{hab}$

a constant k_1. The Helmholtz number can then be written in terms of this constant k_1 as $He = \frac{\sqrt{2}\sigma_r}{c_0 \Delta t_{ha}} = \frac{2\sqrt{2}R_{ha}}{7c_0\Delta t_{ha}} = \frac{2\sqrt{2}R_{ha}^4}{7c_0 k_1}$. It should be noted that $\sigma_r = \frac{2R_{ha}}{7}$. Substituting $R_{ha} = \left(\frac{7c_0k_1}{2\sqrt{2}}\right)^{\frac{1}{4}} He^{\frac{1}{4}}$ and $q_{ha,s}$ into the $p_{max}\Big|_{He>\sqrt{2}}$ expression leads to

$$\begin{aligned} p_{max}\Big|_{He>\sqrt{2}} - p_0 &= \frac{(\gamma-1)E_{ha}}{2\sqrt{\pi^3}c_0\sigma_r^2\Delta t_{ha}He}e^{-\frac{1}{He^2}} \\ &= \frac{7^2\left(\gamma-1\right)q_{ha,s}}{6\sqrt{\pi}c_0}\frac{R_{ha}}{He}e^{-\frac{1}{He^2}} = k_2He^{-\frac{3}{4}}e^{-\frac{1}{He^2}} \end{aligned} \tag{4.47}$$

where k_2 is a constant that encompasses all the constant terms of Eq. (4.47). Differentiating Eq. (4.47) with respect to He, and equating it to 0 in order to find the maximum, the critical Helmholtz number for the heat source with Gaussian spherical distribution and step temporal profile results in

$$He_{cr} = \sqrt{\frac{8}{3}} = 1.633 \tag{4.48}$$

As shown in Fig. 4.2 (L), the He_{cr} separates the pressure response into two recognizable regimes, the compact and noncompact regime, respectively. Figs. 4.8-4.16 show more results of the flow field response for compact and noncompact regime with Gaussian spherical distribution and step temporal profile.

4.6 Heat Source with Gaussian Spherical Distribution and Gaussian Temporal Profile

The present case consists of a heat source per unit volume $q_1(x,y,z,t) = q_1(r,t)$ with a Gaussian spherical distribution and Gaussian temporal profile defined as

$$q_1(r,t) = K_{ha_4}\ exp\left[-\frac{1}{2}\left(\frac{r}{\sigma_r}\right)^2\right] exp\left[-\frac{1}{2}\left(\frac{t-t_c}{\sigma_t}\right)^2\right] \tag{4.49}$$

where σ_t and t_c are the standard deviation and the center time of the Gaussian temporal profile, respectively. The Gaussian spherical and temporal standard deviations

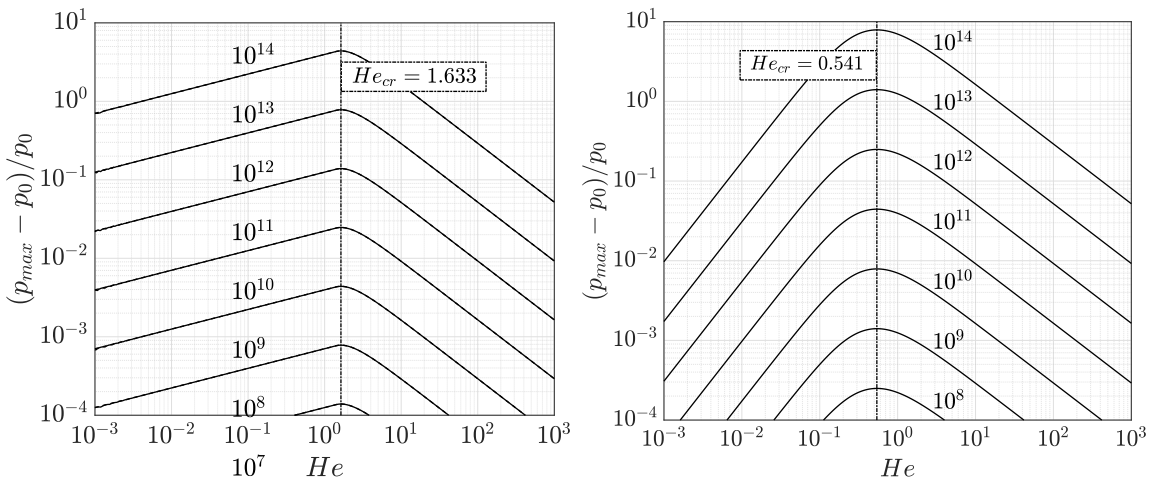

Figure 4.2. Evolution of the maximum amplitude with respect to the Helmholtz number for the response of a perfect gas with properties like that of CO_2 to a heat release source with Gaussian spherical distribution and step temporal profile (L), and Gaussian spherical distribution and temporal profile (R), respectively. $E_{ha} = \frac{4}{3}\pi 10^{-7}$ J.

are set to $\sigma_r = R_{ha}/3.5$ and $\sigma_t = \Delta t_{ha}/7$, respectively. The Gaussian temporal profile center time is $t_c = (t_{hab} + t_{hae})/2$, and it should be set to be $t_c \geq 3.5\sigma_t$ to ensure that the Gaussian temporal profile is not truncated to a fraction of the total energy input. K_{ha_4} is the heat source magnitude parameter defined as

$$K_{ha_4} = \frac{E_{ha}}{4\pi^2\sigma_r^3\sigma_t} = \frac{q_{ha,sph}R_{ha}^3\Delta t_{ha}}{3\pi\sigma_r^3\sigma_t} \tag{4.50}$$

where $q_{ha,sph}$ has the same value as in the previous heat source profile as defined in Eq. (4.35). Applying the temporal derivative of the heat source of Eq. (4.49) as stated in Eq. (4.20) yields to

$$\begin{aligned} f(r,t) &= (\gamma-1)\frac{\partial}{\partial t}(rq_1) \\ &= -\frac{(\gamma-1)K_{ha_4}}{\sigma_t^2} r\ exp\left[-\frac{1}{2}\left(\frac{r}{\sigma_r}\right)^2\right](t-t_c)\,exp\left[-\frac{1}{2}\left(\frac{t-t_c}{\sigma_t}\right)^2\right] \end{aligned} \tag{4.51}$$

The substitution of Eq. (4.51) into Eq. (4.22) provides the expression to be integrated to solve the pressure response

$$p_1(r,t) = -\frac{(\gamma-1)K_{ha_4}}{2c_0\sigma_t^2 r}\int_0^t\int_{r-c_0(t-s)}^{r+c_0(t-s)} ze^{-\frac{1}{2}\left(\frac{z}{\sigma_r}\right)^2}(s-t_c)\,e^{-\frac{1}{2}\left(\frac{s-t_c}{\sigma_t}\right)^2}dzds \tag{4.52}$$

Integrating Eq. (4.52) with respect to the spatial variable z yields to

$$p_1(r,t) = \frac{(\gamma-1)K_{ha_4}}{2c_0\sigma_t^2 r}\int_0^t\left[\sigma_r^2 e^{-\frac{1}{2}\left(\frac{z}{\sigma_r}\right)^2}(s-t_c)\,e^{-\frac{1}{2}\left(\frac{s-t_c}{\sigma_t}\right)^2}\right]_{r-c_0(t-s)}^{r+c_0(t-s)}ds \tag{4.53}$$

The pressure response $p_1(r,t)$ can be decomposed into inward travelling wave $p_1^-(r,t)$, following $r + c_0(t-s)$, and outward travelling wave $p_1^+(r,t)$, following $r - c_0(t-s)$, reading as

$$p_1(r,t) = p_1^-(r,t) + p_1^+(r,t) \tag{4.54}$$

where the inwards and outwards travelling waves are respectively

$$p_1^-(r,t) = \frac{(\gamma-1)K_{ha_4}\sigma_r^2}{2c_0\sigma_t^2 r}\int_0^t e^{-\frac{1}{2}\left(\frac{r+c_0(t-s)}{\sigma_r}\right)^2}(s-t_c)\,e^{-\frac{1}{2}\left(\frac{s-t_c}{\sigma_t}\right)^2}ds \tag{4.55}$$

$$p_1^+(r,t) = -\frac{(\gamma-1)K_{ha_4}\sigma_r^2}{2c_0\sigma_t^2 r}\int_0^t e^{-\frac{1}{2}\left(\frac{r-c_0(t-s)}{\sigma_r}\right)^2}(s-t_c)\,e^{-\frac{1}{2}\left(\frac{s-t_c}{\sigma_t}\right)^2}ds \tag{4.56}$$

The integral of Eq. (4.56) can be rewritten in terms of a new variable $\tau = s - t_c$ as

$$p_1^+(r,t) = -\frac{(\gamma-1)K_{ha_4}\sigma_r^2}{2c_0\sigma_t^2 r}\int_{-t_c}^{t-t_c} e^{-\frac{1}{2}\left(\frac{r-c_0(t-\tau-t_c)}{\sigma_r}\right)^2}\tau e^{-\frac{1}{2}\left(\frac{\tau}{\sigma_t}\right)^2}d\tau \tag{4.57}$$

We now focus on the integral term of Eq. (4.57)

$$I_1 = \int_{-t_c}^{t-t_c}\tau e^{-(a_1\tau+b_1)^2}e^{-a_2^2\tau^2}d\tau \tag{4.58}$$

where the constants are given by

$$\begin{cases} a_1 = \dfrac{c_0}{\sqrt{2}\sigma_r} \\ b_1 = \dfrac{r - c_0\,(t-t_c)}{\sqrt{2}\sigma_r} \\ a_2 = \dfrac{1}{\sqrt{2}\sigma_t} \end{cases} \tag{4.59}$$

Eq. (4.58) can be further developed into

$$I_1 = e^{-b_1^2}\int_{-t_c}^{t-t_c}\tau e^{-\left(a_1^2+a_2^2\right)\tau^2-2a_1b_1\tau}d\tau \tag{4.60}$$

This integral has a known solution that is developed in [86] and presented here

$$\int \tau e^{-a^2\tau^2+b\tau}d\tau = \frac{1}{2a^2}exp\left(\frac{b^2}{4a^2}\right)\left\{\frac{b\sqrt{\pi}}{2a}erf\left(a\tau-\frac{b}{2a}\right) - exp\left[-\left(a\tau-\frac{b}{2a}\right)^2\right]\right\} \tag{4.61}$$

where the constants are given by

$$a = \sqrt{a_1^2 + a_2^2} = \frac{c_0}{\sqrt{2}\sigma_r}\sqrt{1 + \frac{\sigma_r^2}{c_0^2\sigma_t^2}} = \frac{\zeta_{rt}}{\tau_{ac}} \tag{4.62}$$

$$b = -2a_1b_1 = -\frac{c_0^2}{\sigma_r^2}\left(\frac{r}{c_0} - (t - t_c)\right) = -2\left(\frac{\frac{r}{c_0} - (t - t_c)}{\tau_{ac}^2}\right) \tag{4.63}$$

The constants a and b contain relevant characteristic time scales such as the acoustic time, τ_{ac}, and the ratio of characteristic times, ζ_{rt}, respectively.

$$\tau_{ac} = \frac{\sqrt{2}\sigma_r}{c_0} \tag{4.64}$$

$$\zeta_{rt} = \sqrt{1 + \frac{\sigma_r^2}{c_0^2\sigma_t^2}} = \sqrt{1 + \frac{1}{2}\left(\frac{\tau_{ac}}{\sigma_t}\right)^2} \tag{4.65}$$

Integrating Eq. (4.60) with respect to the temporal variable τ using the results of Eqs. (4.61)-(4.63) yields to

$$\begin{aligned} I_1 = \frac{1}{2}\left(\frac{\tau_{ac}}{\zeta_{rt}}\right)^2 exp\left(-\left(\frac{\frac{r}{c_0} - (t - t_c)}{\sqrt{2}\sigma_t\zeta_{rt}}\right)^2\right) \cdot \\ \left[-\frac{\sqrt{\pi}\left(\frac{r}{c_0} - (t - t_c)\right)}{\tau_{ac}\zeta_{rt}} erf\left(\frac{\frac{r}{c_0} - (t - t_c) + \zeta_{rt}^2\tau}{\tau_{ac}\zeta_{rt}}\right)\right. \\ \left. -exp\left(-\left(\frac{\frac{r}{c_0} - (t - t_c) + \zeta_{rt}^2\tau}{\tau_{ac}\zeta_{rt}}\right)^2\right)\right]\Bigg|_{-t_c}^{t-t_c} \end{aligned} \tag{4.66}$$

Evaluating the integral limits of Eq. (4.66) results in

$$I_1 = \frac{1}{2}\left(\frac{\tau_{ac}}{\zeta_{rt}}\right)^2 exp\left(-\left(\frac{\frac{r}{c_0}-(t-t_c)}{\sqrt{2}\sigma_t\zeta_{rt}}\right)^2\right)\cdot$$
$$\left\{\frac{\sqrt{\pi}\left(\frac{r}{c_0}-(t-t_c)\right)}{\tau_{ac}\zeta_{rt}}\left[erf\left(\frac{\frac{r}{c_0}-t-(\zeta_{rt}^2-1)t_c}{\tau_{ac}\zeta_{rt}}\right)-erf\left(\frac{\frac{r}{c_0}+(\zeta_{rt}^2-1)(t-t_c)}{\tau_{ac}\zeta_{rt}}\right)\right]\right.$$
$$\left.+exp\left(-\left(\frac{\frac{r}{c_0}-t-(\zeta_{rt}^2-1)t_c}{\tau_{ac}\zeta_{rt}}\right)^2\right)-exp\left(-\left(\frac{\frac{r}{c_0}+(\zeta_{rt}^2-1)(t-t_c)}{\tau_{ac}\zeta_{rt}}\right)^2\right)\right\} \tag{4.67}$$

Combining the result of I_1 from Eq. (4.67) with Eq. (4.57) leads to the pressure response of the outwards travelling wave $p_1^+(r,t)$ as

$$\text{For} \quad r>0 \qquad p_1^+(r,t) = -\frac{A_{p4}}{r}exp\left(-\left(\frac{\frac{r}{c_0}-(t-t_c)}{\sqrt{2}\sigma_t\zeta_{rt}}\right)^2\right)\cdot$$
$$\left\{\frac{\sqrt{\pi}\left(\frac{r}{c_0}-(t-t_c)\right)}{\tau_{ac}\zeta_{rt}}\left[erf\left(\frac{\frac{r}{c_0}-t-(\zeta_{rt}^2-1)t_c}{\tau_{ac}\zeta_{rt}}\right)-erf\left(\frac{\frac{r}{c_0}+(\zeta_{rt}^2-1)(t-t_c)}{\tau_{ac}\zeta_{rt}}\right)\right]\right.$$
$$\left.+exp\left(-\left(\frac{\frac{r}{c_0}-t-(\zeta_{rt}^2-1)t_c}{\tau_{ac}\zeta_{rt}}\right)^2\right)-exp\left(-\left(\frac{\frac{r}{c_0}+(\zeta_{rt}^2-1)(t-t_c)}{\tau_{ac}\zeta_{rt}}\right)^2\right)\right\} \tag{4.68}$$

Following the same procedure for the inward travelling wave $p_1^-(r,t)$ defined by Eq. (4.55) results in

$$\text{For} \quad r>0 \qquad p_1^-(r,t) = -\frac{A_{p4}}{r}exp\left(-\left(\frac{\frac{r}{c_0}+(t-t_c)}{\sqrt{2}\sigma_t\zeta_{rt}}\right)^2\right)\cdot$$
$$\left\{\frac{\sqrt{\pi}\left(\frac{r}{c_0}+(t-t_c)\right)}{\tau_{ac}\zeta_{rt}}\left[erf\left(\frac{\frac{r}{c_0}-(\zeta_{rt}^2-1)(t-t_c)}{\tau_{ac}\zeta_{rt}}\right)-erf\left(\frac{\frac{r}{c_0}+t+(\zeta_{rt}^2-1)t_c}{\tau_{ac}\zeta_{rt}}\right)\right]\right.$$
$$\left.+exp\left(-\left(\frac{\frac{r}{c_0}-(\zeta_{rt}^2-1)(t-t_c)}{\tau_{ac}\zeta_{rt}}\right)^2\right)-exp\left(-\left(\frac{\frac{r}{c_0}+t+(\zeta_{rt}^2-1)t_c}{\tau_{ac}\zeta_{rt}}\right)^2\right)\right\} \tag{4.69}$$

Substituting the results from Eqs. (4.68)-(4.69) into Eq. (4.54), the pressure response to a heat source with Gaussian spherical distribution and Gaussian temporal profile reads as

$$\text{For} \quad r > 0 \qquad p_1(r,t) = -\frac{A_{p4}}{r}\Bigg[exp\left(-\left(\frac{\frac{r}{c_0}+(t-t_c)}{\sqrt{2}\sigma_t\zeta_{rt}}\right)^2\right)\cdot$$
$$\Bigg\{\frac{\sqrt{\pi}\left(\frac{r}{c_0}+(t-t_c)\right)}{\tau_{ac}\zeta_{rt}}\left[erf\left(\frac{\frac{r}{c_0}-(\zeta_{rt}^2-1)(t-t_c)}{\tau_{ac}\zeta_{rt}}\right)-erf\left(\frac{\frac{r}{c_0}+t+(\zeta_{rt}^2-1)t_c}{\tau_{ac}\zeta_{rt}}\right)\right]$$
$$+exp\left(-\left(\frac{\frac{r}{c_0}-(\zeta_{rt}^2-1)(t-t_c)}{\tau_{ac}\zeta_{rt}}\right)^2\right)-exp\left(-\left(\frac{\frac{r}{c_0}+t+(\zeta_{rt}^2-1)t_c}{\tau_{ac}\zeta_{rt}}\right)^2\right)\Bigg\}$$
$$+exp\left(-\left(\frac{\frac{r}{c_0}-(t-t_c)}{\sqrt{2}\sigma_t\zeta_{rt}}\right)^2\right)\cdot$$
$$\Bigg\{\frac{\sqrt{\pi}\left(\frac{r}{c_0}-(t-t_c)\right)}{\tau_{ac}\zeta_{rt}}\left[erf\left(\frac{\frac{r}{c_0}-t-(\zeta_{rt}^2-1)t_c}{\tau_{ac}\zeta_{rt}}\right)-erf\left(\frac{\frac{r}{c_0}+(\zeta_{rt}^2-1)(t-t_c)}{\tau_{ac}\zeta_{rt}}\right)\right]$$
$$+exp\left(-\left(\frac{\frac{r}{c_0}-t-(\zeta_{rt}^2-1)t_c}{\tau_{ac}\zeta_{rt}}\right)^2\right)-exp\left(-\left(\frac{\frac{r}{c_0}+(\zeta_{rt}^2-1)(t-t_c)}{\tau_{ac}\zeta_{rt}}\right)^2\right)\Bigg\}\Bigg] \tag{4.70}$$

where A_{p4} is defined as

$$A_{p4} = \frac{(\gamma-1)K_{ha_4}\sigma_r^2\tau_{ac}^2}{4c_0\sigma_t^2\zeta_{rt}^2} = \frac{(\gamma-1)E_{ha}(\zeta_{rt}^2-1)}{8\pi^2 c_0\sigma_r\sigma_t\zeta_{rt}^2} \tag{4.71}$$

In Eq. (4.70) two of the exponential terms cancel out mutually as their product is equivalent

$$
\begin{aligned}
exp\left(-\left(\frac{\frac{r}{c_0}+(t-t_c)}{\sqrt{2}\sigma_t\zeta_{rt}}\right)^2\right) exp\left(-\left(\frac{\frac{r}{c_0}-(\zeta_{rt}^2-1)\,(t-t_c)}{\tau_{ac}\zeta_{rt}}\right)^2\right) = \\
exp\left(-\left(\frac{\frac{r}{c_0}-(t-t_c)}{\sqrt{2}\sigma_t\zeta_{rt}}\right)^2\right) exp\left(-\left(\frac{\frac{r}{c_0}+(\zeta_{rt}^2-1)\,(t-t_c)}{\tau_{ac}\zeta_{rt}}\right)^2\right) = \\
exp\left(-\left(\frac{r}{c_0\tau_{ac}}\right)^2\right) exp\left(-\left(\frac{t-t_c}{\sqrt{2}\sigma_t}\right)^2\right)
\end{aligned}
\tag{4.72}
$$

The two other products of exponential terms yield to the following simpler expressions after decomposing and rearranging the terms

$$
\begin{aligned}
E_1 = exp\left(-\left(\frac{\frac{r}{c_0}+(t-t_c)}{\sqrt{2}\sigma_t\zeta_{rt}}\right)^2\right) exp\left(-\left(\frac{\frac{r}{c_0}+t+(\zeta_{rt}^2-1)t_c}{\tau_{ac}\zeta_{rt}}\right)^2\right) = \\
exp\left(-\left(\frac{\frac{r}{c_0}+t}{\tau_{ac}}\right)^2\right) exp\left(-\left(\frac{t_c}{\sqrt{2}\sigma_t}\right)^2\right)
\end{aligned}
\tag{4.73}
$$

$$
\begin{aligned}
E_2 = exp\left(-\left(\frac{\frac{r}{c_0}-(t-t_c)}{\sqrt{2}\sigma_t\zeta_{rt}}\right)^2\right) exp\left(-\left(\frac{\frac{r}{c_0}-t-(\zeta_{rt}^2-1)t_c}{\tau_{ac}\zeta_{rt}}\right)^2\right) = \\
exp\left(-\left(\frac{\frac{r}{c_0}-t}{\tau_{ac}}\right)^2\right) exp\left(-\left(\frac{t_c}{\sqrt{2}\sigma_t}\right)^2\right)
\end{aligned}
\tag{4.74}
$$

Combining both terms E_1 and E_2 and carrying the signs from Eq. (4.70) results in the grouping of the remaining products of exponential terms

$$
-E_1 + E_2 = exp\left(-\left(\frac{t_c}{\sqrt{2}\sigma_t}\right)^2\right)\left[exp\left(-\left(\frac{\frac{r}{c_0}-t}{\tau_{ac}}\right)^2\right) - exp\left(-\left(\frac{\frac{r}{c_0}+t}{\tau_{ac}}\right)^2\right)\right]
\tag{4.75}
$$

Although the exponential terms E_1 and E_2 do not cancel out, they are orders of magnitude smaller by a factor of $\sqrt{\pi}/(\tau_{ac}\zeta_{rt})$ with respect to the remaining terms

of Eq. (4.70), which are composed of the combined product of exponential, linear and error function terms. For all practical combustion engineering cases, with flame thicknesses on the order of $10^{-2}-10^{-5}$ m, and speeds of sound on the order of $10^{2}-10^{3}$ m/s, the factor $\sqrt{\pi}/(\tau_{ac}\zeta_{rt})$ is a large number (order 10^4 or larger). Therefore, the exponential product terms E_1 and E_2 are negligible in comparison with the rest of terms of Eq. (4.70), and hence, they can be dropped from said equation thereby simplifying the pressure response solution as follows

$$\text{For} \quad r > 0 \qquad p_1(r,t) = -\frac{A_{p4}}{r}\Bigg\{ exp\left(-\left(\frac{\frac{r}{c_0}+(t-t_c)}{\sqrt{2}\sigma_t\zeta_{rt}}\right)^2\right)\cdot \frac{\sqrt{\pi}\left(\frac{r}{c_0}+(t-t_c)\right)}{\tau_{ac}\zeta_{rt}}\left[erf\left(\frac{\frac{r}{c_0}-(\zeta_{rt}^2-1)(t-t_c)}{\tau_{ac}\zeta_{rt}}\right)-erf\left(\frac{\frac{r}{c_0}+t+(\zeta_{rt}^2-1)t_c}{\tau_{ac}\zeta_{rt}}\right)\right] + exp\left(-\left(\frac{\frac{r}{c_0}-(t-t_c)}{\sqrt{2}\sigma_t\zeta_{rt}}\right)^2\right)\cdot \frac{\sqrt{\pi}\left(\frac{r}{c_0}-(t-t_c)\right)}{\tau_{ac}\zeta_{rt}}\left[erf\left(\frac{\frac{r}{c_0}-t-(\zeta_{rt}^2-1)t_c}{\tau_{ac}\zeta_{rt}}\right)-erf\left(\frac{\frac{r}{c_0}+(\zeta_{rt}^2-1)(t-t_c)}{\tau_{ac}\zeta_{rt}}\right)\right]\Bigg\} \tag{4.76}$$

Eq. (4.76) is the final result of the pressure response to a heat source with Gaussian spherical distribution and Gaussian temporal profile. As in the previous case, the velocity field can be computed from the pressure solution using the linearized momentum conservation equation (Eq. (4.27)) as follows

$$\text{For} \quad r > 0 \qquad u_1(r,t) = \frac{A_{p4}}{\rho_0 c_0 r}\Bigg\{ exp\left(-\left(\frac{\frac{r}{c_0}+(t-t_c)}{\sqrt{2}\sigma_t\zeta_{rt}}\right)^2\right)\cdot$$

$$\frac{\sqrt{\pi}\left(\frac{r}{c_0}+(t-t_c)\right)}{\tau_{ac}\zeta_{rt}}\left[erf\left(\frac{\frac{r}{c_0}-(\zeta_{rt}^2-1)(t-t_c)}{\tau_{ac}\zeta_{rt}}\right)-erf\left(\frac{\frac{r}{c_0}+t+(\zeta_{rt}^2-1)t_c}{\tau_{ac}\zeta_{rt}}\right)\right]$$

$$-exp\left(-\left(\frac{\frac{r}{c_0}-(t-t_c)}{\sqrt{2}\sigma_t\zeta_{rt}}\right)^2\right)\cdot$$

$$\frac{\sqrt{\pi}\left(\frac{r}{c_0}-(t-t_c)\right)}{\tau_{ac}\zeta_{rt}}\left[erf\left(\frac{\frac{r}{c_0}-t-(\zeta_{rt}^2-1)t_c}{\tau_{ac}\zeta_{rt}}\right)-erf\left(\frac{\frac{r}{c_0}+(\zeta_{rt}^2-1)(t-t_c)}{\tau_{ac}\zeta_{rt}}\right)\right]$$

$$-\frac{2}{\zeta_{rt}^2-1}exp\left(-\left(\frac{r}{c_0\tau_{ac}}\right)^2\right)\left[exp\left(-\left(\frac{t-t_c}{\sqrt{2}\sigma_t}\right)^2\right)-exp\left(-\left(\frac{t_c}{\sqrt{2}\sigma_t}\right)^2\right)\right]\Bigg\}$$

$$+\frac{A_{p4}\sqrt{\pi}}{\rho_0 r^2}\cdot\frac{\sigma_t^2\zeta_{rt}}{\tau_{ac}}\Bigg\{ exp\left(-\left(\frac{\frac{r}{c_0}+(t-t_c)}{\sqrt{2}\sigma_t\zeta_{rt}}\right)^2\right)\cdot$$

$$\left[erf\left(\frac{\frac{r}{c_0}-(\zeta_{rt}^2-1)(t-t_c)}{\tau_{ac}\zeta_{rt}}\right)-erf\left(\frac{\frac{r}{c_0}+t+(\zeta_{rt}^2-1)t_c}{\tau_{ac}\zeta_{rt}}\right)\right]$$

$$-exp\left(-\left(\frac{\frac{r}{c_0}-(t-t_c)}{\sqrt{2}\sigma_t\zeta_{rt}}\right)^2\right)\cdot$$

$$\left[erf\left(\frac{\frac{r}{c_0}-t-(\zeta_{rt}^2-1)t_c}{\tau_{ac}\zeta_{rt}}\right)-erf\left(\frac{\frac{r}{c_0}+(\zeta_{rt}^2-1)(t-t_c)}{\tau_{ac}\zeta_{rt}}\right)\right]$$

$$+\frac{1}{\zeta_{rt}}exp\left(-\left(\frac{t_c}{\sqrt{2}\sigma_t}\right)^2\right)\cdot\left[erf\left(\frac{\frac{r}{c_0}+t}{\tau_{ac}}\right)+erf\left(\frac{\frac{r}{c_0}-t}{\tau_{ac}}\right)-2erf\left(\frac{r}{c_0\tau_{ac}}\right)\right]\Bigg\} \tag{4.77}$$

Similarly to the previous case, the density field can be computed using the linearized mass conservation equation (Eq. (4.31)), reading as

$$\text{For} \quad r > 0 \qquad \rho_1(r,t) = -\frac{A_{p4}}{c_0^2 r}\Bigg\{ exp\left(-\left(\frac{\frac{r}{c_0}+(t-t_c)}{\sqrt{2}\sigma_t\zeta_{rt}}\right)^2\right)\cdot$$
$$\frac{\sqrt{\pi}\left(\frac{r}{c_0}+(t-t_c)\right)}{\tau_{ac}\zeta_{rt}}\left[erf\left(\frac{\frac{r}{c_0}-(\zeta_{rt}^2-1)(t-t_c)}{\tau_{ac}\zeta_{rt}}\right)-erf\left(\frac{\frac{r}{c_0}+t+(\zeta_{rt}^2-1)t_c}{\tau_{ac}\zeta_{rt}}\right)\right]$$
$$+exp\left(-\left(\frac{\frac{r}{c_0}-(t-t_c)}{\sqrt{2}\sigma_t\zeta_{rt}}\right)^2\right)\cdot$$
$$\frac{\sqrt{\pi}\left(\frac{r}{c_0}-(t-t_c)\right)}{\tau_{ac}\zeta_{rt}}\left[erf\left(\frac{\frac{r}{c_0}-t-(\zeta_{rt}^2-1)t_c}{\tau_{ac}\zeta_{rt}}\right)-erf\left(\frac{\frac{r}{c_0}+(\zeta_{rt}^2-1)(t-t_c)}{\tau_{ac}\zeta_{rt}}\right)\right]\Bigg\}$$
$$-\frac{4\sqrt{\pi}A_{p4}\sigma_t\zeta_{rt}^2}{\sqrt{2}(\zeta_{rt}^2-1)c_0^3\tau_{ac}^2}exp\left(-\left(\frac{r}{c_0\tau_{ac}}\right)^2\right)\left[erf\left(\frac{t-t_c}{\sqrt{2}\sigma_t}\right)+erf\left(\frac{t_c}{\sqrt{2}\sigma_t}\right)\right.$$
$$\left.-\frac{\sqrt{2}}{\sqrt{\pi}\sigma_t\zeta_{rt}^2}exp\left(-\left(\frac{t_c}{\sqrt{2}\sigma_t}\right)^2\right)t\right] \tag{4.78}$$

The linear term in the density Eq. (4.78) is dropped because it is very small compared to the rest of the terms, and otherwise it would continue growing after the heat release source stops acting. This latter fact does not have a physical sense and hence, after dropping the linear term, the final density expression becomes

$$\text{For} \quad r > 0 \qquad \rho_1(r,t) = -\frac{A_{p4}}{c_0^2 r}\Bigg\{ exp\left(-\left(\frac{\frac{r}{c_0}+(t-t_c)}{\sqrt{2}\sigma_t\zeta_{rt}}\right)^2\right)\cdot$$
$$\frac{\sqrt{\pi}\left(\frac{r}{c_0}+(t-t_c)\right)}{\tau_{ac}\zeta_{rt}}\left[erf\left(\frac{\frac{r}{c_0}-(\zeta_{rt}^2-1)(t-t_c)}{\tau_{ac}\zeta_{rt}}\right)-erf\left(\frac{\frac{r}{c_0}+t+(\zeta_{rt}^2-1)t_c}{\tau_{ac}\zeta_{rt}}\right)\right]$$
$$+exp\left(-\left(\frac{\frac{r}{c_0}-(t-t_c)}{\sqrt{2}\sigma_t\zeta_{rt}}\right)^2\right)\cdot$$
$$\frac{\sqrt{\pi}\left(\frac{r}{c_0}-(t-t_c)\right)}{\tau_{ac}\zeta_{rt}}\left[erf\left(\frac{\frac{r}{c_0}-t-(\zeta_{rt}^2-1)t_c}{\tau_{ac}\zeta_{rt}}\right)-erf\left(\frac{\frac{r}{c_0}+(\zeta_{rt}^2-1)(t-t_c)}{\tau_{ac}\zeta_{rt}}\right)\right]\Bigg\}$$
$$-\frac{4\sqrt{\pi}A_{p4}\sigma_t\zeta_{rt}^2}{\sqrt{2}(\zeta_{rt}^2-1)c_0^3\tau_{ac}^2}exp\left(-\left(\frac{r}{c_0\tau_{ac}}\right)^2\right)\left[erf\left(\frac{t-t_c}{\sqrt{2}\sigma_t}\right)+erf\left(\frac{t_c}{\sqrt{2}\sigma_t}\right)\right] \tag{4.79}$$

Finally, the temperature field can be calculated from the solutions of the pressure Eq. (4.76) and density response Eq. (4.79) by using the linearized equation of state (Eq. (4.32)), resulting in

$$\text{For} \quad r > 0 \qquad T_1(r,t) = -\frac{(\gamma-1)T_0A_{p4}}{\rho_0 c_0^2 r}\Bigg\{ exp\left(-\left(\frac{\frac{r}{c_0}+(t-t_c)}{\sqrt{2}\sigma_t\zeta_{rt}}\right)^2\right)\cdot$$
$$\frac{\sqrt{\pi}\left(\frac{r}{c_0}+(t-t_c)\right)}{\tau_{ac}\zeta_{rt}}\left[erf\left(\frac{\frac{r}{c_0}-(\zeta_{rt}^2-1)(t-t_c)}{\tau_{ac}\zeta_{rt}}\right)-erf\left(\frac{\frac{r}{c_0}+t+(\zeta_{rt}^2-1)t_c}{\tau_{ac}\zeta_{rt}}\right)\right]$$
$$+exp\left(-\left(\frac{\frac{r}{c_0}-(t-t_c)}{\sqrt{2}\sigma_t\zeta_{rt}}\right)^2\right)\cdot$$
$$\frac{\sqrt{\pi}\left(\frac{r}{c_0}-(t-t_c)\right)}{\tau_{ac}\zeta_{rt}}\left[erf\left(\frac{\frac{r}{c_0}-t-(\zeta_{rt}^2-1)t_c}{\tau_{ac}\zeta_{rt}}\right)-erf\left(\frac{\frac{r}{c_0}+(\zeta_{rt}^2-1)(t-t_c)}{\tau_{ac}\zeta_{rt}}\right)\right]\Bigg\}$$
$$+\frac{4\sqrt{\pi}A_{p4}T_0\sigma_t\zeta_{rt}^2}{\sqrt{2}(\zeta_{rt}^2-1)\rho_0 c_0^3\tau_{ac}^2}exp\left(-\left(\frac{r}{c_0\tau_{ac}}\right)^2\right)\left[erf\left(\frac{t-t_c}{\sqrt{2}\sigma_t}\right)+erf\left(\frac{t_c}{\sqrt{2}\sigma_t}\right)\right] \tag{4.80}$$

For the Gaussian spherical distribution and temporal profile, there is again a critical Helmholtz number, He_{cr} that separates the pressure response into two recognizable regimes, the compact and noncompact regime, respectively as shown in Fig. 4.2 (R). Figs. 4.17-4.25 show more results of the flow field response for compact and noncompact regime with Gaussian spherical distribution and step temporal profile. For this particular case, the value of He_{cr} is numerically computed and is equal to $He_{cr} = 0.541$.

4.7 Parametric Study

The maximum pressure from Fig. 4.3 and Fig. 4.5 clearly distinguishes between the acoustically compact regime above the critical Helmholtz number diagonal, and the noncompact regime below He_{cre}. The noncompact regime resembles the trends shown in Chapter 3 for the one-dimensional cases. However, the compact regime is different with respect to the one-dimensional case in the fact that the maximum pressure continues to be a function of the heat release duration and the length scale of the heat source (R_{ha} in this case).

The $p\nu$ work efficiency, $\eta_{p\nu}$, is a metric of interest that represents the efficiency of converting heat release into acoustic pressure energy. The control volume is conveniently located away from the heat release center in order to capture the far field pressure response. In the spherical case, the $p\nu$ work efficiency reads as

$$\eta_{p\nu} = \frac{\int_0^T \oint_{\partial\Omega} p\left(\vec{u}\cdot\vec{n}\right) ds dt}{\int_0^T \int_\Omega q dV dt} = \frac{1}{E_{ha}} \int_0^T \int_0^{R_{cv}} (p_0 + p_1) u_1 4\pi r^2 dr dt \tag{4.81}$$

As shown in Fig. 4.3, the $p\nu$ work efficiency levels for the Gaussian spherical distribution and step temporal profile are much higher than in the one-dimensional case. This higher efficiency of the spherical case is due to the heat source is acting as a monopole of sound, which is the most efficient way of radiating sound. This effect also occurs for the Gaussian spherical distribution and temporal profile from

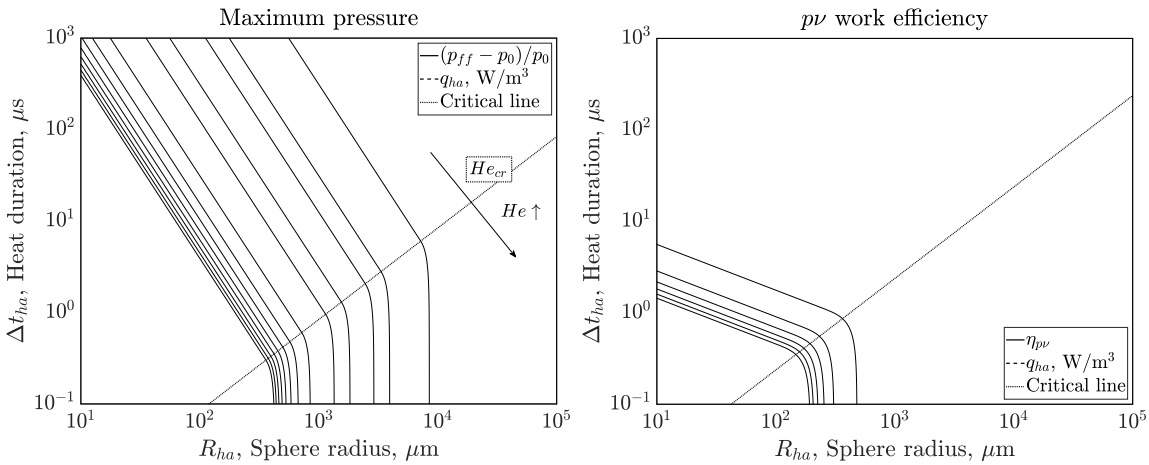

Figure 4.3. Map of the maximum pressure amplitude (L) and $p\nu$ work efficiency (R) of the response of a perfect gas with properties like that of CO_2 to a heat release source with Gaussian spherical distribution and step temporal profile.

and Fig. 4.5. For both heat source profiles, the $p\nu$ work efficiency plateaus for low heat release rates reaching a constant pressure limit efficiency. In turn, the minimum temperature and maximum temperature solutions follow the same trends featured in Chapter 3 for the one-dimensional cases.

Finally, it should be pointed out that for extreme rates of heat release, the analytical model starts to deviate from the numerical solution due to the presence of nonlinear effects and the deviation from the model assumptions, such as temperature dependence of the local speed of sound, using constant mean flow properties, and neglecting loss mechanisms such as viscosity and heat conduction. However, these deviations are not as evident as in the case of the one-dimensional case presented in Chapter 3 due to the predominant effect of the decay of pressure fluctuations over the radial distance.

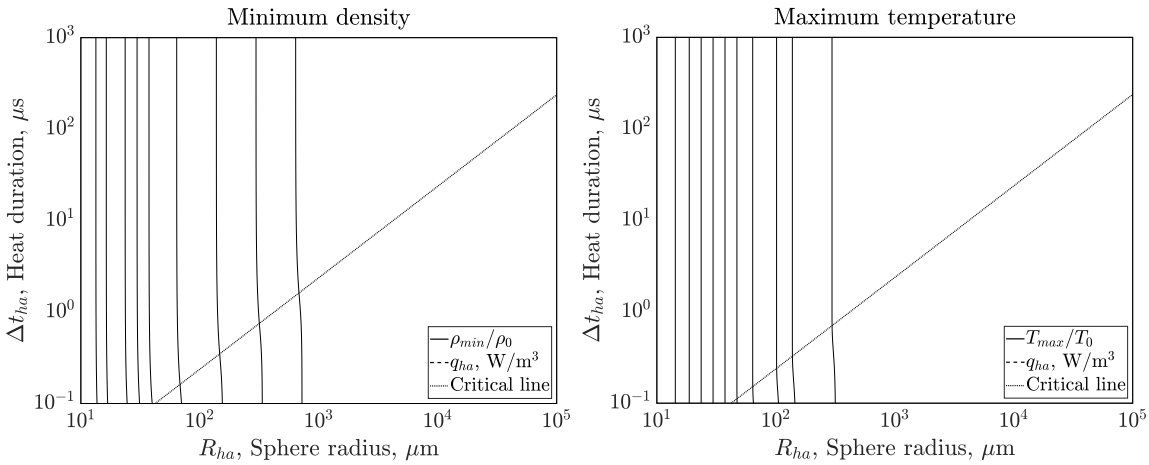

Figure 4.4. Map of the minimum density (L) and maximum temperature (R) of the response of a perfect gas with properties like that of CO_2 to a heat release source with Gaussian spherical distribution and step temporal profile.

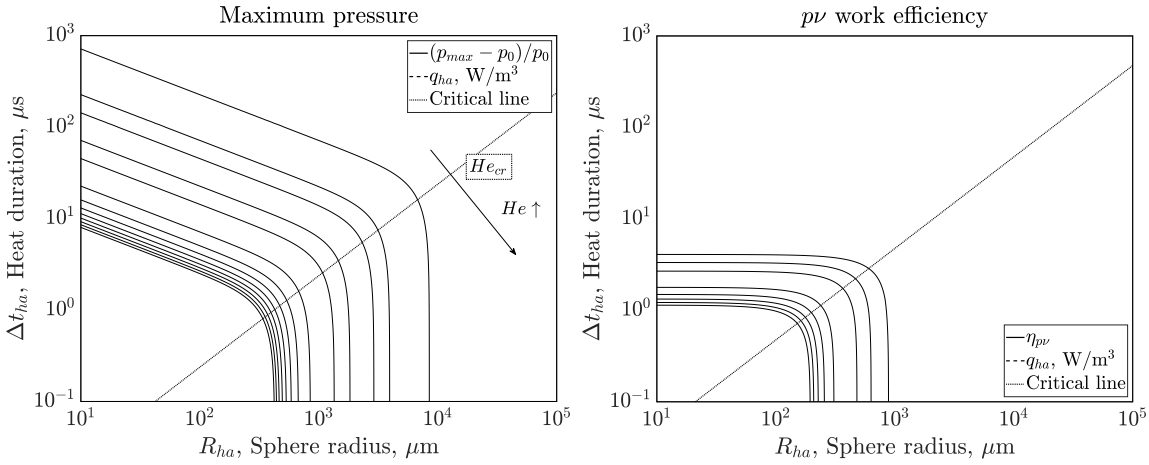

Figure 4.5. Map of the maximum pressure amplitude (L) and $p\nu$ work efficiency (R) of the response of a perfect gas with properties like that of CO_2 to a heat release source with Gaussian spherical distribution and temporal profile.

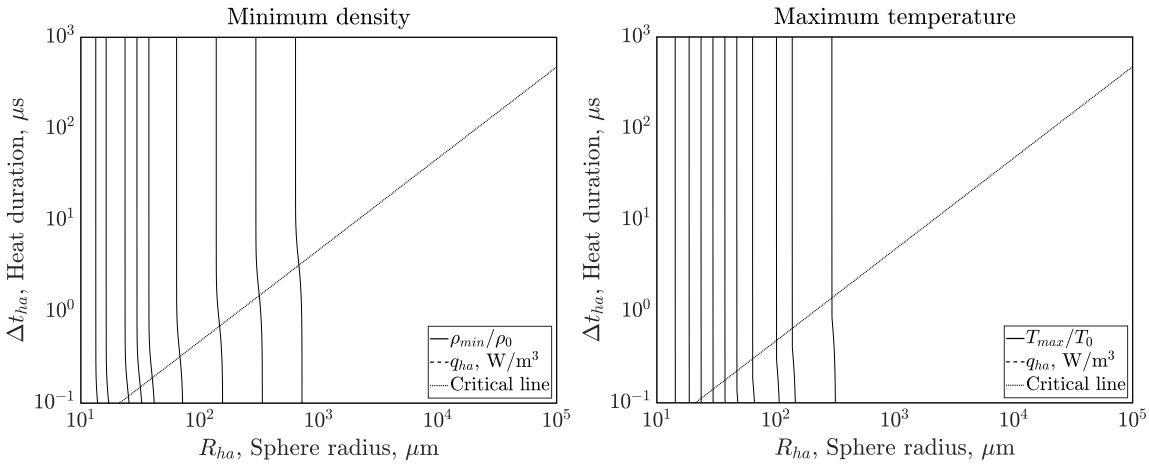

Figure 4.6. Map of the minimum density (L) and maximum temperature (R) of the response of a perfect gas with properties like that of CO_2 to a heat release source with Gaussian spherical distribution and temporal profile.

Table 4.2. Perfect gas mean flow properties like that of CO_2 used for all the analytical and numerical simulations of Chapter 4.

p_0 (MPa)	T_0 (K)	u_0 (m/s)	ρ_0 (kg/m^3)	c_0 (m/s)	γ_0 (-)
1.0	500.0	0.0	10.59	340.72	1.2253

4.8 Comparison of Analytical and Numerical Results

4.8.1 Simulation Setup

The case study consists of an uniform quiescent fluid that responds to two unsteady heat release source profiles, consisting of a Gaussian spherical distribution and step temporal profile, and a Gaussian spherical and temporal distribution, respectively. In order to maintain the unconfined domain condition of the problem, the dimensions of the domain are set such that the simulation concludes before pressure waves induced from the heat release pulse reach the boundaries of the domain, thereby preventing any pressure reflection from affecting the zone of study. The computational domain is depicted in Fig. 4.7 and it consists of a three-dimensional spherical cavity with 5 mm outer radius. The outer boundary is modeled as an inviscid, adiabatic wall. The unsteady heat release is modeled as an external heat source in the energy equation, located at the center of the spherical domain. The total number of cells is 107,136, and the mesh is divided in 200 partitions. The structured grid evolves the cell size from 3 μm in the to 100 μm. To accurately capture the transient, the time step is limited to 2 ns and the simulations capture 12.5 μs of physical time.

The study has been conducted using perfect gas with properties like that of CO_2 as the working fluid with the conditions and energy level summarized in Table 4.2. A pressure of 1 MPa and a temperature of 500 K are chosen as the initial conditions, which are representative of the interaction between hot and cold gases in the shear layer region of a non-premixed, shear-coaxial injector used in rocket engines. All

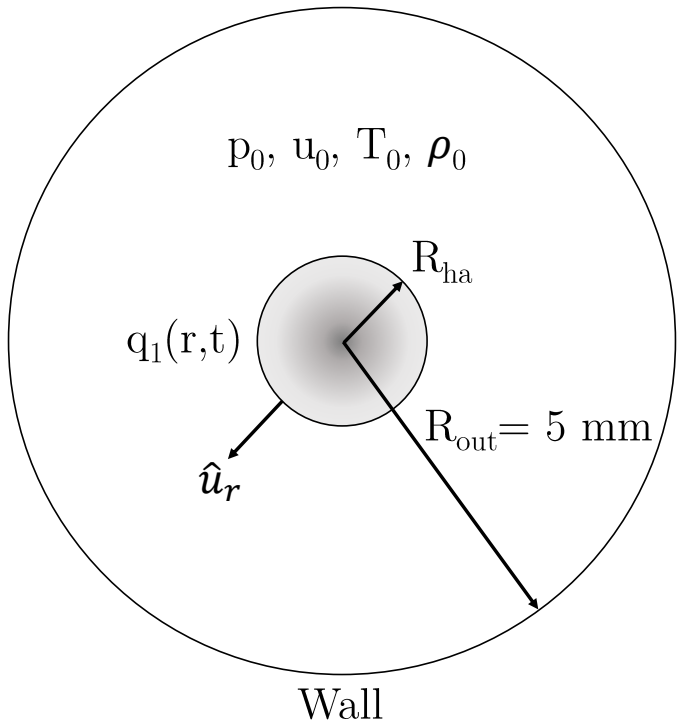

Figure 4.7. Schematic of the spherical computational domain used in the numerical simulations.

the highly-resolved DES simulations have been performed using the in-house Navier-Stokes solver GEMS, which has been presented in Section 3.6.1.

4.8.2 Results Discussion

The comparison of the analytical and numerical solutions of the fluid response to a heat source with Gaussian spherical distribution and step temporal profile are presented in Figs. 4.8-4.16. An acoustically compact case is studied in Figs. 4.8-4.11, whereas a noncompact case is presented in Figs. 4.12-4.15. For both cases, the analytical solution is able to predict with a good level of agreement the results from the numerical simulations. It should be pointed out that in this case the heat release rate is moderate so as to avoid excessive temperature increase at the center of the heat source.

The compact and noncompact regimes exhibit a different type of pressure response, with certain similarities to the one-dimensional cases from Chapter 3. The most relevant difference between the one-dimensional and three-dimensional case is that in the latter the amplitude of the pressure fluctuation decays with the radial distance, whereas in the former the amplitude of the pulse remains constant after reaching the far field distance. Furthermore, in the one-dimensional case the pressure fluctuation is always larger or equal than the mean flow pressure p_0. In contrast, in the three-dimensional spherical case the amplitude of the pressure fluctuation falls below p_0 after the heat release source stops. For both heat source profiles, in the compact case the analytical solution predicts a symmetric increase and decrease of the pressure fluctuation as the heat source ramps up and down the heat release rate. For both heat sources, the analytical solution is able to better predict the compression portion of the pressure fluctuation than the rarefaction portion. In the noncompact cases the pressure compression and rarefaction are not symmetric with respect to p_0.

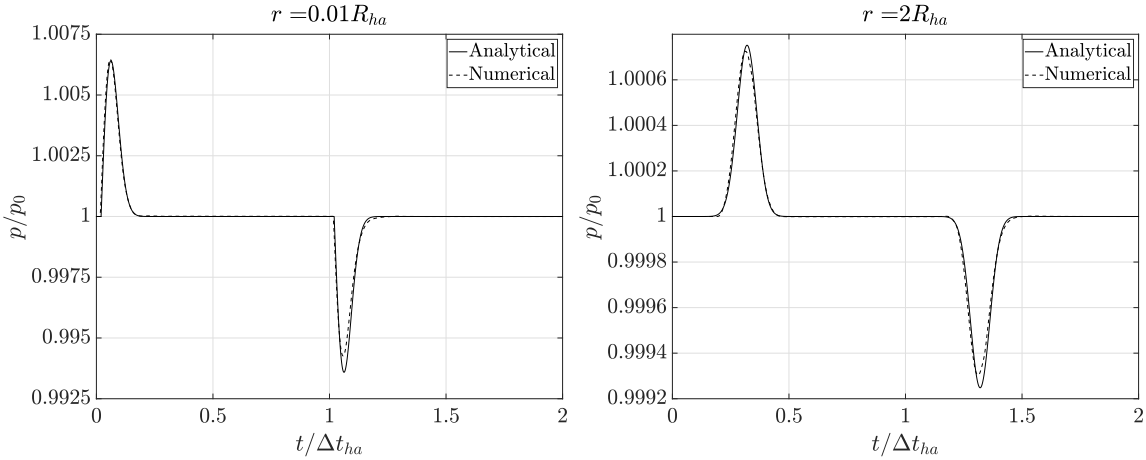

Figure 4.8. Compact case, $He = 0.0593 < \sqrt{8/3}$. Pressure response of a perfect gas with properties like that of CO_2 to a heat source with Gaussian spherical distribution and step temporal profile. Heat release parameters: $q_{ha,sph} = 10^{11}$ W/m^3, $R_{ha} = 50$ μm, $\Delta t_{ha} = 1$ μs, and $E_{ha} = \frac{5}{3}\pi 10^{-8}$ J.

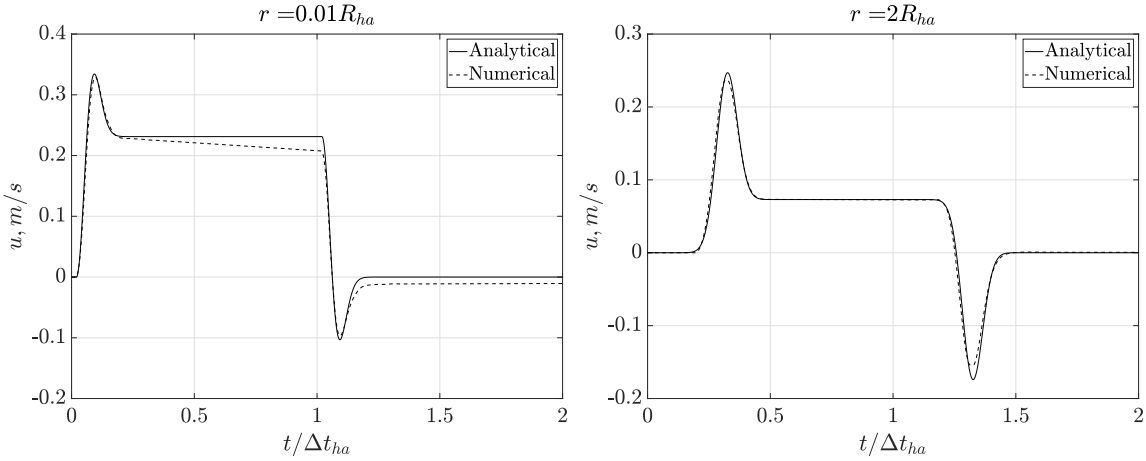

Figure 4.9. Compact case, $He = 0.0593 < \sqrt{8/3}$. Velocity response of a perfect gas with properties like that of CO_2 to a heat source with Gaussian spherical distribution and step temporal profile. Heat release parameters: $q_{ha,sph} = 10^{11}$ W/m^3, $R_{ha} = 50$ μm, $\Delta t_{ha} = 1$ μs, and $E_{ha} = \frac{5}{3}\pi 10^{-8}$ J.

In addition, as shown in Fig. 4.16 and Fig. 4.25, the amplitude of the pressure fluctuation decays over the radial distance in a sharper way in the noncompact regime with respect to the compact regime.

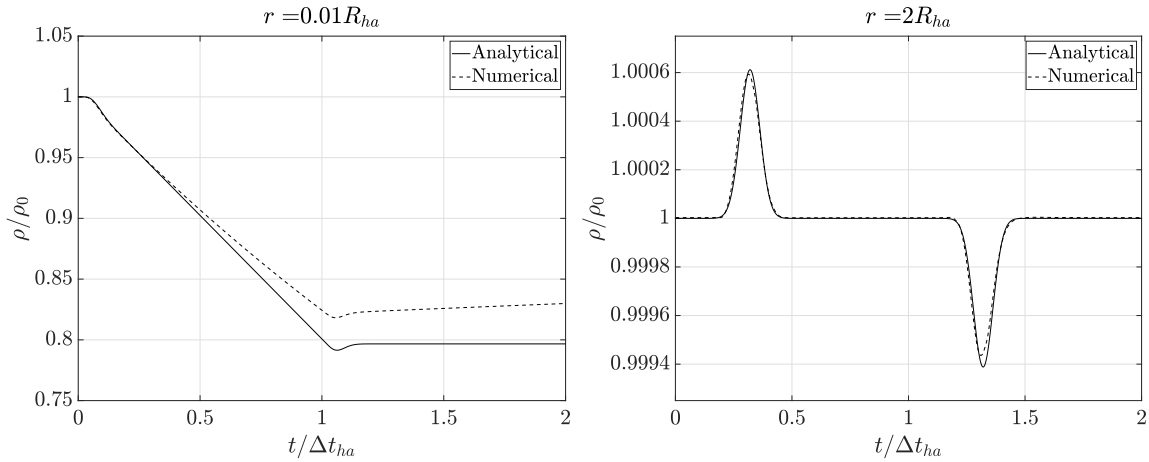

Figure 4.10. Compact case, $He = 0.0593 < \sqrt{8/3}$. Density response of a perfect gas with properties like that of CO_2 to a heat source with Gaussian spherical distribution and step temporal profile. Heat release parameters: $q_{ha,sph} = 10^{11}$ W/m^3, $R_{ha} = 50$ μm, $\Delta t_{ha} = 1$ μs, and $E_{ha} = \frac{5}{3}\pi 10^{-8}$ J.

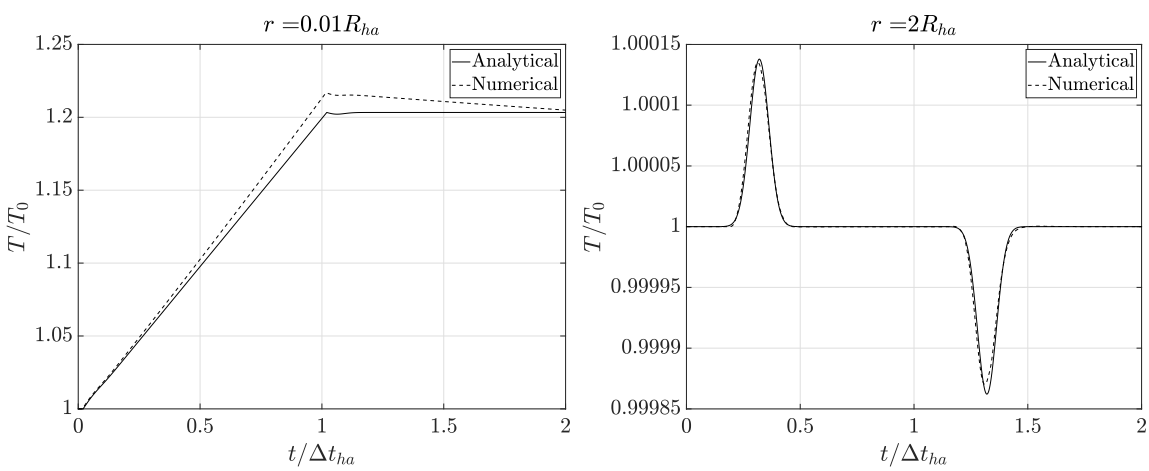

Figure 4.11. Compact case, $He = 0.0593 < \sqrt{8/3}$. Temperature response of a perfect gas with properties like that of CO_2 to a heat source with Gaussian spherical distribution and step temporal profile. Heat release parameters: $q_{ha,sph} = 10^{11}$ W/m^3, $R_{ha} = 50$ μm, $\Delta t_{ha} = 1$ μs, and $E_{ha} = \frac{5}{3}\pi 10^{-8}$ J.

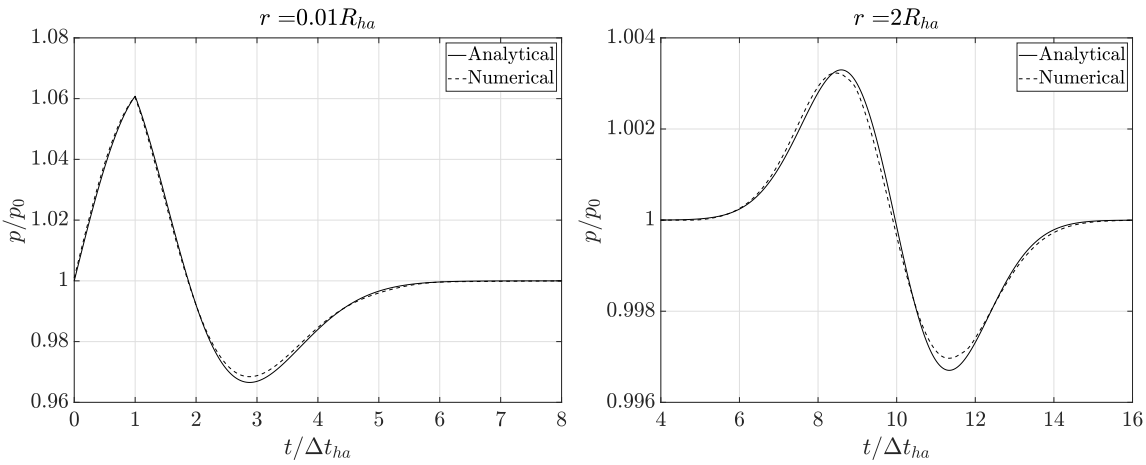

Figure 4.12. Noncompact case, $He = 1.897 > \sqrt{8/3}$. Pressure response of a perfect gas with properties like that of CO_2 to a heat source with Gaussian spherical distribution and step temporal profile. Heat release parameters: $q_{ha,sph} = 1.25 \cdot 10^{11}$ W/m^3, $R_{ha} = 400$ μm, $\Delta t_{ha} = 0.25$ μs, and $E_{ha} = \frac{8}{3}\pi 10^{-6}$ J.

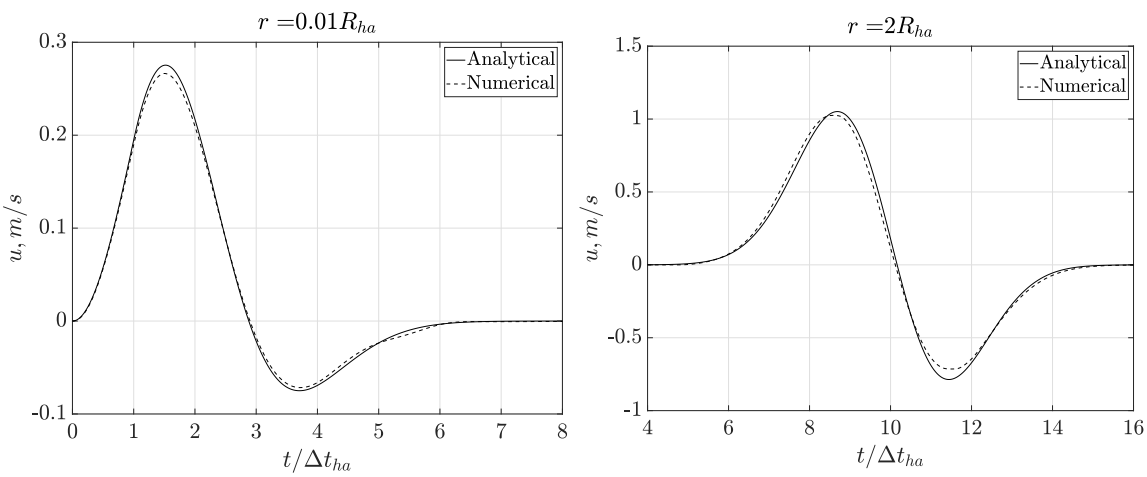

Figure 4.13. Noncompact case, $He = 1.897 > \sqrt{8/3}$. Velocity response of a perfect gas with properties like that of CO_2 to a heat source with Gaussian spherical distribution and step temporal profile. Heat release parameters: $q_{ha,sph} = 1.25 \cdot 10^{11}$ W/m^3, $R_{ha} = 400$ μm, $\Delta t_{ha} = 0.25$ μs, and $E_{ha} = \frac{8}{3}\pi 10^{-6}$ J.

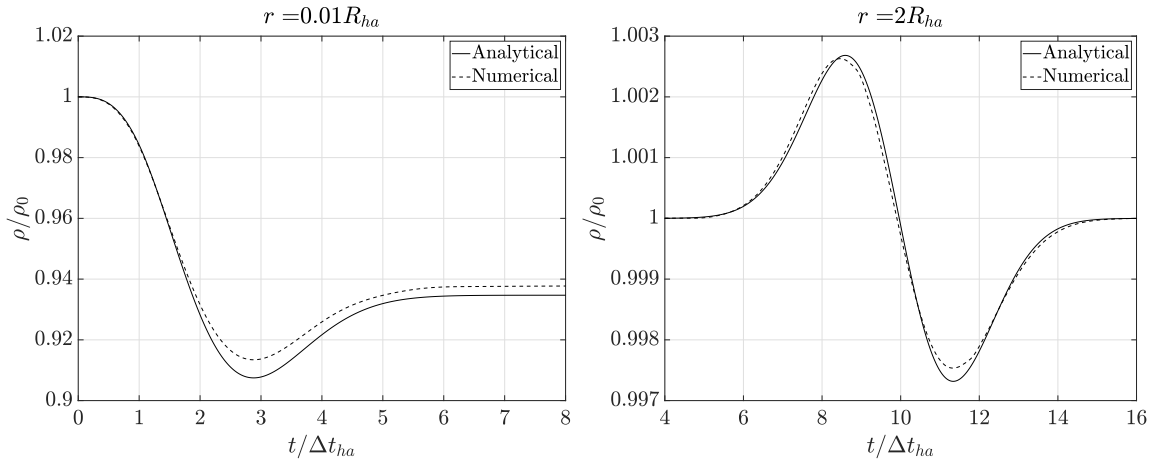

Figure 4.14. Noncompact case, $He = 1.897 > \sqrt{8/3}$. Density response of a perfect gas with properties like that of CO_2 to a heat source with Gaussian spherical distribution and step temporal profile. Heat release parameters: $q_{ha,sph} = 1.25 \cdot 10^{11}$ W/m^3, $R_{ha} = 400$ μm, $\Delta t_{ha} = 0.25$ μs, and $E_{ha} = \frac{8}{3}\pi 10^{-6}$ J.

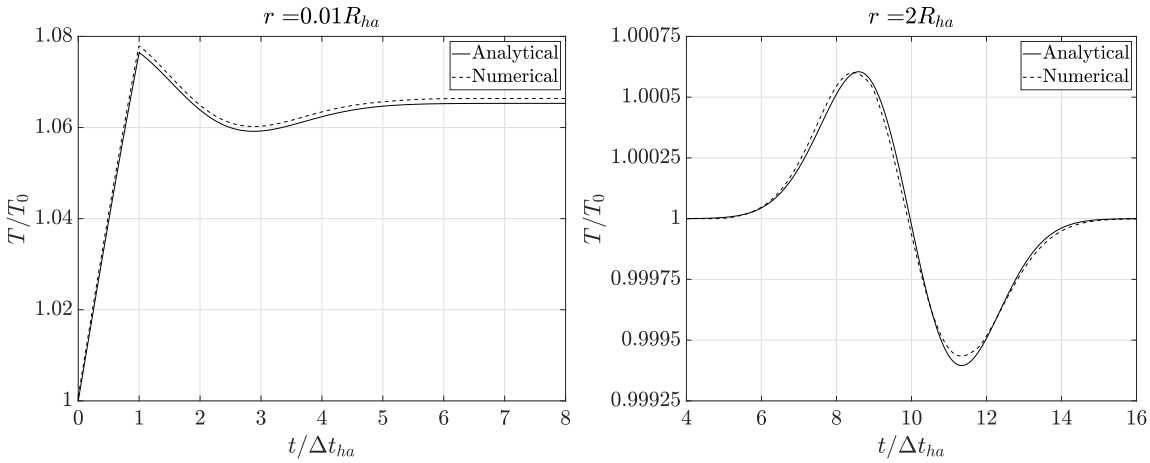

Figure 4.15. Noncompact case, $He = 1.897 > \sqrt{8/3}$. Temperature response of a perfect gas with properties like that of CO_2 to a heat source with Gaussian spherical distribution and step temporal profile. Heat release parameters: $q_{ha,sph} = 1.25 \cdot 10^{11}$ W/m^3, $R_{ha} = 400$ μm, $\Delta t_{ha} = 0.25$ μs, and $E_{ha} = \frac{8}{3}\pi 10^{-6}$ J.

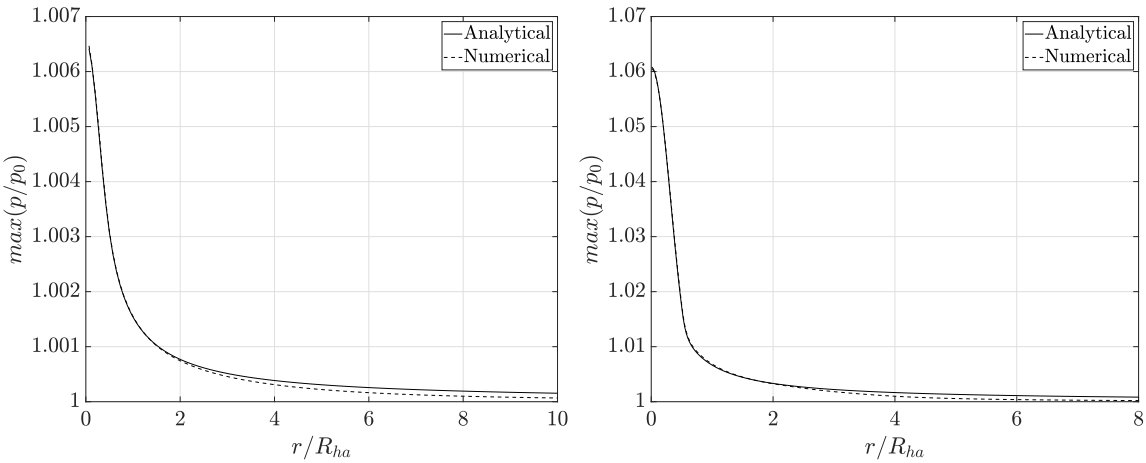

Figure 4.16. Evolution of the maximum pressure over the radial distance for a heat source with Gaussian spherical distribution and step temporal profile. L) Compact case: $He = 0.0593$, $q_{ha,sph} = 10^{11}$ W/m^3, $R_{ha} = 50$ μm, $\Delta t_{ha} = 1$ μs, and $E_{ha} = \frac{5}{3}\pi 10^{-8}$ J. R) Noncompact case: $He = 1.897$, $q_{ha,sph} = 1.25 \cdot 10^{11}$ W/m^3, $R_{ha} = 400$ μm, $\Delta t_{ha} = 0.25$ μs, and $E_{ha} = \frac{8}{3}\pi 10^{-6}$ J.

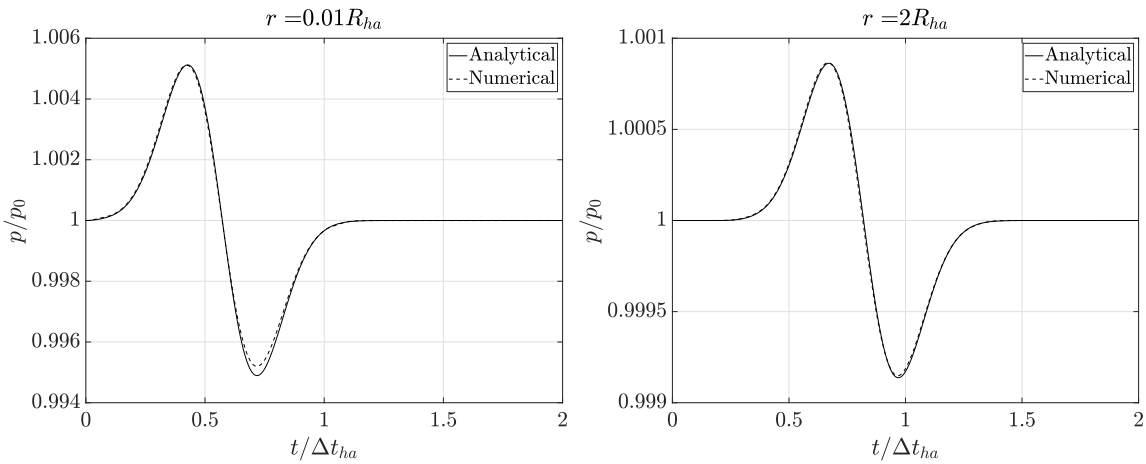

Figure 4.17. Compact case, $He = 0.0593 < \sqrt{8/3}$. Pressure response of a perfect gas with properties like that of CO_2 to a heat source with Gaussian spherical distribution and temporal profile. Heat release parameters: $q_{ha,sph} = 10^{11}$ W/m^3, $R_{ha} = 50$ μm, $\Delta t_{ha} = 1$ μs, and $E_{ha} = \frac{5}{3}\pi 10^{-8}$ J.

The comparison of the analytical and numerical solutions of the fluid response to a heat source with Gaussian spherical distribution and Gaussian temporal profile are presented in Figs. 4.17-4.25. The flow field results from the compact regime are depicted in Figs. 4.17-4.20 and the ones of the noncompact regime in Figs. 4.21-4.24. Similarly to what happens with the Gaussian spherical distribution and step temporal profile, both regimes exhibit different behaviors.

In addition to the aforementioned differences with the one-dimensional case, the nonlinear effects appear to play a smaller role in the three-dimensional spherical case due to the dominant effect of the fluctuation decay with the radial distance r. Indeed, whereas in the one-dimensional case the pressure fluctuations tended to steepen and eventually form weak shocks, in the three-dimensional case the fast decay caused by the spherical symmetry acts as a counter to reduce the pressure fluctuation. Since the pressure fluctuation decays with the distance, the temperature dependence of the local speed of sound becomes smaller and smaller the further the pressure fluctuation travels away from the source. This condition leads to a better agreement of the analytical solution with the numerical simulations.

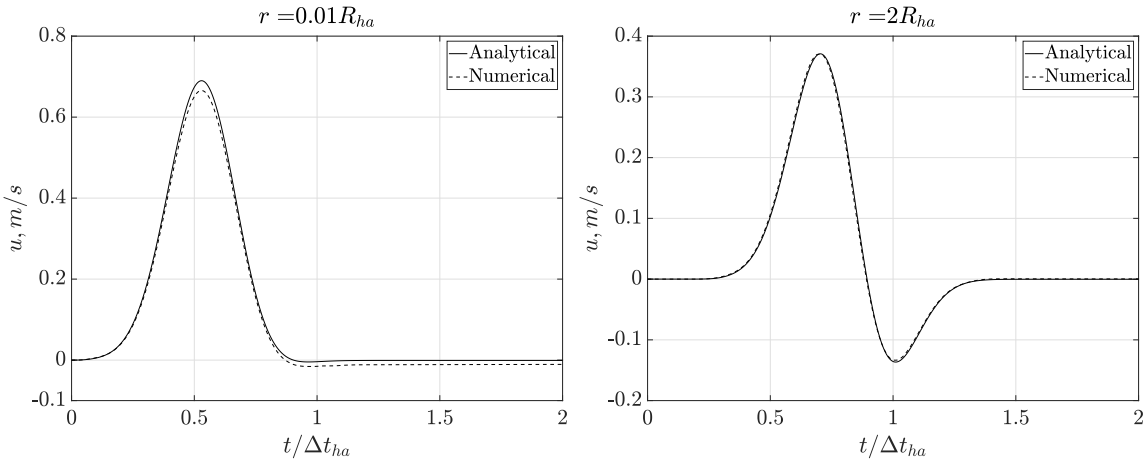

Figure 4.18. Compact case, $He = 0.0593 < \sqrt{8/3}$. Velocity response of a perfect gas with properties like that of CO_2 to a heat source with Gaussian spherical distribution and temporal profile. Heat release parameters: $q_{ha,sph} = 10^{11}$ W/m^3, $R_{ha} = 50$ μm, $\Delta t_{ha} = 1$ μs, and $E_{ha} = \frac{5}{3}\pi 10^{-8}$ J.

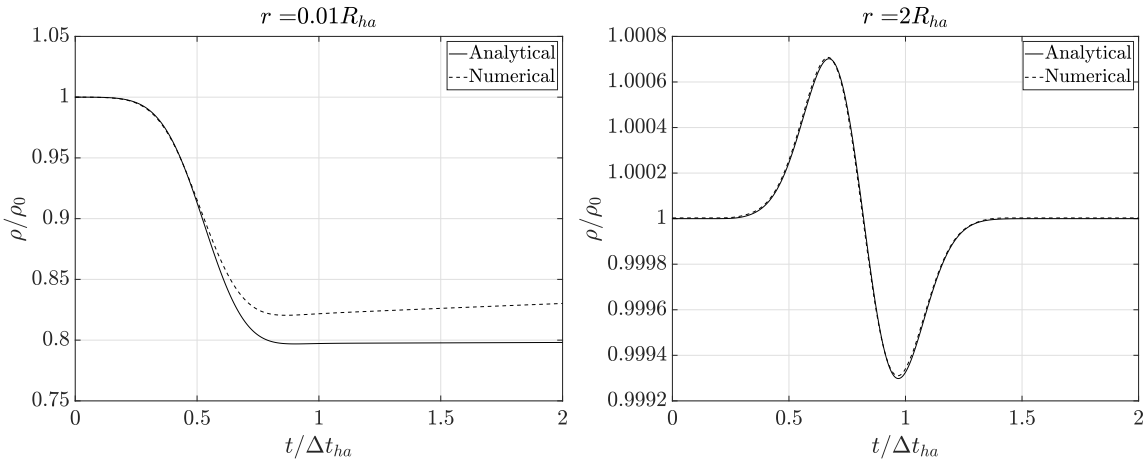

Figure 4.19. Compact case, $He = 0.0593 < \sqrt{8/3}$. Density response of a perfect gas with properties like that of CO_2 to a heat source with Gaussian spherical distribution and temporal profile. Heat release parameters: $q_{ha,sph} = 10^{11}$ W/m^3, $R_{ha} = 50$ μm, $\Delta t_{ha} = 1$ μs, and $E_{ha} = \frac{5}{3}\pi 10^{-8}$ J.

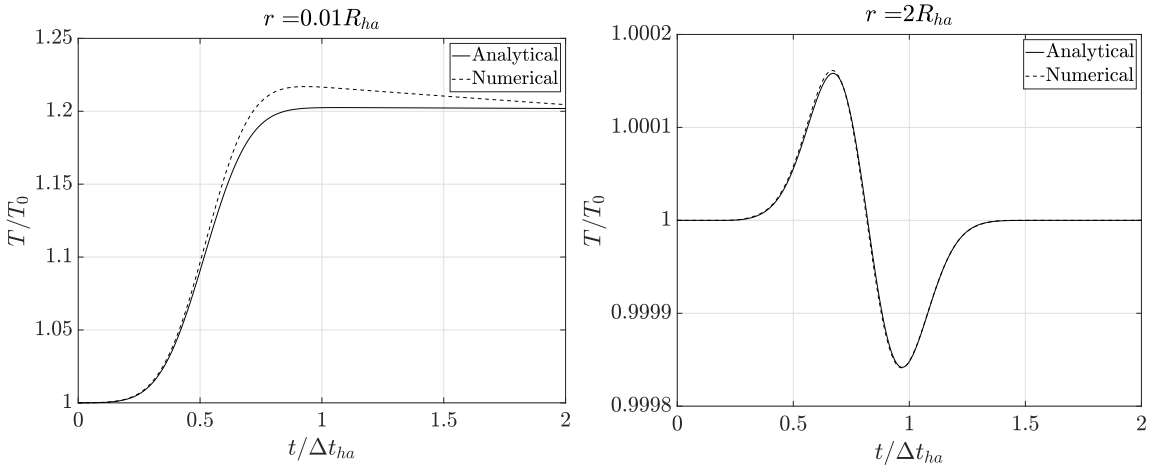

Figure 4.20. Compact case, $He = 0.0593 < \sqrt{8/3}$. Temperature response of a perfect gas with properties like that of CO_2 to a heat source with Gaussian spherical distribution and temporal profile. Heat release parameters: $q_{ha,sph} = 10^{11}$ W/m^3, $R_{ha} = 50$ μm, $\Delta t_{ha} = 1$ μs, and $E_{ha} = \frac{5}{3}\pi 10^{-8}$ J.

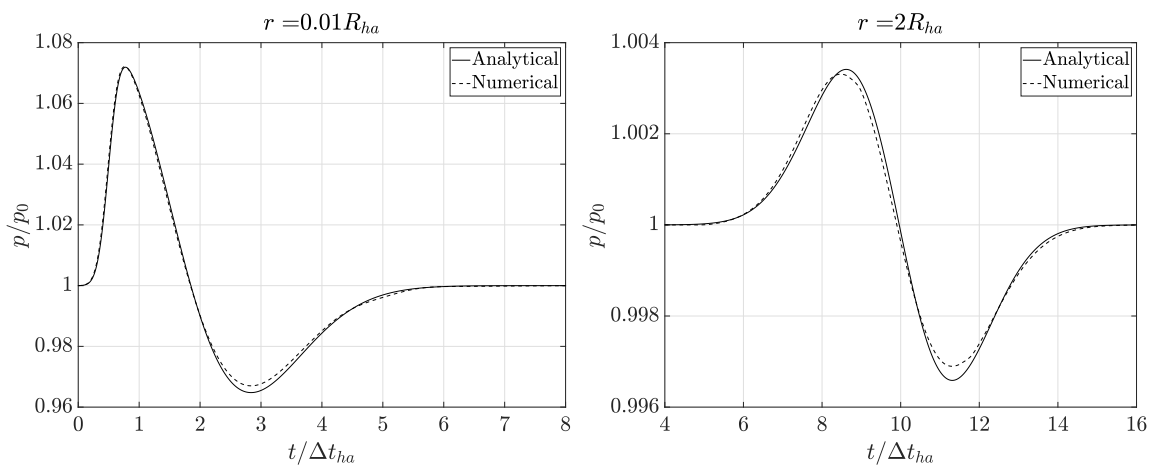

Figure 4.21. Noncompact case, $He = 1.897 > \sqrt{8/3}$. Pressure response of a perfect gas with properties like that of CO_2 to a heat source with Gaussian spherical distribution and temporal profile. Heat release parameters: $q_{ha,sph} = 1.25 \cdot 10^{11}$ W/m^3, $R_{ha} = 400$ μm, $\Delta t_{ha} = 0.25$ μs, and $E_{ha} = \frac{8}{3}\pi 10^{-6}$ J.

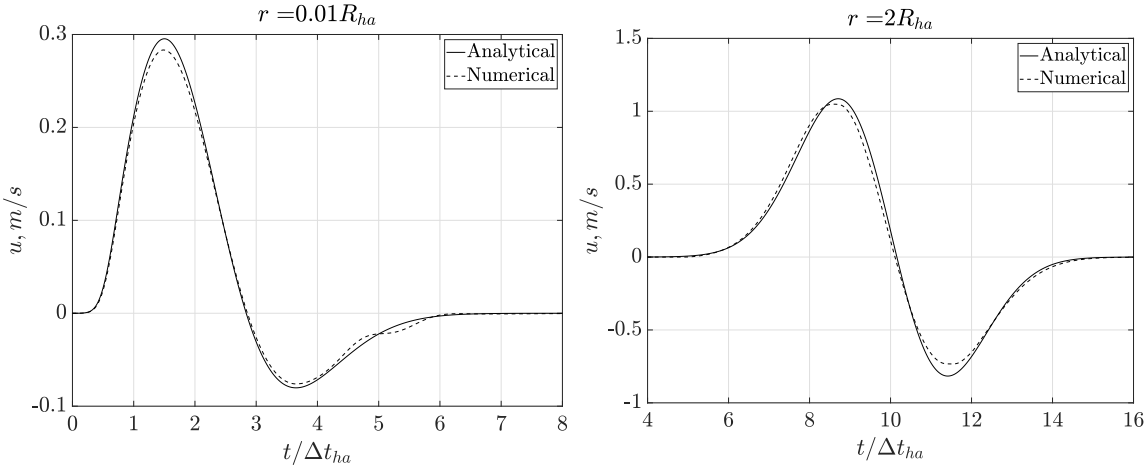

Figure 4.22. Noncompact case, $He = 1.897 > \sqrt{8/3}$. Velocity response of a perfect gas with properties like that of CO_2 to a heat source with Gaussian spherical distribution and temporal profile. Heat release parameters: $q_{ha,sph} = 1.25 \cdot 10^{11}$ W/m^3, $R_{ha} = 400$ μm, $\Delta t_{ha} = 0.25$ μs, and $E_{ha} = \frac{8}{3}\pi 10^{-6}$ J.

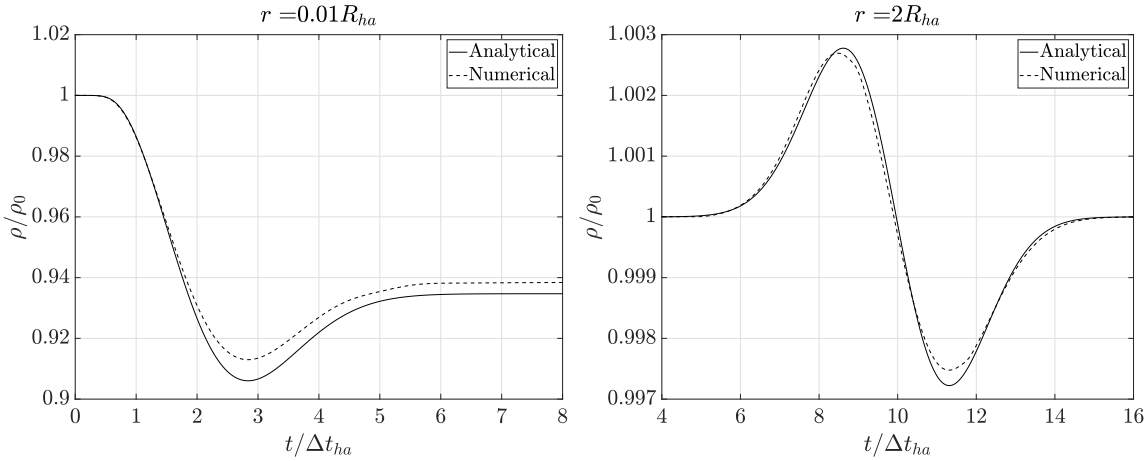

Figure 4.23. Noncompact case, $He = 1.897 > \sqrt{8/3}$. Density response of a perfect gas with properties like that of CO_2 to a heat source with Gaussian spherical distribution and temporal profile. Heat release parameters: $q_{ha,sph} = 1.25 \cdot 10^{11}$ W/m^3, $R_{ha} = 400$ μm, $\Delta t_{ha} = 0.25$ μs, and $E_{ha} = \frac{8}{3}\pi 10^{-6}$ J.

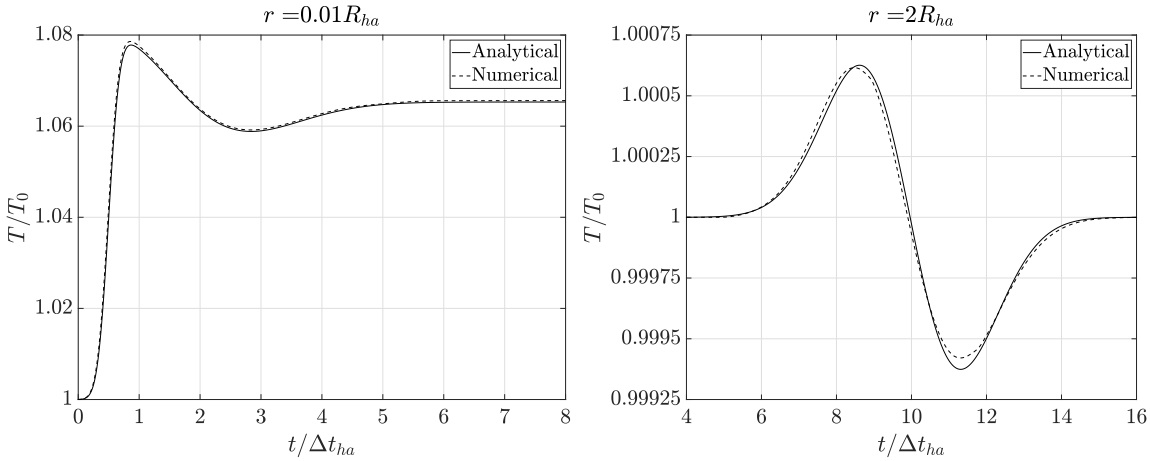

Figure 4.24. Noncompact case, $He = 1.897 > \sqrt{8/3}$. Temperature response of a perfect gas with properties like that of CO_2 to a heat source with Gaussian spherical distribution and temporal profile. Heat release parameters: $q_{ha,sph} = 1.25 \cdot 10^{11}$ W/m^3, $R_{ha} = 400$ μm, $\Delta t_{ha} = 0.25$ μs, and $E_{ha} = \frac{8}{3}\pi 10^{-6}$ J.

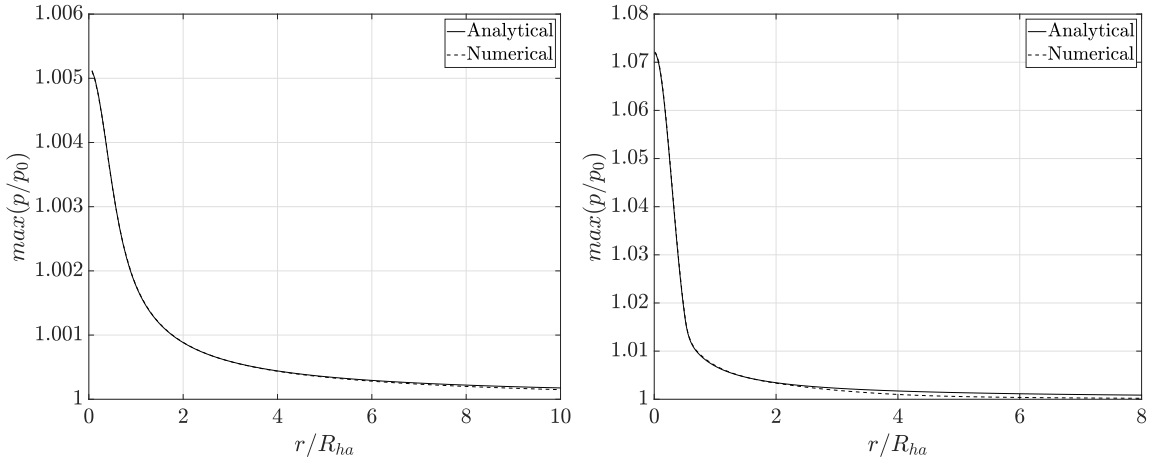

Figure 4.25. Evolution of the maximum pressure over the radial distance for a heat source with Gaussian spherical distribution and temporal profile. L) Compact case: $He = 0.0593$, $q_{ha,sph} = 10^{11}$ W/m^3, $R_{ha} = 50$ μm, $\Delta t_{ha} = 1$ μs, and $E_{ha} = \frac{5}{3}\pi 10^{-8}$ J. R) Noncompact case: $He = 1.897$, $q_{ha,sph} = 1.25 \cdot 10^{11}$ W/m^3, $R_{ha} = 400$ μm, $\Delta t_{ha} = 0.25$ μs, and $E_{ha} = \frac{8}{3}\pi 10^{-6}$ J.

4.9 Summary

The extension of the fluid response to an unsteady heat release pulse in an unconfined three-dimensional domain was presented in this chapter. The objective was to identify and evaluate the similarities and differences between the phenomena captured with the planar symmetry presented in Chapter 3 and a three-dimensional case, which more closely resembles the sudden reaction of a pocket of propellants. The chapter derived an analytical model based on the acoustic wave equation with spherical symmetry. To do so, the analytical methodology developed for the one-dimensional cases from Chapter 3 has been adapted to model three-dimensional cases with spherical symmetry. For modeling purposes, two different heat profiles have been used corresponding to a Gaussian spherical distribution and step temporal profile, and a Gaussian spherical and temporal profile have been considered.

In the analytical derivation, the Helmholtz number, continues to play a major role in distinguishing between different pressure response regime. He is defined as the ratio of the acoustic time over the duration of the heat release pulse. The analytical solutions have been compared against highly-resolved numerical simulation to evaluate the accuracy and limitations of the spherical wave equation. The analytical fluid response exhibited excellent agreement with the highly-resolved numerical solutions for moderate values of heat release.

Although the one-dimensional and three-dimensional cases exhibited important similarities, there are a few key differences that separate their pressure response to unsteady heat release. The most important difference between the two cases is that the amplitude of the pressure fluctuation decays with the radial distance in the three-dimensional case, whereas it remains constant after reaching the far field distance in the one-dimensional case. Furthermore, the nonlinear effects appear to be of less significance in the three-dimensional spherical case due to the dominant effect of the pressure decay with the radial distance r. In the one-dimensional case, for large values of heat release, the pressure fluctuations tend to steepen and form weak shocks. In

contrast, in the three-dimensional case the fast decay caused by the spherical symmetry acts as a counter to reduce the amplitude of the pressure fluctuation. In this way, the dependence of the speed of sound on the local temperature decreases the further the pressure fluctuation travels away from the source. This dimensional phenomenon results in a better agreement of the analytical solution with the numerical simulations for the three-dimensional case with respect to the one-dimensional case.

5. FLOW RESPONSE TO A FLUCTUATING HEAT RELEASE SOURCE IN 1D

This chapter presents an analytical model of the fluid response to a fluctuating unsteady heat release source for two different profiles, consisting of a flat spatial distribution and sinusoidal temporal profile, and a Gaussian spatial distribution and sinusoidal temporal profile. The analytical solution is based on the acoustic wave equation applied to an unconfined one-dimensional domain in a non-reacting fluid.

In Chapter 3 and Chapter 4 the heat release source generated a single pressure pulse. In these previous cases, the heat source would activate, follow a certain temporal profile, and then deactivate after which the heat source would cease to act, thereby allowing the pressure pulse to propagate across the medium without further external influence. These types of unsteady heat release pulses often occur in liquid rocket engines when a pocket of mixed propellants quickly reacts after accumulating in the recirculation zone close to the dump plane of a combustor. However, an even more common occurrence are heat release sources that fluctuate over time at the frequency of the acoustic modes of a combustor. Indeed, self-excited combustion instabilities require a coupling of the combustion heat release with the acoustic pressure field in the combustor. The flame is then assumed to respond to the pressure or velocity fluctuations following a given flame transfer model, such as Crocco's $n-\tau$ model [25, 26], for instance. This unit problem takes the opposite approach by analyzing the pressure response to a fluctuating heat release source. The pressure response is therefore not limited to a single pulse, but it is a continuous pressure signal.

The derivation of the analytical model confirms again the importance of the Helmholtz number, He, as the parameter that combines the relevant length and time scales. In a fluctuating heat source the Helmholtz number is defined as ratio of

the acoustic time over the fluctuating period, which can also be expressed as the ratio of the heat release length scale over the fluctuating wavelength. A critical Helmholtz number separates the pressure response into acoustically compact and noncompact regimes. In the compact regime, the amplitude of the pressure fluctuations is constant over the distance. In contrast, in the noncompact regime, the amplitude of the pressure fluctuations is larger within the heat source area of application, and then decays to a far field pressure value outside the heat source. A parametric study has been conducted to further investigate the two pressure response regimes. The study parameters are selected to be representative of the extreme conditions in a rocket combustor.

In order to assess the accuracy and limitations of the model, the analytical solutions have been compared against highly-resolved numerical simulations. As described in previous chapters, the analytical model shows a good agreement with the numerical simulations for moderate values of heat release rate. This holds true while the flow conditions remain close to the model assumptions. Nevertheless, for large rates of heat release, the presence of nonlinear effects deviate the numerical solution from the analytical model. For such large values, as the conditions separate ever more from the model assumptions, such as the constant mean flow speed of sound, the analytical model cannot capture the rapid accumulation of nonlinear effects.

5.1 Heat Source with Flat Spatial Distribution and Sinusoidal Temporal Profile

The present case consists of a heat source per unit volume $q_1(x,t)$ with a flat spatial distribution and a sinusoidal temporal profile defined as

$$q_1(x,t) = K_{ha_5} \sin(\omega t) \left[H\left(x + \frac{L_{hab}}{2}\right) - H\left(x - \frac{L_{hab}}{2}\right) \right] \tag{5.1}$$

where $H(x-L)$ is the unit Heaviside function, ω is the angular frequency of the fluctuating heat source, L_{ha} is the length of the heat source, and K_{ha_5} is the heat source magnitude parameter defined as

$$K_{ha_5} = \frac{E_{ha}\pi f}{2L_{ha}H_{ha}W_{ha}} = \frac{E_{ha}\omega}{4L_{ha}H_{ha}W_{ha}} \tag{5.2}$$

where f is the frequency of the fluctuating heat source. It is noted that for the present case cold flame is assumed [49], which implies not using a constant heat source term along the sinusoidal term, i.e. $q_0(1+\sin(\omega t))$. If the cold flame assumption is not considered, the mean flow temperature would increase over time due to the constant heat source. This in turn will increase the speed of sound of the fluid and hence separate further and further the analytical solution from the actual case. The cold flame assumption has been adopted by many researchers [49, 87] to obtain analytical scaling regarding thermoacoustic instabilities, but it may have non-negligible effect compared to actual phenomena [88].

The total energy inputted by the heat source during a full period cycle ($T_{per} = \frac{1}{f} = \frac{2\pi}{\omega}$) has a zero net contribution

$$Q_c = \int_0^{T_{per}} \int_{-\infty}^{\infty} q_1(x,t)dVdt =$$
$$\int_0^{T_{per}} \int_{-\frac{L_{ha}}{2}}^{\frac{L_{ha}}{2}} K_{ha_5}\left[H\left(z+\frac{L_{hab}}{2}\right) - H\left(z-\frac{L_{hab}}{2}\right)\right]\sin(\omega s)H_{ha}W_{ha}dzds =$$
$$K_{ha_5}L_{ha}H_{ha}W_{ha}\left[-\frac{1}{\omega}\cos(\omega s)\right]_0^{T_{per}} = \frac{K_{ha_5}L_{ha}H_{ha}W_{ha}}{\omega}\left[-\cos(2\pi)+\cos(0)\right] = 0 \tag{5.3}$$

For a half period cycle, the net energy contribution is

$$Q_{1/2c} = \int_0^{\frac{T_{per}}{2}} \int_{-\frac{L_{ha}}{2}}^{\frac{L_{ha}}{2}} q_1(x,t) dV dt = \\ K_{ha_5} L_{ha} H_{ha} W_{ha} \left[-\frac{1}{\omega} \cos(\omega s) \right]_0^{\frac{T_{per}}{2}} = \frac{2K_{ha_5} L_{ha} H_{ha} W_{ha}}{\omega} = \frac{E_{ha}}{2} \tag{5.4}$$

Then, the flat profile heat release intensity for the fluctuating heat source, $q_{ha,s}$, can be defined based on $Q_{1/2c}$ as follows

$$Q_{1/2c} = \frac{E_{ha}}{2} = \int_0^{\frac{T_{per}}{2}} \int_{-\frac{L_{ha}}{2}}^{\frac{L_{ha}}{2}} q_{ha,s} dV dt = q_{ha,s} L_{ha} H_{ha} W_{ha} \frac{T_{per}}{2} \tag{5.5}$$

Thus, the flat profile heat release intensity reads as

$$q_{ha,s} = \frac{E_{ha} f}{L_{ha} H_{ha} W_{ha}} \tag{5.6}$$

All cases in Chapter 5 report the heat release intensity using the value $q_{ha,s}$ from Eq. (5.6). The source term $f(x,t)$ in Eq. (2.33) is computed by applying the temporal derivative of the heat source of Eq. (5.1) as follows

$$f(x,t) = (\gamma - 1) \frac{\partial q_1}{\partial t} = (\gamma - 1) K_{ha_5} \omega \cos(\omega t) \left[H\left(x + \frac{L_{hab}}{2}\right) - H\left(x - \frac{L_{hab}}{2}\right) \right] \tag{5.7}$$

The substitution of Eq. (5.7) into Eq. (2.35) provides the expression to be integrated to solve the pressure response

$$p_{1,p}(x,t) = \frac{(\gamma - 1) K_{ha_5} \omega}{2c_0} \int_0^t \int_{x - c_0(t-s)}^{x + c_0(t-s)} \cos(\omega s) \left[H\left(z + \frac{L_{hab}}{2}\right) - H\left(z - \frac{L_{hab}}{2}\right) \right] dz ds \tag{5.8}$$

After integrating with respect to the spatial variable z, and recalling that $p_1(x,t) = p_{1,p}(x,t)$ as presented in Section 2.3, the integral reads as

$$p_1(x,t) = \frac{(\gamma-1)K_{ha_5}\omega}{2c_0}\int_0^t \cos(\omega s)\left[max\left(0, z+\frac{L_{hab}}{2}\right)\right. \\ \left. -max\left(0, z-\frac{L_{hab}}{2}\right)\right]_{x-c_0(t-s)}^{x+c_0(t-s)} ds \tag{5.9}$$

After integrating Eq. (5.9) with respect to the temporal variable s, the solution of the pressure response of a quiescent fluid to a heat source with flat spatial distribution and sinusoidal temporal profile reads as

$$\begin{aligned} p_1(x,t) = A_{p5}\Bigg\{ & \left[1+\cos\left(\frac{\omega}{c_0}\xi_1\right)(H(\chi_1)-1) - \cos(\omega t)H(\chi_1)\right]H(\xi_1) \\ & - \left[1+\cos\left(\frac{\omega}{c_0}\xi_2\right)(H(\chi_2)-1) - \cos(\omega t)H(\chi_2)\right]H(\xi_2) \\ & - \left[\cos(\omega t)+\cos\left(\frac{\omega}{c_0}\eta_1\right)(H(\eta_1)-1) - H(\eta_1)\right]H(\chi_1) \\ & + \left[\cos(\omega t)+\cos\left(\frac{\omega}{c_0}\eta_2\right)(H(\eta_2)-1) - H(\eta_2)\right]H(\chi_2)\Bigg\} \end{aligned} \tag{5.10}$$

where the auxiliar variables ξ_1, ξ_2, η_1, η_2, χ_1, and χ_2 are defined as

$$\begin{cases} \xi_1 = x + c_0 t + \frac{L_{ha}}{2}\ ; & \xi_2 = x + c_0 t - \frac{L_{ha}}{2}\ ; \\ \eta_1 = x - c_0 t + \frac{L_{ha}}{2}\ ; & \eta_2 = x - c_0 t - \frac{L_{ha}}{2}\ ; \\ \chi_1 = x + \frac{L_{ha}}{2}\ ; & \chi_2 = x - \frac{L_{ha}}{2}\ ; \end{cases} \tag{5.11}$$

In addition, the amplitude constant A_{p5} is given by

$$A_{p5} = \frac{(\gamma-1)\,E_{ha}}{8L_{ha}H_{ha}W_{ha}} \tag{5.12}$$

The velocity field can be calculated from the pressure solution Eq. (5.10) using the linearized momentum conservation equation (Eq. (2.19)). The velocity field then reads as

$$u_1(x,t) = \frac{A_{p5}}{\rho_0 c_0}\left\{\left[1-\cos\left(\frac{\omega}{c_0}\xi_1\right)\right](H(\chi_1)-1)\,H(\xi_1)\right.$$
$$-\left[1-\cos\left(\frac{\omega}{c_0}\xi_2\right)\right](H(\chi_2)-1)\,H(\xi_2)+\left[1-\cos\left(\frac{\omega}{c_0}\eta_1\right)\right](H(\eta_1)-1)\,H(\chi_1)$$
$$\left.-\left[1-\cos\left(\frac{\omega}{c_0}\eta_2\right)\right](H(\eta_2)-1)\,H(\chi_2)\right\} \tag{5.13}$$

In turn, the density field can computed from the velocity field solution using the linearized mass conservation equation assuming that the mean flow properties are uniform (see Eq. (3.17)). The density field then reads as

$$\rho_1(x,t) = \frac{A_{p5}}{c_0^2}\left\{\left[1-\cos\left(\frac{\omega}{c_0}\xi_1\right)\right](1-H(\chi_1))\,H(\xi_1)\right.$$
$$-\left[1-\cos\left(\frac{\omega}{c_0}\xi_2\right)\right](1-H(\chi_2))\,H(\xi_2)+\left[1-\cos\left(\frac{\omega}{c_0}\eta_1\right)\right](H(\eta_1)-1)\,H(\chi_1)$$
$$\left.-\left[1-\cos\left(\frac{\omega}{c_0}\eta_2\right)\right](H(\eta_2)-1)\,H(\chi_2)\right\} \tag{5.14}$$

Finally, the temperature field can be computed using the linearized equation of state (Eq. (3.19)) as

$$T_1(x,t) = \frac{(\gamma-1)\,A_{p5}T_0}{\rho_0 c_0^2}\Bigg\{\left[1+\cos\left(\frac{\omega}{c_0}\xi_1\right)(H(\chi_1)-1)\right]H(\xi_1)$$
$$-\left[1+\cos\left(\frac{\omega}{c_0}\xi_2\right)(H(\chi_2)-1)\right]H(\xi_2)+\left[H(\eta_1)-\cos\left(\frac{\omega}{c_0}\eta_1\right)(H(\eta_1)-1)\right]H(\chi_1)$$
$$-\left[H(\eta_2)-\cos\left(\frac{\omega}{c_0}\eta_2\right)(H(\eta_2)-1)\right]H(\chi_2)$$
$$+\frac{\gamma\cos(\omega t)-1}{\gamma-1}\left[(1+H(\xi_2))\,H(\chi_2)-(1+H(\xi_1))\,H(\chi_1)\right]\Bigg\} \tag{5.15}$$

5.1.1 Acoustically Compact vs Noncompact Regime

Analogously as in Chapter 3, a Helmholtz number can be defined as the ratio of the characteristic acoustic time over the heat release fluctuating time period (i.e. $\tau_{ha} = 1/f$) as

$$He = \frac{fL_{ha}}{c_0} = \frac{\omega L_{ha}}{2\pi c_0} \tag{5.16}$$

A careful examination of the solutions of pressure, velocity, density and temperature from Eqs. (5.10, 5.13, 5.14, 5.15) allows the extraction of the limits for the main flow field variables as presented in Table 5.1. It should be noted that the results in Table 5.1 are reported as the steady state, which happens at least after $t > \frac{L_{ha}}{2c_0}$.

The critical Helmholtz number can be derived from the far field pressure expression from Table 5.1 for low He numbers, $p_{ff}\Big|_{He\leq 0.5}$. Following the same process as in Section 3.3, we vary He for a constant value of heat release intensity $q_{ha,s}$, while maintaining also constant E_{ha}, H_{ha}, and W_{ha}. This is equivalent to maintaining the ratio f/L_{ha} equal to a constant k_1. The Helmholtz number can be written in terms

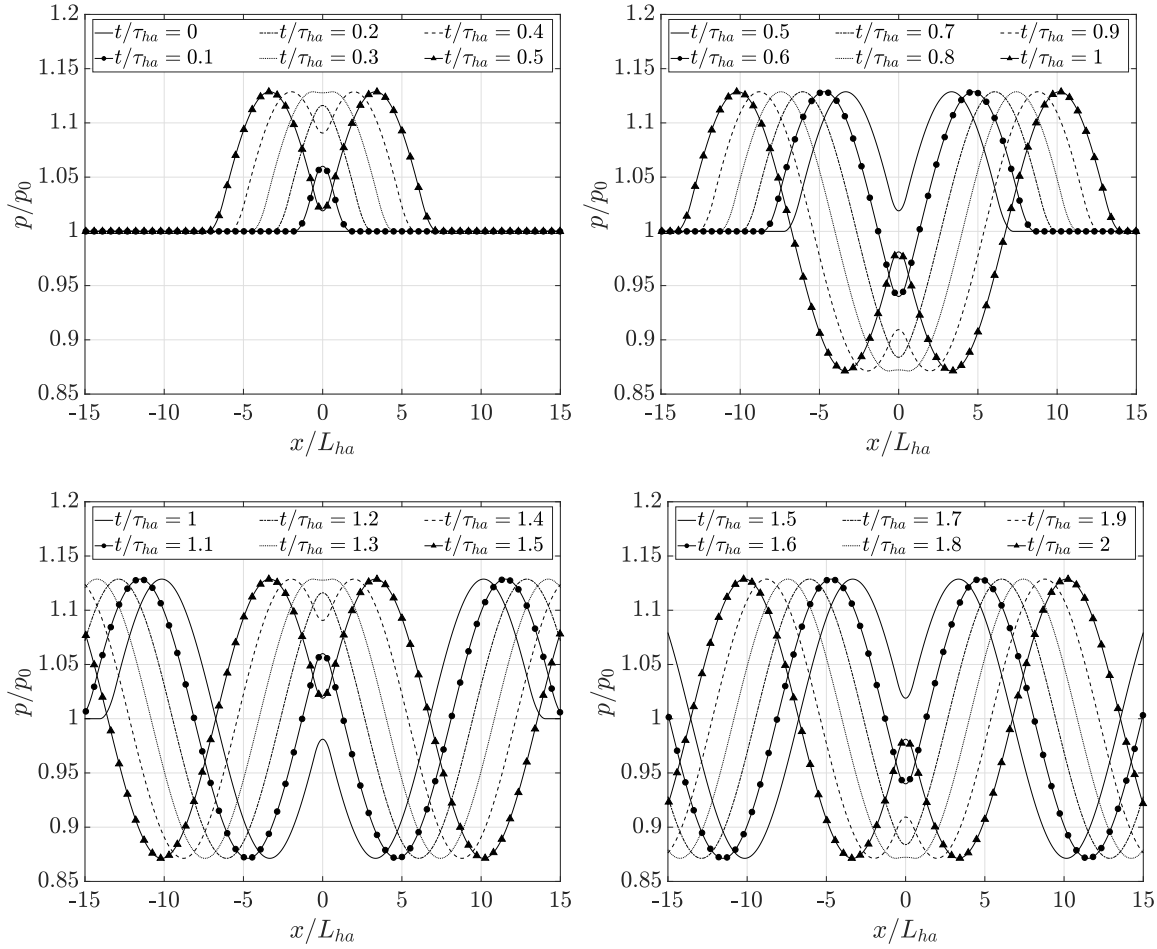

Figure 5.1. Compact case. Pressure response of a perfect gas with properties like that of CO_2 to a heat release source with flat spatial distribution and sinusoidal temporal profile. $He = 0.0734$, $q_{ha,s} = 2.5 \cdot 10^{12}$ W/m^3, $E_{ha}/(H_{ha}W_{ha}) = 1000$ J/m^2, $L_{ha} = 100$ μm and $f = 2.5 \cdot 10^5$ Hz.

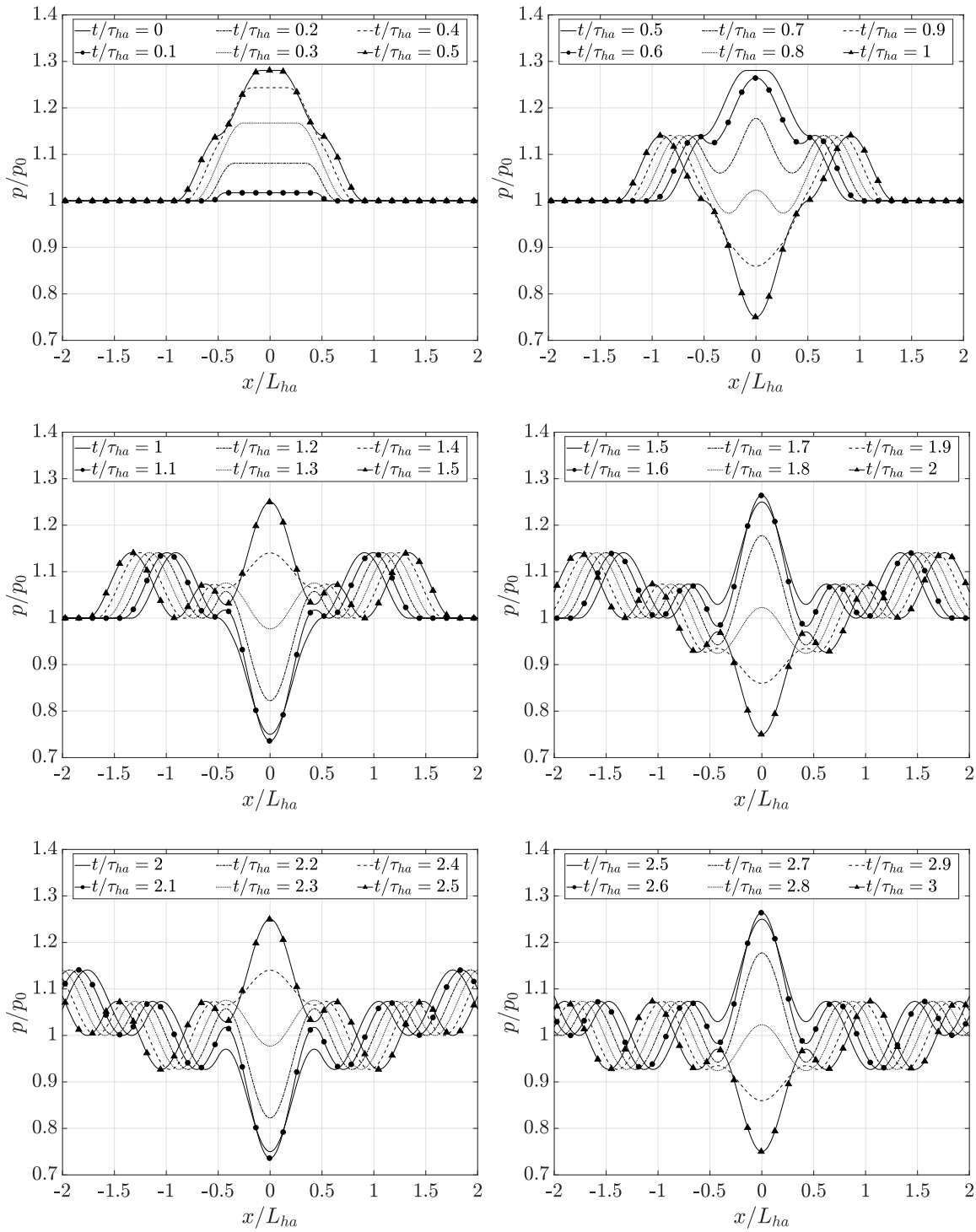

Figure 5.2. Noncompact case. Pressure response of a perfect gas with properties like that of CO_2 to a heat release source with flat spatial distribution and sinusoidal temporal profile. $He = 1.174$, $q_{ha,s} = 2.5 \cdot 10^{12}$ W/m^3, $E_{ha}/(H_{ha}W_{ha}) = 1000$ J/m^2, $L_{ha} = 400$ μm and $f = 10^6$ Hz.

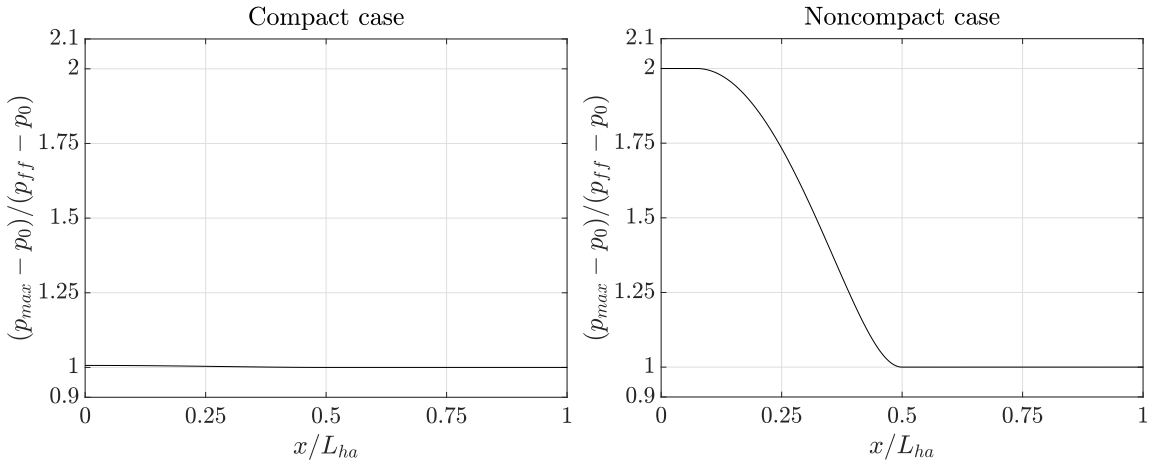

Figure 5.3. Evolution of pressure amplitude over the distance for the response of a perfect gas with properties like that of CO_2 to a heat release source with flat spatial distribution and sinusoidal temporal profile. Compact case (L): $He = 0.0734$, $q_{ha,s} = 2.5{\cdot}10^{12}$ W/m^3, $L_{ha} = 100$ μm and $f = 2.5{\cdot}10^5$ Hz; Noncompact case (R): $He = 1.174$, $q_{ha,s} = 2.5 \cdot 10^{12}$ W/m^3, $L_{ha} = 400$ μm and $f = 10^6$ Hz. $E_{ha}/(H_{ha}W_{ha}) = 1000$ J/m^2 for both cases.

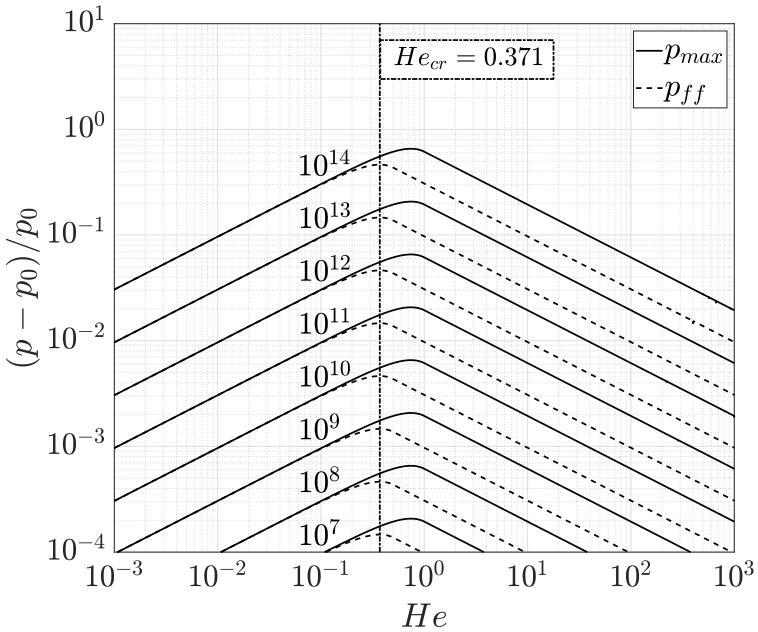

Figure 5.4. Evolution of the maximum and far field pressure amplitude with respect to the Helmholtz number for the response of a perfect gas with properties like that of CO_2 to a heat release source with flat spatial distribution and sinusoidal temporal profile. $E_{ha}/(H_{ha}W_{ha}) = 1000$ J/m^2.

Table 5.1. Limiting expressions for the flow field response to a heat source with flat spatial distribution and sinusoidal temporal profile. The subscript "ff" refers to far field values.

Variable	Location	Formula
$p_{max}\Big\vert_{He\leq 1}$	$x=0$	$p_0+\frac{(\gamma-1)E_{ha}}{2L_{ha}W_{ha}W_{ha}}\cos\left(\frac{\pi}{2}\left(1-He\right)\right)$
$p_{max}\Big\vert_{He>1}$	$x=0$	$p_0+\frac{(\gamma-1)E_{ha}}{2L_{ha}W_{ha}W_{ha}}$
$p_{ff}\Big\vert_{He\leq 0.5}$	$\vert x\vert > L_{ff}$	$p_0+\frac{(\gamma-1)E_{ha}}{4L_{ha}W_{ha}W_{ha}}\cos\left(\frac{\pi}{2}\left(1-2He\right)\right)$
$p_{ff}\Big\vert_{He>0.5}$	$\vert x\vert > L_{ff}$	$p_0+\frac{(\gamma-1)E_{ha}}{4L_{ha}W_{ha}W_{ha}}$
$u_{ff}\Big\vert_{He\leq 0.5}$	$\vert x\vert > L_{ff}$	$\frac{(\gamma-1)E_{ha}}{4\rho_0 c_0 L_{ha}W_{ha}W_{ha}}\cos\left(\frac{\pi}{2}\left(1-2He\right)\right)$
$u_{ff}\Big\vert_{He>0.5}$	$\vert x\vert > L_{ff}$	$\frac{(\gamma-1)E_{ha}}{4\rho_0 c_0 L_{ha}W_{ha}W_{ha}}$
ρ_{min}	$x=0$	$\rho_0-\frac{(\gamma-1)E_{ha}}{2c_0^2 L_{ha}H_{ha}W_{ha}}$
T_{max}	$x=0$	$T_0+\frac{(\gamma-1)^2E_{ha}T_0}{4\rho_0 c_0^2 L_{ha}H_{ha}W_{ha}}\left[\cos\left(\omega t_m-\pi He\right)-\frac{\gamma\cos\left(\omega t_m\right)-1}{\gamma-1}\right]$ where $t_m=\frac{1}{\omega}\tan^{-1}\left(\frac{\sin\left(\pi He\right)}{\cos\left(\pi He\right)-\frac{\gamma}{\gamma-1}}\right)$

of this constant k_1 as $He = \frac{fL_{ha}}{c_0} = \frac{f^2}{k_1 c_0}$. Substituting $f = \sqrt{k_1 c_0}\sqrt{He}$ and $q_{ha,s}$ into the $p_{ff}\Big|_{He\leq 0.5}$ expression leads to

$$p_{ff}\Big|_{He\leq 0.5} - p_0 = \frac{(\gamma-1)E_{ha}}{4L_{ha}W_{ha}W_{ha}}\cos\left(\frac{\pi}{2}(1-2He)\right) = \frac{(\gamma-1)\,q_{ha,s}}{4\sqrt{k_1 c_0}\sqrt{He}}\cos\left(\frac{\pi}{2}(1-2He)\right) = \frac{k_2}{\sqrt{He}}\cos\left(\frac{\pi}{2}(1-2He)\right) \tag{5.17}$$

where k_2 is a constant that encompasses all the constant terms of Eq. (5.17). The cosine term from Eq. (5.17) can be approximated for small values using a Taylor expansion centered around the origin as $\cos(x) \approx 1 - \frac{x^2}{2}$, leading to the following approximation

$$p_{ff}\Big|_{He\leq 0.5} - p_0 \approx \frac{k_2}{\sqrt{He}}\left(1 - \frac{\pi^2}{8}\left(1-2He^2\right)\right) \tag{5.18}$$

Differentiating Eq. (5.18) with respect to He and finding the maximum result, the approximate critical Helmholtz number for the heat source with flat spatial distribution and sinusoidal temporal profile is given by

$$He_{cr} \approx \frac{1+\sqrt{1-3\left(\frac{8}{\pi^2}-1\right)}}{6} = 0.3754 \tag{5.19}$$

Alternatively, the numerical computation of the maximum from Eq. (5.17) leads to $He_{cr} = 0.371$, which is close to the approximate value from Eq. (5.19). $He_{cr} = 0.371$ has been set as the critical Helmholtz number for this heat source profile.

5.2 Heat Source with Gaussian Spatial Distribution and Sinusoidal Temporal Profile

The present case consists of a heat source per unit volume $q_1(x,t)$ with a Gaussian spatial distribution and a sinusoidal temporal profile defined as

$$q_1(x,t) = K_{ha_6} exp\left[-\frac{1}{2}\left(\frac{x}{\sigma_x}\right)^2\right]\sin(\omega t) \tag{5.20}$$

where σ_x is the standard deviation of the Gaussian spatial profile, which has been set to $\sigma_x = L_{ha}/7$ for all cases, and K_{ha_6} is the heat source magnitude parameter defined as

$$K_{ha_6} = \frac{E_{ha}\pi f}{\sqrt{8\pi}\sigma_x H_{ha} W_{ha}} = \frac{E_{ha}\omega}{\sqrt{32\pi}\sigma_x H_{ha} W_{ha}} \tag{5.21}$$

The source term $f(x,t)$ in Eq. (2.33) is computed by applying the temporal derivative of the heat source of Eq. (5.20) as follows

$$f(x,t) = (\gamma - 1)\frac{\partial q_1}{\partial t} = (\gamma - 1)K_{ha_6}\omega\cos(\omega t)exp\left[-\frac{1}{2}\left(\frac{x}{\sigma_x}\right)^2\right] \tag{5.22}$$

The substitution of Eq. (5.22) into Eq. (2.35) provides the expression to be integrated to solve the pressure response

$$p_{1,p}(x,t) = \frac{(\gamma - 1)K_{ha_6}\omega}{2c_0}\int_0^t \int_{x-c_0(t-s)}^{x+c_0(t-s)} e^{-\frac{1}{2}\left(\frac{x}{\sigma_x}\right)^2}\cos(\omega s)dzds \tag{5.23}$$

After integrating with respect to the spatial variable z, and recalling that $p_1(x,t) = p_{1,p}(x,t)$ as presented in Section 2.3, the integral reads as

$$p_1(x,t) = \frac{(\gamma - 1)K_{ha_6}\omega}{2c_0}\int_0^t \left[\frac{\sqrt{2\pi}\sigma_x}{2}erf\left(\frac{z}{\sqrt{2}\sigma_x}\right)\cos(\omega s)\right]_{x-c_0(t-s)}^{x+c_0(t-s)} ds \tag{5.24}$$

Applying the integral spatial limits, the pressure response can be decomposed as $p_1(r,t) = p_1^-(r,t) + p_1^+(r,t)$ with inward and outward travelling waves, $p_1^-(r,t)$ and $p_1^+(r,t)$, respectively. The inwards and outwards travelling waves are respectively

$$p_1^-(r,t) = \frac{(\gamma - 1)K_{ha_6}\omega\sqrt{2\pi}\sigma_x}{4c_0}\int_0^t erf\left(\frac{x + c_0(t-s)}{\sqrt{2}\sigma_x}\right)\cos(\omega s)ds \tag{5.25}$$

$$p_1^+(r,t) = -\frac{(\gamma - 1)K_{ha_6}\omega\sqrt{2\pi}\sigma_x}{4c_0}\int_0^t erf\left(\frac{x - c_0(t-s)}{\sqrt{2}\sigma_x}\right)\cos(\omega s)ds \tag{5.26}$$

The integral of Eq. (5.25) can be written in simpler terms as

$$p_1^-(r,t) = C\int_0^t erf\left(a_1 s + b_1\right)\cos\left(\omega s\right)ds \tag{5.27}$$

where the constants are given by

$$\begin{cases} a_1 = -\dfrac{c_0}{\sqrt{2}\sigma_x} & b_1 = \dfrac{x + c_0 t}{\sqrt{2}\sigma_x} \\ C = \dfrac{(\gamma-1)K_{ha_6}\omega\sqrt{2\pi}\sigma_x}{4c_0} \end{cases} \tag{5.28}$$

Similar integrals with respect to Eq. (5.27) have known solutions that are developed in [86] and presented here

$$\int erf\left(az\right)\cos\left(bz\right)dz = \frac{1}{b}\sin\left(bz\right)erf\left(az\right) + \frac{i}{2b}exp\left(-\frac{b^2}{4a^2}\right)\left[erf\left(az - \frac{ib}{2a}\right) - erf\left(az + \frac{ib}{2a}\right)\right] \tag{5.29}$$

$$\int erf\left(az\right)\sin\left(bz\right)dz = -\frac{1}{b}\cos\left(bz\right)erf\left(az\right) + \frac{1}{2b}exp\left(-\frac{b^2}{4a^2}\right)\left[erf\left(az - \frac{ib}{2a}\right) + erf\left(az + \frac{ib}{2a}\right)\right] \tag{5.30}$$

Eq. (5.27) can be rewritten again with the aim of condensing the $a_1 s + b_1$ term inside the error function into a single term $a_1\xi$ as follows

$$p_1^-(r,t) = C\int_{\frac{b_1}{a_1}}^{t+\frac{b_1}{a_1}} erf\left(a_1\xi\right)\cos\left(\omega\left(\xi - \frac{b_1}{a_1}\right)\right)d\xi \tag{5.31}$$

where $\xi = s + \frac{b_1}{a_1}$. In turn, the cosine term can be expanded as follows

$$\cos\left(\omega\left(\xi - \frac{b_1}{a_1}\right)\right) = \cos(\omega\xi)\cos\left(\frac{\omega b_1}{a_1}\right) + \sin(\omega\xi)\sin\left(\frac{\omega b_1}{a_1}\right) \tag{5.32}$$

With this expansion, the integral of Eq. (5.31) can be expressed in the same form as the solutions Eq. (5.29) and Eq. (5.30), reading as

$$\begin{aligned} p_1^-(r,t) = C\cos\left(\frac{\omega b_1}{a_1}\right)\int_{\frac{b_1}{a_1}}^{t+\frac{b_1}{a_1}} erf\left(a_1\xi\right)\cos(\omega\xi)d\xi \\ +C\sin\left(\frac{\omega b_1}{a_1}\right)\int_{\frac{b_1}{a_1}}^{t+\frac{b_1}{a_1}} erf\left(a_1\xi\right)\sin(\omega\xi)d\xi \end{aligned} \tag{5.33}$$

where the cosine and sine terms of $\frac{\omega b_1}{a_1}$ are constants that can be moved outside of the integral. Integrating Eq. (5.33) using the results of Eq. (5.29) and Eq. (5.30) yields to the pressure response to Gaussian spatial distribution and sinusoidal temporal profile

$$\begin{aligned} p_1(x,t) = A_{p6}\Bigg\{\cos\left(\omega\frac{x}{c_0}\right)erf\left(\hat{x}\right)\Big[\sin(\omega\alpha_1) + \sin(\omega\alpha_2)\Big] \\ -\sin\left(\omega\frac{x}{c_0}\right)erf\left(\hat{x}\right)\Big[\cos(\omega\alpha_1) + \cos(\omega\alpha_2)\Big]\Bigg\} + \frac{A_{p6}}{2}exp\left(-He_x^2\right)\Bigg\{ \\ -\sin(\omega\alpha_1)\Big[erf\left(\hat{x}+iHe_x\right) + erf\left(\hat{x}-iHe_x\right) - erf\left(\beta_1+iHe_x\right) - erf\left(\beta_1-iHe_x\right)\Big] \\ -\sin(\omega\alpha_2)\Big[erf\left(\hat{x}+iHe_x\right) + erf\left(\hat{x}-iHe_x\right) - erf\left(\beta_2+iHe_x\right) - erf\left(\beta_2-iHe_x\right)\Big] \\ +i\cos(\omega\alpha_1)\Big[erf\left(\hat{x}+iHe_x\right) - erf\left(\hat{x}-iHe_x\right) - erf\left(\beta_1+iHe_x\right) + erf\left(\beta_1-iHe_x\right)\Big] \\ +i\cos(\omega\alpha_2)\Big[erf\left(\hat{x}+iHe_x\right) - erf\left(\hat{x}-iHe_x\right) - erf\left(\beta_2+iHe_x\right) + erf\left(\beta_2-iHe_x\right)\Big]\Bigg\} \end{aligned} \tag{5.34}$$

where the variables α_1, α_2, β_1, β_2, and $\hat{x}$, and the Helmholtz number He_x are defined as

$$\begin{cases} \alpha_1 = \frac{x}{c_0} + t \ ; & \alpha_2 = \frac{x}{c_0} - t \ ; \\ \beta_1 = \frac{\frac{x}{c_0}+t}{\tau_{ac}} \ ; & \beta_2 = \frac{\frac{x}{c_0}-t}{\tau_{ac}} \ ; \\ \hat{x} = \frac{x}{\sqrt{2}\sigma_x} \ ; & He_x = \frac{\omega\sigma_x}{\sqrt{2}c_0} = 2\omega\tau_{ac} \ ; \end{cases} \tag{5.35}$$

The characteristic acoustic time τ_{ac} appears again in the pressure solution, reading as

$$\tau_{ac} = \frac{\sqrt{2}\sigma_x}{c_0} \tag{5.36}$$

In addition, the amplitude constant A_{p6} is defined as

$$A_{p6} = \frac{C}{\omega} = \frac{(\gamma-1)K_{ha_6}\sqrt{2\pi}\sigma_x}{4c_0} = \frac{(\gamma-1)E_{ha}\omega}{16c_0H_{ha}W_{ha}} \tag{5.37}$$

The Helmholtz number He_x can be related to the He defined for the previous case in Eq. (5.16) as

$$He_x = \frac{\omega\sigma_x}{\sqrt{2}c_0} = 2\omega\tau_{ac} = \frac{\sqrt{2}\pi}{7}He \tag{5.38}$$

The relation of Eq. (5.38) considers that $\sigma_x = L_{ha}/7$. To facilitate the comparison of both heat source profiles, the results in Chapter 5 are reported using the He defined in Eq. (5.16).

It should be noted that the result of pressure fluctuation given by Eq. (5.34) corresponds to a real value, as it can be rewritten as

$$
\begin{aligned}
p_1(x,t) = A_{p6}\Bigg\{ & \cos\left(\omega\frac{x}{c_0}\right) erf\left(\hat{x}\right)\Big[\sin\left(\omega\alpha_1\right)+\sin\left(\omega\alpha_2\right)\Big] \\
-\sin\left(\omega\frac{x}{c_0}\right) & erf\left(\hat{x}\right)\Big[\cos\left(\omega\alpha_1\right)+\cos\left(\omega\alpha_2\right)\Big]\Bigg\} - A_{p6}\cdot exp\left(-He_x^2\right)\Bigg\{ \\
& \sin\left(\omega\alpha_1\right)\Big[\Re\left(erf\left(\hat{x}+iHe_x\right)\right)-\Re\left(erf\left(\beta_1+iHe_x\right)\right)\Big] \\
& +\sin\left(\omega\alpha_2\right)\Big[\Re\left(erf\left(\hat{x}+iHe_x\right)\right)-\Re\left(erf\left(\beta_2+iHe_x\right)\right)\Big] \\
& +\cos\left(\omega\alpha_1\right)\Big[\Im\left(erf\left(\hat{x}+iHe_x\right)\right)-\Im\left(erf\left(\beta_1+iHe_x\right)\right)\Big] \\
& +\cos\left(\omega\alpha_2\right)\Big[\Im\left(erf\left(\hat{x}+iHe_x\right)\right)-\Im\left(erf\left(\beta_2+iHe_x\right)\right)\Big]\Bigg\}
\end{aligned}
\tag{5.39}
$$

Similarly to the previous case, the velocity field can be calculated from the pressure solution Eq. (5.34) using the linearized momentum conservation equation (Eq. (2.19)). The velocity field then reads as

$$
\begin{aligned}
u_1(x,t) = -\frac{A_{p6}}{2\rho_0} exp\left(-He_x^2\right) \Bigg\{ \\
+\frac{1}{c_0}\sin\left(\omega\alpha_1\right)\Big[-erf\left(\hat{x}+iHe_x\right) - erf\left(\hat{x}-iHe_x\right) + erf\left(\beta_1+iHe_x\right) + erf\left(\beta_1-iHe_x\right)\Big] \\
-\frac{1}{c_0}\sin\left(\omega\alpha_2\right)\Big[-erf\left(\hat{x}+iHe_x\right) - erf\left(\hat{x}-iHe_x\right) + erf\left(\beta_2+iHe_x\right) + erf\left(\beta_2-iHe_x\right)\Big] \\
+\frac{i}{c_0}\cos\left(\omega\alpha_1\right)\Big[erf\left(\hat{x}+iHe_x\right) - erf\left(\hat{x}-iHe_x\right) - erf\left(\beta_1+iHe_x\right) + erf\left(\beta_1-iHe_x\right)\Big] \\
-\frac{i}{c_0}\cos\left(\omega\alpha_2\right)\Big[erf\left(\hat{x}+iHe_x\right) - erf\left(\hat{x}-iHe_x\right) - erf\left(\beta_2+iHe_x\right) + erf\left(\beta_2-iHe_x\right)\Big] \\
+\frac{\sqrt{2}}{\omega\sqrt{\pi}\sigma_x}\Big[\cos\left(\omega\alpha_1\right) - \cos\left(\omega\alpha_2\right)\Big]\Big[exp\left(-\left(\hat{x}+iHe_x\right)^2\right) + exp\left(-\left(\hat{x}-iHe_x\right)^2\right)\Big]\Bigg\} \\
+\frac{\sqrt{2}i}{\omega\sqrt{\pi}\sigma_x}\Big[\sin\left(\omega\alpha_1\right) - \sin\left(\omega\alpha_2\right)\Big]\Big[exp\left(-\left(\hat{x}+iHe_x\right)^2\right) - exp\left(-\left(\hat{x}-iHe_x\right)^2\right)\Big]\Bigg\}
\end{aligned}
\tag{5.40}
$$

The velocity field given in Eq. (5.40) also corresponds to a real value, as it can be simplified as

$$
\begin{aligned}
u_1(x,t) = -\frac{A_{p6}}{2\rho_0} exp\left(-He_x^2\right) \Bigg\{ \\
\frac{2}{c_0}\sin\left(\omega\alpha_1\right)\Bigg[-\Re(erf\left(\hat{x}+iHe_x\right)) + \Re(erf\left(\beta_1+iHe_x\right))\Bigg] \\
-\frac{2}{c_0}\sin\left(\omega\alpha_2\right)\Bigg[-\Re(erf\left(\hat{x}+iHe_x\right)) + \Re(erf\left(\beta_2+iHe_x\right))\Bigg] \\
+\frac{2}{c_0}\cos\left(\omega\alpha_1\right)\Bigg[-\Im(erf\left(\hat{x}+iHe_x\right)) + \Im(erf\left(\beta_1+iHe_x\right))\Bigg] \\
-\frac{2}{c_0}\cos\left(\omega\alpha_2\right)\Bigg[-\Im(erf\left(\hat{x}+iHe_x\right)) + \Im(erf\left(\beta_2+iHe_x\right))\Bigg] \\
+\frac{\sqrt{2}}{\omega\sqrt{\pi}\sigma_x}\Bigg[\cos\left(\omega\alpha_1\right)-\cos\left(\omega\alpha_2\right)\Bigg]\Bigg[exp\left(-\left(\hat{x}+iHe_x\right)^2\right)+exp\left(-\left(\hat{x}-iHe_x\right)^2\right)\Bigg]\Bigg\} \\
+\frac{\sqrt{2}i}{\omega\sqrt{\pi}\sigma_x}\Bigg[\sin\left(\omega\alpha_1\right)-\sin\left(\omega\alpha_2\right)\Bigg]\Bigg[exp\left(-\left(\hat{x}+iHe_x\right)^2\right)-exp\left(-\left(\hat{x}-iHe_x\right)^2\right)\Bigg]\Bigg\}
\end{aligned}
\tag{5.41}
$$

Then, the density field can computed from the velocity field given in Eq. (5.40) using the linearized mass conservation equation assuming uniform mean flow properties (see Eq. (3.17)). The density field reads as

$$
\begin{aligned}
\rho_1(x,t) = \frac{A_{p6}}{2c_0} exp\left(-He_x^2\right) \Bigg\{ \\
+\frac{1}{c_0}\sin\left(\omega\alpha_1\right)\Big[-erf\left(\hat{x}+iHe_x\right)-erf\left(\hat{x}-iHe_x\right)+erf\left(\beta_1+iHe_x\right)+erf\left(\beta_1-iHe_x\right)\Big] \\
+\frac{1}{c_0}\sin\left(\omega\alpha_2\right)\Big[-erf\left(\hat{x}+iHe_x\right)-erf\left(\hat{x}-iHe_x\right)+erf\left(\beta_2+iHe_x\right)+erf\left(\beta_2-iHe_x\right)\Big] \\
+\frac{i}{c_0}\cos\left(\omega\alpha_1\right)\Big[erf\left(\hat{x}+iHe_x\right)-erf\left(\hat{x}-iHe_x\right)-erf\left(\beta_1+iHe_x\right)+erf\left(\beta_1-iHe_x\right)\Big] \\
+\frac{i}{c_0}\cos\left(\omega\alpha_2\right)\Big[erf\left(\hat{x}+iHe_x\right)-erf\left(\hat{x}-iHe_x\right)-erf\left(\beta_2+iHe_x\right)+erf\left(\beta_2-iHe_x\right)\Big] \\
+\frac{2\sqrt{2}}{\omega\sqrt{\pi}\sigma_x}\left[\cos\left(\omega\alpha_1\right)+\cos\left(\omega\alpha_2\right)-2\cos\left(\omega\frac{x}{c_0}\right)\right] \\
\left[exp\left(-\left(\hat{x}+iHe_x\right)^2\right)+exp\left(-\left(\hat{x}-iHe_x\right)^2\right)\right] \\
+\frac{2\sqrt{2}i}{\omega\sqrt{\pi}\sigma_x}\left[\sin\left(\omega\alpha_1\right)+\sin\left(\omega\alpha_2\right)-2\sin\left(\omega\frac{x}{c_0}\right)\right] \\
\left[exp\left(-\left(\hat{x}+iHe_x\right)^2\right)-exp\left(-\left(\hat{x}-iHe_x\right)^2\right)\right] \\
-\frac{2c_0}{\omega^2\sqrt{\pi}\sigma_x^2}\left[\sin\left(\omega\alpha_1\right)+\sin\left(\omega\alpha_2\right)-2\sin\left(\omega\frac{x}{c_0}\right)\right] \\
\left[\left(\hat{x}+iHe_x\right)exp\left(-\left(\hat{x}+iHe_x\right)^2\right)+\left(\hat{x}-iHe_x\right)exp\left(-\left(\hat{x}-iHe_x\right)^2\right)\right] \\
+\frac{2c_0\ i}{\omega^2\sqrt{\pi}\sigma_x^2}\left[\cos\left(\omega\alpha_1\right)+\cos\left(\omega\alpha_2\right)-2\cos\left(\omega\frac{x}{c_0}\right)\right] \\
\left[\left(\hat{x}+iHe_x\right)exp\left(-\left(\hat{x}+iHe_x\right)^2\right)-\left(\hat{x}-iHe_x\right)exp\left(-\left(\hat{x}-iHe_x\right)^2\right)\right]\Bigg\}
\end{aligned}
\tag{5.42}
$$

Similarly to the pressure and velocity fields, the result of the density field is a real value, as Eq. (5.42) can be simplified as

$$
\begin{aligned}
\rho_1(x,t) = \frac{A_{p6}}{c_0} exp\left(-He_x^2\right) \Bigg\{ \\
+\frac{1}{c_0}\sin\left(\omega\alpha_1\right)\Bigg[-\Re(erf\left(\hat{x}+iHe_x\right)) + \Re(erf\left(\beta_1+iHe_x\right))\Bigg] \\
+\frac{1}{c_0}\sin\left(\omega\alpha_2\right)\Bigg[-\Re(erf\left(\hat{x}+iHe_x\right)) + \Re(erf\left(\beta_2+iHe_x\right))\Bigg] \\
+\frac{1}{c_0}\cos\left(\omega\alpha_1\right)\Bigg[-\Im(erf\left(\hat{x}+iHe_x\right)) + \Im(erf\left(\beta_1+iHe_x\right))\Bigg] \\
+\frac{1}{c_0}\cos\left(\omega\alpha_2\right)\Bigg[-\Im(erf\left(\hat{x}+iHe_x\right)) + \Im(erf\left(\beta_2+iHe_x\right))\Bigg] \\
+\frac{\sqrt{2}}{\omega\sqrt{\pi}\sigma_x}\Bigg[\cos\left(\omega\alpha_1\right)+\cos\left(\omega\alpha_2\right)-2\cos\left(\omega\frac{x}{c_0}\right)\Bigg] \\
\Bigg[exp\left(-\left(\hat{x}+iHe_x\right)^2\right)+exp\left(-\left(\hat{x}-iHe_x\right)^2\right)\Bigg] \\
+\frac{\sqrt{2}i}{\omega\sqrt{\pi}\sigma_x}\Bigg[\sin\left(\omega\alpha_1\right)+\sin\left(\omega\alpha_2\right)-2\sin\left(\omega\frac{x}{c_0}\right)\Bigg] \\
\Bigg[exp\left(-\left(\hat{x}+iHe_x\right)^2\right)-exp\left(-\left(\hat{x}-iHe_x\right)^2\right)\Bigg] \\
-\frac{c_0}{\omega^2\sqrt{\pi}\sigma_x^2}\Bigg[\sin\left(\omega\alpha_1\right)+\sin\left(\omega\alpha_2\right)-2\sin\left(\omega\frac{x}{c_0}\right)\Bigg] \\
\Bigg[\left(\hat{x}+iHe_x\right)exp\left(-\left(\hat{x}+iHe_x\right)^2\right)+\left(\hat{x}-iHe_x\right)exp\left(-\left(\hat{x}-iHe_x\right)^2\right)\Bigg] \\
+\frac{c_0\ i}{\omega^2\sqrt{\pi}\sigma_x^2}\Bigg[\cos\left(\omega\alpha_1\right)+\cos\left(\omega\alpha_2\right)-2\cos\left(\omega\frac{x}{c_0}\right)\Bigg] \\
\Bigg[\left(\hat{x}+iHe_x\right)exp\left(-\left(\hat{x}+iHe_x\right)^2\right)-\left(\hat{x}-iHe_x\right)exp\left(-\left(\hat{x}-iHe_x\right)^2\right)\Bigg]\Bigg\}
\end{aligned}
\tag{5.43}
$$

Finally, the temperature field can be computed using the linearized equation of state (Eq. (3.19)) as

$$
\begin{aligned}
T_1(x,t) = \frac{A_{p6}T_0\gamma}{\rho_0 c_0^2} erf\left(\frac{x}{\sqrt{2}\sigma_x}\right)\Bigg\{\cos\left(\omega\frac{x}{c_0}\right) erf\left(\frac{x}{\sqrt{2}\sigma_x}\right)\Big[\sin(\omega\alpha_1)+\sin(\omega\alpha_2)\Big] \\
-\sin\left(\omega\frac{x}{c_0}\right) erf\left(\frac{x}{\sqrt{2}\sigma_x}\right)\Big[\cos(\omega\alpha_1)+\cos(\omega\alpha_2)\Big]\Bigg\} + \frac{A_{p6}(\gamma-1)T_0}{2c_0^2\rho_0} exp\left(-He_x^2\right)\Bigg\{ \\
-\sin(\omega\alpha_1)\Big[erf(\hat{x}+iHe_x)+erf(\hat{x}-iHe_x)-erf(\beta_1+iHe_x)-erf(\beta_1-iHe_x)\Big] \\
-\sin(\omega\alpha_2)\Big[erf(\hat{x}+iHe_x)+erf(\hat{x}-iHe_x)-erf(\beta_2+iHe_x)-erf(\beta_2-iHe_x)\Big] \\
+i\cos(\omega\alpha_1)\Big[erf(\hat{x}+iHe_x)-erf(\hat{x}-iHe_x)-erf(\beta_1+iHe_x)+erf(\beta_1-iHe_x)\Big] \\
+i\cos(\omega\alpha_2)\Big[erf(\hat{x}+iHe_x)-erf(\hat{x}-iHe_x)-erf(\beta_2+iHe_x)+erf(\beta_2-iHe_x)\Big]\Bigg\} \\
-\frac{A_{p6}T_0}{2c_0\rho_0} exp\left(-He_x^2\right)\Bigg\{\frac{2\sqrt{2}}{\omega\sqrt{\pi}\sigma_x}\Big[\cos(\omega\alpha_1)+\cos(\omega\alpha_2)-2\cos\left(\omega\frac{x}{c_0}\right)\Big] \\
\Big[exp\left(-(\hat{x}+iHe_x)^2\right)+exp\left(-(\hat{x}-iHe_x)^2\right)\Big] \\
+\frac{2\sqrt{2}i}{\omega\sqrt{\pi}\sigma_x}\Big[\sin(\omega\alpha_1)+\sin(\omega\alpha_2)-2\sin\left(\omega\frac{x}{c_0}\right)\Big] \\
\Big[exp\left(-(\hat{x}+iHe_x)^2\right)-exp\left(-(\hat{x}-iHe_x)^2\right)\Big] \\
-\frac{2c_0}{\omega^2\sqrt{\pi}\sigma_x^2}\Big[\sin(\omega\alpha_1)+\sin(\omega\alpha_2)-2\sin\left(\omega\frac{x}{c_0}\right)\Big] \\
\Big[(\hat{x}+iHe_x)\,exp\left(-(\hat{x}+iHe_x)^2\right)+(\hat{x}-iHe_x)\,exp\left(-(\hat{x}-iHe_x)^2\right)\Big] \\
+\frac{2c_0\ i}{\omega^2\sqrt{\pi}\sigma_x^2}\Big[\cos(\omega\alpha_1)+\cos(\omega\alpha_2)-2\cos\left(\omega\frac{x}{c_0}\right)\Big] \\
\Big[(\hat{x}+iHe_x)\,exp\left(-(\hat{x}+iHe_x)^2\right)-(\hat{x}-iHe_x)\,exp\left(-(\hat{x}-iHe_x)^2\right)\Big]\Bigg\}
\end{aligned}
\tag{5.44}
$$

Similarly to the previous cases, the temperature field is a real value, as it can be simplified as

$$
\begin{aligned}
T_1(x,t) = \frac{A_{p6}T_0\gamma}{\rho_0 c_0^2} erf\left(\frac{x}{\sqrt{2}\sigma_x}\right)\Bigg\{\cos\left(\omega\frac{x}{c_0}\right) erf\left(\frac{x}{\sqrt{2}\sigma_x}\right)\Big[\sin(\omega\alpha_1)+\sin(\omega\alpha_2)\Big] \\
-\sin\left(\omega\frac{x}{c_0}\right) erf\left(\frac{x}{\sqrt{2}\sigma_x}\right)\Big[\cos(\omega\alpha_1)+\cos(\omega\alpha_2)\Big]\Bigg\} - \frac{A_{p6}(\gamma-1)T_0}{c_0^2\rho_0} exp\left(-He_x^2\right)\Bigg\{ \\
\sin(\omega\alpha_1)\Big[\Re(erf(\hat{x}+iHe_x)) - \Re(erf(\beta_1+iHe_x))\Big] \\
\sin(\omega\alpha_2)\Big[\Re(erf(\hat{x}+iHe_x)) - \Re(erf(\beta_2+iHe_x))\Big] \\
+\cos(\omega\alpha_1)\Big[\Im(erf(\hat{x}+iHe_x)) - \Im(erf(\beta_1+iHe_x))\Big]\Bigg\} \\
+\cos(\omega\alpha_2)\Big[\Im(erf(\hat{x}+iHe_x)) - \Im(erf(\beta_2+iHe_x))\Big]\Bigg\} \\
-\frac{A_{p6}T_0}{c_0\rho_0} exp\left(-He_x^2\right)\Bigg\{\frac{\sqrt{2}}{\omega\sqrt{\pi}\sigma_x}\Big[\cos(\omega\alpha_1)+\cos(\omega\alpha_2)-2\cos\left(\omega\frac{x}{c_0}\right)\Big] \\
\Big[exp\left(-(\hat{x}+iHe_x)^2\right)+exp\left(-(\hat{x}-iHe_x)^2\right)\Big] \\
+\frac{\sqrt{2}i}{\omega\sqrt{\pi}\sigma_x}\Big[\sin(\omega\alpha_1)+\sin(\omega\alpha_2)-2\sin\left(\omega\frac{x}{c_0}\right)\Big] \\
\Big[exp\left(-(\hat{x}+iHe_x)^2\right)-exp\left(-(\hat{x}-iHe_x)^2\right)\Big] \\
-\frac{c_0}{\omega^2\sqrt{\pi}\sigma_x^2}\Big[\sin(\omega\alpha_1)+\sin(\omega\alpha_2)-2\sin\left(\omega\frac{x}{c_0}\right)\Big] \\
\Big[(\hat{x}+iHe_x)\,exp\left(-(\hat{x}+iHe_x)^2\right)+(\hat{x}-iHe_x)\,exp\left(-(\hat{x}-iHe_x)^2\right)\Big] \\
+\frac{c_0\ i}{\omega^2\sqrt{\pi}\sigma_x^2}\Big[\cos(\omega\alpha_1)+\cos(\omega\alpha_2)-2\cos\left(\omega\frac{x}{c_0}\right)\Big] \\
\Big[(\hat{x}+iHe_x)\,exp\left(-(\hat{x}+iHe_x)^2\right)-(\hat{x}-iHe_x)\,exp\left(-(\hat{x}-iHe_x)^2\right)\Big]\Bigg\}
\end{aligned}
\tag{5.45}
$$

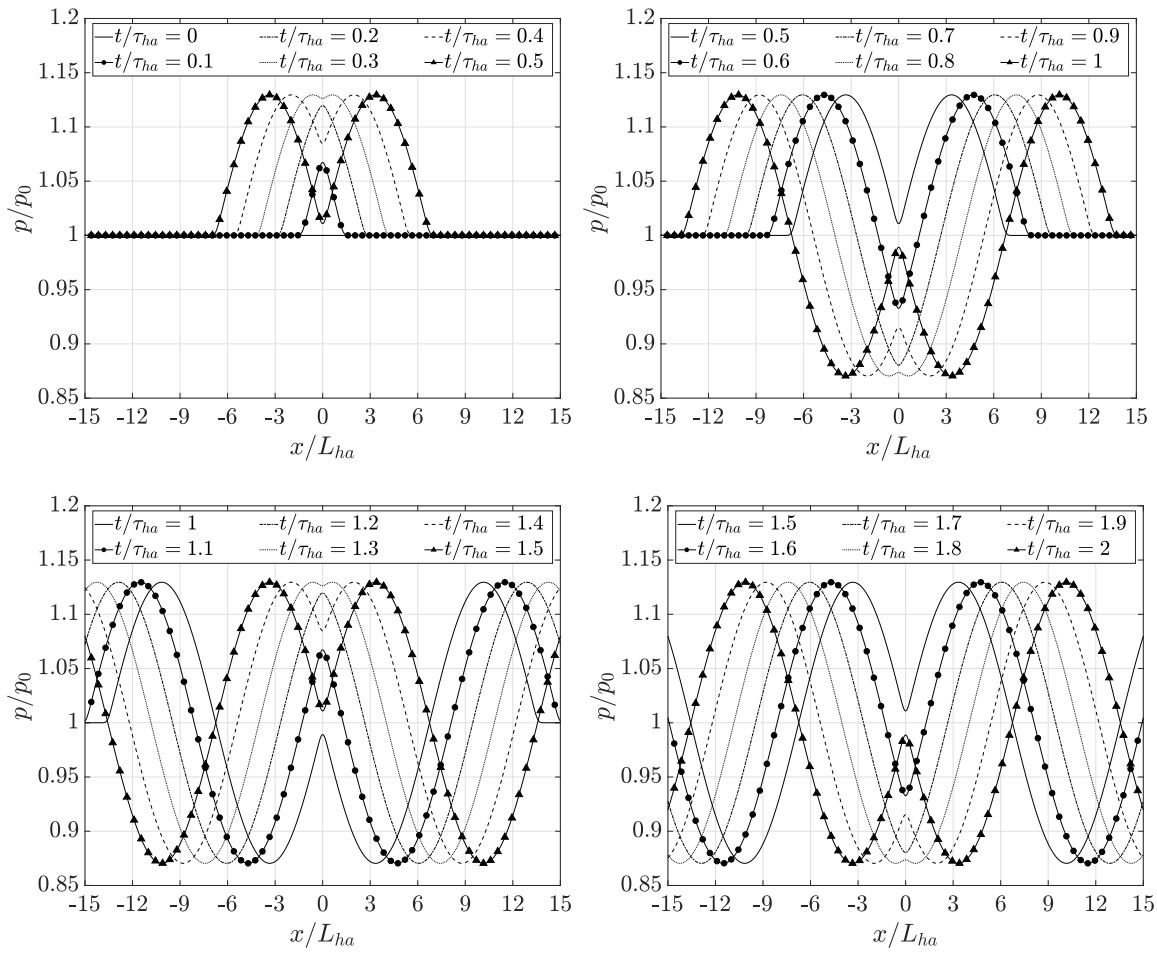

Figure 5.5. Compact case. Pressure response of a perfect gas with properties like that of CO_2 to a heat release source with Gaussian spatial distribution and sinusoidal temporal profile. $He = 0.0734$, $q_{ha,s} = 2.5 \cdot 10^{12}$ W/m^3, $E_{ha}/(H_{ha}W_{ha}) = 1000$ J/m^2, $L_{ha} = 100$ μm and $f = 2.5 \cdot 10^5$ Hz.

5.2.1 Acoustically Compact vs Noncompact Regime

From the examination of the solutions of pressure, velocity, density and temperature from Eqs. (5.34, 5.40, 5.42, 5.44) the limits for the main flow field variables as presented in Table 5.2 are extracted. It should be noted that the results in Table 5.2

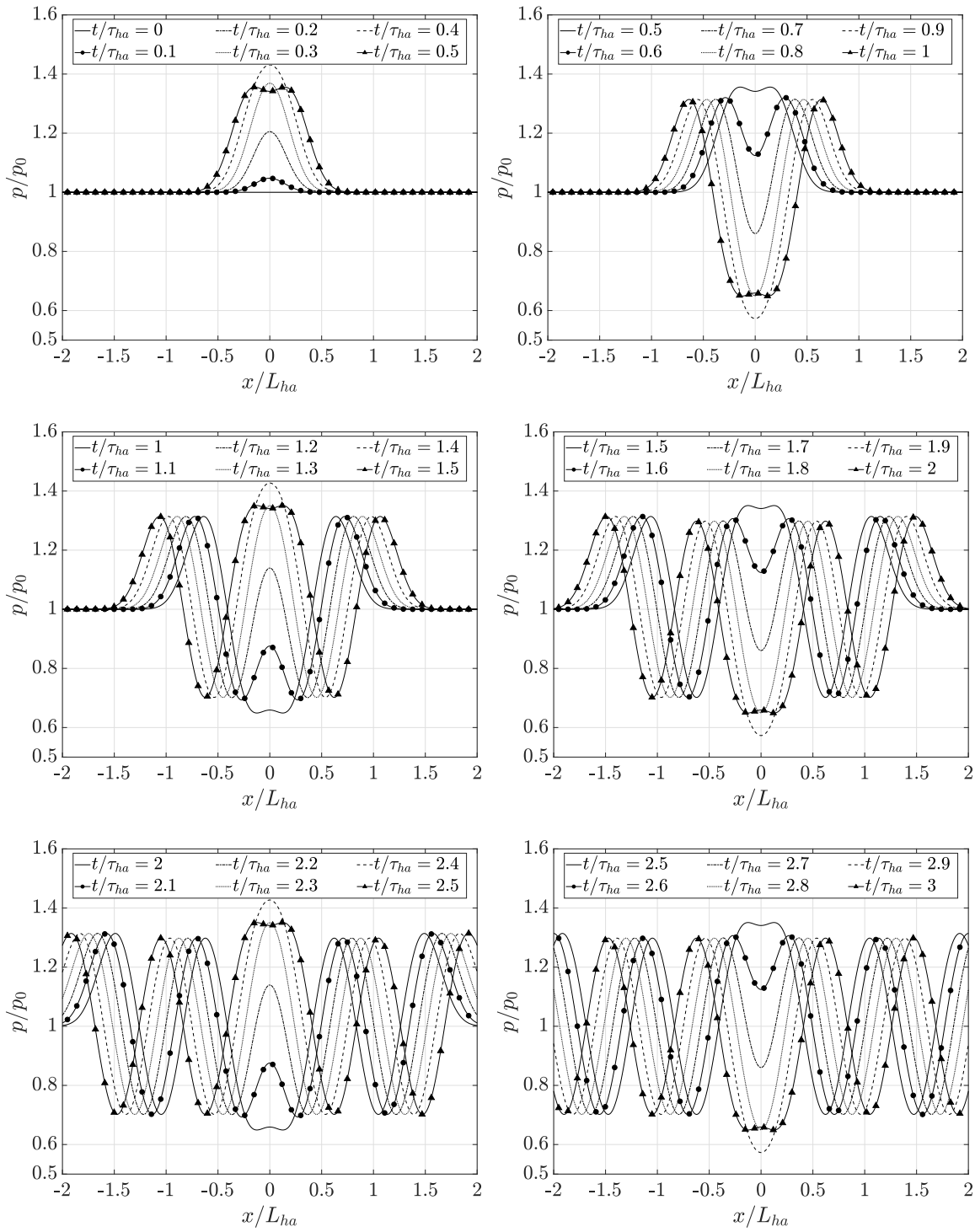

Figure 5.6. Noncompact case. Pressure response of a perfect gas with properties like that of CO_2 to a heat release source with Gaussian spatial distribution and sinusoidal temporal profile. $He = 1.174$, $q_{ha,s} = 2.5 \cdot 10^{12}$ W/m^3, $E_{ha}/(H_{ha}W_{ha}) = 1000$ J/m^2, $L_{ha} = 400$ μm and $f = 10^6$ Hz.

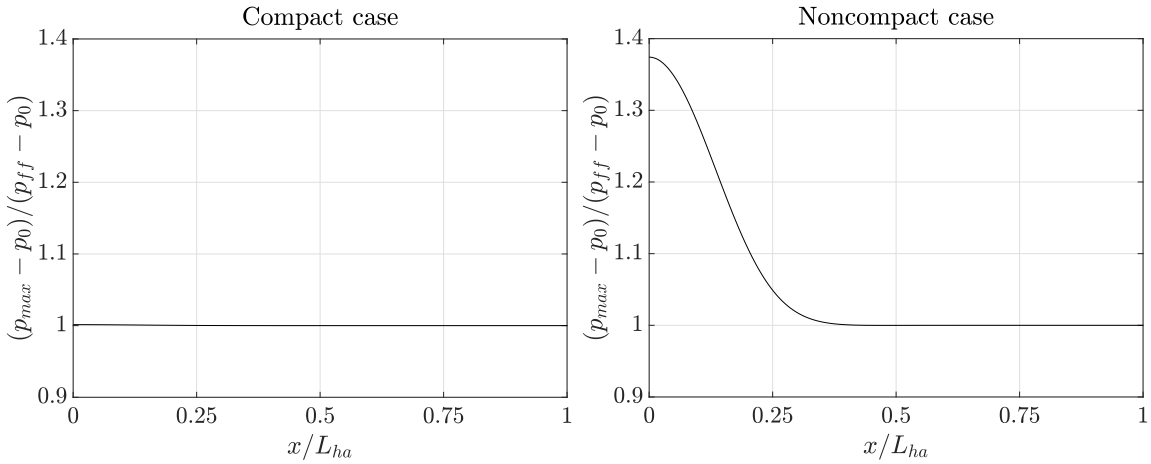

Figure 5.7. Evolution of pressure amplitude over the distance for the response of a perfect gas with properties like that of CO_2 to a heat release source with Gaussian spatial distribution and sinusoidal temporal profile. Compact case (L): $He = 0.0734$, $q_{ha,s} = 2.5 \cdot 10^{12}$ W/m^3, $L_{ha} = 100$ μm and $f = 2.5 \cdot 10^5$ Hz; Noncompact case (R): $He = 1.174$, $q_{ha,s} = 2.5 \cdot 10^{12}$ W/m^3, $L_{ha} = 400$ μm and $f = 10^6$ Hz. $E_{ha}/(H_{ha}W_{ha}) =$ 1000 J/m^2 for both cases.

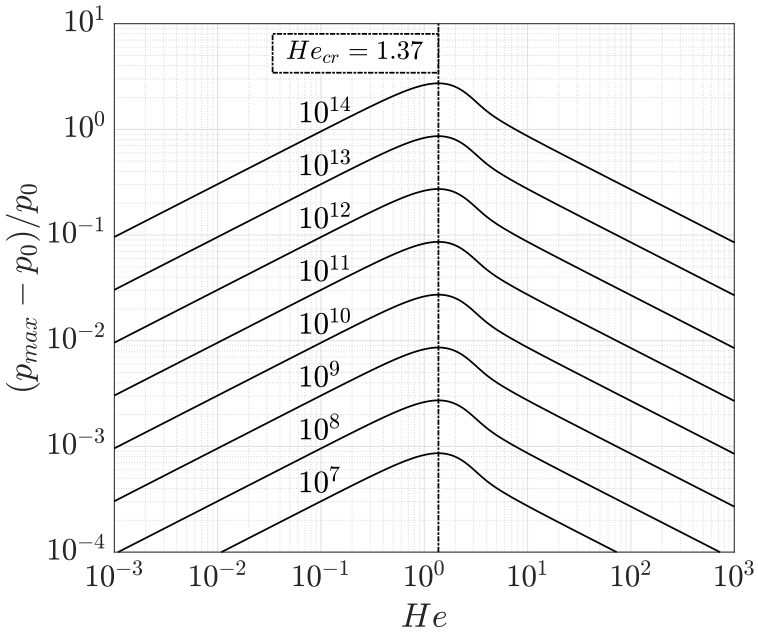

Figure 5.8. Evolution of the maximum pressure amplitude with respect to the Helmholtz number for the response of a perfect gas with properties like that of CO_2 to a heat release source with Gaussian spatial distribution and sinusoidal temporal profile. $E_{ha}/(H_{ha}W_{ha}) = 1000$ J/m^2.

Table 5.2. Limiting expressions for the flow field response to a heat source with Gaussian spatial distribution and sinusoidal temporal profile. The subscript "ff" refers to far field values.

Variable	Location	Formula
$p_{max}\Big\vert_{He_x \leq 4}$	$x = 0$	$p_0 + \frac{(\gamma-1)E_{ha}\omega}{8c_0 H_{ha} W_{ha}} e^{-He_x^2}\left[\sin\left(\omega t_{m_p}\right) - \cos\left(\omega t_{m_p}\right) erfi\left(He_x\right)\right]$
		where $t_{m_p} = \frac{1}{\omega}\tan^{-1}\left(\frac{1}{-erfi(He_x)}\right)$
$p_{max}\Big\vert_{He_x > 4}$	$x = 0$	$p_0 + \frac{(\gamma-1)E_{ha}\omega}{4\sqrt{\pi}c_0 H_{ha} W_{ha}} D_+(He_x)$
$p_{ff}\Big\vert_{He_x < \frac{L_{ha}}{\sqrt{2}\sigma_x}}$	$\vert x\vert > L_{ff}$	$p_0 + \vert 2C_1 \sin^2\left(2\pi He\right) - 2C_2\cos^2\left(2\pi He\right) + C_3 \sin\left(4\pi He\right)\vert$
$u_{ff}\Big\vert_{He_x < \frac{L_{ha}}{\sqrt{2}\sigma_x}}$	$\vert x\vert > L_{ff}$	$\frac{1}{\rho_0 c_0}\vert 2C_1 \sin^2\left(2\pi He\right) - 2C_2\cos^2\left(2\pi He\right) + C_3 \sin\left(4\pi He\right)\vert$
$\rho_{min}\Big\vert_{He_x \leq 4}$	$x = 0$	$\rho_0 + \frac{(\gamma-1)E_{ha}\omega}{8c_0^3 L_{ha} H_{ha} W_{ha}} e^{-He_x^2}\left[\sin\left(\omega t_{m_\rho}\right) - \cos\left(\omega t_{m_\rho}\right) erfi\left(He_x\right)\right]$
		$+\frac{(\gamma-1)E_{ha}}{4\sqrt{2\pi}c_0^2 L_{ha} H_{ha} W_{ha}\sigma_x}\left[\cos\left(\omega t_{m_\rho}\right) - 1\right]$
		where $t_{m_\rho} = \frac{1}{\omega}\left[\pi + \tan^{-1}\left(\frac{e^{-He_x^2}}{\frac{1}{\sqrt{\pi}He_x} - erfi(He_x)e^{-He_x^2}}\right)\right]$
$\rho_{min}\Big\vert_{He_x > 4}$	$x = 0$	$\rho_0 - \frac{(\gamma-1)E_{ha}\omega}{4\sqrt{\pi}c_0^3 H_{ha} W_{ha}} D_+(He_x)$
$T_{max}\Big\vert_{He_x \leq 4}$	$x = 0$	$T_0 + \frac{(\gamma-1)^2 E_{ha} T_0 \omega}{8c_0^3 \rho_0 L_{ha} H_{ha} W_{ha}} e^{-He_x^2}\left[\sin\left(\omega t_{m_T}\right) - \cos\left(\omega t_{m_T}\right) erfi\left(He_x\right)\right]$
		$-\frac{(\gamma-1)E_{ha}T_0}{4\sqrt{2\pi}c_0^2 \rho_0 L_{ha} H_{ha} W_{ha}\sigma_x}\left[\cos\left(\omega t_{m_T}\right) - 1\right]$
		$t_{m_T} = \frac{1}{\omega}\tan^{-1}\left(\frac{(\gamma-1)e^{-He_x^2}}{-\frac{1}{\sqrt{\pi}He_x} - (\gamma-1)erfi(He_x)e^{-He_x^2}}\right)$
$T_{max}\Big\vert_{He_x > 4}$	$x = 0$	$T_0 + \frac{(\gamma-1)E_{ha}T_0\omega}{4\sqrt{\pi}c_0^3 \rho_0 H_{ha} W_{ha}}\left[\left(\gamma - 1\right) D_+(He_x) + \frac{1}{He_x}\right]$

are reported as the steady state, which happens at least at $t > 2\omega\tau_{ac}^2$. It is noted that in Table 5.2, $erfi(x)$ is the imaginary error function, which is given by

$$erfi(x) = -ierf(ix) = \frac{2}{\sqrt{\pi}} \int_0^x e^{t^2} dt \tag{5.46}$$

and $D_+(x)$ is the Dawson function, which reads as

$$D_+(x) = e^{-x^2} \int_0^x e^{t^2} dt \tag{5.47}$$

The Dawson function and the imaginary error function can be related as $erfi(x) = \frac{2}{\sqrt{\pi}} e^{x^2} D_+(x)$. The constants C_1, C_2, and C_3 of Table 5.2 are defined as

$$\begin{cases} C_1 = A_{p6} \left[\cos(2\pi He)\, erf\left(\frac{L_{ha}}{\sqrt{2}\sigma_x}\right) - e^{-He_x^2} \Re\left(erf\left(\frac{L_{ha}}{\sqrt{2}\sigma_x} + iHe_x\right)\right)\right] \\ C_2 = A_{p6} e^{-He_x^2} \\ C_3 = -A_{p6} \left[\sin(2\pi He)\, erf\left(\frac{L_{ha}}{\sqrt{2}\sigma_x}\right) - e^{-He_x^2} \Im\left(erf\left(\frac{L_{ha}}{\sqrt{2}\sigma_x} + iHe_x\right)\right)\right] \end{cases} \tag{5.48}$$

The critical Helmholtz number, He_{cr} has been computed from the maximum pressure expression from Table 5.2 for $He_x \leq 4$. In this numerical computation, the maximum of said expression while maintaining constant E_{ha}, H_{ha}, W_{ha} and $q_{ha,s}$, which leads to $He_{cr} = 1.37$.

5.3 Parametric Study

A parametric study with quiescent perfect gas with properties like that of CO_2 has been conducted to assess the trends of the fluid response to the heat release profile with Gaussian spatial distribution and sinusoidal temporal profile. Table 5.3 summarizes the mean flow conditions. The heat release band size L_{ha} varies from 10 to 10^5 μm, and the heat release oscillation frequency f ranges from 10^3 to 10^6 Hz.

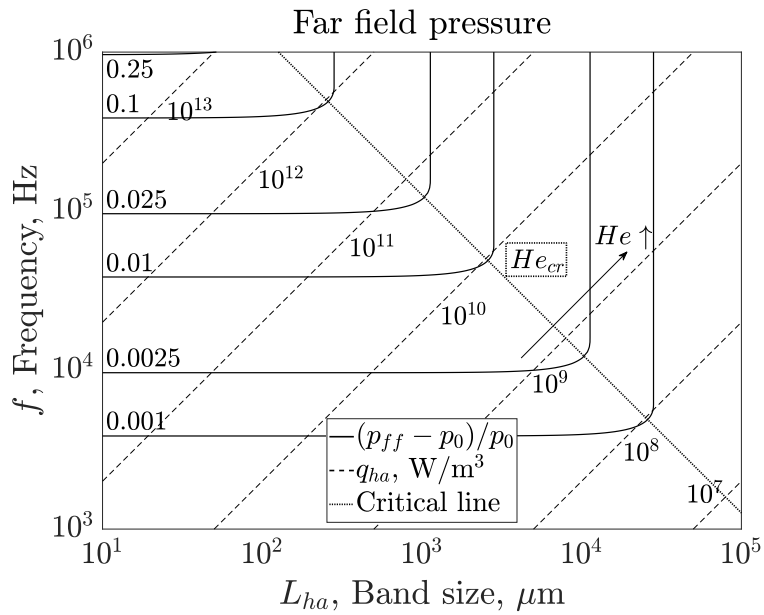

Figure 5.9. Map of the far field pressure amplitude of the response of a perfect gas with properties like that of CO_2 to a heat release source with flat spatial distribution and sinusoidal temporal profile ($He_{cr} = 0.371$). Constant energy $E_{ha}/(H_{ha}W_{ha}) = 500$ J/m^2.

The energy level, mean flow conditions, and range of length and time scales of the heat source have been sized to be representative of unsteady heat release events in a high pressure rocket engine.

As discussed in Section 3.4, the parametric study covers a wide range of length and time scales, but the applicability of the analytical model is limited to low and moderate heat release rates. For large heat release values the assumptions of the analytical model deviate from the actual conditions due to the presence of nonlinear effects such as temperature dependence of the local speed of sound, wave front steepening, formation of weak shocks, and neglecting loss mechanisms such as viscosity and heat conduction.

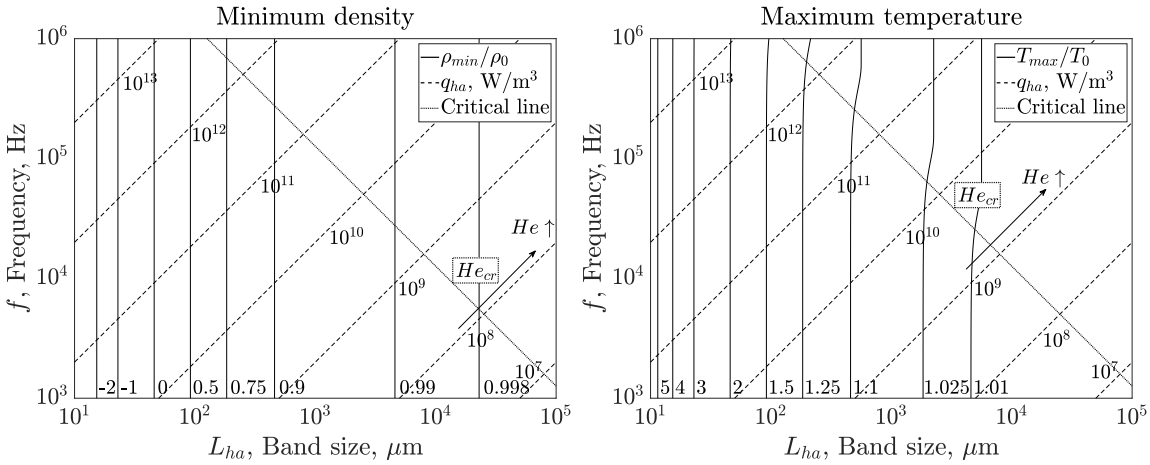

Figure 5.10. Map of the minimum density (L) and maximum temperature (R) of the response of a perfect gas with properties like that of CO_2 to a heat release source with flat spatial distribution and sinusoidal temporal profile. Constant energy $E_{ha}/(H_{ha}W_{ha}) = 500$ J/m^2.

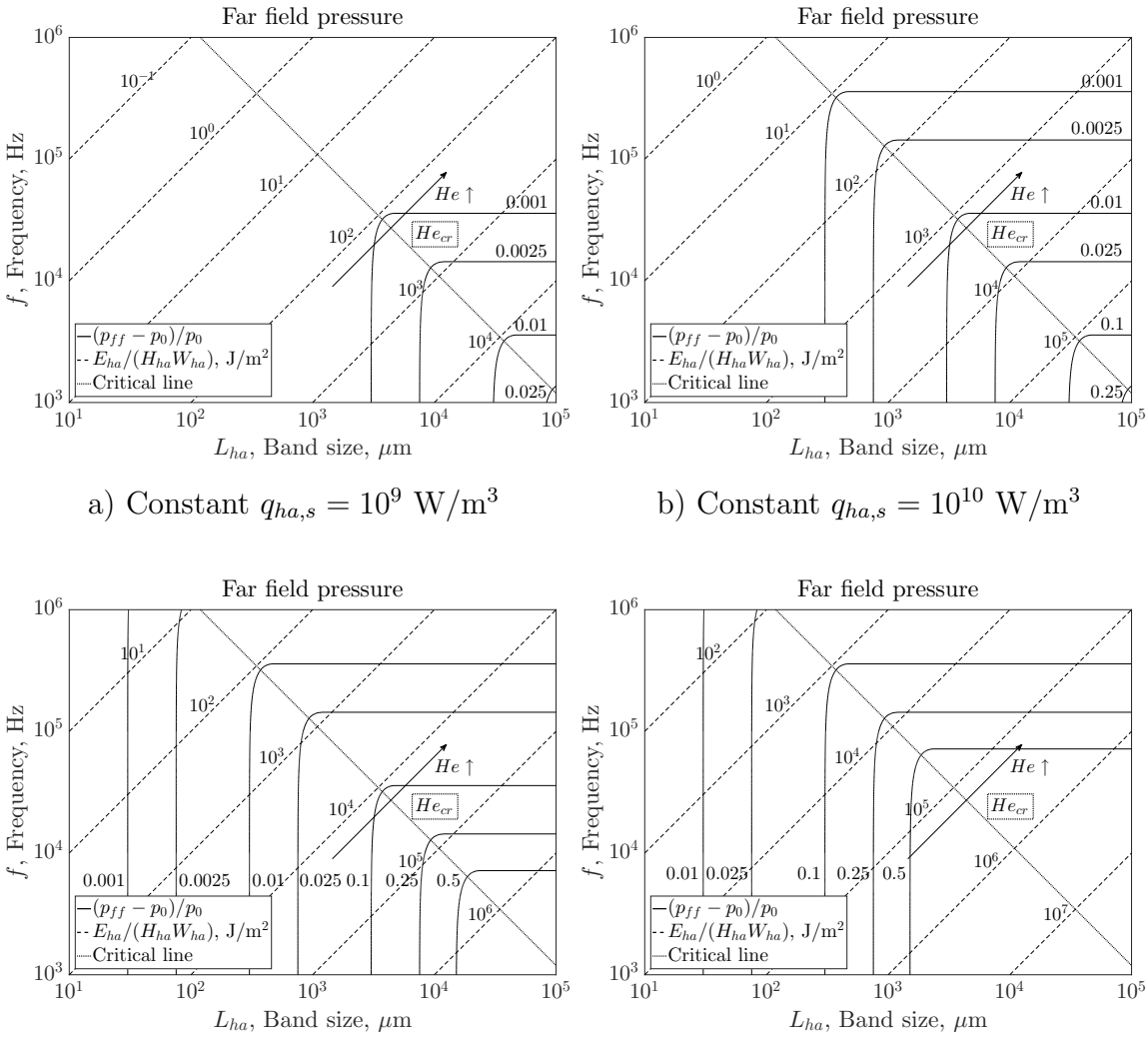

a) Constant $q_{ha,s} = 10^9$ W/m^3

b) Constant $q_{ha,s} = 10^{10}$ W/m^3

c) Constant $q_{ha,s} = 10^{11}$ W/m^3

d) Constant $q_{ha,s} = 10^{12}$ W/m^3

Figure 5.11. Map of the far field pressure amplitude of the response of a perfect gas with properties like that of CO_2 to a heat release source with flat spatial distribution and sinusoidal temporal profile, for constant values of heat release intensity $q_{ha,s}$ ($He_{cr} = 0.371$). Note that in this case the energy level $E_{ha}/(H_{ha}W_{ha})$ is not constant across the map of L_{ha} and f.

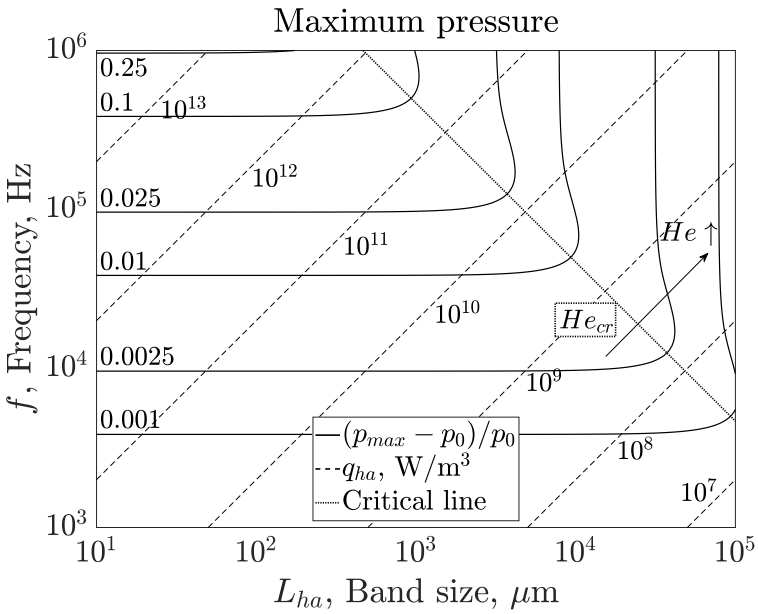

Figure 5.12. Map of the maximum pressure amplitude of the response of a perfect gas with properties like that of CO_2 to a heat release source with Gaussian spatial distribution and sinusoidal temporal profile ($He_{cr} = 1.37$). Constant energy $E_{ha}/(H_{ha}W_{ha}) = 500$ J/m^2.

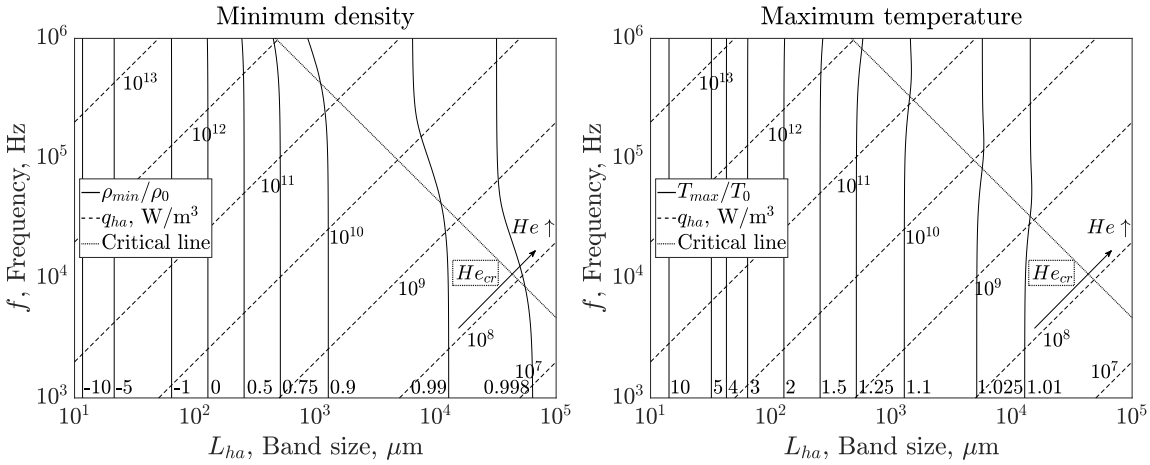

Figure 5.13. Map of the minimum density (L) and maximum temperature (R) of the response of a perfect gas with properties like that of CO_2 to a heat release source with Gaussian spatial distribution and sinusoidal temporal profile. Constant energy $E_{ha}/(H_{ha}W_{ha}) = 500$ J/m^2.

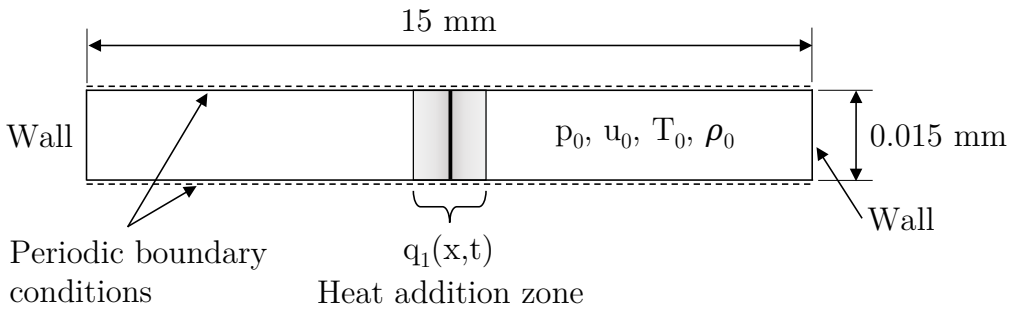

Figure 5.14. Schematic of the computational domain used in the numerical simulations.

5.4 Comparison of Analytical and Numerical Results

5.4.1 Simulation Setup

The case study consists of an uniform quiescent fluid that responds to two unsteady heat release source profiles; one with flat spatial distribution and sinusoidal temporal profile, and the other with Gaussian spatial distribution and sinusoidal temporal distribution, respectively. The dimensions of the domain are set such that the simulation concludes before the induced pressure waves reach the vertical boundaries. The influence of the boundary conditions in the solution are limited by this condition and acoustic reflections are eliminated. The computational domain, which is the same as the one presented in Chapter 3. It consists of a two-dimensional cavity of 15 mm $\times$0.015 mm. Periodic boundary conditions are set at the bottom and top boundaries to keep a one-dimensional solution. Both left and right boundaries are treated as inviscid, adiabatic walls. An external source in the energy equation is used to model the heat release, which is located in the center of the domain. In this case, the heat source does not generate a single pulse but a continuous sinusoidal signal. The total number of cells is 100,0000, and the mesh is divided in 100 partitions. The structured grid is uniform with a cell size from 1.5 μm in the x and y directions across the entire domain. The time step is limited to 2 ns and the simulations capture 12.5 μs of physical time to be able to properly capture the transient behavior.

Table 5.3. Perfect gas mean flow properties like that of CO_2 used for all the analytical and numerical simulations of Chapter 5.

p_0 (MPa)	T_0 (K)	u_0 (m/s)	ρ_0 (kg/m^3)	c_0 (m/s)	γ_0
1.0	500.0	0.0	10.59	340.72	1.2253

The study has been conducted using perfect gas with properties like that of CO_2 as the working fluid with the conditions summarized in Table 5.3. A pressure of 1 MPa and a temperature of 500 K are chosen as the initial conditions, which are representative of the interaction between hot and cold gases in the shear layer region of a non-premixed, shear-coaxial injector used in rocket engines. All the highly-resolved DES simulations have been performed using the in-house Navier-Stokes solver GEMS, which has been presented in Section 3.6.1.

In order to study cases with similar length and time scales as in Chapter 3, the same computational domain has been used for convenience. Thus, the frequencies of the heat source are very high, on the order of $10^5 - 10^6$ Hz, compared to normal liquid rocket engines which feature frequencies of order $10^3 - 10^4$ Hz. Heat sources with very high frequencies, at the megahertz range, may trigger nonlinear gas dynamics effects such as quick steepening of the wave fronts and formation of shocks [89]. Section 5.4.2 reveals the presence of these nonlinear effects in the comparison of the analytical solutions against the highly-resolved numerical simulations.

5.4.2 Results Discussion

The comparison of the analytical and numerical solutions of the fluid response to a heat source with flat spatial profile and sinusoidal temporal distribution are depicted in Figs. 5.15-5.18. Flow field results at two points of interests are shown, $x = 0$ which represents the central location of the heat source and $x = L_{ha}$ which is outside the area of application of heat addition, respectively. For this heat source profile, results of the noncompact regime are presented for two heat release intensities, q_{ha}, one representing a moderate level of heat release ($q_{ha} = 1 \cdot 10^{11}$ W/m^3) and the other being a large level of heat release rate (i.e. $q_{ha} = 2.5 \cdot 10^{12}$ W/m^3). The latter heat release intensity is a representative of rocket combustor. For moderate levels of heat release, the analytical and high-resolved numerical solutions show a good agreement regardless of the point selected. However, for large heat release values the

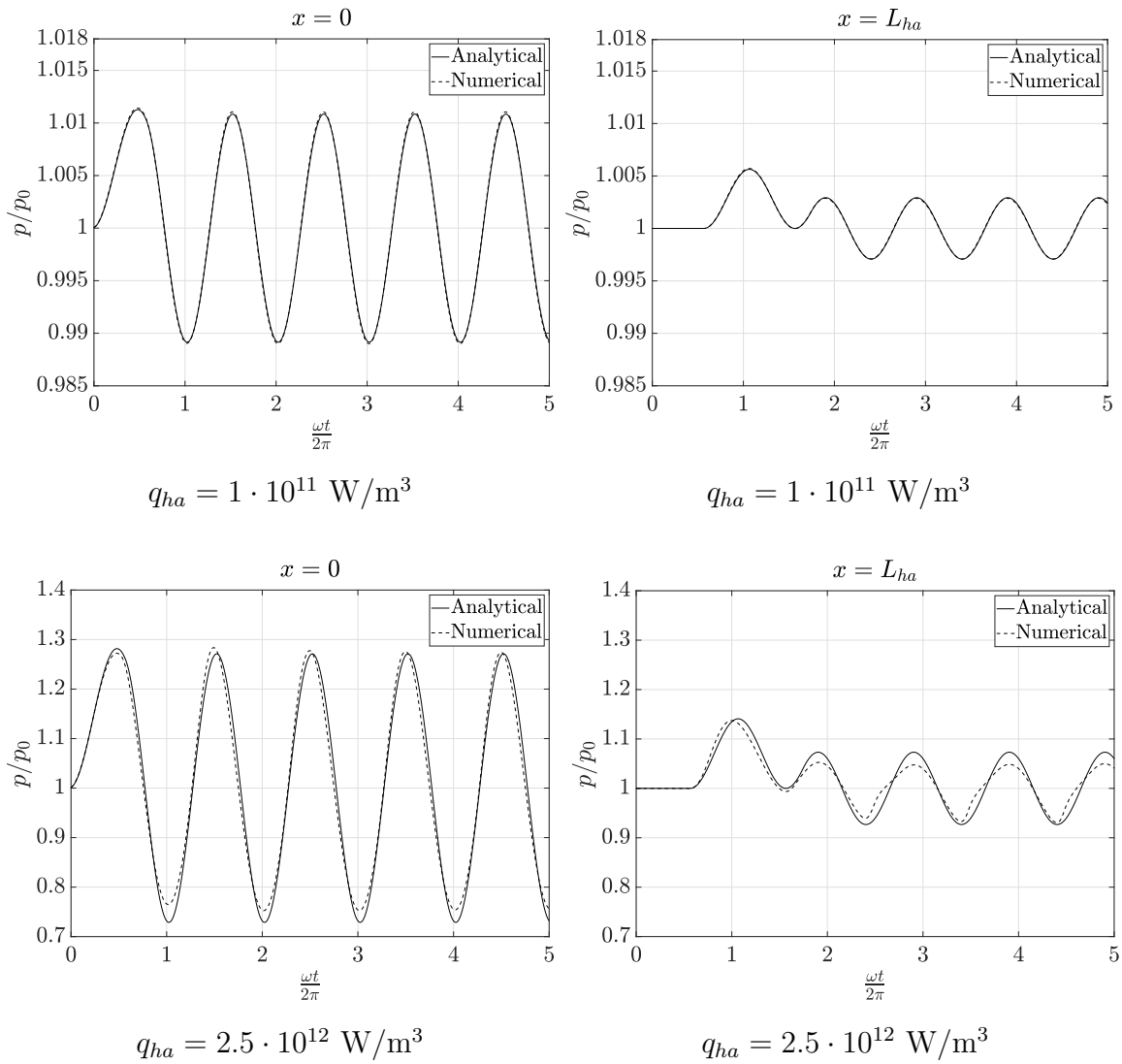

Figure 5.15. Noncompact case, $He = 1.174$. Pressure response of a perfect gas with properties like that of CO_2 to a heat release source with flat spatial distribution and sinusoidal temporal profile. Heat release parameters: $L_{ha} = 400$ μm and $f = 10^6$ Hz.

numerical solution diverges from the analytical model as the nonlinear effects start to become important. The assumption of constant speed of sound, which relies on a constant mean flow temperature, quickly breaks down for large values of heat release as the local temperature deviates from the mean. Since the velocity, density and temperature are computed from the pressure solution, any deviation from the latter will drag the error for the former solutions.

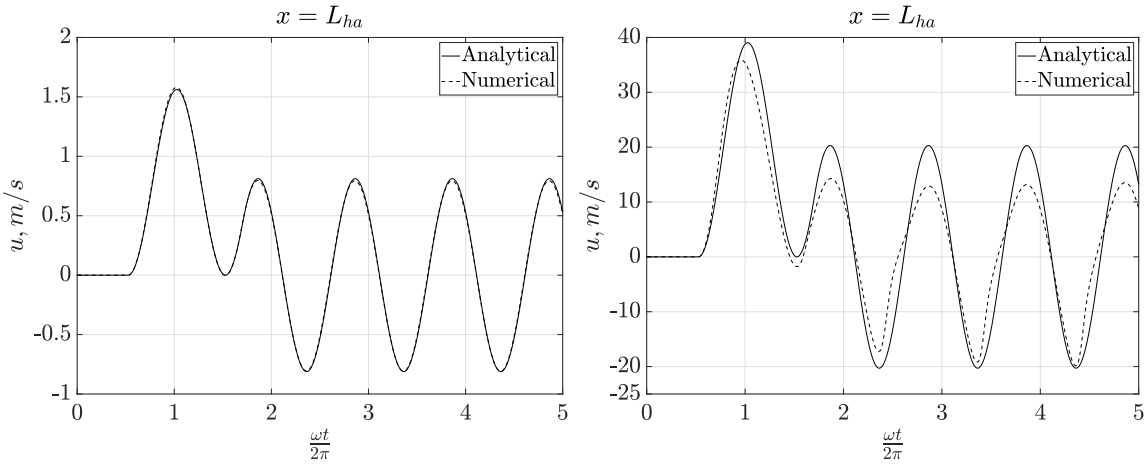

$q_{ha} = 1 \cdot 10^{11}$ W/m^3 $\qquad$ $q_{ha} = 2.5 \cdot 10^{12}$ W/m^3

Figure 5.16. Noncompact case, $He = 1.174$. Velocity response of a perfect gas with properties like that of CO_2 to a heat release source with flat spatial distribution and sinusoidal temporal profile. Heat release parameters: $L_{ha} = 400$ μm and $f = 10^6$ Hz.

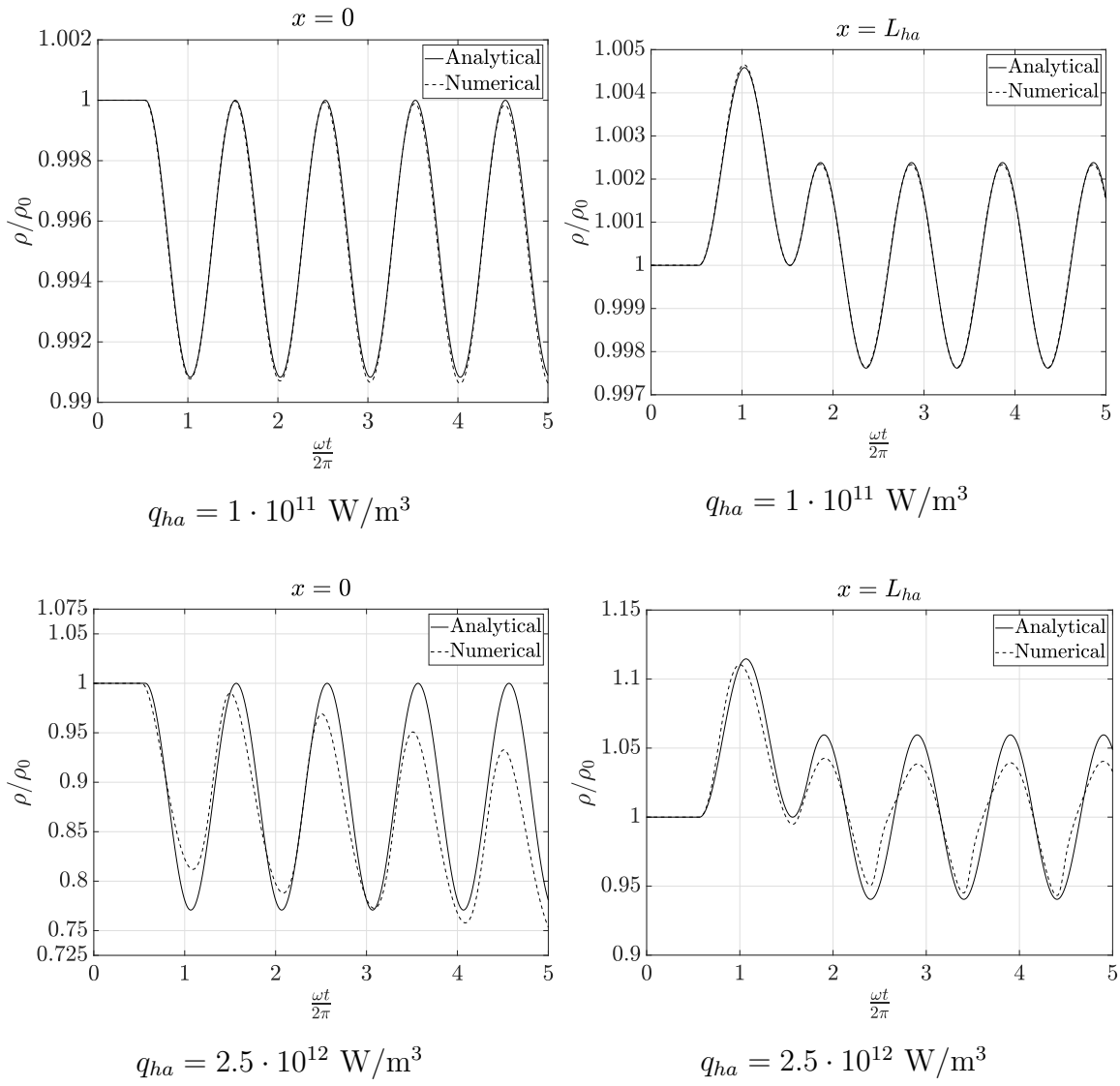

Figure 5.17. Noncompact case, $He = 1.174$. Density response of a perfect gas with properties like that of CO_2 to a heat release source with flat spatial distribution and sinusoidal temporal profile. Heat release parameters: $L_{ha} = 400$ μm and $f = 10^6$ Hz.

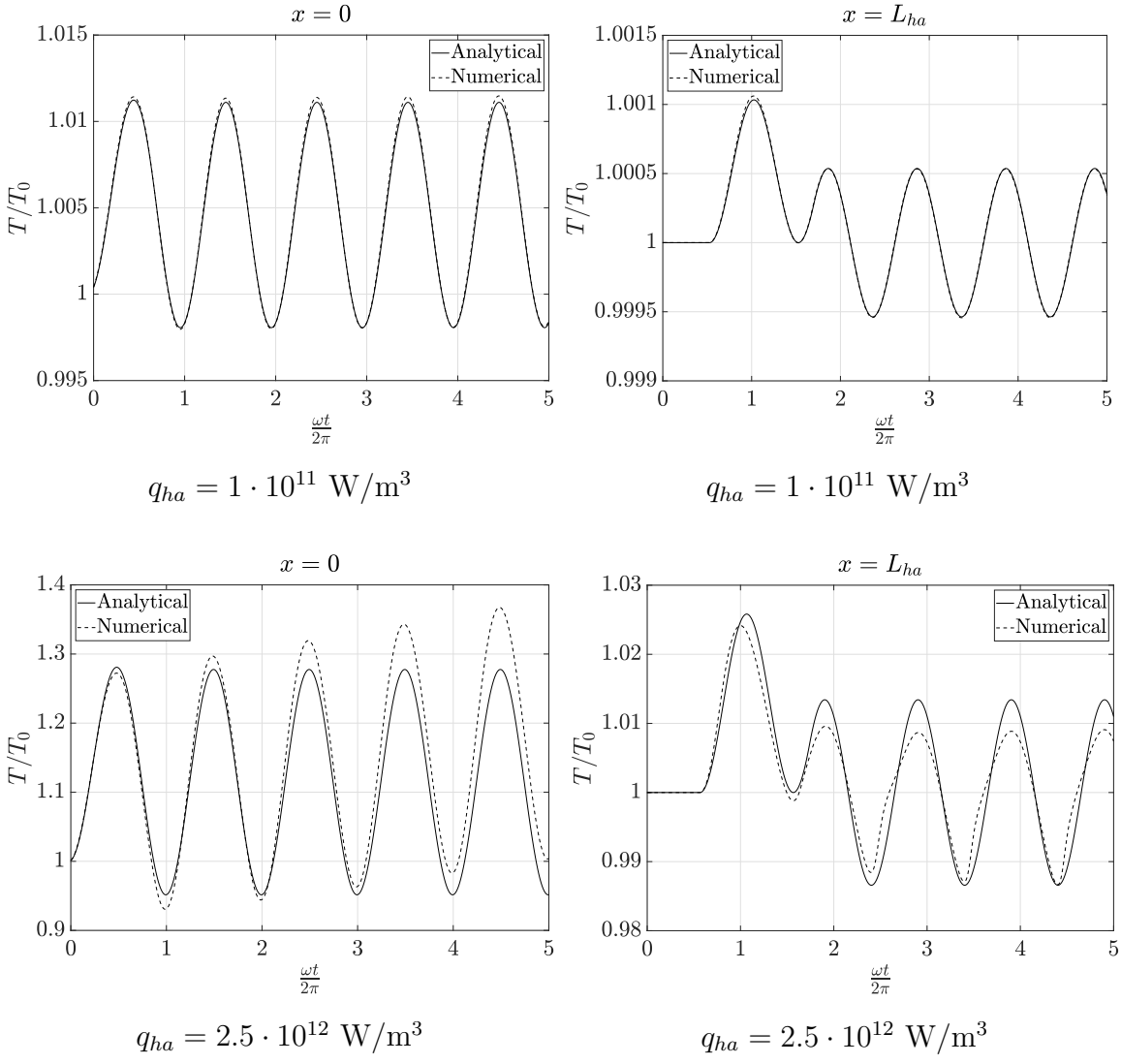

Figure 5.18. Noncompact case, $He = 1.174$. Temperature response of a perfect gas with properties like that of CO_2 to a heat release source with flat spatial distribution and sinusoidal temporal profile. Heat release parameters: $L_{ha} = 400$ μm and $f = 10^6$ Hz.

The comparison of the analytical and numerical solutions of the fluid response to a heat source with Gaussian spatial profile and sinusoidal temporal distribution are depicted in Figs. 5.19-5.22. The flow field results are reported for a compact case at two locations inside and outside the heat addition zone, as well as for two levels of heat release intensity. The two heat release intensities q_{ha} represent a moderate level of heat release ($q_{ha} = 1 \cdot 10^{11}$ W/m^3) and a larger level of heat release ($q_{ha} = 2.5 \cdot 10^{12}$ W/m^3). It is noted that the variation from compact to noncompact can be achieved by varying the value of the Helmholtz number, He. For moderate levels of heat release, the analytical and high-resolved numerical solutions show a good agreement regardless of the point selected. Nonetheless, for large values of heat release, both results diverge considerably regardless of the point selected as the analytical model is unable to capture the nonlinear effects. In addition, as it occurred in Chapter 3, for the compact cases the amplitude of the pressure fluctuations is constant over the distance. In contrast, for the noncompact regime the pressure fluctuations are larger within the heat source area of application and then, these decay to a far field value once the pressure waves travel outside the heat source.

The discrepancy of the analytical model with the numerical solutions for large values of heat release is mostly caused by the deviation from the model assumptions. For large values of heat release, the local temperature increases significantly thereby deviating the local speed of sound from the mean flow value. In addition, the large pressure amplitudes for the extreme heat release intensities provokes the steepening of the wave front. As shown in Fig. 5.23, a harmonic pressure fluctuation tends to a sawtooth profile over time due to nonlinear gas dynamics effects. These nonlinear phenomena are the steepening of the wave front and the eventual formation of weak shocks. A more detailed discussion regarding the nonlinear effects is provided in Section 6.6 from Chapter 6.

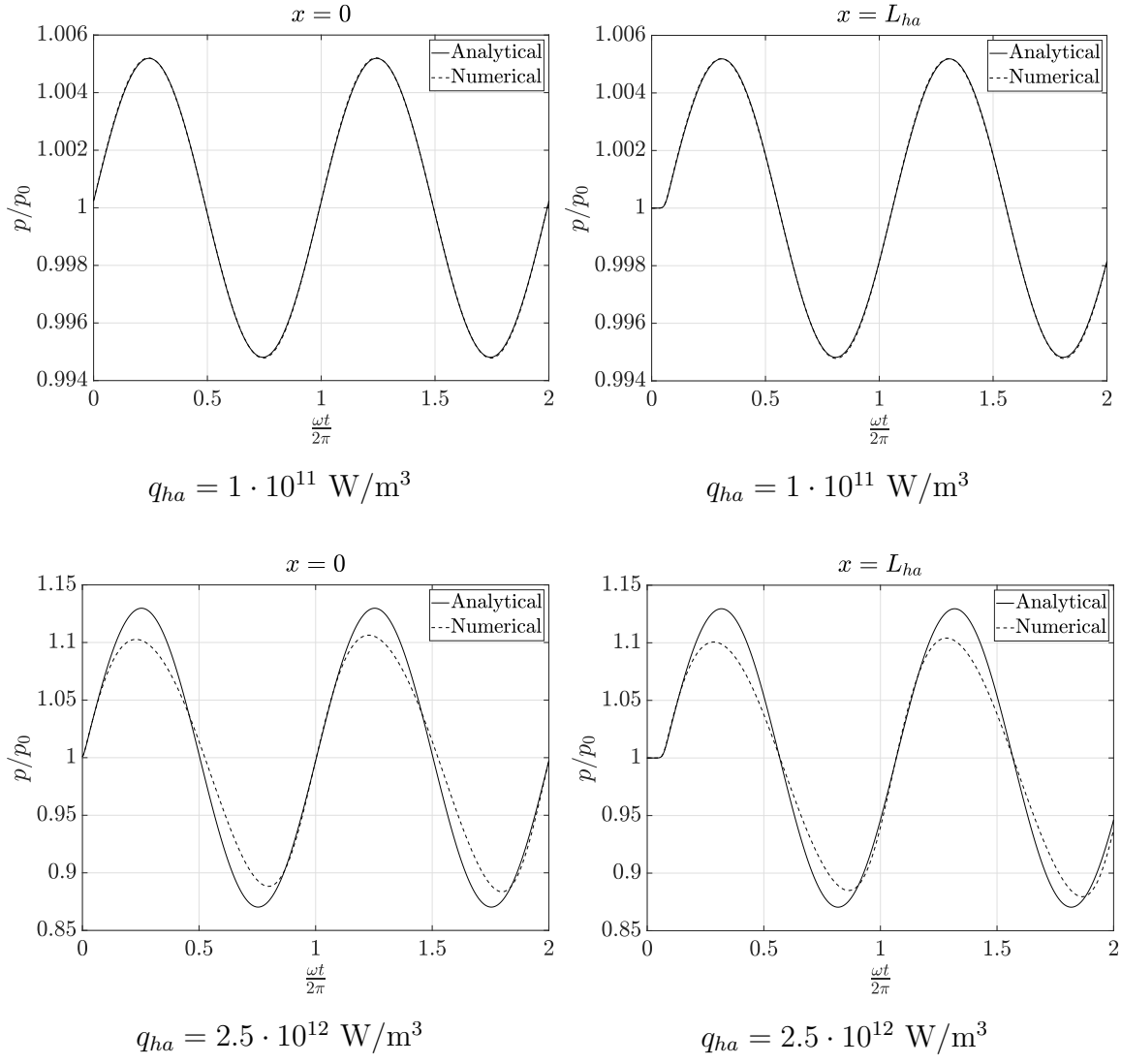

Figure 5.19. Compact case, $He = 0.0734$. Pressure response of a perfect gas with properties like that of CO_2 to a heat release source with Gaussian spatial distribution and sinusoidal temporal profile. Heat release parameters: $L_{ha} = 100$ μm and $f = 2.5 \cdot 10^5$ Hz.

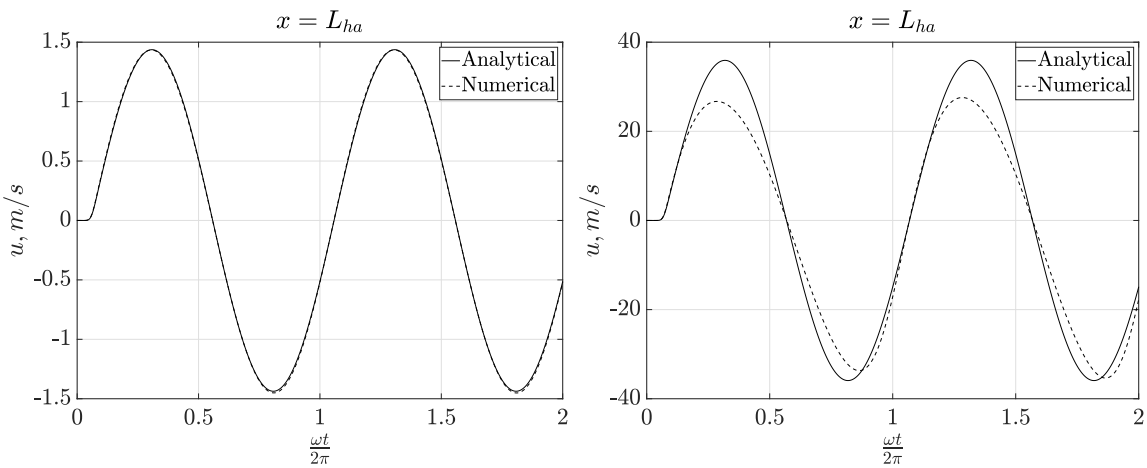

$q_{ha} = 1 \cdot 10^{11}$ W/m^3 $\qquad$ $q_{ha} = 2.5 \cdot 10^{12}$ W/m^3

Figure 5.20. Compact case, $He = 0.0734$. Velocity response of a perfect gas with properties like that of CO_2 to a heat release source with Gaussian spatial distribution and sinusoidal temporal profile. Heat release parameters: $L_{ha} = 100$ μm and $f = 2.5 \cdot 10^5$ Hz.

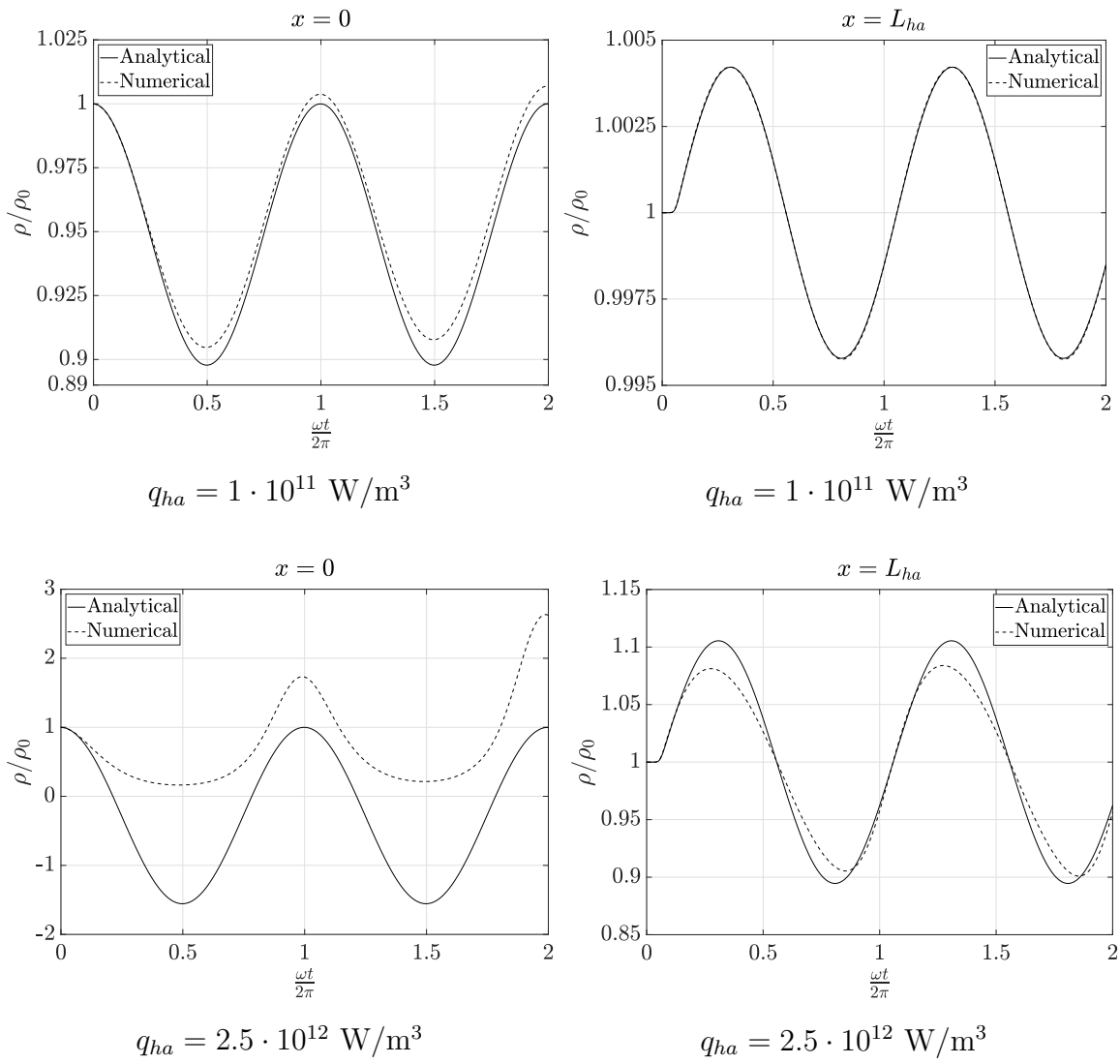

Figure 5.21. Compact case, $He = 0.0734$. Density response of a perfect gas with properties like that of CO_2 to a heat release source with Gaussian spatial distribution and sinusoidal temporal profile. Heat release parameters: $L_{ha} = 100$ μm and $f = 2.5 \cdot 10^5$ Hz.

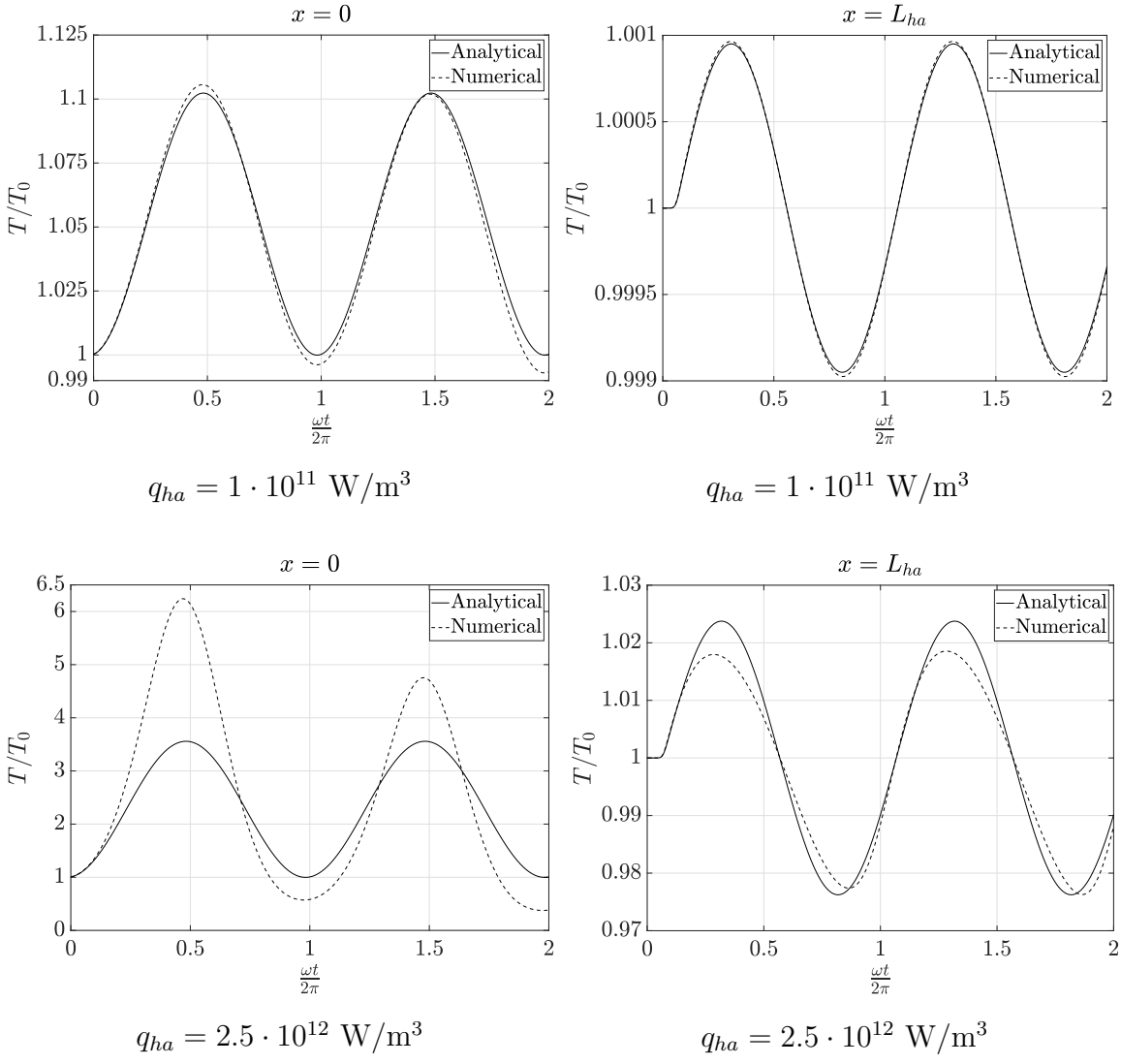

Figure 5.22. Compact case, $He = 0.0734$. Temperature response of a perfect gas with properties like that of CO_2 to a heat release source with Gaussian spatial distribution and sinusoidal temporal profile. Heat release parameters: $L_{ha} = 100$ μm and $f = 2.5 \cdot 10^5$ Hz.

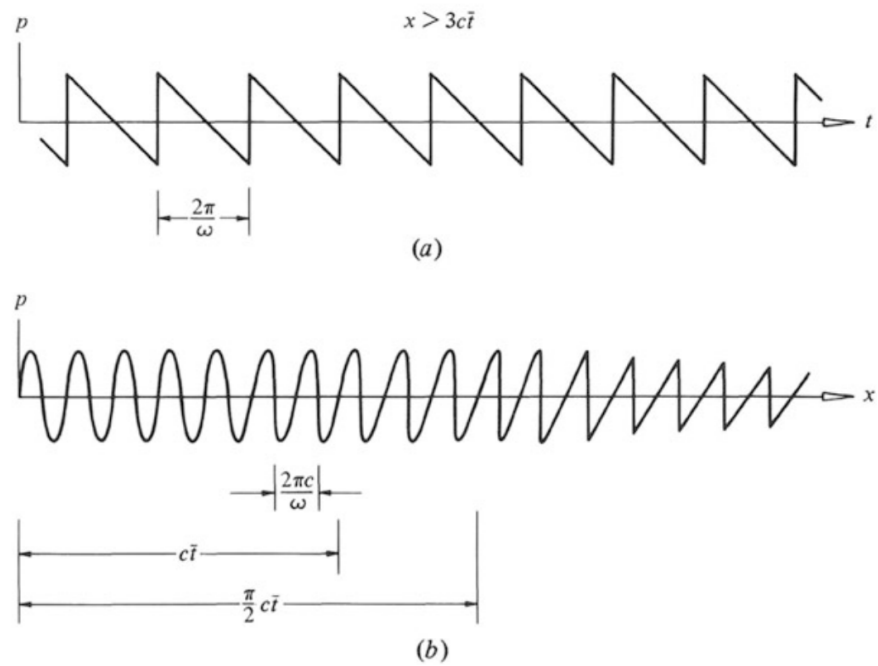

Figure 5.23. a) Sketch of acoustic pressure over time at a sufficiently distant point from an oscillating transducer for the formation of a sawtooth profile; b) sketch of acoustic pressure over the distance for a particular instant of time, depicting the evolution of the pressure from a harmonic signal to a sawtooth profile (Source [90]).

5.5 Summary

The chapter sought to analyze the interaction of the pressure response to a fluctuating heat release source. The coupling of the combustion heat release with the acoustic pressure field in a combustor may lead to combustion instabilities. Heat release sources that fluctuate over time at the frequency of the acoustic modes of the combustor are then a precursor to these phenomena. An opposite viewpoint to the traditional flame transfer models such as Crocco's $n - \tau$ model [25, 26] is proposed in order to study the pressure response to a fluctuating heat release source.

An unconfined one-dimensional domain in a non-reacting fluid has been set as a unit problem to derive analytical models based on the acoustic wave equation. Two different heat release sources, one consisting of a flat spatial distribution and sinusoidal temporal profile and the other a Gaussian spatial distribution and sinusoidal temporal profile have been considered. For both of the profiles, the Helmholtz number, He, emerged as the parameter that drives the pertinent length and time scales, and separates the regimes of pressure response. For a fluctuating heat source, He is specified as the ratio of the acoustic time over the fluctuating period. Acoustically compact and noncompact regimes were also identified in the pressure response as a function of the critical Helmholtz number, He_{cr}. While in the compact regime the amplitude of the pressure fluctuations is constant over the distance, in the noncompact regime the amplitude of the pressure fluctuations is larger within the heat source area of application. Then, for the noncompact regime, the amplitude of the pressure fluctuation decays to a far field pressure value outside the heat source. The two pressure response regimes have been further analyzed by means of a parametric study that varied the parameters so as to be representative of the extreme conditions in a rocket combustor.

Highly-resolved numerical simulations have been used to compare against the analytical solutions to evaluate the accuracy and limitations posed by the adoption of the wave equation. Similarly to the results presented in previous chapters, for

moderate values of heat release rate, the analytical and numerical results agree well. If the flow conditions remain close to the model assumptions, this holds true. However, for large rates of heat release the analytical model is not able to capture the nonlinear physics of the problem such as steepening of the wave front, formation of weak shocks, as well as local variation of the speed of sound.

6. EFFECTS OF UNSTEADY HEAT RELEASE ON A LONGITUDINAL ACOUSTIC MODE

The coupling of unsteady heat release with the acoustic modes of a combustor may generate high amplitude pressure fluctuations that result in combustion instability. Traditionally, the Rayleigh criterion has been used to determine the stability of a combustor by assessing the relative phase of unsteady heat release with respect to acoustic pressure fluctuations. If the unsteady heat release is in phase with the pressure field, the amplitude of the pressure fluctuations will grow over time. To better understand the spatio-temporal effects of heat release on this fundamental phenomenon, a study is made of the interaction of an unsteady heat release pulse with a longitudinal acoustic mode of a one-dimensional duct in a non-reacting gas mixture.

The aim is to evaluate and quantify how pressure fluctuations due to unsteady heat release amplify a longitudinal acoustic mode. The high rates of unsteady heat release characteristic of rocket engines along with the presence of nonlinearities such

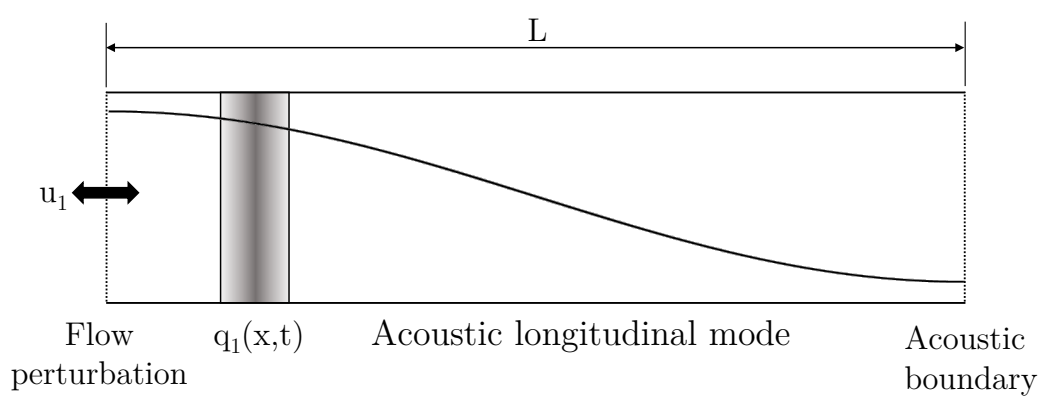

Figure 6.1. One-dimensional duct with a velocity forcing perturbation that excites the system to an acoustic longitudinal mode. An external heat source provokes pressure fluctuations that interact with the acoustic modes of the duct.

as nonlinear acoustics [91], may provoke that the addition of pressure fluctuations due to unsteady heat release to acoustic pressure oscillations differs from a linear superposition. The non-premixed turbulent combustion regime of rocket engines is characterized by high pressure, high degree of unsteadiness, near-stoichiometric combustion, multiple ignition and extinction events, and extremely large heat release rates [78, 92]. Altogether, these characteristics contribute to introduce a stochastic behavior to the system that differs from purely harmonic oscillations. The analytical models are compared against highly-resolved numerical simulations to assess nonlinear effects and limitations of models based on the acoustic wave equation.

As shown in Fig. 6.1, the model of the interaction between an unsteady heat release pulse and a longitudinal acoustic mode is built by sequentially adding unit problems, which combined, result in a simplified model with a closed analytical solution. The first unit problem consists of the pressure response to a moving rigid surface that generates a velocity harmonic fluctuation in a one-dimensional open-ended cavity. This forced velocity perturbation provokes in turn harmonic pressure fluctuations that propagate freely without the presence of an acoustic boundary away from the moving surface. Section 6.2 presents the second unit problem which combines the analytical solution from the velocity harmonic fluctuation with an unsteady heat pulse with Gaussian spatial and temporal distribution (see Section 3.3). This case, which still remains as an open-ended cavity, allows the analysis of how an unsteady heat release pulse superposed with a harmonic pressure fluctuation that propagates as a traveling wave. The choice of an open-ended cavity simplifies the analysis and serves as a stepping stone to the next unit problem which includes pressure reflections provoked by the acoustic boundaries of the duct.

Section 6.3 describes the third unit problem as the establishment of a 1L acoustic longitudinal mode inside a closed duct using the harmonic velocity fluctuations from Section 6.1. Departing from a quiescent fluid, a moving wall on the left end of the duct is used to generate pressure fluctuations at the 1L mode frequency for one cycle after which the wall stops its motion and the 1L mode acoustic pressure field is

established. The fourth unit problem is described in Section 6.4 by combining the analytical solution of the 1L mode acoustic field from Section 6.3 with an unsteady heat release pulse with Gaussian spatial and temporal distribution from Section 3.3. This unit problem includes pressure reflections in the analysis thereby approaching the model one step closer to a real scenario.

The derivation of the present analytical models include the identification of relevant length and time scales that are condensed into the Helmholtz number, He, the phase shift between the longitudinal fluctuating pressure field and the heat source, ϕ_{pq}, and ratio of the fluctuating periods, Θ_{pq}. The study parameters are selected to be representative of the conditions in a rocket combustor. Finally, a comparison of the analytical and numerical simulations is presented in Section 6.5.

6.1 Pressure Solution for a Harmonic Velocity Fluctuation in an Open-ended Cavity

This case consists of a forcing harmonic velocity fluctuation that generates pressure fluctuations in an open-ended one-dimensional cavity. To generate velocity fluctuations, a moving surface on the left end of the cavity vibrates with an angular frequency ω and a velocity amplitude u_f (see Fig. 6.2).

The velocity fluctuation imparted by the moving surface reads as

$$u_s(t) = u_f \sin(\omega t) \tag{6.1}$$

Departing from the homogeneous acoustic wave equation, which is recalled here

$$\frac{\partial^2 p_1}{\partial t^2} = c_0^2 \frac{\partial^2 p_1}{\partial x^2} \tag{6.2}$$

We seek a pressure solution using the principle of separation of variables

$$p_1(x,t) = \eta(t)\psi(x) \tag{6.3}$$

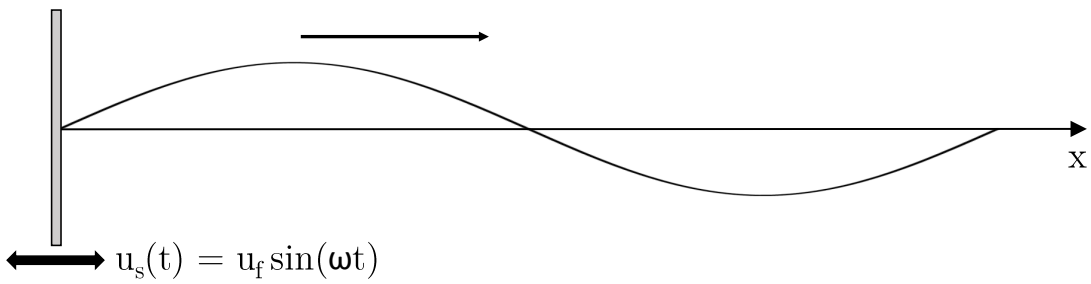

Figure 6.2. Diagram of a moving surface generating harmonic velocity fluctuations.

Differentiating $p_1(x,t)$ following Eq. (6.2) yields to

$$\psi(x)\ddot{\eta}(t) = c_0^2\psi''(x)\eta(t) \tag{6.4}$$

where $\ddot{\eta}(t) = \frac{\partial^2\eta}{\partial t^2}$ and $\psi''(x) = \frac{\partial^2\psi}{\partial x^2}$, respectively. Rearranging Eq. (6.4) results in

$$\frac{\ddot{\eta}(t)}{\eta(t)} = c_0^2\frac{\psi''(x)}{\psi(x)} = -\lambda^2 \tag{6.5}$$

For Eq. (6.5) to have solution, both quotients have to be equal to a constant (being λ in this case). Thus, Eq. (6.5) can be separated into two equations each depending on x and t. The equation for the temporal function $\eta(t)$ is given by

$$\ddot{\eta}(t) + \lambda^2\eta(t) = 0 \tag{6.6}$$

Applying a harmonic solution $\eta(t) = e^{j\omega t}$ in Eq. (6.6), it follows that the constant $\lambda = \omega$. In turn, the equation for the spatial function $\psi(x)$ reads as

$$c_0^2\psi''(x) + \lambda^2\psi(x) = 0 \tag{6.7}$$

Eq. (6.7) has a harmonic solution $\psi(x) = \overline{X}e^{jkx}$, yielding to

$$\psi(x) = \overline{A}e^{jkx} + \overline{B}e^{-jkx} \tag{6.8}$$

where $k = \frac{\omega}{c_0}$. Combining the harmonic temporal and spatial solutions, $\eta(t)$ and $\psi(x)$, respectively, leads to the pressure solution

$$p_1(x,t) = \overline{A}e^{j(\omega t + kx)} + \overline{B}e^{j(\omega t - kx)} \tag{6.9}$$

where $\overline{A}$ corresponds to the complex constant for the left-traveling wave, and $\overline{B}$ to the right-traveling wave. As there are no reflections moving leftwards due to the vibrating surface, the left-traveling wave term is $\overline{A} = 0$ [93], thereby simplifying Eq. (6.9) into

$$p_1(x,t) = \overline{B}e^{j(\omega t - kx)} \tag{6.10}$$

The fluctuating pressure and velocity are related through the linearized momentum equation (Eq. (2.19)) as

$$\frac{\partial u_1}{\partial t} = -\frac{1}{\rho_0}\frac{\partial p_1}{\partial x} = \frac{jk}{\rho_0}\overline{B}e^{j(\omega t - kx)} \tag{6.11}$$

At the vibrating surface, the fluid velocity is equal to the surface velocity with the condition $u_1(x = 0, t) = u_s(t)$, which extends to its temporal derivatives

$$\frac{\partial u_1}{\partial t}(0,t) = \frac{j\omega}{\rho_0 c_0}\overline{B}e^{j\omega t} = \omega u_f \cos(\omega t) \tag{6.12}$$

Rearranging the terms of Eq. (6.12), the complex constant $\overline{B}$ results in

$$\overline{B} = -ju_f\rho_0 c_0 \tag{6.13}$$

Taking the real part of $p_1(x,t)$ from Eq. (6.10), the pressure solution of a moving rigid surface reads as

$$p_h(x,t) = \Re\left(-ju_f\rho_0 c_0 e^{j(\omega t - kx)}\right) \tag{6.14}$$

The real part is equal to

$$\text{For} \quad x > 0 \qquad p_h(x,t) = u_f \rho_0 c_0 \sin\left(\omega\left(t - \frac{x}{c_0}\right)\right) \tag{6.15}$$

The velocity field can be computed using Eq. (2.19), reading as

$$\text{For} \quad x > 0 \qquad u_h(x,t) = u_f \sin\left(\omega\left(t - \frac{x}{c_0}\right)\right) \tag{6.16}$$

6.2 Interaction of a Fluctuating Pressure Field with an Unsteady Heat Release Pulse in an Open-ended Cavity

Since the acoustic wave equation Eq. (2.32) is linear, it admits the use of the superposition principle so that a pressure solution can be derived by superposing multiple particular solutions to the homogeneous solution. This case consists of the superposition between a harmonic fluctuating pressure field and an unsteady heat release pulse. The goal is to assess the effect of an unsteady heat release pulse on the harmonic fluctuating pressure field after one cycle. The one-dimensional domain is constrained by the moving surface on the left end ($x = 0$) but it is open-ended on the right side ($x = \infty$). Since the right end is at $x = \infty$, there are no pressure reflections from the right end. The pressure solution is then composed of the pressure solution for a harmonic velocity fluctuation presented in Section 6.1, and the pressure response to a heat release pulse with Gaussian spatial and temporal distribution as described in Section 3.3.

$$p_1(x,t) = p_h(x,t) + p_q(x,t) \tag{6.17}$$

where $p_h(x,t)$ is the homogeneous solution from Eq. (6.15) and $p_q(x,t)$ is the particular solution corresponding to the pressure pulse from Eq. (3.35). The unsteady heat release pulse is given by the heat source profile $q_1(x,t)$ from Eq. (3.25). The pressure response to the heat source with Gaussian spatial and temporal distribution

Eq. (3.35) is recalled here, displacing the center of the heat source a distance x_f from the origin

$$
\begin{aligned}
&p_q(x,t) = \\
&A_{p,2}\Bigg[\, exp\left(-\left(\frac{\frac{x-x_f}{c_0}-(t-t_c)}{\sqrt{2}\sigma_t\zeta_{xt}}\right)^2\right)\left\{erf\left(\frac{\frac{x-x_f}{c_0}+(\zeta_{xt}^2-1)(t-t_c)}{\tau_{ac}\zeta_{xt}}\right)\right. \\
&\left.-\,erf\left(\frac{\frac{x-x_f}{c_0}-t-(\zeta_{xt}^2-1)t_c}{\tau_{ac}\zeta_{xt}}\right)\right\}+exp\left(-\left(\frac{\frac{x-x_f}{c_0}+(t-t_c)}{\sqrt{2}\sigma_t\zeta_{xt}}\right)^2\right)\cdot \\
&\left\{erf\left(\frac{-\frac{x-x_f}{c_0}+(\zeta_{xt}^2-1)(t-t_c)}{\tau_{ac}\zeta_{xt}}\right)+erf\left(\frac{\frac{x-x_f}{c_0}+t+(\zeta_{xt}^2-1)t_c}{\tau_{ac}\zeta_{xt}}\right)\right\}\Bigg]
\end{aligned}
\tag{6.18}
$$

where x_f represents the center of the "flame", which in this case is the center of the heat source in a non-reacting fluid. The phase shift between the longitudinal fluctuating pressure field $p_h(x,t)$ and the heat source $q_1(x,t)$ is given by

$$\phi_{pq} = \angle p_h q_1 \tag{6.19}$$

This phase shift can be set as an independent parameter of the study. The time parameters of the heat source can be a made function of the phase between the pressure and heat release as follows

$$t_{hab} = \frac{x_f}{c_0} + \frac{1}{\omega}\left(\frac{\pi}{2} + \phi_{pq} + 2k_{c_1}\pi\right) - \frac{\Delta t_{ha}}{2} \tag{6.20}$$

where k_{c_1} ensures that $t_{hab} > 0$ as follows

$$k_{c_1} = \left\lceil \frac{1}{2\pi}\left(\frac{\omega\Delta t_{ha}}{2} - \frac{\omega x_f}{c_0} - \frac{\pi}{2} - \phi_{pq}\right)\right\rceil \tag{6.21}$$

where $\lceil x \rceil$ is the ceiling of x. In addition, $\Delta t_{ha} = t_{hae} - t_{hab}$ and $t_c = (t_{hab} + t_{hae})/2$. The period of the fluctuating pressure field $p_h(x,t)$ is given by

$$\tau_h = \frac{2\pi}{\omega} \tag{6.22}$$

In turn, the period of the pressure pulse caused by the unsteady heat release source depends on the Helmholtz number He from Eq. (3.14), which is recalled here

$$He_q = \frac{\tau_{ac}}{\Delta t_{ha}} = \frac{\sqrt{2}\sigma_x}{c_0 \Delta t_{ha}} \tag{6.23}$$

Assuming $\sigma_x = L_{ha}/7$, the above expression becomes $He_q = \frac{\sqrt{2}L_{ha}}{7c_0\Delta t_{ha}}$. In addition, there is another relevant Helmholtz number that relates the flame thickness (i.e. heat source length scale L_{ha}) with the harmonic fluctuating pressure field wavelength as follows

$$He_f = \frac{\omega L_{ha}}{2\pi c_0} \tag{6.24}$$

After reaching the far field response ($x - x_f > L_{ff}$), the period of the pressure pulse from Eq. (6.18) can be approximated to

$$\tau_q \approx 5\sqrt{2}\sigma_t \zeta_{xt} = 5\Delta t_{ha}\sqrt{\frac{2}{7^2} + He^2} \tag{6.25}$$

where the right-most expression assumes that $\sigma_t = \Delta t_{ha}/7$. The result of Eq. (6.25) confirms the analysis of the compact and noncompact regimes from Chapter 3:

$$\begin{cases} \text{Compact regime:} & He_q \ll He_{cr} \rightarrow \tau_q \approx \Delta t_{ha} \\ \text{Noncompact regime:} & He_q \gg He_{cr} \rightarrow \tau_q \approx \frac{L_{ha}}{c_0} \end{cases}$$

The ratio of both periods, Θ_{pq}, is an important relationship for the interaction of the fluctuating pressure field with the unsteady heat release pulse

$$\Theta_{pq} = \frac{\tau_h}{\tau_q} \tag{6.26}$$

The far field pressure can be computed combining Eq. (6.15) and the far field value from Table 3.2, reading as

$$\text{For} \quad x - x_f > L_{ff} \qquad p_{ff,pq} = p_0 + p_{h0} \sin\left(\frac{\pi}{2} + \phi_{pq}\right) + \frac{(\gamma - 1)\, E_{ha}}{4\sqrt{2\pi} c_0 \sigma_t \zeta_{xt} H_{ha} W_{ha}} \left[1 + erf\left(\frac{\zeta_{xt} \Delta t_{ha}}{2\tau_{ac}}\right)\right] \tag{6.27}$$

where $p_{h0} = u_f \rho_0 c_0$ and is the amplitude of the fluctuating pressure $p_h(x,t)$.

Fig 6.3 depicts the amplitude of the combination of the fluctuating pressure field with the pressure pulse caused by the unsteady heat source, as described in Eq. (6.27). As expected, the amplitude of the combined pressure fluctuation is maximum when the unsteady heat release source is in phase with the fluctuating pressure field, i.e. $\phi_{pq} = 0$, $\phi_{pq} = 2\pi$. In addition, higher Helmholtz numbers of the heat release source lead to higher pressure fluctuation amplitudes. This effect comes from the result depicted in Fig. 3.14, which shows that, for a given heat release length scale L_{ha}, the amplitude of the pressure pulse grows as He increases until reaching the maximum value corresponding to the constant volume limit.

A parametric analysis of the far field pressure fluctuation amplitude from Eq. (6.27) is presented in Fig. 6.4(L). The parameters used in the results from Fig. 6.3 and Fig. 6.4 are presented in Table 6.2. The maximum far field far field pressure in Fig. 6.4 (L) is mapped for a range of He_f and He_q values so as to reflect the trends of the pressure fluctuation amplitudes for different conditions. As shown in Fig. 6.4(L), the amplitude of the far field pressure fluctuation increases for lower He_f values which corresponds to concentrating the heat release source to smaller length scale L_{ha}. In addition, there is a very clear distinction in the trends marked by the critical Helmholtz number of the heat source $He_{q,cr} = \sqrt{2}/7$. Below $He_{q,cr}$, for compact cases, the isolines of the maximum far field pressure amplitude follow a linear trend with He_f. In contrast, above $He_{q,cr}$, for noncompact cases, the isolines follow a vertical line with fixed He_f. Fig. 6.4(R) shows that the ratio of periods

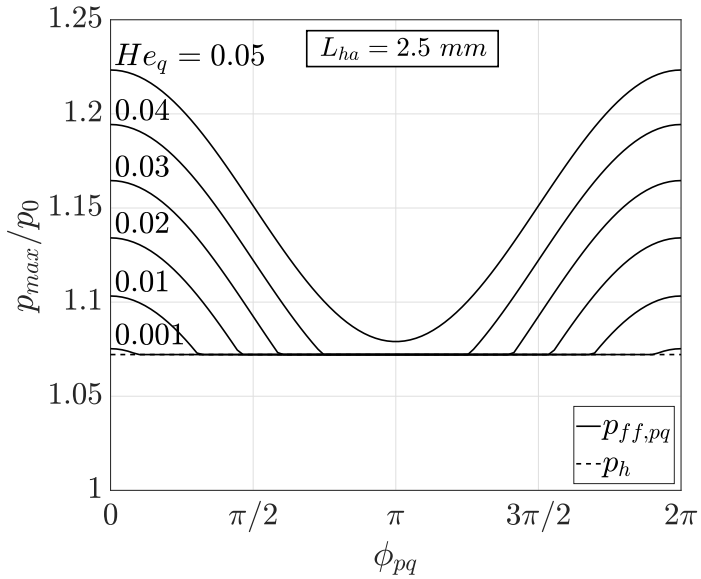

Figure 6.3. Evolution of the far field pressure of a harmonic pressure fluctuation interacting with a heat release pulse with a Gaussian spatial and temporal distribution, for different Helmholtz numbers and constant heat addition length L_{ha}, and energy $E_{ha}/(H_{ha}W_{ha}) = 5000$ J/m^2.

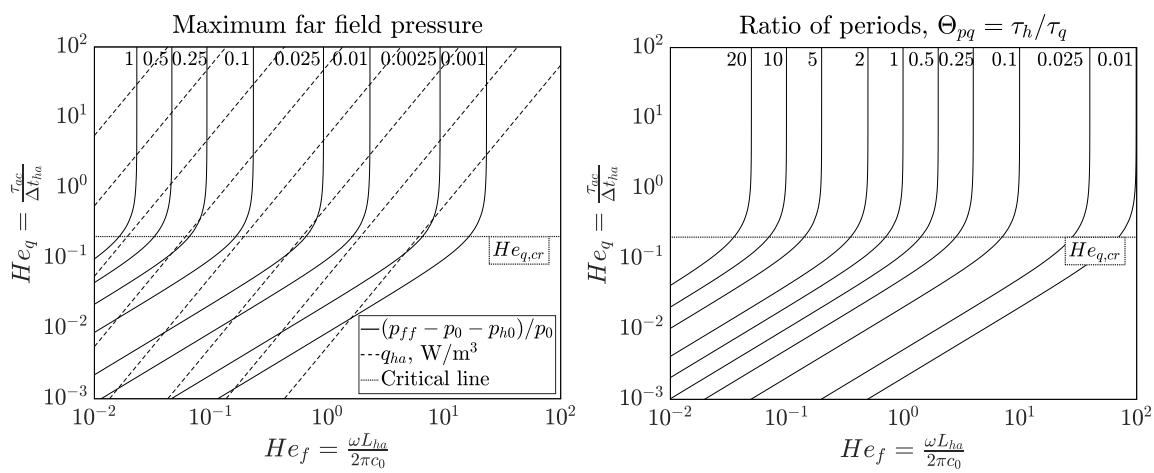

Figure 6.4. Map of the maximum far field pressure (L) and ratio of periods (R) of a harmonic pressure fluctuation interacting with a heat release pulse with a Gaussian spatial and temporal distribution. In the left plot, the constant heat addition q_{ha} lines range from 10^7 to 10^{14} W/m^3 growing from right to left. Parameters: $f = 5000$ Hz, $\phi_{pq} = 0$, and $E_{ha}/(H_{ha}W_{ha}) = 5000$ J/m^2.

follows the same trends as the maximum far field pressure amplitude. The pressure amplitude thus grows with Θ_{pq}.

6.3 Establishment of a Longitudinal Acoustic Mode in a Combustor

In contrast with the open-ended cavity from the previous case in Section 6.2, a combustor is a cavity that is constrained by boundaries from all sides such as inlets, outlets, walls, inter-alia. In a one-dimensional case, a combustor can be represented by a constant area duct of length L. The combustor can be modeled with different types of boundary conditions such as a plenum ($p_1 = 0$), a wall ($u_1 = 0$), or a complex function representing a more realistic impedance such as a nozzle.

This case consists of the establishment of a longitudinal acoustic mode in a combustor. The case can be derived using the pressure solution from Eq. (6.9) and applying appropriate boundary conditions. In a real combustor, $x = 0$ represents the dump plane whereas $x = L$ represents the nozzle entrance. In a simplified scenario, both ends can be modeled with a wall condition, i.e. $u_1(0,t) = u_1(L,t) = 0$. Using the linearized momentum equation Eq. (2.19), the velocity fluctuation can be computed on the pressure solution from Eq. (6.9) as follows

$$\frac{\partial u_1}{\partial t} = -\frac{1}{\rho_0}\frac{\partial p_1}{\partial x} = \frac{j\omega}{\rho_0 c_0}\left[-\overline{A}e^{j\left(\omega t + \frac{\omega}{c_0}x\right)} + \overline{B}e^{j\left(\omega t - \frac{\omega}{c_0}x\right)}\right] \tag{6.28}$$

Integrating Eq. (6.28) with respect to time the velocity fluctuation reads as

$$u_1(x,t) = \frac{1}{\rho_0 c_0}\left[-\overline{A}e^{j\left(\omega t + \frac{\omega}{c_0}x\right)} + \overline{B}e^{j\left(\omega t - \frac{\omega}{c_0}x\right)}\right] \tag{6.29}$$

Applying the boundary condition at left boundary of the combustor, $u_1(0,t) = 0$, leads to $\overline{A} = \overline{B}$. Then, applying the boundary condition at right boundary, $u_1(L,t) = 0$ results in the following condition

$$\cos\left(\frac{2\omega L}{c_0}\right) = 1 \tag{6.30}$$

Eq. (6.30) is satisfied by the duct resonant frequencies, ω_n, which read as

$$\omega_n = \frac{n\pi c_0}{L} \qquad \text{with} \quad n = 1, 2, 3, ... \tag{6.31}$$

At these frequencies the pressure oscillations do not decay [6]. Thus, the pressure solution becomes

$$p_1(x,t) = \overline{A}\left[e^{j\left(\omega_n t + \frac{\omega_n}{c_0}x\right)} + e^{j\left(\omega_n t - \frac{\omega_n}{c_0}x\right)}\right] \tag{6.32}$$

A longitudinal acoustic mode can be established by applying harmonic velocity fluctuations on the left end ($x = 0$) of the combustor during one cycle ($T = \frac{2\pi}{\omega}$), and then letting the ensuing pressure waves propagate back and forth across the combustor. The harmonic velocity fluctuations are generated by the moving surface described in Section 6.1 with the following velocity profile

$$\begin{cases} 0 \leq t \leq \frac{2\pi}{\omega_n} & \rightarrow \quad u_s(t) = u_f \sin(\omega_n t) \\ t > \frac{2\pi}{\omega_n} & \rightarrow \quad u_s(t) = 0 \end{cases} \tag{6.33}$$

In this way, the solution from Eq. (6.32) can be related to Eq. (6.15) by setting the complex constant $\overline{A}$ equal to $\overline{B} = -ju_f\rho_0 c_0$ from Eq. (6.13). Taking the resulting real part from Eq. (6.32), the pressure solution for the longitudinal acoustic mode reads as

$$p_L(x,t) = \Re\left(-ju_f\rho_0 c_0\left[e^{j\left(\omega_n t + \frac{\omega_n}{c_0}x\right)} + e^{j\left(\omega_n t - \frac{\omega_n}{c_0}x\right)}\right]\right) \tag{6.34}$$

The real part from Eq. (6.34) is given by

$$p_L(x,t) = u_f\rho_0 c_0\left[\sin\left(\omega_n t - \frac{\omega_n}{c_0}x\right) + \sin\left(\omega_n t - \frac{\omega_n}{c_0}x\right)\right] \tag{6.35}$$

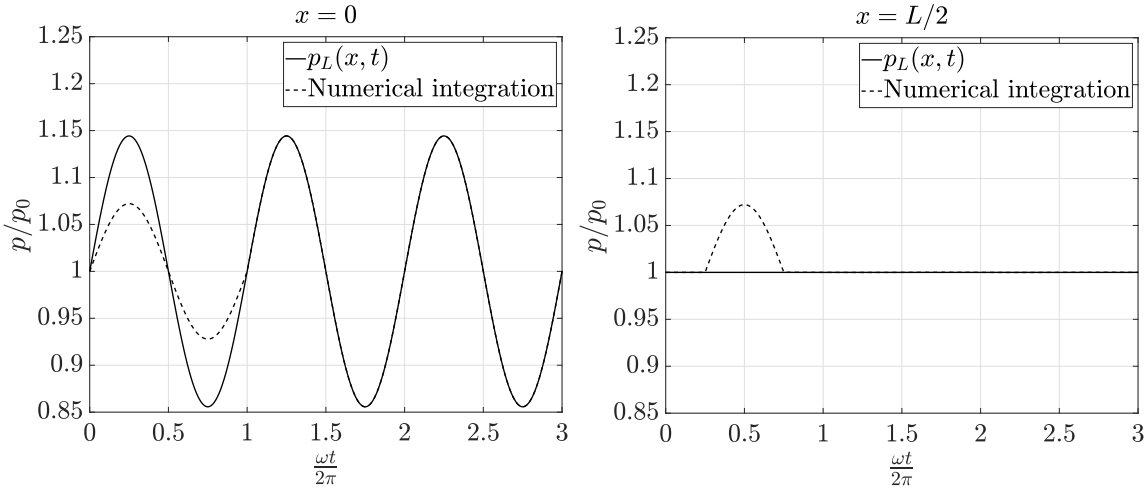

Figure 6.5. Pressure trace comparison of the solution of a 1L longitudinal acoustic mode with the resulting pressure field started with a moving surface fluctuating over one full cycle. Parameters: $L = 0.1$ m, $n = 1$, and $u_f = 20$ m/s.

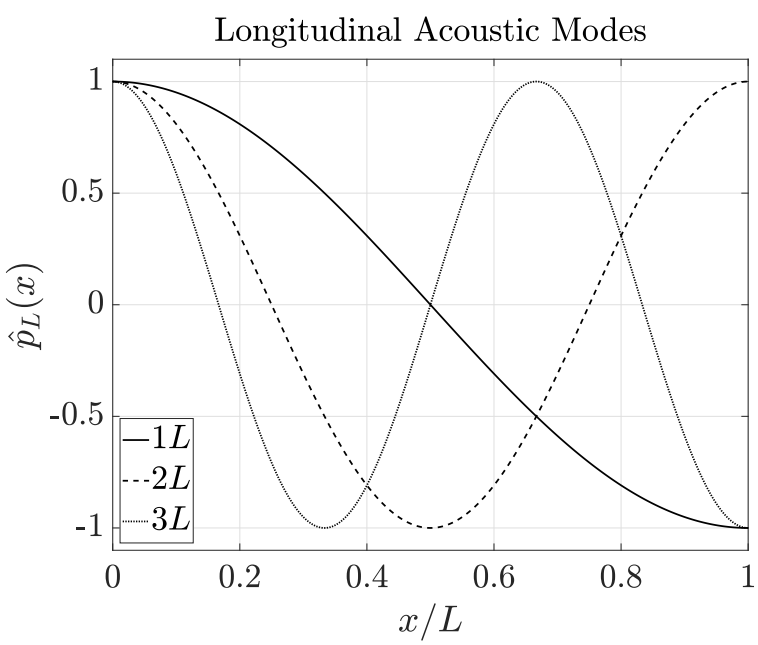

Figure 6.6. Normalized longitudinal acoustic mode shapes for the first three modes.

Rearranging the sine terms from Eq. (6.35), the pressure solution of a longitudinal acoustic mode established after the vibration of the left wall of the duct for one full cycle with a harmonic velocity fluctuation results in

$$p_L(x,t) = 2u_f\rho_0 c_0 \cos\left(\frac{\omega_n}{c_0}x\right)\sin\left(\omega_n t\right) \tag{6.36}$$

In contrast with Eq. (6.15), which represents a right-traveling wave, the pressure solution of a longitudinal acoustic mode from Eq. (6.36) is a standing wave that varies over time in an harmonic fashion. In addition, the longitudinal acoustic pressure mode shapes are given by

$$\hat{p}_L(x) = 2u_f\rho_0 c_0 \cos\left(\frac{n\pi x}{L}\right) \qquad \text{with} \quad n = 1, 2, 3, ... \tag{6.37}$$

After one full cycle, i.e. $t > \frac{2\pi}{\omega_n}$, the resulting pressure field started with the moving surface from Eq. (6.33) will match the pressure solution from the longitudinal acoustic mode of Eq. (6.36), as shown in Fig. 6.5. The numerical integration of Fig. 6.5 has been performed by integrating Eq. (6.38) with a central differences spatial discretization and Runge-Kutta 4 time marching scheme.

$$\begin{cases} \dfrac{\partial u_1}{\partial t} = -\dfrac{1}{\rho_0}\dfrac{\partial p_1}{\partial x} \\ \dfrac{\partial p_1}{\partial t} = -\rho_0 c_0^2 \dfrac{\partial u_1}{\partial x} \end{cases} \tag{6.38}$$

The first equation from Eq. (6.38) is the linearized momentum equation Eq. (2.19), whereas the second equation comes from Eq. (2.30) with the absence of a heat source term.

In Fig. 6.5 (R), the pressure fluctuation is zero after one cycle since $x = L/2$ is a pressure node in the 1L longitudinal acoustic mode. Fig. 6.6 shows the first three longitudinal modes, clearly marking the presence of pressure nodes and anti-nodes.

6.4 Interaction of a 1L acoustic Mode with an Unsteady Heat Release Pulse

The pressure response to a Gaussian spatial and temporal distribution from Eq. (3.35) consists of a left and right-traveling wave, $p_q(x,t) = A^-(x,t) + A^+(x,t)$. The left-traveling wave reads as

$$A^-(x,t) = A_{p,2}\ exp\left(-\left(\frac{\frac{x}{c_0} + (t-t_c)}{\sqrt{2}\sigma_t\zeta_{xt}}\right)^2\right)\left\{erf\left(\frac{-\frac{x}{c_0} + (\zeta_{xt}^2 - 1)(t-t_c)}{\tau_{ac}\zeta_{xt}}\right)\right. \\ \left. +erf\left(\frac{\frac{x}{c_0} + t + (\zeta_{xt}^2 - 1)t_c}{\tau_{ac}\zeta_{xt}}\right)\right\} \tag{6.39}$$

and the right-traveling wave is given by

$$A^+(x,t) = A_{p,2}\ exp\left(-\left(\frac{\frac{x}{c_0} - (t-t_c)}{\sqrt{2}\sigma_t\zeta_{xt}}\right)^2\right)\left\{erf\left(\frac{\frac{x}{c_0} + (\zeta_{xt}^2 - 1)(t-t_c)}{\tau_{ac}\zeta_{xt}}\right)\right. \\ \left. -erf\left(\frac{\frac{x}{c_0} - t - (\zeta_{xt}^2 - 1)t_c}{\tau_{ac}\zeta_{xt}}\right)\right\} \tag{6.40}$$

Eq. (3.35) is the pressure response to an unsteady heat release pulse in an unconfined one-dimensional domain. If the same unsteady heat source was introduced inside a 1D duct, the boundaries at $x = 0$ and $x = L$ would provoke pressure reflections. The 1D duct boundary conditions at $x = 0$ and $x = L$ are assumed to behave as walls. The wall boundary condition is modeled as a pressure plane-wave reflection at a flat rigid surface, with the condition $\vec{u}(x_s,t)\cdot\vec{n}_s = 0$, where x_s is the x-coordinate of the wall surface and $\vec{n}_s$ is the normal vector of the surface. Alternatively, this boundary condition can be expressed as $\frac{\partial}{\partial x}p(x_s,t) = 0$. In this way, the $\vec{u}(x_s,t)\cdot\vec{n}_s = 0$ condition requires that $(\vec{u}_I + \vec{u}_R)\cdot\vec{n}_s = 0$ at $x = x_s$ [90], where the subscript I stands for incident wave and R for the reflected wave at the surface, respectively. Using these boundary conditions, Table 6.1 presents the relationship between the initial left and right travelling waves from Eq. (6.39) and Eq. (6.40)

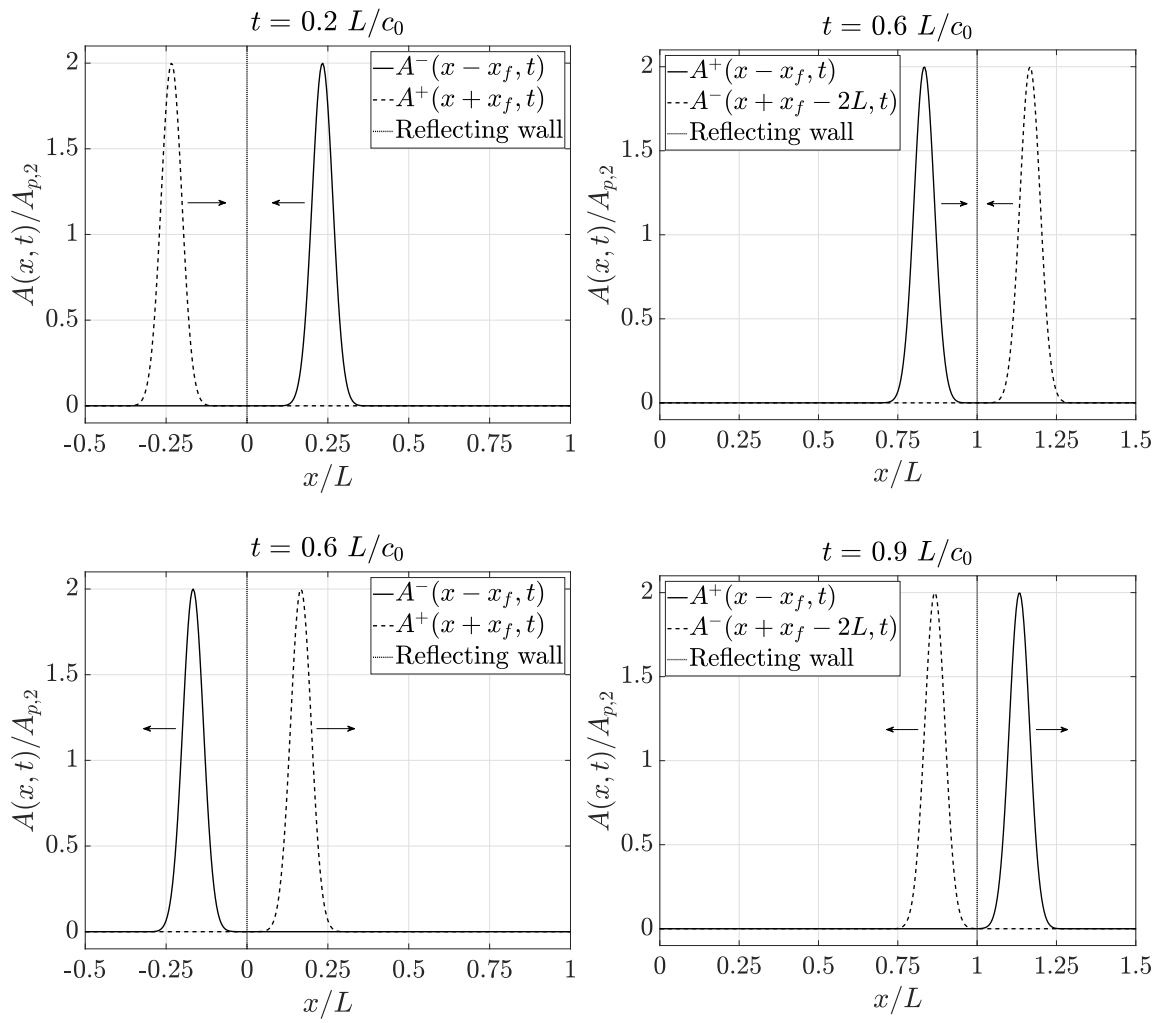

Figure 6.7. Pressure trace for the heat release pulse left-traveling wave (L) and right-traveling wave (R), and their reflections against the duct walls at $x = 0$ and $x = L$, respectively. Parameters: $L = 0.1$ m, $L_{ha} = L/10$, $\Delta t_{ha} = \frac{L}{5c_0}$, $x_f = L/3$, and $t_{hab} = 0$.

with their corresponding reflections at the walls in $x = 0$ and $x = L$, as shown in Fig. 6.7.

Table 6.1. Expressions for the heat release pulse left and right-traveling waves and their reflections against the combustor walls at $x = 0$ and $x = L$. Where $0 \leq x_f \leq L$.

Incident left-traveling wave	Reflection at $x = 0$
$A^{-}(x - x_f, t)$	$A^{+}(x + x_f, t)$
Incident right-traveling wave	Reflection at $x = L$
$A^{+}(x - x_f, t)$	$A^{-}(x + x_f - 2L, t)$

Based on the expressions from Table 6.1, we can build a pressure solution to the heat release pulse that propagates back and forth between the two walls of the duct for N_c cycles as follows

$$p_q(x,t) = \sum_{k=0}^{N_c} A^+\left(x - x_f + 2kL, t\right) + A^-\left(x + x_f - 2L\left(k+1\right), t\right) \\ + A^-\left(x - x_f - 2kL, t\right) + A^+\left(x + x_f + 2kL, t\right) \tag{6.41}$$

The number of cycles N_c represents the number of times the pressure pulse resonates inside the duct before fading away due to loss mechanisms such as viscosity and heat conduction. In the analytical model there are no loss mechanisms as it based on the acoustic wave equation, and hence, a pressure pulse would reflect against the duct walls an infinite number of times. Therefore, N_c is introduced in the model as an artifice in order to provoke the extinction of the pressure pulse after a few 1L mode cycles. This artificial parameter is used to better approach the numerical model as the latter contains loss mechanisms that will provoke the decay of the pressure pulse over time. In this case, the assumption of wall boundary conditions with perfect reflection leads to pick a small N_c so as to be more representative of actual scenarios in a combustor, in which a large unsteady heat release pressure pulse will decay rapidly.

As in the previous case, the phase shift $\phi_{pq} = \angle p_L q_1$ between the longitudinal acoustic mode and the heat release pulse can be set as an independent parameter of the study. Thus, the heat source time parameters can be related to the phase between the pressure and heat release as follows

$$t_{hab} = \frac{1}{\omega}\left(\frac{\pi}{2} + \phi_{pq} + 2k_{c_2}\pi\right) - \frac{\Delta t_{ha}}{2} \tag{6.42}$$

where k_{c_2} ensures that $t_{hab} > 0$ as follows

$$k_{c_2} = \left\lceil \frac{1}{2\pi}\left(\frac{\omega \Delta t_{ha}}{2} - \frac{\pi}{2} - \phi_{pq}\right)\right\rceil \tag{6.43}$$

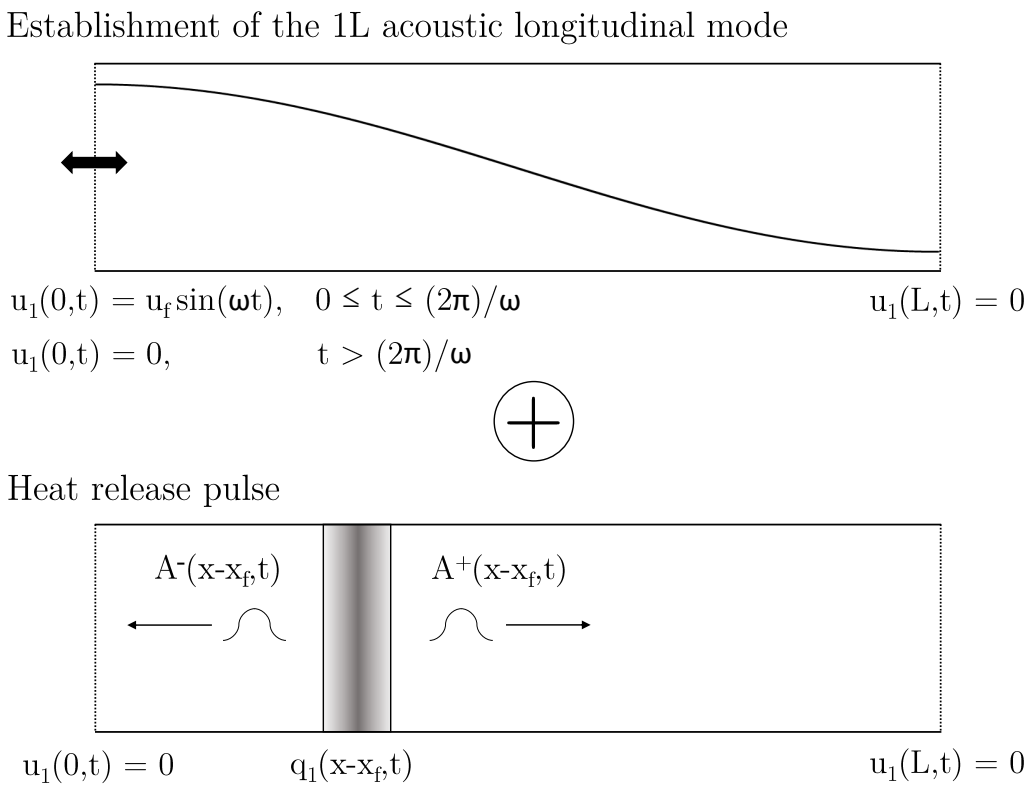

Figure 6.8. Superposition of an acoustic longitudinal mode and an unsteady heat release pulse in a 1D duct.

Since the acoustic wave equation admits the principle of superposition, the interaction of a longitudinal acoustic mode with an unsteady heat release pulse can be derived from the combination of the two individual solutions as follows

$$p_1(x,t) = p_L(x,t) + p_q(x,t) \tag{6.44}$$

where $p_L(x,t)$ comes from Eq. (6.36) and $p_q(x,t)$ from Eq. (6.41), respectively. As described in Section 6.3, $p_L(x,t)$ is the solution of the longitudinal acoustic mode once it is fully established. To reach the 1L mode acoustic pressure field departing from a fluid at rest, the wall at $x = 0$ vibrates during one full cycle following the velocity profile from Eq. (6.33). Fig. 6.8 depicts the construction of this superposition model by following the next steps:

1. Establishment of the 1L acoustic mode ($0 \leq t \leq \frac{\omega}{2\pi}$)
2. 1L mode fully established ($t > \frac{\omega}{2\pi}$)
3. Heat release pulse applied
4. Interaction of 1L mode with heat release pulse, along with pressure reflections against the duct walls

Parametric analyses of the pressure solution to the interaction of a 1L acoustic mode with an unsteady heat release pulse from Eq. (6.44) are presented in Figs. 6.9 - 6.10. The parameters for these results are described in Tables 6.2 - 6.3. Figs. 6.9 - 6.10 depict the maximum amplitude of the resulting pressure fluctuation for a short heat release pulse typical of combustors 1L mode, and a long heat release pulse representing a chugging or bulk mode, respectively. In both cases, the heat release pulse center location x_f and phase with the 1L mode pressure field ϕ_{pq} is varied in order to study the effects of the "flame" location and its relative phase with the pressure.

The short pulse case in Fig. 6.9 features a shorter heat release duration ($\Delta t_{ha} = \tau_{1L}/10$) than the period of the 1L mode ($\tau_{1L} = \frac{c_0}{2L}$), whereas the bulk mode case of

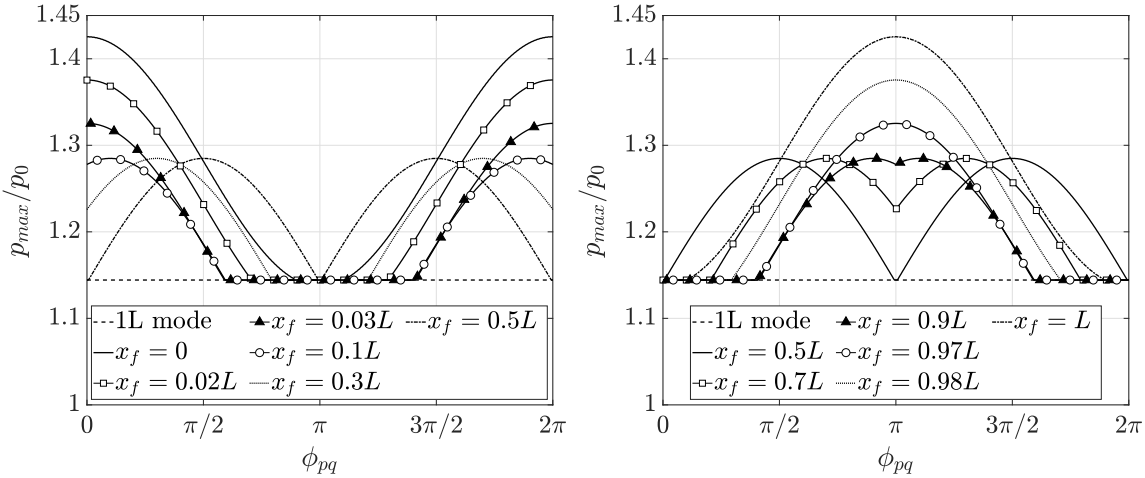

Figure 6.9. Short heat release pulse for a 1L mode. Evolution of the maximum pressure in the interaction between a 1L acoustic mode and a heat release source with Gaussian spatial and temporal distribution.

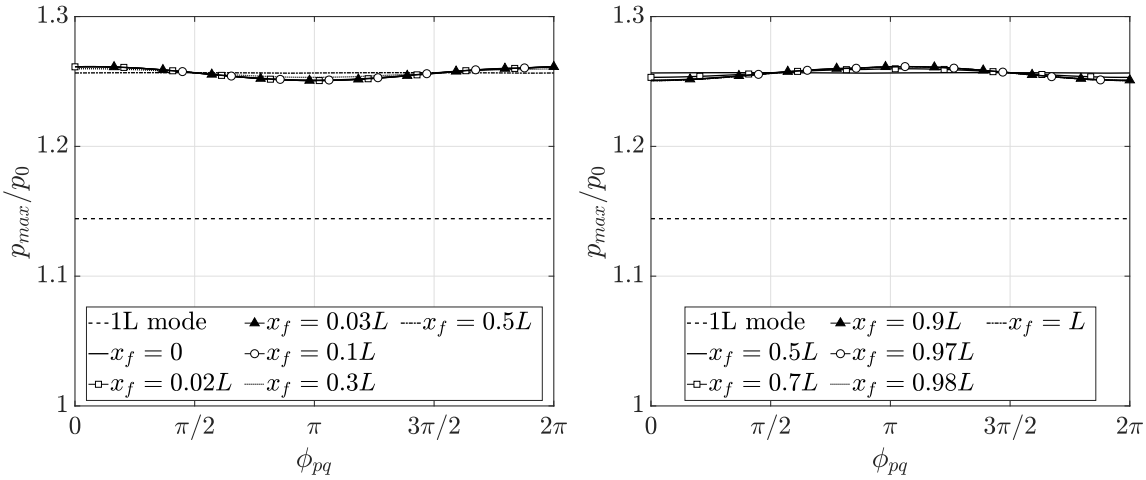

Figure 6.10. Heat release pulse representing a bulk mode. Evolution of the maximum pressure in the interaction between a 1L acoustic mode and a heat release source with Gaussian spatial and temporal distribution.

Fig 6.10 has a heat release pulse with a longer duration ($\Delta t_{ha} = 3\tau_{1L}$). By comparing these two characteristic cases it is possible to discern the effect of the heat release duration on the interaction of a 1L acoustic mode with an unsteady heat release pulse.

As shown in Fig. 6.9, for flame locations very close to the left wall and short heat release pulses ($\Delta t_{ha} < \tau_{1L}$), the maximum amplitude of the resulting pressure

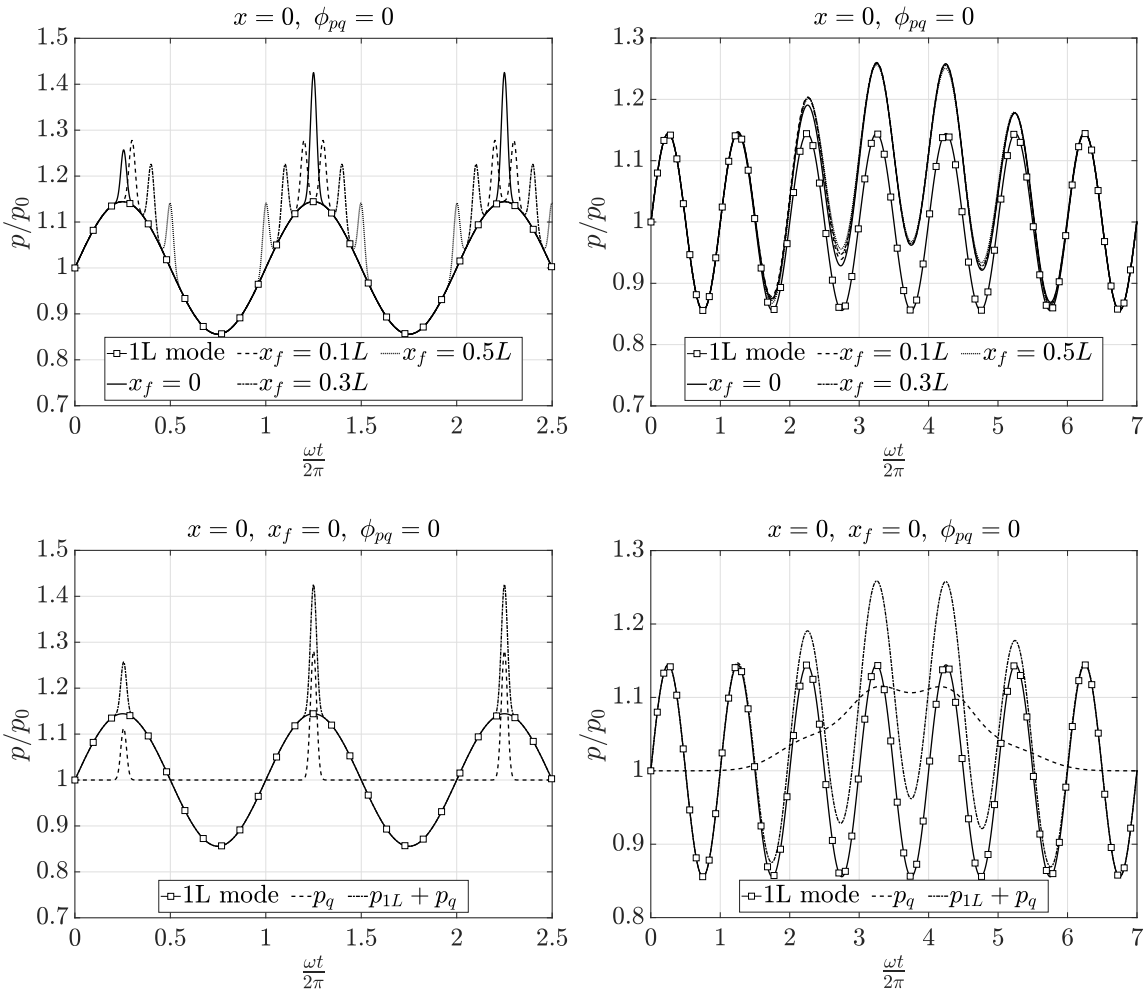

Figure 6.11. Pressure trace (T) and its decomposition (B) of the interaction between a 1L acoustic mode and a heat release source with Gaussian spatial and temporal distribution. Short heat release pulse for a 1L mode (L) and heat release pulse representing a bulk mode (R). $N_c = 2$ for both cases.

fluctuation occurs when the unsteady heat release pulse is in phase with the 1L compression of the acoustic mode, i.e. $\phi_{pq} = 0, 2\pi$. When the heat release pulse occurs during the expansion of the 1L mode, i.e. $\phi_{pq} = \pi$, the resulting maximum pressure falls back to the baseline amplitude of the 1L acoustic mode $|p_L| = 2u_f\rho_0 c_0$ (assuming $max(p_q) < |p_L|$). However, as the flame location x_f moves away from $x = 0$, the optimum phase between the unsteady heat release pulse and the 1L acoustic mode changes. This variation of the optimum ϕ_{pq} as a function of x_f is caused by the fact that the unsteady heat release pulse will take a time x_f/c_0 and $(L - x_f)/c_0$ to reach the walls at $x = 0$ and $x = L$, respectively. Therefore, short heat release pulses with respect to the 1L mode exhibit a variation of the maximum resulting pressure fluctuation as a function of the flame location and the phase between the heat release pulse and the 1L mode.

In contrast with the short heat release pulse behavior from Fig. 6.9, the bulk mode heat release pulse from Fig. 6.10 reveals that for long heat release duration ($\Delta t_{ha} > \tau_{1L}$) the resulting amplitude of the pressure fluctuation is independent from the flame location and the phase between the heat release pulse and the 1L mode. Indeed, a heat release pulse with a long duration with respect to the 1L mode effectively behaves as a bulk mode or chug mode, with no spatial or phase dependence of the flame.

Fig. 6.11 depicts the pressure trace and its decomposition of the short and bulk mode heat release pulses for a given spatial location, flame location and phase. For the short heat release pulse case shown in Fig. 6.11 (L), the unsteady heat release pulse rides on top of the pre-existing 1L mode and bounces back and forth the walls at $x = 0$ and $x = L$. For $x_f = 0$ the combination of the unsteady heat release pressure pulse and the 1L mode leads to the maximum pressure from all the flame locations (only equaled at $x = L$). In turn, the bulk mode heat release pulse presented in Fig. 6.11 (R) exhibits a much smoother increase in the pressure fluctuation caused by the unsteady heat release pulse that lasts several 1L mode cycles. In this case, the slow bulk mode pressure pulse gradually varies the overall mean pressure level so that the

1L acoustic mode maintains its harmonic behavior but displaced to higher and lower baseline pressures based on the heat release pulse.

6.5 Comparison of Analytical and Numerical Results

6.5.1 Simulation Setup

This case study consists of the interaction of an unsteady heat release pulse with a 1L longitudinal acoustic mode in a 1D duct, as presented in Section 6.4. Initially the fluid is quiescent, and then the wall at $x = 0$ vibrates at a frequency $\omega = \frac{n\pi c_0}{L}$, with $n = 1$ in order to generate pressure oscillations that match the frequency of the first longitudinal mode of the combustor. As described in Section 6.3, after one full cycle the wall at $x = 0$ stops its motion and the 1L mode acoustic pressure field is established. Once the 1L mode is fully established, an external heat source with a Gaussian spatial and temporal distribution generates a pressure pulse that interacts with the pre-existing 1L mode pressure field. The external heat source is not affected by the 1L mode pressure field, but considered as an independent source. The walls at $x = 0$ and $x = L$ provoke pressure reflections on the resulting pressure response. In addition, the number of cycles that the unsteady heat release pulse reflects against the walls has been set to $N_c = 4$. This number of cycles has been chosen in order to better approach the analytical solution to the numerical simulation, so as to better represent the fact that large unsteady heat release pressure pulses only reflect a few cycles before rapidly decaying.

Highly-resolved numerical simulations have been conducted using GEMS with the aim of investigating the accuracy and limitations of the analytical solutions derived in Section 6.4. The computational domain is depicted in Fig. 6.12 and it consists of a two-dimensional cavity with dimensions L x H of 100 mm x 0.1 mm, respectively. During the establishment of the 1L mode ($0 \leq t \leq \frac{2\pi}{\omega}$), the wall at $x = 0$ is modeled as a viscous, adiabatic wall that vibrates in a sinusoidal fashion at an angular frequency ω. After the 1L mode is established ($t > \frac{2\pi}{\omega}$), the same wall is modeled as an inviscid,

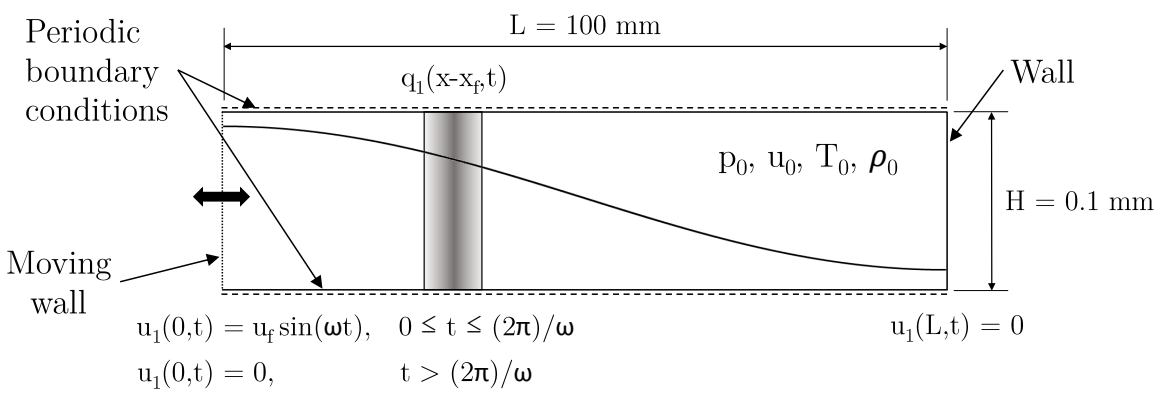

Figure 6.12. Schematic of the computational domain used in the numerical simulations.

Table 6.2. Perfect gas mean flow properties like that of CO_2 and parameters used for all the analytical and numerical simulations of Chapter 6.

p_0 (MPa)	T_0 (K)	u_0 (m/s)	u_f (m/s)	L (m)	$f = \frac{\omega}{2\pi}$ (Hz)	ρ_0 (kg/m^3)	c_0 (m/s)	γ_0 (-)
1.0	500.0	0.0	20.0	0.1	1703.6	10.59	340.72	1.2253

adiabatic wall. The wall at $x = L$ is modeled as an inviscid, adiabatic wall throughout the whole simulation. The unsteady heat release is modeled as an external heat source in the energy equation, centered around $x_f = L/4$. The total number of cells is 25,000, and the mesh is divided in 200 partitions. The structured grid has an uniform cell size with $\Delta x = \Delta y = 20\ \mu m$. To accurately capture the transient and several 1L mode acoustic cycles, the time step is limited to 50 ns and the simulations capture 5 ms of physical time.

6.5.2 Results Discussion

Two representative cases commonly found in liquid rocket engines combustion instabilities are presented in this section, corresponding to a typical short heat release pulse for a 1L mode and a heat release pulse representing a bulk mode. The parameters for both cases are presented in Table 6.3. In addition, Section 6.4 also shows results on these two cases in Fig. 6.9 and Fig. 6.10.

In the short heat release pulse case, the heat addition duration (Δt_{ha}) is a tenth of the 1L mode period (τ_{1L}), whereas the bulk mode heat release pulse duration is three times as long. Thus, the short heat release pulse case represents a typical unsteady heat release event occurring in the 1L mode cycle that will trigger a pressure pulse. These type of events can for instance be caused by the quick combustion of a pocket of mixed propellants that in the recirculation zone close to the dump plane of a combustor. In contrast, the chug pulse represents a combustion process driven by the bulk pressure of the combustor. The acoustic dynamics of a combustor interconnected

Table 6.3. Parameters of the two cases of Section 6.5.

Case	$\frac{E_{ha}}{H_{ha}W_{ha}}$ (J/m^2)	q_{ha} (W/m^3)	He_q (-)	He_f (-)	L_{ha} (m)	x_f (m)	τ_{1L} (s)	Δt_{ha} (s)	Θ_{pq} (-)	ϕ_{pq} (rad)
Short pulse	5000	$8.52{\cdot}10^9$	0.101	0.05	$\frac{L}{10}$	$\frac{L}{4}$	$\frac{2L}{c_0}$	$\frac{\tau_{1L}}{10}$	8.85	0
Bulk pulse	50000	$2.84{\cdot}10^9$	0.0034	0.05	$\frac{L}{10}$	$\frac{L}{4}$	$\frac{2L}{c_0}$	$3\tau_{1L}$	0.33	0

with a pressure manifold may lead to a degree of Helmholtz resonance in the form of an acoustic bulk mode, in which the chamber pressure varies at a low frequency with no spatial variation of the pressure mode. As a reference, Fig 6.17 from [94] depicts an example of a real liquid rocket engine experimental pressure trace featuring a strong 1L and chug modes.

Fig. 6.13 and Fig. 6.14 show the comparison of the pressure trace of the analytical and numerical solutions for the short heat release pulse case for different spatial locations. For the first two cycles of the 1L mode ($\frac{\omega t}{2\pi} < 2$) the analytical solution is able to follow the pressure trace of the numerical solution with a fair level of agreement. However, as time progresses the numerical simulation quickly deviates very significantly from the analytical solution.

The main cause for the discrepancy between the analytical and numerical solution for both cases is the steepening of the pressure waves with the eventual formation of weak shocks. This nonlinear acoustic phenomenon is described in more detail in Section 6.6. As the pressure waves propagate with the local speed of sound, and the latter is a function of the local temperature, the compression portion of the wave propagates at a faster speed than the rarefaction portion, leading to a distortion of the wave front. In the compression portion of the wave front, the velocity and temperature gradients increase monotonically over time until forming a weak shock. At this point, the assumption of negligible viscosity and heat conduction is no longer valid, so that the isentropic relations no longer apply. The weak shock wave propagates at the at the local sound speed.

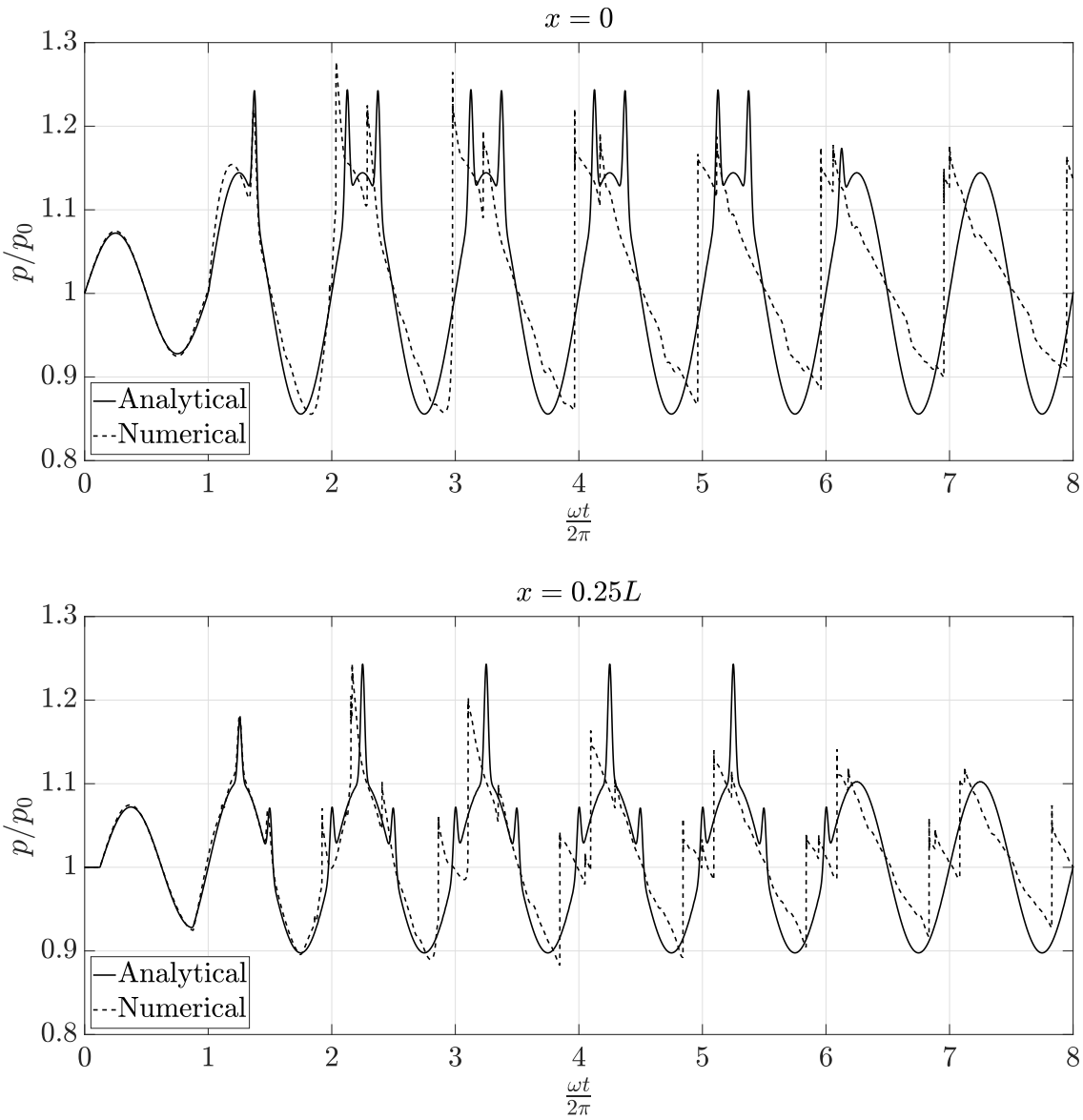

Figure 6.13. Short heat release pulse for a 1L mode. Comparison of the analytical and numerical solution of the interaction between a 1L acoustic mode and a heat release source with Gaussian spatial and temporal distribution.

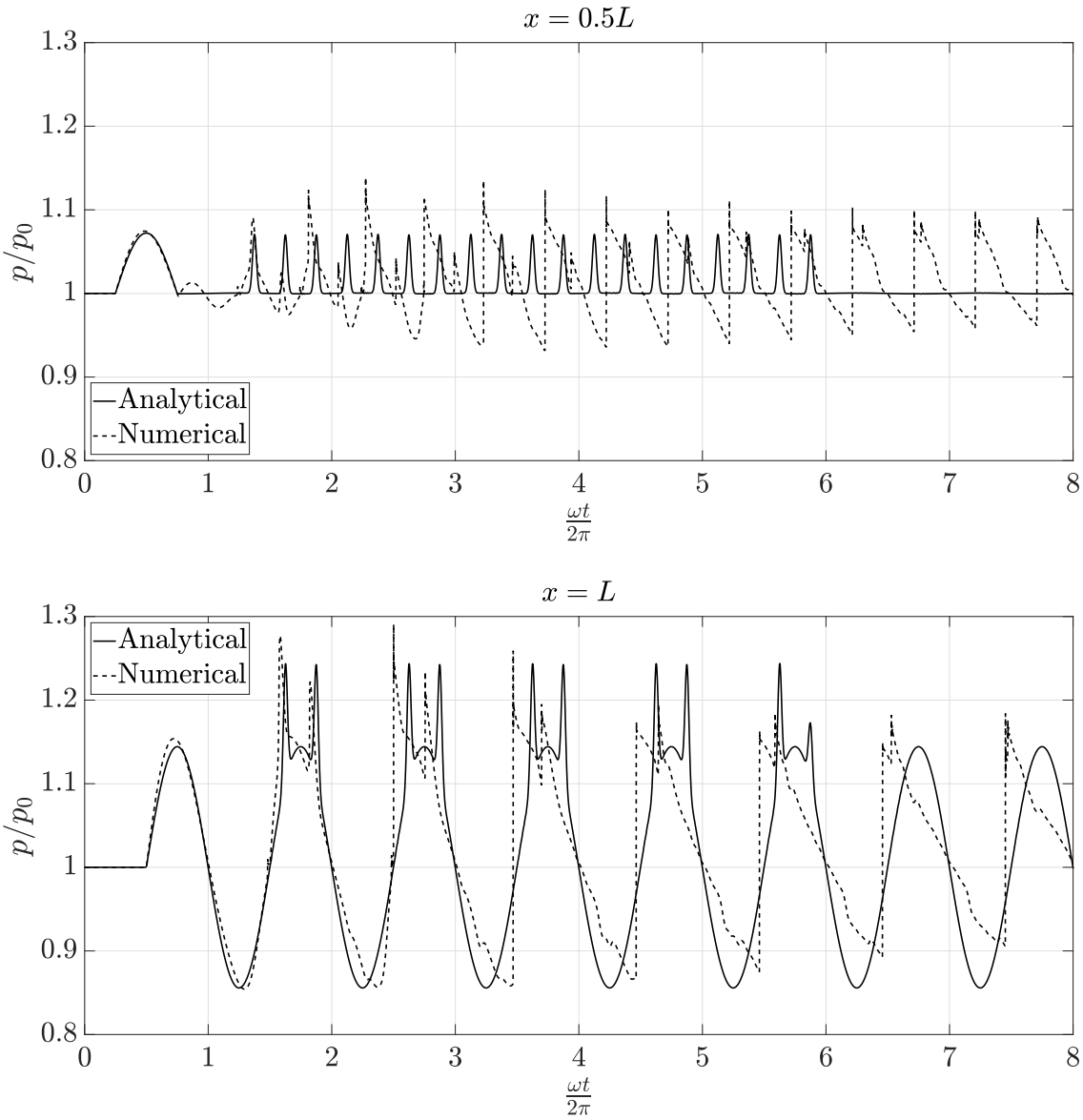

Figure 6.14. Short heat release pulse for a 1L mode. Comparison of the analytical and numerical solution of the interaction between a 1L acoustic mode and a heat release source with Gaussian spatial and temporal distribution.

Figs. 6.15 - 6.16 present the comparison between the analytical and numerical solutions for the bulk mode heat release pulse. As it occurred in the short heat release pulse case, the analytical solution follows the numerical solution with a good agreement until the second cycle of the 1L mode. After the second cycle, the numerical solution quickly differs from the analytical solution due to mostly the nonlinear steepening of the wave front.

For both cases, away from the pressure node (at $x = 0.5L$), the analytical solution is able to capture with a reasonable degree of accuracy the pressure amplitude of the numerical solution for the fist few cycles of the 1L mode. After several cycles, the nonlinear weak shock formation and propagation, as well as the effects of viscous losses provoke the pressure amplitude of the numerical solution to decay. Since the analytical solution is based on the acoustic wave equation, which neglects loss mechanisms such as viscous losses or heat conduction, it cannot predict the decay of the amplitude of the pressure waves. Furthermore, the analytical model assumes that the pressure waves propagate at a constant speed of sound c_0, whereas in reality pressure waves propagate at the local speed of sound, which provokes the steepening of the wave front and eventual weak shock formation. In addition, as described in Eq. (6.50), the irreversibility of shocks provokes their amplitude decay over time.

Fig. 6.17 shows an experimental pressure trace in a liquid rocket engine with strong 1L and chug modes. The comparison of the pressure trace from Fig. 6.17 with Figs. 6.13-6.16 reveals that real rocket combustors exhibit steep fronted waves and weak shocks that differ significantly from harmonic pressure fluctuations. Whereas highly-resolved numerical simulations are able to capture the nonlinear dynamics of real combustors, analytical models based on the acoustic wave equation will not be able to predict weak shocks or the effects of loss mechanisms (viscosity, heat conduction).

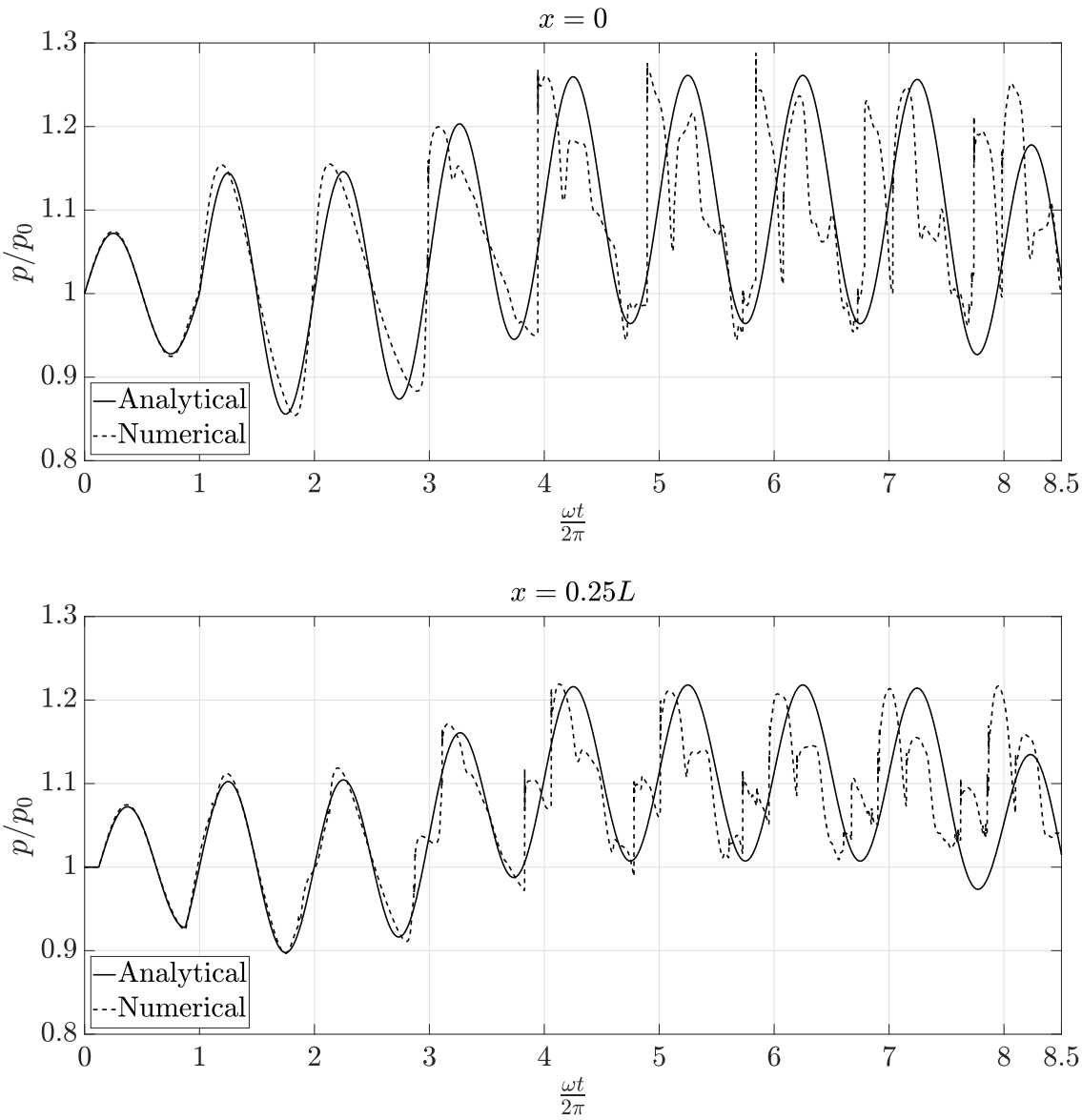

Figure 6.15. Heat release pulse representing a bulk mode. Comparison of the analytical and numerical solution of the interaction between a 1L acoustic mode and a heat release source with Gaussian spatial and temporal distribution.

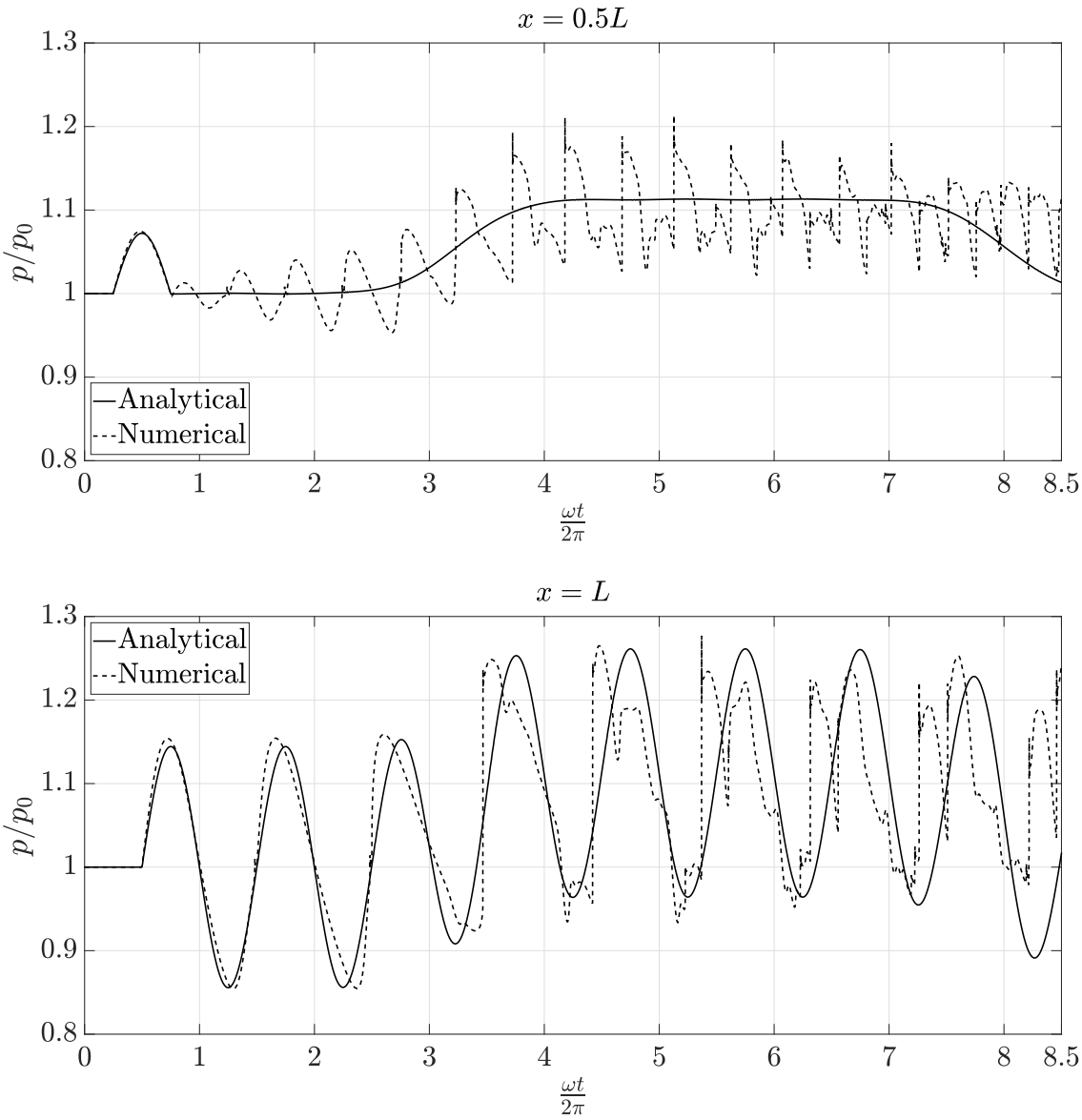

Figure 6.16. Heat release pulse representing a bulk mode. Comparison of the analytical and numerical solution of the interaction between a 1L acoustic mode and a heat release source with Gaussian spatial and temporal distribution.

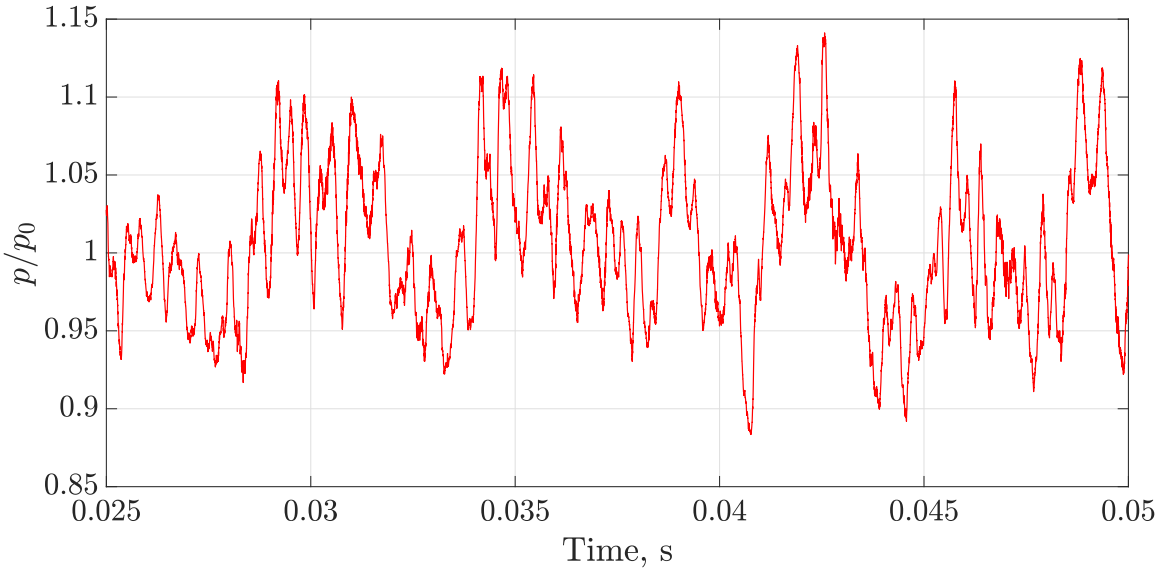

Figure 6.17. Example of experimental pressure trace in a liquid rocket combustor (Source [94]). Pressure trace at 0.3" downstream the dump plane for the case $T_{ox} =$ 730 K.

6.6 Nonlinear effects

In contrast with electromagnetic waves, which propagate at the constant speed of light (an absolute constant), acoustic pressure waves propagate with the local speed of sound, c.

$$c^2 = \left.\frac{\partial p}{\partial \rho}\right|_s \tag{6.45}$$

For an ideal gas, the speed of sound is given by

$$c = \sqrt{\gamma R T} = \sqrt{\frac{\gamma p}{\rho}} \tag{6.46}$$

Using the isentropic relationship $p/\rho^\gamma =$ constant, Eq. (6.46) becomes

$$c = \sqrt{\frac{\gamma p_0}{\rho_0}\left(\frac{\rho}{\rho_0}\right)^{\gamma-1}} = c_0\left(\frac{\rho}{\rho_0}\right)^{\frac{\gamma-1}{2}} \tag{6.47}$$

Using the linearized state variables, $\rho = \rho_0 + \rho_1$ and $p = p_0 + p_1$, the speed of sound reads as

$$c = c_0\left(1 + \frac{\rho_1}{\rho_0}\right)^{\frac{\gamma-1}{2}} = c_0\left(1 + \frac{p_1}{p_0}\right)^{\frac{\gamma-1}{2\gamma}} \tag{6.48}$$

With $\gamma > 1$, Eq. (6.48) shows that the portion of pressure fluctuations above the mean flow p_0 will propagate at a higher local speed of sound than c_0, thereby steepening the compression portion of the pressure fluctuations. On the contrary, in the rarefaction portion the pressure fluctuations are below the mean flow p_0, and hence, propagate at a lower local speed of sound than c_0. The steepening of wave fronts and formation of shocks are derived from the momentum equation in the Navier-Stokes equations. Indeed, the $\vec{u}\cdot\nabla\vec{u}$ term from the velocity substantial derivative from Eq. (2.2) $\frac{D\vec{u}}{Dt} = \frac{\partial\vec{u}}{\partial t} + \vec{u}\cdot\nabla\vec{u}$ is responsible for the wave steepening, which provokes the eventual formation of shocks. However, the viscous terms of the Navier-Stokes equations generate a dissipating effect that competes with the wave steepening.

In liquid rocket combustors, in extreme cases of combustion instabilities, the large amplitude pressure fluctuations may evolve into weak shocks [91]. These weak shocks

are caused by the steepening of the wave front due to the dependence of the speed of sound on the local temperature, as well as due to unsteady heat release pulses with very large heat release rates [63, 95].

If no shocks are present, nonlinear effects do not change the net acoustic energy associated with a pulse, but they cause a rearrangement of the frequency distribution of the energy [90]. However, once shocks form, their peak pressure decreases over the distance [90,96]. From [90], the net energy per unit area transverse to the propagation direction for a pulse of finite duration is given by

$$E(t) = \frac{1}{\rho c^2} \int_{-\infty}^{\infty} p^2 dx \tag{6.49}$$

For the case in which there is a shock present, Pierce [90] presents an expression for the energy time rate of change from Rudnick [97], which reads as

$$\frac{dE}{dt} = -\frac{\beta}{6\rho^2 c^3} \left[f(\phi_-) - f(\phi_+) \right]^3 = -\rho c T_0 \Delta s \tag{6.50}$$

where T_0 is the temperature, β is the coefficient of thermal expansion (fractional increase in volume per unit increase in temperature at constant pressure), and Δs is the entropy change across the shock, respectively. Eq. (6.50) reveals that the presence of shock waves causes the energy in the pressure wave to decrease over time due to the entropy increase across the shock, $\Delta s > 0$. Nonlinear effects can therefore provoke dissipation of acoustic energy even when no dissipation mechanisms are explicitly considered (i.e. no viscosity or heat conduction) [90]. Since the analytical model assumes a constant speed of sound c_0, and it neglects viscous losses and heat conduction, it cannot capture these nonlinear gas dynamics phenomena.

As an example of these nonlinear gas dynamics phenomena, Fig. 6.18 from [96] shows the evolution over the distance of an originally sinusoidal pressure wave evolving into a sawtooth profile due to nonlinear steepening of the wave front. The initial sinusoidal wave steepens its profile over the distance due to the temperature dependence on the local speed of sound until it eventually becomes a weak shock. Once the

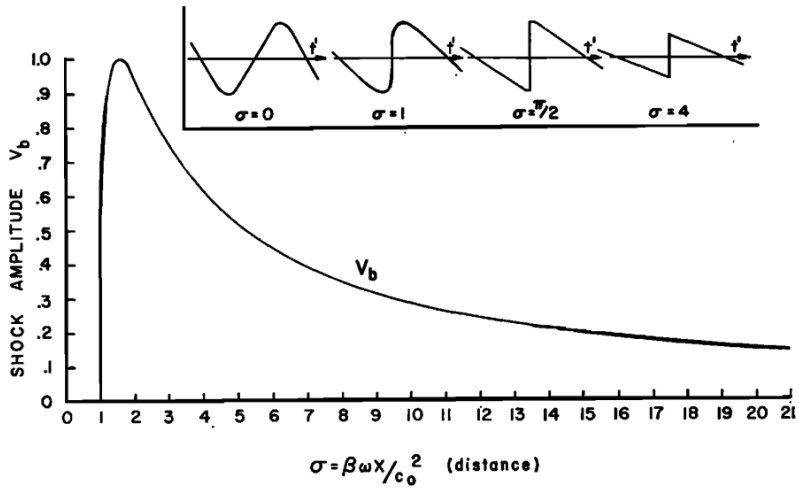

Figure 6.18. Shock amplitude of an originally sinusoidal wave. Inset depicts the waveform at various distances from the source (Source [96]).

shock forms, the peak pressure decays over the distance as described in Eq. (6.50). For an originally sinusoidal pressure wave evolving into a sawtooth profile, Pierce [90] provides the following expression to compute the peak overpressure at fixed x at large distances, reading as

$$p_{max}(x) \approx \frac{P_0 \pi \bar{x}}{x} = \frac{\pi \rho c^3}{\beta \omega x} \tag{6.51}$$

Therefore, the shock peak overpressure decreases inversely with x, which is a phenomenon known as saturation. Indeed, the numerical results from Figs. 6.13-6.16 show that the weak shocks peak pressure decays over time. This pressure decay is caused by the aforementioned effects as well as losses due to viscosity and heat conduction.

6.7 Summary

This chapter studied the interaction of an unsteady heat release pulse with a longitudinal acoustic mode on a one-dimensional duct with a non-reacting gas mixture. Analytical solutions based on the acoustic wave equation have been derived for four unit problems to evaluate and quantify how pressure fluctuations due to unsteady heat

release amplify a longitudinal acoustic mode. These analytical models have been then compared against highly-resolved numerical simulations to asses the nonlinear effects and the limitations of the acoustic wave equation. Four different unit problems with their corresponding analytical solutions have been derived throughout the chapter. The study parameters have been selected to be representative of the conditions in a rocket combustor. Relevant length and time scales such as the Helmholtz number, the phase shift between the fluctuating pressure field and the heat source, and ratio of the fluctuating periods are identified in the derivation of the analytical models.

The first unit problem of the chapter presents an analytical model of the pressure response to a moving rigid surface that generates a velocity harmonic fluctuation in a one-dimensional open-ended cavity. The second unit problem combines the previous analytical solution from the velocity harmonic fluctuation with the pressure response to an unsteady heat release pulse with Gaussian spatial and temporal distribution developed in Chapter 3. The analysis of the relevant time scales confirmed the behavior encountered for compact and noncompact regimes in Chapter 3. The maximum amplitude of the combined pressure fluctuation is reached when the fluctuating pressure field is in phase with the unsteady heat release source. There are two relevant Helmholtz number that influence the amplitude of the resulting pressure fluctuations. On the one hand, the heat source Helmholtz number, He_q, relates the characteristic acoustic time with the duration of the heat release pulse. On the other hand, He_f, represents the ratio of the flame thickness over the fluctuating pressure field wavelength. The amplitude of the pressure fluctuations increases with the heat source Helmholtz number, He_q. The parametric analysis also reveals that the critical Helmholtz number of the heat source $He_{q,cr}$ marks the onset of the compact and noncompact behavior. Reducing He_f effectively translates in concentrating the heat source in a smaller characteristic length, thereby increasing the resulting pressure fluctuation.

The third unit problem consists of the establishment of a 1L acoustic mode in a 1D duct using the analytical solution of the first unit problem. In this case, the

model takes into account the pressure reflections provoked by the acoustic boundaries of the duct, both of which are assumed to be walls. The analytical solution models the establishment of a 1L acoustic longitudinal using the solution from the harmonic velocity fluctuations developed in the first unit problem. Departing from a quiescent fluid, the wall on the left end of the duct vibrates in a harmonic fashion for one cycle at the 1L mode resonance frequency. After vibrating for one full cycle, the left wall stops its motion and the 1L acoustic mode pressure field is established.

The fourth, and last, unit problem combines the analytical solution of the 1L mode acoustic field developed in the third unit problem with an unsteady heat release pulse with Gaussian spatial and temporal distribution. Pressure reflections against the duct walls are also included in the analysis in order to provide a more realistic model. The model has been applied to two representative cases commonly encountered in combustion instabilities of liquid rocket combustors, corresponding to a short heat release pulse for a 1L mode and a long heat release pulse representing a bulk mode. A parametric analysis has been conducted to study the maximum amplitude of the resulting pressure fluctuations as a function of the flame location and the phase between the heat release pulse and the 1L acoustic mode. For the short heat release pulse, the amplitude of pressure fluctuations depends on the flame location and the phase between the heat release pulse and the 1L mode. When the flame is close to the duct left wall, the pressure is maximum when the heat release pulse is in phase with the 1L pressure field. In contrast, in the bulk mode heat release pulse case, the resulting amplitude of the pressure fluctuations is independent from the phase between the heat release pulse and the 1L mode, and flame location. Indeed, the long duration of the heat release pulse with respect to the 1L mode effectively drives the pressure response to behaves as a bulk mode or chug mode, with no spatial or phase dependence of the flame.

Finally, the analytical solution of the fourth unit problem has been compared against highly-resolved numerical simulations in order to assess the accuracy and limitations of the model, as well as the importance of nonlinear effects in modeling

combustion instabilities. For both cases studies, the analytical solution is able to capture with an acceptable degree of accuracy the pressure trace of the numerical solution during the fist two cycles of the 1L mode. However, after a few cycles the numerical solution quickly deviates very significantly from the analytical solutions due to wave steepening and the formation of weak shocks. These nonlinear gas dynamic effects are caused by the steepening of the wave front due to the temperature dependence of the local speed of sound, as well as due to unsteady heat release pulses with very large heat release rates [54, 87]. The analytical model does not capture the steepening of the wave front and eventual weak shock formation as it assumes a spatially constant speed of sound c_0, whereas in reality the pressure wave propagate at the local speed of sound. Since the acoustic wave equation used to develop the analytical solutions also neglects loss mechanisms such as viscous losses or heat conduction, it cannot predict the decay of the amplitude of the pressure waves. In addition, other nonlinear phenomena such as the irreversibility of shocks provokes the decay of their amplitude over time. All in all, models based on the acoustic wave equation can provide a good understanding of the combustion instability behavior, but not accurately predict the evolution of the pressure fluctuations as the nonlinear effects play a major role in the combustion dynamics of liquid rocket engines.

7. CONCLUSIONS

Combustion instabilities are a common phenomena in rocket combustors and other high-performance chemical propulsion systems. Highly-resolved numerical simulation of rocket combustors using detailed kinetics indicate that the presence of high rates of heat release may question the constant pressure assumption. This research work explored the effects of these high rates of heat addition on the local pressure as well as the interactions between the acoustic field and heat release. Simplified unit problems that dealt with some of the particular interactions of physical phenomena involved in combustion instability have been used to decompose the entire problem. Seven unit problems have been proposed in this study. Each of them analyzed fundamental problems with simplified scenarios and then, more phenomena haven been added to the analysis increasing the complexity to model a more realistic behavior.

In the first unit problem, departing from the acoustic wave equation, an analytical model of the pressure response to an unsteady heat release source has been derived for an unconfined one-dimensional domain. An uniform and initially quiescent perfect gas with properties like that of CO_2 is subjected to a heat release source with a Gaussian spatial distribution with either a step or a Gaussian temporal profile. The magnitude of the heat source is based on large eddy simulations of a rocket combustor using detailed kinetics. The analytical solutions contain important length and time scales that can be condensed into the Helmholtz number. This non-dimensional number is defined as the ratio between the characteristic acoustic time and the duration of the heat release pulse. For both heat source profiles, a critical Helmholtz number is identified as a threshold to distinguish between two regimes of pressure response. For compact cases, in the subcritical regime, the amplitude of the pressure response is determined by the duration of the heat release and it is independent of the length scale of heat source. Applied to a flame, this implies that the pressure fluctuation

amplitude will only depend on the time rate of change of the heat release and not on the flame thickness. For noncompact cases, above the critical Helmholtz number, the amplitude of the pressure response is determined by both the length and time scales of the heat source.

Whereas in compact cases the amplitude of the generated pressure pulse remains constant over the distance, in noncompact cases the pressure pulse peaks at the center of the heat source, and then decays until converging to a constant far field pressure amplitude. As such, He represents an effective metric to determine to which extent the pressure response to an unsteady heat release event approaches to a constant pressure or a constant volume process. For $He \ll He_{cr}$, the pressure response tends to a constant pressure process, whereas for $He \gg He_{cr}$ the response tends to a constant volume process. The analytical model shows that the maximum amplitude of the pressure response to an unsteady heat release event is limited to the same constant volume limit regardless of the temporal profiles of the heat sources considered.

The comparison between the analytical and high-fidelity numerical solutions reveals that, within its range of application, the analytical model effectively captures the dynamics of the pressure response to an unsteady heat release event. Overshoots in the pressure amplitude, however, are observed to be common for both the heat sources. The density drop is shown to be overestimated in general and the presence of unphysical values indicate the limitations of the analytical assumptions for extremes rates of heat release. The maximum temperature error is shown to depend on He. In the heated zone, which determines the shape of the pressure pulse, the assumption of constant mean flow properties is the major cause of discrepancy between the analytical model and the numerical simulation. Away from the heated zone, the numerical solutions reveal the presence of important nonlinear effects that are not captured by methods based on the acoustic wave equation. Indeed, the addition of extreme rates of heat release induces weak shocks in the pressure pulses.

The analytical models show a good agreement with the numerical simulations for moderate values of heat release rate. This holds true while the flow conditions remain

close to the model assumptions. Nevertheless, for large rates of heat release, the presence of nonlinear effects deviate the numerical solution from the analytical model. For such large values, as the conditions separate ever more from the model assumptions, such as the constant mean flow speed of sound, the analytical model cannot capture the rapid accumulation of nonlinear effects. In liquid rocket combustors, in extreme cases of combustion instabilities, the large amplitude pressure fluctuations may evolve into weak shocks [91]. These weak shocks are caused by the steepening of the wave front due to the dependence of the speed of sound on the local temperature, as well as due to unsteady heat release pulses with very large heat release rates [63, 95].

In Chapter 6 the analytical solution is able to capture with a reasonable degree of accuracy the pressure amplitude of the numerical solution for the fist few cycles of the 1L mode. After several cycles, the nonlinear weak shock formation and propagation, as well as the effects of viscous losses provoke the pressure amplitude of the numerical solution to decay. Since the analytical solution is based on the acoustic wave equation, which neglects loss mechanisms such as viscous losses or heat conduction, it cannot predict the decay of the amplitude of the pressure waves. Furthermore, the analytical model assumes that the pressure waves propagate at a constant speed of sound c_0, whereas in reality pressure waves propagate at the local speed of sound, which provokes the steepening of the wave front and eventual weak shock formation. In addition, the irreversibility of shocks provokes their amplitude decay over time.

Whereas highly-resolved numerical simulations are able to capture the nonlinear dynamics of real combustors, analytical models based on the acoustic wave equation will not be able to predict weak shocks or the effects of loss mechanisms such as viscosity or heat conduction. All in all, models based on the acoustic wave equation can contribute to providing a good understanding of combustion instabilities, but not accurately predict the evolution of the pressure fluctuations as the nonlinear effects play a major role in the combustion dynamics of liquid rocket engines.

From an application point of view based on the magnitudes of heat release, gas turbines operate in an isentropic compression regime, liquid rocket engines experience

weak shocks, and pressure-gain combustion devices feature strong shocks. For low and moderate heat release rates, characteristic of gas turbines, models based on the acoustic wave equation will show a good agreement in the prediction of the amplitude and shape of the pressure response of a fluid to unsteady heat release events. However, this type of methods such as 1D acoustic models, network models, or Helmholtz solvers, will overpredict the pressure response as the local speed of sound deviates more than 5% from the mean flow value. For high-pressure liquid rocket engines, these methods will accumulate significant errors, worsening with increasing operating pressure due to the extreme rates of heat release. In addition, such methods will fail to capture important nonlinear effects such as weak shocks, which are common in longitudinal acoustic modes of liquid rocket engine combustors [61]. Even though some acoustic solvers can incorporate a time-varying mean speed of sound, their inability to capture rapid increases in the local speed of sound due to unsteady combustion will remain a source of error.

7.1 Recommendations

The numerical simulations have revealed the presence of nonlinear gas dynamics effects that appear to be very important in the pressure response to unsteady heat release. The current work has identified the main nonlinear phenomena such as wave front steepening and the formation of weak shocks, which separate the analytical solution from the real pressure response. It would be very useful to investigate in detail at which point the assumptions from the analytical models start to break in a real case. In particular, the investigation of the range of heat release values at which the shocks start to form would greatly contribute to better assess the range of operation in which acoustic models can be used versus more complex models.

The assumption of constant mean flow speed of sound appears to be the most restricting assumption limiting the range of application of the acoustic wave equation for predicting the pressure response to unsteady heat release. In order to test this

assumption, it would be very practical to compare the relative accuracy of the analytical solution based on the acoustic wave equation with constant speed of sound, a numerically-integrated acoustic wave equation with a temperature-dependent speed of sound, a 1D Euler model with temperature-dependent speed of sound, and finally highly-resolved Navier-Stokes equations.

Furthermore, the current model assumes zero Mach number for the mean flow. Although this assumption greatly simplifies the derivation, it also eliminates any convective effects such as entropy waves. It would be very useful to test the current models in cases with low mean flow velocity, such as a planar flame in a 1D duct with an inlet and outlet as boundaries.

This work showed that the Helmholtz number represents an effective metric to determine to which extend a combustion process tends to either a constant pressure or a constant volume process. This analysis was then applied to a real combustor, the CVRC, in order to assess the regime of the combustion flame. Although this application was focused on gaining a deeper understanding of the fundamental combustion process, the use of the Helmholtz number could also be extended to inform the development of numerical combustion models for LES.

REFERENCES

[1] T. C. Lieuwen and V. Yang. *Combustion Instabilities In Gas Turbine Engines*. American Institute of Aeronautics and Astronautics, jan 2006.

[2] W. E. Anderson and V. Yang, editors. *Liquid Rocket Engine Combustion Instability*. American Institute of Aeronautics and Astronautics, jan 1995.

[3] F. Nicoud and T. Poinsot. Thermoacoustic instabilities: Should the Rayleigh criterion be extended to include entropy changes? *Combustion and Flame*, 142(1-2):153–159, jul 2005.

[4] Rayleigh. The explanation of certain acoustical phenomena. *Nature*, 18(455):319–321, jul 1878.

[5] T. Poinsot and D. Veynante. *Theoretical and Numerical Combustion, Second Edition*. R.T. Edwards, Inc., 2005.

[6] A. P. Dowling and S. R. Stow. Acoustic analysis of gas turbine combustors. *Journal of Propulsion and Power*, 19(5):751–764, sep 2003.

[7] A. P. Dowling and Y. Mahmoudi. Combustion noise. *Proceedings of the Combustion Institute*, 35(1):65–100, 2015.

[8] S. L. Bragg. Combustion noise. *Journal of the Institute of Fuel*, 36:12–16, 1963.

[9] W. C. Strahle. Combustion noise. *Progress in Energy and Combustion Science*, 4(3):157–176, jan 1978.

[10] P. E. Hamlington, A. Y. Poludnenko, and E. S. Oran. Interactions between turbulence and flames in premixed reacting flows. *Physics of Fluids*, 23(12):125111, dec 2011.

[11] S. V. Sardeshmukh, S. D. Heister, and W. E. Anderson. Prediction of combustion instability with detailed chemical kinetics. In *53rd AIAA Aerospace Sciences Meeting*. American Institute of Aeronautics and Astronautics, jan 2015.

[12] S. V. Sardeshmukh, M. J. Bedard, A. Pons Lorente, and W. E. Anderson. Investigating heat release dynamics in a self-excited unstable combustor using high fidelity chemiluminescence measurements and modeling. In *2018 AIAA Aerospace Sciences Meeting*. American Institute of Aeronautics and Astronautics, jan 2018.

[13] T. Poinsot and D. Veynante. *Theoretical and numerical combustion*. R.T. Edwards, 2nd edition edition, 2005.

[14] J. P. Hathout, M. Fleifil, A. M. Annaswamy, and A. F. Ghoniem. Combustion instability active control using periodic fuel injection. *Journal of Propulsion and Power*, 18(2):390–399, mar 2002.

[15] S. Candel, D. Durox, S. Ducruix, A. L. Birbaud, N. Noiray, and T. Schuller. Flame dynamics and combustion noise: Progress and challenges. *International Journal of Aeroacoustics*, 8(1):1–56, jan 2009.

[16] A. Steinberg, J. Driscoll, and S. Ceccio. Turbulence-flame interactions - the mechanisms of flame strain and wrinkling. In *44th AIAA/ASME/SAE/ASEE Joint Propulsion Conference and Exhibit*. American Institute of Aeronautics and Astronautics, jul 2008.

[17] B. T. Chu and L. S. G. Kovásznay. Non-linear interactions in a viscous heat-conducting compressible gas. *Journal of Fluid Mechanics*, 3(05):494, feb 1958.

[18] A. S. Morgans and I. Duran. Entropy noise: A review of theory, progress and challenges. *International Journal of Spray and Combustion Dynamics*, 8(4):285–298, sep 2016.

[19] K. Wieczorek and F. Nicoud. Prediction of thermoacoustic instabilities: Numerical study of Mach number effects. In *16th AIAA/CEAS Aeroacoustics Conference*. American Institute of Aeronautics and Astronautics, jun 2010.

[20] A. P. Dowling. A kinematic model of a ducted flame. *Journal of Fluid Mechanics*, 394:51–72, sep 1999.

[21] M. Bauerheim, J. F. Parmentier, P. Salas, F. Nicoud, and T. Poinsot. An analytical model for azimuthal thermoacoustic modes in an annular chamber fed by an annular plenum. *Combustion and Flame*, 161(5):1374–1389, 2013.

[22] F. Nicoud, L. Benoit, C. Sensiau, and T. Poinsot. Acoustic modes in combustors with complex impedances and multidimensional active flames. *AIAA Journal*, 45(2):426–441, feb 2007.

[23] F. Nicoud and K. Wieczorek. About the zero Mach number assumption in the calculation of thermoacoustic instabilities. *International Journal of Spray and Combustion Dynamics*, 1(1):67–111, mar 2009.

[24] E. Motheau, L. Selle, and F. Nicoud. Accounting for convective effects in zero-Mach-number thermoacoustic models. *Journal of Sound and Vibration*, 333(1):246–262, jan 2014.

[25] L. Crocco. Aspects of combustion stability in liquid propellant rocket motors part I: Fundamentals. Low frequency instability with monopropellants. *Journal of the American Rocket Society*, 21(6):163–178, nov 1951.

[26] L. Crocco. Aspects of combustion stability in liquid propellant rocket motors part II: Low frequency instability with bipropellants. High frequency instability. *Journal of the American Rocket Society*, 22(1):7–16, jan 1952.

[27] D. Laera, T. Schuller, K. Prieur, D. Durox, S. M. Camporeale, and S. Candel. Flame describing function analysis of spinning and standing modes in an annular combustor and comparison with experiments. *Combustion and Flame*, 184:136–152, oct 2017.

[28] A. Orchini, G. A. Mensah, and J. P. Moeck. Effects of nonlinear modal interactions on the thermoacoustic stability of annular combustors. *Journal of Engineering for Gas Turbines and Power*, 141(2), sep 2018.

[29] M. Wierman, B. Pomeroy, and W. Anderson. Development of combustion response functions in a subscale high-pressure transverse combustor. In M. Calabro, L. DeLuca, S. Frolov, L. Galfetti, and O. Haidn, editors, *Progress in Propulsion Physics*. EDP Sciences, 2016.

[30] L. Selle, R. Blouquin, M. Théron, L. H. Dorey, M. Schmid, and W. Anderson. Prediction and analysis of combustion instabilities in a model rocket engine. *Journal of Propulsion and Power*, 30(4):978–990, jul 2014.

[31] D. R. Kassoy. The response of a compressible gas to extremely rapid transient, spatially resolved energy addition: An asymptotic formulation. *Journal of Engineering Mathematics*, 68(3-4):249–262, aug 2010.

[32] D. R. Kassoy. Mechanical disturbances arising from thermal power deposition in a gas. *AIAA Journal*, 52(10):2328–2335, oct 2014.

[33] D. R. Kassoy. Non-diffusive ignition of a gaseous reactive mixture following time-resolved, spatially distributed energy deposition. *Combustion Theory and Modelling*, 18(1):101–116, jan 2014.

[34] D. R. Kassoy. The Zeldovich spontaneous reaction wave propagation concept in the fast/modest heating limits. *Journal of Fluid Mechanics*, 791:439–463, feb 2016.

[35] D. R. Kassoy. Thermomechanical concepts and modeling for stability physics in liquid-propellant rocket engines. *AIAA Journal*, 55(6):2043–2051, jun 2017.

[36] J. W. Meyer and A. K. Oppenheim. Dynamic response of a plane-symmetrical exothermic reaction center. *AIAA Journal*, 10(11):1509–1513, nov 1972.

[37] L. J. Zajac and A. K. Oppenheim. Dynamics of an explosive reaction center. *AIAA Journal*, 9(4):545–553, apr 1971.

[38] L. M. Cohen, J. M. Short, and A. K. Oppenheim. A computational technique for the evaluation of dynamic effects of exothermic reactions. *Combustion and Flame*, 24:319–334, feb 1975.

[39] C. Vázquez-Espí and A. Liñán. Fast, non-diffusive ignition of a gaseous reacting mixture subject to a point energy source. *Combustion Theory and Modelling*, 5(3):485–498, sep 2001.

[40] C. Vázquez-Espí and A. Liñán. Thermal-diffusive ignition and flame initiation by a local energy source. *Combustion Theory and Modelling*, 6(2):297–315, jun 2002.

[41] H. Q. Zhang, Y. J. Ga, B. Wang, and X. L. Wang. Analysis of combustion instability via constant volume combustion in a LOX/RP-1 bipropellant liquid rocket engine. *Science China Technological Sciences*, 55(4):1066–1077, feb 2012.

[42] I. Duran and S. Moreau. Solution of the quasi-one-dimensional linearized Euler equations using flow invariants and the Magnus expansion. *Journal of Fluid Mechanics*, 723:190–231, apr 2013.

[43] L. Magri, J. O'Brien, and M. Ihme. Effects of nozzle Helmholtz number on indirect combustion noise by compositional perturbations. *Journal of Engineering for Gas Turbines and Power*, 140(3), oct 2017.

[44] D. G. Crighton. Basic principles of aerodynamic noise generation. *Progress in Aerospace Sciences*, 16(1):31–96, jan 1975.

[45] G. Lacaze, E. Richardson, and T. Poinsot. Large eddy simulation of spark ignition in a turbulent methane jet. *Combustion and Flame*, 156(10):1993–2009, oct 2009.

[46] N. Swaminathan, G. Xu, A. P. Dowling, and R. Balachandran. Heat release rate correlation and combustion noise in premixed flames. *Journal of Fluid Mechanics*, 681:80–115, jun 2011.

[47] T. Steinbacher. *Analysis and Low-Order Modeling of Interactions between Acoustics, Hydrodynamics and Premixed Flames*. PhD thesis, Technical University of Munich, 2019.

[48] B. T. Chu. Pressure waves generated by addition of heat in a gaseous medium. Technical Report NACA-TN-3411, National Advisory Committee for Aeronautics, 1955.

[49] M. Leyko, F. Nicoud, and T. Poinsot. Comparison of direct and indirect combustion noise mechanisms in a model combustor. *AIAA Journal*, 47(11):2709–2716, nov 2009.

[50] M. L. Frezzotti, F. Nasuti, C. Huang, C. Merkle, and W. E. Anderson. Response function modeling in the study of longitudinal combustion instability by a quasi-1D eulerian solver. In *51st AIAA/SAE/ASEE Joint Propulsion Conference*. American Institute of Aeronautics and Astronautics, jul 2015.

[51] M. J. Lighthill. On sound generated aerodynamically. I. General theory. *Proceedings of the Royal Society A: Mathematical, Physical and Engineering Sciences*, 211(1107):564–587, mar 1952.

[52] D. G. Crighton, A. P. Dowling, J. E. Ffowcs Williams, M. Heckl, and F. G. Leppington. *Modern Methods in Analytical Acoustics*. Springer London, 1992.

[53] C. Bailly, C. Bogey, and S. Candel. Modelling of sound generation by turbulent reacting flows. *International Journal of Aeroacoustics*, 9(4-5):461–489, jun 2010.

[54] B. T. Chu. On the energy transfer to small disturbances in fluid flow (part I). *Acta Mechanica*, 1(3):215–234, sep 1965.

[55] M. K. Myers. Transport of energy by disturbances in arbitrary steady flows. *Journal of Fluid Mechanics*, 226(-1):383, may 1991.

[56] G. A. Flandro. On the oscilatory behavior of liquid propellant rockets. *International Journal of Energetic Materials and Chemical Propulsion*, 7(4):315–358, 2008.

[57] B. T. Zinn. A theoretical study of nonlinear combustion instability in liquid-propellant rocket engines. *AIAA Journal*, 6(10):1966–1972, oct 1968.

[58] T. Poinsot and S. Candel. A nonlinear model for ducted flame combustion instabilities. *Combustion Science and Technology*, 61(4-6):121–153, oct 1988.

[59] N. Noiray, D. Durox, T. Schuller, and S. Candel. A unified framework for nonlinear combustion instability analysis based on the flame describing function. *Journal of Fluid Mechanics*, 615:139, nov 2008.

[60] W. A. Sirignano. Driving mechanisms for combustion instability. *Combustion Science and Technology*, 187(1-2):162–205, dec 2014.

[61] W. A. Sirignano and L. Crocco. A shock wave model of unstable rocket combustors. *AIAA Journal*, 2(7):1285–1296, July 1964.

[62] P. Gupta, G. Lodato, and C. Scalo. Spectral energy cascade in thermoacoustic shock waves. *Journal of Fluid Mechanics*, 831:358–393, oct 2017.

[63] M. T. Migliorino and C. Scalo. Heat-induced planar shock waves in supercritical fluids. *Shock Waves*, 30(2):153–167, dec 2019.

[64] M. T. Migliorino and C. Scalo. Real-fluid effects on standing-wave thermoacoustic instability. *Journal of Fluid Mechanics*, 883, nov 2019.

[65] P. Schmitt, T. Poinsot, B. Schuermans, and K. P. Geigle. Large-eddy simulation and experimental study of heat transfer, nitric oxide emissions and combustion instability in a swirled turbulent high-pressure burner. *Journal of Fluid Mechanics*, 570:17, jan 2007.

[66] P. Wolf, R. Balakrishnan, G. Staffelbach, L. Y. M. Gicquel, and T. Poinsot. Using LES to study reacting flows and instabilities in annular combustion chambers. *Flow, Turbulence and Combustion*, 88(1-2):191–206, sep 2011.

[67] Y. Huang and V. Yang. Dynamics and stability of lean-premixed swirl-stabilized combustion. *Progress in Energy and Combustion Science*, 35(4):293–364, aug 2009.

[68] R. Garby. *Simulations of flame stabilization and stability in high-pressure propulsion systems*. PhD thesis, Institut National Polytechnique de Toulouse, 2013.

[69] M. E. Harvazinski, W. E. Anderson, and C. L. Merkle. Analysis of self-excited combustion instabilities using two- and three-dimensional simulations. *Journal of Propulsion and Power*, 29(2):396–409, mar 2013.

[70] M. E. Harvazinski, C. Huang, V. Sankaran, T. W. Feldman, W. E. Anderson, C. L. Merkle, and D. G. Talley. Coupling between hydrodynamics, acoustics, and heat release in a self-excited unstable combustor. *Physics of Fluids*, 27(4):045102, apr 2015.

[71] R. Smith, G. Xia, W. A. Anderson, and C. L. Merkle. Computational simulations of the effect of backstep height on nonpremixed combustion instability. *AIAA Journal*, 48(9):1857–1868, sep 2010.

[72] R. Smith, G. Xia, W. Anderson, and C. L. Merkle. Computational studies of the effects of oxidiser injector length on combustion instability. *Combustion Theory and Modelling*, 16(2):341–368, nov 2011.

[73] S. Sardeshmukh, M. Bedard, and W. Anderson. The use of OH^* and CH^* as heat release markers in combustion dynamics. *International Journal of Spray and Combustion Dynamics*, 9(4):409–423, jul 2017.

[74] C. J. Morgan, K. J. Shipley, and W. E. Anderson. Comparative evaluation between experiment and simulation for a transverse instability. *Journal of Propulsion and Power*, 31(6):1696–1706, nov 2015.

[75] W. Mayer, A. Schik, M. Schrffler, and H. Tamura. Injection and mixing processes in high-pressure liquid oxygen/gaseous hydrogen rocket combustors. *Journal of Propulsion and Power*, 16(5):823–828, sep 2000.

[76] T. Schmitt, J. Rodriguez, I. A. Leyva, and S. Candel. Experiments and numerical simulation of mixing under supercritical conditions. *Physics of Fluids*, 24(5):055104, may 2012.

[77] T. Lieuwen. Modeling premixed combustion-acoustic wave interactions: A review. *Journal of Propulsion and Power*, 19(5):765–781, sep 2003.

[78] Y. Yu, J. C. Sisco, S. Rosen, A. Madhav, and W. E. Anderson. Spontaneous longitudinal combustion instability in a continuously-variable resonance combustor. *Journal of Propulsion and Power*, 28(5):876–887, sep 2012.

[79] L. J. Zajac and A. K. Oppenheim. Thermodynamic computations for the gasdynamic analysis of explosion phenomena. *Combustion and Flame*, 13(5):537–550, oct 1969.

[80] D. Li, G. Xia, V. Sankaran, and C. L. Merkle. Computational framework for complex fluid physics applications. In *Computational Fluid Dynamics 2004*, pages 619–624. Springer Berlin Heidelberg, 2006.

[81] C. Lian, G. Xia, and C. L. Merkle. Solution-limited time stepping to enhance reliability in CFD applications. *Journal of Computational Physics*, 228(13):4836–4857, jul 2009.

[82] C. Lian, G. Xia, and C. L. Merkle. Impact of source terms on reliability of CFD algorithms. *Computers & Fluids*, 39(10):1909–1922, dec 2010.

[83] C. K. W. Tam. *Computational Aeroacoustics*. Cambridge University Press, 2012.

[84] S. Srinivasan, R. Ranjan, and S. Menon. Flame dynamics during combustion instability in a high-pressure, shear-coaxial injector combustor. *Flow, Turbulence and Combustion*, 94(1):237–262, sep 2014.

[85] V. Giurgiutiu. *Structural Health Monitoring with Piezoelectric Wafer Active Sensors*. Elsevier, 2014.

[86] E. W. Ng and M. Geller. A table of integrals of the error functions. *Journal of Research of the National Bureau of Standards - B. Mathematical Sciences*, 73B(1), 1969.

[87] K.R. McManus, T. Poinsot, and S.M. Candel. A review of active control of combustion instabilities. *Progress in Energy and Combustion Science*, 19(1):1–29, jan 1993.

[88] A.P. Dowling. The calculation of thermoacoustic oscillations. *Journal of Sound and Vibration*, 180(4):557–581, mar 1995.

[89] P. Gupta and C. Scalo. Spectral energy cascade and decay in nonlinear acoustic waves. *Physical Review E*, 98(3), sep 2018.

[90] A. D. Pierce. *Acoustics*. Springer International Publishing, 2019.

[91] F. E. C. Culick. Unsteady motions in combustion chambers for propulsion systems. Technical Report AG-AVT-039, NATO RTO AGARDograph, 2006.

[92] A. R. Madhav. Efficacy of a nonlinear acoustic model for combustion instability prediction. Master's thesis, Aeronautics and Astronautics, Purdue University, May 2011.

[93] D. N. Manik. *Vibro-Acoustics*. Taylor & Francis Inc, 2017.

[94] A. Pons, T. Fuller, S. V. Sardeshmukh, and W. E. Anderson. Analysis of the interactions between acoustics and unsteady heat release in a self-excited single element combustor. In *2018 Joint Propulsion Conference*. American Institute of Aeronautics and Astronautics, jul 2018.

[95] J. F. Clarke, D. R. Kassoy, and N. Riley. Shocks generated in a confined gas due to rapid heat addition at the boundary. i. weak shock waves. *Proceedings of the Royal Society of London. A. Mathematical and Physical Sciences*, 393(1805):309–329, jun 1984.

[96] D. T. Blackstock. Connection between the fay and fubini solutions for plane sound waves of finite amplitude. *The Journal of the Acoustical Society of America*, 39(6):1019–1026, jun 1966.

[97] I. Rudnick. On the attenuation of a repeated sawtooth shock wave. *The Journal of the Acoustical Society of America*, 25(5):1012–1013, sep 1953.

A. APPENDIX A

A.1 Total Heat for Gaussian Spherical Distribution and Step Temporal Profile

The total heat addition is given by

$$Q = \int_t \int_V q dV dt = \int_{t_{hab}}^{t_{hae}} \int_0^{R_{ha}} K_{ha_3} e^{\left(-\frac{1}{2}\left(\frac{r}{\sigma_r}\right)^2\right)} 4\pi r^2 dr dt \tag{A.1}$$

where K_{ha_3} is defined as

$$K_{ha_3} = \frac{E_{ha}}{(2\pi)^{3/2}\sigma_r^3 \Delta t_{ha}} \tag{A.2}$$

where Δt_{ha} is defined as

$$\Delta t_{ha} = t_{hae} - t_{hab} \tag{A.3}$$

Integrating by parts Eq. (A.1) leads to

$$Q = \frac{2E_{ha}}{\sqrt{2\pi}} \left[-\frac{R_{ha}}{\sigma_r} e^{-\frac{1}{2}\left(\frac{R_{ha}}{\sigma_r}\right)^2} + \frac{\sqrt{2\pi}}{2} erf\left(\frac{R_{ha}}{\sqrt{2}\sigma_r}\right) \right] \tag{A.4}$$

A.2 Total Heat for Gaussian Spherical Distribution and Temporal Profile

$$Q = \int_t \int_V q dV dt = \int_{t_{hab}}^{t_{hae}} \int_0^{R_{ha}} K_{ha_4} e^{\left(-\frac{1}{2}\left(\frac{r}{\sigma_r}\right)^2\right)} e^{\left(-\frac{1}{2}\left(\frac{t-t_c}{\sigma_t}\right)^2\right)} 4\pi r^2 dr dt \tag{A.5}$$

where K_{ha_4} is defined as

$$K_{ha_4} = \frac{E_{ha}}{4\pi^2 \sigma_r^3 \sigma_t} \tag{A.6}$$

Integrating by parts Eq. (A.5) leads to

$$Q = \frac{2E_{ha}}{\sqrt{2\pi}}\left[-\frac{R_{ha}}{\sigma_r}e^{-\frac{1}{2}\left(\frac{R_{ha}}{\sigma_r}\right)^2} + \frac{\sqrt{2\pi}}{2}erf\left(\frac{R_{ha}}{\sqrt{2}\sigma_r}\right)\right]erf\left(\frac{\Delta t_{ha}}{2\sqrt{2}\sigma_r}\right) \tag{A.7}$$

where Δt_{ha} is defined in Eq. (A.3).

B. APPENDIX B

B.1 Derivation of the pressure response to a heat source with Gaussian spatial and temporal distribution

The heat source with with Gaussian spatial and temporal distribution is given by

$$q_1(x,t) = K_{xt}\ exp\left[-\frac{1}{2}\left(\frac{x}{\sigma_x}\right)^2\right] exp\left[-\frac{1}{2}\left(\frac{t-t_c}{\sigma_t}\right)^2\right] \tag{B.1}$$

where t_c is the center time of the Gaussian temporal profile, and K_{xt} is the heat source magnitude parameter defined as

$$K_{xt} = \frac{E_{ha}}{2\pi\sigma_x\sigma_t H_{ha} W_{ha}} = \frac{q_{ha} L_{ha} \Delta t_{ha}}{2\pi\sigma_x\sigma_t} \tag{B.2}$$

where q_{ha} is the flat profile heat release value defined in Eq. (3.4). The shape of the heat source is depicted in Fig. 3.2 (R). The standard deviations that define the Gaussian spatial and temporal profiles are set to $\sigma_x = L_{ha}/7$ and $\sigma_t = \Delta t_{ha}/7$. The source term $f(x,t)$ in Eq. (2.33) is computed by applying the temporal derivative of the heat source of Eq. (B.1) as follows

$$\begin{aligned} f(x,t) &= (\gamma-1)\frac{\partial q_1}{\partial t} \\ &= -\frac{(\gamma-1)K_{xt}}{\sigma_t^2} exp\left[-\frac{1}{2}\left(\frac{x}{\sigma_x}\right)^2\right](t-t_c)\ exp\left[-\frac{1}{2}\left(\frac{t-t_c}{\sigma_t}\right)^2\right] \end{aligned} \tag{B.3}$$

The substitution of Eq. (B.3) into Eq. (2.35) provides the expression to be integrated to solve the pressure response

$$p_{1,p}(x,t) = \frac{1}{2c_0}\int_0^t \int_{x-c_0(t-s)}^{x+c_0(t-s)} \frac{(1-\gamma)K_{xt}}{\sigma_t^2} e^{-\frac{1}{2}\left(\frac{z}{\sigma_x}\right)^2}(s-t_c)\ e^{-\frac{1}{2}\left(\frac{s-t_c}{\sigma_t}\right)^2} dzds \tag{B.4}$$

After integrating with respect to the spatial variable z, and recalling that $p_1(x,t) = p_{1,p}(x,t)$ as presented in Section 2.3, the integral reads as

$$p_1(x,t) = \frac{(1-\gamma)K_{xt}}{2c_0\sigma_t^2}\int_0^t \left[\frac{\sqrt{2\pi}\sigma_x}{2} erf\left(\frac{z}{\sqrt{2}\sigma_x}\right)\right]_{x-c_0(t-s)}^{x+c_0(t-s)} (s-t_c)\ e^{-\frac{1}{2}\left(\frac{s-t_c}{\sigma_t}\right)^2} ds\ . \tag{B.5}$$

For the sake of easing the derivation, the integral of Eq. (B.5) is fully derived for the left traveling term $p_{1,p}^-(x,t)$ related to $x + c_0(t-s)$. The derivation of the right traveling term $p_{1,p}^+(x,t)$ related to $x - c_0(t-s)$ is identical and displayed in the final result. Thus, adding the left and right traveling parts yields to the complete solution as follows

$$p_{1,p}(x,t) = p_{1,p}^+(x,t) + p_{1,p}^-(x,t)\ , \tag{B.6}$$

where the left and right traveling solutions are, respectively

$$p_{1,p}^-(x,t) = \frac{(1-\gamma)K_{xt}\sqrt{2\pi}\sigma_x}{4c_0\sigma_t^2}\int_0^t erf\left(\frac{x+c_0(t-s)}{\sqrt{2}\sigma_x}\right)(s-t_c)\ e^{-\frac{1}{2}\left(\frac{s-t_c}{\sigma_t}\right)^2} ds\ , \tag{B.7}$$

$$p_{1,p}^+(x,t) = -\frac{(1-\gamma)K_{xt}\sqrt{2\pi}\sigma_x}{4c_0\sigma_t^2}\int_0^t erf\left(\frac{x-c_0(t-s)}{\sqrt{2}\sigma_x}\right)(s-t_c)\ e^{-\frac{1}{2}\left(\frac{s-t_c}{\sigma_t}\right)^2} ds\ . \tag{B.8}$$

The term $\left(\frac{x\pm c_0(t-s)}{\sqrt{2}\sigma_x}\right)$ inside the error function in Eq. (B.7) and Eq.(B.8) is rewritten in Eq.(B.9) in terms of constants accompanying the temporal integration variable s to simplify the calculations

$$\begin{cases} \left(\frac{x+c_0(t-s)}{\sqrt{2}\sigma_x}\right) = (a_1 s + b_1) \rightarrow a_1 = -\frac{c_0}{\sqrt{2}\sigma_x}; \quad b_1 = \frac{x+c_0 t}{\sqrt{2}\sigma_x}. \\ \left(\frac{x-c_0(t-s)}{\sqrt{2}\sigma_x}\right) = (a_2 s + b_2) \rightarrow a_2 = \frac{c_0}{\sqrt{2}\sigma_x}; \quad b_2 = \frac{x-c_0 t}{\sqrt{2}\sigma_x}. \end{cases} \tag{B.9}$$

Integrating Eq. (B.7) by parts using $\int u dv = uv - \int v du$

$$\begin{cases} u = erf\left(a_1 s + b_1\right) & du = \frac{2a_1}{\sqrt{\pi}} e^{-(a_1 s + b_1)^2} \\ v = -\sigma_t^2 e^{-\frac{1}{2}\left(\frac{s-t_c}{\sigma_t}\right)^2} & dv = (s-t_c)\ e^{-\frac{1}{2}\left(\frac{s-t_c}{\sigma_t}\right)^2} ds \end{cases} \tag{B.10}$$

$$p_{1,p}^{-}(x,t) = -Cerf\left(a_1 s + b_1\right)\sigma_t^2 e^{-\frac{1}{2}\left(\frac{s-t_c}{\sigma_t}\right)^2}\Big|_0^t + C\int_0^t \sigma_t^2 e^{-\frac{1}{2}\left(\frac{s-t_c}{\sigma_t}\right)^2}\frac{2a_1}{\sqrt{\pi}}e^{-(a_1 s+b_1)^2}ds \ , \tag{B.11}$$

where the constant C multiplying both terms in Eq. (B.11) is given by

$$C = \frac{(1-\gamma)K_{xt}\sqrt{2\pi}\sigma_x}{4c_0\sigma_t^2} \ . \tag{B.12}$$

$p_{1,p}^{-}(x,t)$ is split into two terms $I_1 + I_2$ in Eq. (B.11). After evaluating the integral limits, the first term is given by

$$I_1 = -Cerf\left(a_1 t + b_1\right)\sigma_t^2 e^{-\frac{1}{2}\left(\frac{t-t_c}{\sigma_t}\right)^2} + Cerf\left(b_1\right)\sigma_t^2 e^{-\frac{1}{2}\left(\frac{t_c}{\sigma_t}\right)^2} \ . \tag{B.13}$$

Substituting C, plugging in the parameters of Eq. (B.9), and writing $x + c_0 t$ as $c_0\left(\frac{x}{c_0} + t\right)$ yields to

$$I_1 = \frac{(\gamma-1)K_{xt}\sqrt{2\pi}\sigma_x}{4c_0}\left[erf\left(\frac{x}{\sqrt{2}\sigma_x}\right)e^{-\frac{1}{2}\left(\frac{t-t_c}{\sigma_t}\right)^2} - erf\left(\frac{c_0}{\sqrt{2}\sigma_x}\left(\frac{x}{c_0}+t\right)\right)e^{-\frac{1}{2}\left(\frac{t_c}{\sigma_t}\right)^2}\right] \ . \tag{B.14}$$

The second term I_2 in Eq. (B.11) is given by

$$I_2 = \frac{2a_1 C\sigma_t^2}{\sqrt{\pi}}\int_0^t e^{-\frac{1}{2}\left(\frac{s-t_c}{\sigma_t}\right)^2-(a_1 s+b_1)^2}ds \ . \tag{B.15}$$

Expanding the exponent of e yields to

$$I_2 = \frac{2a_1 C\sigma_t^2}{\sqrt{\pi}}e^{-\frac{1}{2}\left(\frac{t_c}{\sigma_t}\right)^2}e^{-b_1^2}\int_0^t e^{-s^2\left(\frac{1+2\sigma_t^2 a_1^2}{2\sigma_t^2}\right)+s\left(\frac{t_c}{\sigma_t^2}-2a_1 b_1\right)}ds \ . \tag{B.16}$$

It should be pointed out that the terms $e^{-\frac{1}{2}\left(\frac{t_c}{\sigma_t}\right)^2}$ and $e^{-b_1^2}$ are constant with respect to the integration variable s, and hence, can be put outside of the integral. This integral can be solved analytically as presented in [86] as

$$\int e^{-a^2z^2+bz}dz = \frac{\sqrt{\pi}}{2a}exp\left[\left(\frac{b}{2a}\right)^2\right]erf\left(az-\frac{b}{2a}\right) . \tag{B.17}$$

In case of Eq. (B.16), the equivalent a, b and z terms of Eq. (B.17) are

$$\begin{cases} a = \sqrt{\frac{1+2\sigma_t^2a_1^2}{2\sigma_t^2}} \\ b = \frac{t_c}{\sigma_t^2} - 2a_1b_1 \\ z = s \end{cases} \tag{B.18}$$

Using the reference solution of Eq. (B.17), the integral of Eq. (B.16) results in

$$\begin{aligned} I_2 = \frac{a_1C\sigma_t^2\sqrt{2}\sigma_t}{\sqrt{1+2\sigma_t^2a_1^2}}\, e^{-\frac{1}{2}\left(\frac{t_c}{\sigma_t}\right)^2} e^{-b_1^2}\, exp\left(\frac{\frac{t_c^2}{2\sigma_t^2} - 2a_1b_1t_c + 2\sigma_t^2a_1^2b_1^2}{1+2\sigma_t^2a_1^2}\right) x \\ erf\left(\sqrt{\frac{1+2\sigma_t^2a_1^2}{2\sigma_t^2}}s + \frac{\sqrt{2}\sigma_t}{\sqrt{1+2\sigma_t^2a_1^2}}\left(a_1b_1 - \frac{t_c}{2\sigma_t^2}\right)\right)\Big|_0^t . \end{aligned} \tag{B.19}$$

After evaluating the limits of the integral in Eq. (B.19), and combining all the exponentials into a single one, I_2 reads as

$$\begin{aligned} I_2 = \frac{a_1C\sigma_t^3\sqrt{2}}{\sqrt{1+2\sigma_t^2a_1^2}}\, exp\left(-\frac{(b_1+a_1t_c)^2}{1+2\sigma_t^2a_1^2}\right) x\left[erf\left(\sqrt{\frac{1+2\sigma_t^2a_1^2}{2\sigma_t^2}}t\right.\right. \\ \left.\left. + \frac{\sqrt{2}\sigma_t}{\sqrt{1+2\sigma_t^2a_1^2}}\left(a_1b_1 - \frac{t_c}{2\sigma_t^2}\right)\right) - erf\left(\frac{\sqrt{2}\sigma_t}{\sqrt{1+2\sigma_t^2a_1^2}}\left(a_1b_1 - \frac{t_c}{2\sigma_t^2}\right)\right)\right] . \end{aligned} \tag{B.20}$$

Substituting the value of C from Eq. (B.12), writing $x + c_0 t$ as $c_0\left(\frac{x}{c_0} + t\right)$, and plugging in the terms from Eq. (B.9) into the result of I_2 yields to

$$I_2 = \frac{(\gamma-1)K_{xt}\sqrt{2\pi}\sigma_x}{4c_0\sqrt{1+\frac{\sigma_x^2}{c_0^2\sigma_t^2}}}\ exp\left(-\frac{\left(\frac{x}{c_0}+t-t_c\right)^2}{2\sigma_t^2\left(1+\frac{\sigma_x^2}{c_0^2\sigma_t^2}\right)}\right) x\left[erf\left(\frac{c_0}{\sqrt{2}\sigma_x}\sqrt{1+\frac{\sigma_x^2}{c_0^2\sigma_t^2}}\ t - \frac{c_0}{\sqrt{2}\sigma_x}\frac{\frac{x}{c_0}+t+\frac{\sigma_x^2}{c_0^2\sigma_t^2}t_c}{\sqrt{1+\frac{\sigma_x^2}{c_0^2\sigma_t^2}}}\right) + erf\left(\frac{c_0}{\sqrt{2}\sigma_x}\frac{\frac{x}{c_0}+t+\frac{\sigma_x^2}{c_0^2\sigma_t^2}t_c}{\sqrt{1+\frac{\sigma_x^2}{c_0^2\sigma_t^2}}}\right)\right]. \tag{B.21}$$

On the last term, the antisymmetry property of the error function is used (i.e. $erf(-x) = -erf(x)$). Finally, the combination of I_1 and I_2 yields to the left traveling portion of the pressure response to unsteady heat release with Gaussian spatial and temporal profile. Substituting also the value of K_{xt} from Eq. (B.2) yields to

$$p_{1,p}^{-}(x,t) = \frac{(\gamma-1)E_{ha}}{4c_0\sqrt{2\pi}\sigma_t H_{ha}W_{ha}}\left[erf\left(\frac{x}{\sqrt{2}\sigma_x}\right)e^{-\frac{1}{2}\left(\frac{t-t_c}{\sigma_t}\right)^2} - erf\left(\frac{c_0}{\sqrt{2}\sigma_x}\left(\frac{x}{c_0}+t\right)\right)e^{-\frac{1}{2}\left(\frac{t_c}{\sigma_t}\right)^2} + \frac{1}{\sqrt{1+\frac{\sigma_x^2}{c_0^2\sigma_t^2}}}\ exp\left(-\frac{\left(\frac{x}{c_0}+t-t_c\right)^2}{2\sigma_t^2\left(1+\frac{\sigma_x^2}{c_0^2\sigma_t^2}\right)}\right)\left[erf\left(\frac{c_0}{\sqrt{2}\sigma_x}\sqrt{1+\frac{\sigma_x^2}{c_0^2\sigma_t^2}}\ t - \frac{c_0}{\sqrt{2}\sigma_x}\frac{\frac{x}{c_0}+t+\frac{\sigma_x^2}{c_0^2\sigma_t^2}t_c}{\sqrt{1+\frac{\sigma_x^2}{c_0^2\sigma_t^2}}}\right) + erf\left(\frac{c_0}{\sqrt{2}\sigma_x}\frac{\frac{x}{c_0}+t+\frac{\sigma_x^2}{c_0^2\sigma_t^2}t_c}{\sqrt{1+\frac{\sigma_x^2}{c_0^2\sigma_t^2}}}\right)\right]\right]. \tag{B.22}$$

Applying the same resolution method for the right traveling portion of the pressure response $p^{+}_{1,p}(x,t)$ yields to

$$p^{+}_{1,p}(x,t) = \frac{(\gamma-1)E_{ha}}{4c_0\sqrt{2\pi}\sigma_t H_{ha}W_{ha}}\Bigg[-erf\left(\frac{x}{\sqrt{2}\sigma_x}\right)e^{-\frac{1}{2}\left(\frac{t-t_c}{\sigma_t}\right)^2}$$
$$+erf\left(\frac{c_0}{\sqrt{2}\sigma_x}\left(\frac{x}{c_0}-t\right)\right)e^{-\frac{1}{2}\left(\frac{t_c}{\sigma_t}\right)^2}+\frac{1}{\sqrt{1+\frac{\sigma_x^2}{c_0^2\sigma_t^2}}}\,exp\left(-\frac{\left(\frac{x}{c_0}-t+t_c\right)^2}{2\sigma_t^2\left(1+\frac{\sigma_x^2}{c_0^2\sigma_t^2}\right)}\right)$$
$$\Bigg[erf\left(\frac{c_0}{\sqrt{2}\sigma_x}\sqrt{1+\frac{\sigma_x^2}{c_0^2\sigma_t^2}}\;t+\frac{c_0}{\sqrt{2}\sigma_x}\frac{\frac{x}{c_0}-t-\frac{\sigma_x^2}{c_0^2\sigma_t^2}t_c}{\sqrt{1+\frac{\sigma_x^2}{c_0^2\sigma_t^2}}}\right)$$
$$-erf\left(\frac{c_0}{\sqrt{2}\sigma_x}\frac{\frac{x}{c_0}-t-\frac{\sigma_x^2}{c_0^2\sigma_t^2}t_c}{\sqrt{1+\frac{\sigma_x^2}{c_0^2\sigma_t^2}}}\right)\Bigg]\Bigg]\,. \tag{B.23}$$

B.2 Derivation of the pressure response to a heat source with flat spatial distribution and sinusoidal temporal profile

The heat source with with a flat spatial distribution and a sinusoidal temporal profile defined as

$$q_1(x,t) = K_{ha_3}\sin(\omega t)\left[H\left(x+\frac{L_{hab}}{2}\right)-H\left(x-\frac{L_{hab}}{2}\right)\right] \tag{B.24}$$

where $H(x-L)$ is the unit Heaviside function, ω is the angular frequency of the fluctuating heat source, L_{ha} is the length of the heat source, and K_{ha_3} is the heat source magnitude parameter defined as

$$K_{ha_3} = \frac{E_{ha}f}{L_{ha}H_{ha}W_{ha}} = \frac{E_{ha}\omega}{2\pi L_{ha}H_{ha}W_{ha}} \tag{B.25}$$

where f is the frequency of the fluctuating heat source. The source term $f(x,t)$ in Eq. (2.33) is computed by applying the temporal derivative of the heat source of Eq. (B.24) as follows

$$f(x,t) = (\gamma-1)\frac{\partial q_1}{\partial t} = (\gamma-1)K_{ha_3}\omega\cos(\omega t)\left[H\left(x+\frac{L_{hab}}{2}\right) - H\left(x-\frac{L_{hab}}{2}\right)\right] \tag{B.26}$$

The substitution of Eq. (B.26) into Eq. (2.35) provides the expression to be integrated to solve the pressure response

$$p_{1,p}(x,t) = \frac{(\gamma-1)K_{ha_3}\omega}{2c_0}\int_0^t\int_{x-c_0(t-s)}^{x+c_0(t-s)}\cos(\omega s)\left[H\left(z+\frac{L_{hab}}{2}\right) - H\left(z-\frac{L_{hab}}{2}\right)\right]dzds \tag{B.27}$$

After integrating with respect to the spatial variable z, and recalling that $p_1(x,t) = p_{1,p}(x,t)$ as presented in Section 2.3, the integral reads as

$$\begin{aligned} p_1(x,t) = \frac{(\gamma-1)K_{ha_3}\omega}{2c_0}\int_0^t\cos(\omega s)\Bigg[&max\left(0, z+\frac{L_{hab}}{2}\right) \\ &-max\left(0, z-\frac{L_{hab}}{2}\right)\Bigg]_{x-c_0(t-s)}^{x+c_0(t-s)}ds \end{aligned} \tag{B.28}$$

Applying the limits of z yields to

$$\begin{aligned} p_1(x,t) = \frac{(\gamma-1)K_{ha_3}\omega}{2c_0}\int_0^t\cos(\omega s)\Bigg[&max\left(0, x+c_0(t-s)+\frac{L_{hab}}{2}\right) \\ -max\left(0, x+c_0(t-s)-\frac{L_{hab}}{2}\right) &- max\left(0, x-c_0(t-s)+\frac{L_{hab}}{2}\right) \\ +max\left(0, x-c_0(t-s)-\frac{L_{hab}}{2}\right)\Bigg]ds &= \Psi_1+\Psi_2+\Psi_3+\Psi_4 \end{aligned} \tag{B.29}$$

where

$$\Psi_1 = \frac{(\gamma-1)K_{ha_3}\omega}{2c_0}\int_0^t\cos(\omega s)\ max\left(0, x+c_0(t-s)+\frac{L_{hab}}{2}\right)ds \tag{B.30}$$

$$\Psi_2 = -\frac{(\gamma-1)K_{ha_3}\omega}{2c_0}\int_0^t \cos(\omega s)\ max\left(0, x + c_0(t-s) - \frac{L_{hab}}{2}\right) ds \tag{B.31}$$

$$\Psi_3 = -\frac{(\gamma-1)K_{ha_3}\omega}{2c_0}\int_0^t \cos(\omega s)\ max\left(0, x - c_0(t-s) + \frac{L_{hab}}{2}\right) ds \tag{B.32}$$

$$\Psi_4 = \frac{(\gamma-1)K_{ha_3}\omega}{2c_0}\int_0^t \cos(\omega s)\ max\left(0, x - c_0(t-s) - \frac{L_{hab}}{2}\right) ds \tag{B.33}$$

Integrating Eqs. (B.30)-(B.33) with respect to the temporal variable s yields to

$$\Psi_1 = A_{p3}\left[1 + \cos\left(\frac{\omega}{c_0}\xi_1\right)(H(\chi_1) - 1) - \cos(\omega t)H(\chi_1)\right] H(\xi_1) \tag{B.34}$$

$$\Psi_2 = -A_{p3}\left[1 + \cos\left(\frac{\omega}{c_0}\xi_2\right)(H(\chi_2) - 1) - \cos(\omega t)H(\chi_2)\right] H(\xi_2) \tag{B.35}$$

$$\Psi_3 = A_{p3}\left\{\left[\cos\left(\frac{\omega}{c_0}\eta_1\right) - \cos(\omega t)\right] H(\chi_1) + \left[1 - \cos\left(\frac{\omega}{c_0}\eta_1\right)\right] H(\eta_1)\right\} \tag{B.36}$$

$$\Psi_4 = A_{p3}\left[\cos(\omega t) + \cos\left(\frac{\omega}{c_0}\eta_2\right)(H(\eta_2) - 1) - H(\eta_2)\right] H(\chi_2) \tag{B.37}$$

where the auxiliar variables ξ_1, ξ_2, η_1, η_2, χ_1, and χ_2 are defined as

$$\begin{cases} \xi_1 = x + c_0 t + \frac{L_{ha}}{2}\ ; & \xi_2 = x + c_0 t - \frac{L_{ha}}{2}\ ; \\ \eta_1 = x - c_0 t + \frac{L_{ha}}{2}\ ; & \eta_2 = x - c_0 t - \frac{L_{ha}}{2}\ ; \\ \chi_1 = x + \frac{L_{ha}}{2}\ ; & \chi_2 = x - \frac{L_{ha}}{2}\ ; \end{cases} \tag{B.38}$$

In addition, the amplitude constant A_{p3} is given by

$$A_{p3} = \frac{(\gamma-1)\,E_{ha}}{4\pi L_{ha} H_{ha} W_{ha}} \tag{B.39}$$

Combining the above expression leads to the solution of the pressure response of a quiescent fluid to a heat source with flat spatial distribution and sinusoidal temporal profile

$$
\begin{aligned}
p_1(x,t) = A_{p3}\Bigg\{ & \left[1+\cos\left(\frac{\omega}{c_0}\xi_1\right)\left(H\left(\chi_1\right)-1\right)-\cos\left(\omega t\right)H\left(\chi_1\right)\right]H\left(\xi_1\right) \\
& -\left[1+\cos\left(\frac{\omega}{c_0}\xi_2\right)\left(H\left(\chi_2\right)-1\right)-\cos\left(\omega t\right)H\left(\chi_2\right)\right]H\left(\xi_2\right) \\
& +\left[\cos\left(\frac{\omega}{c_0}\eta_1\right)-\cos\left(\omega t\right)\right]H\left(\chi_1\right)+\left[1-\cos\left(\frac{\omega}{c_0}\eta_1\right)\right]H\left(\eta_1\right) \\
& +\left[\cos\left(\omega t\right)+\cos\left(\frac{\omega}{c_0}\eta_2\right)\left(H\left(\eta_2\right)-1\right)-H\left(\eta_2\right)\right]H\left(\chi_2\right)\Bigg\}
\end{aligned}
\tag{B.40}
$$

VITA

Arnau Pons was born in Barcelona, Spain. He completed his Bachelor's and Master's Degree in Aeronautical Engineering by the Polytechnic University of Catalonia receiving an honor distinction for his Master's Thesis. During his studies in Barcelona, he founded the Trencalòs research team dedicated to design, build, and fly high performance Unmanned Aerial Vehicles (UAV).

Arnau completed his Master's Degree in Aerospace Propulsion Theory and Engineering at Beihang University in Spring 2015. He also participated at the International Space University (ISU) Space Studies Program 2015 hosted by Ohio University in partnership with Glenn Research Center from June to August 2015. In the Fall 2016, Arnau joined Purdue University to conduct his doctoral studies in Aeronautics and Astronautics majoring in Propulsion and minoring in Dynamics & Controls. For his doctoral thesis he worked at the Maurice J. Zucrow Laboratories under the guidance of Prof. William E. Anderson. He was awarded "la Caixa" fellowship to support the first two years of his PhD. During his studies at Purdue, he also received a travel grant from Purdue to attend the Wernher Von Braun Memorial Symposium in Hunstville, AL, and he won the Third Best Presentation Award at the AAE 2018 Research Symposium Series. Arnau also completed an internship at the North Atlantic Treaty Organization (NATO) in the Allied Command Transformation (ACT) headquarters in Norfolk, VA. After the internship, he joined NATO as a civilian. Arnau defended his doctoral thesis in July 2020 graduating in Summer 2020.

Arnau is happily married to Orzuri, a doctoral candidate in Aeronautics and Astronautics at Purdue University. He is native Catalan and Spanish speaker, fluent in English, and also studied French and Mandarin Chinese.